CYTOCOMPATIBLE COATINGS

TO CONTROL CELL ACTIVITY

A Dissertation
Presented to
The Academic Faculty

by

Irina Drachuk

In Partial Fulfillment
of the Requirements for the Degree
Doctor of Philosophy in the
School of Materials Science and Engineering

Georgia Institute of Technology
August, 2014

CYTOCOMPATIBLE COATINGS

TO CONTROL CELL ACTIVITY

Approved by:

Dr. Vladimir V. Tsukruk, Advisor
School of Materials Science and Engineering
Georgia Institute of Technology

Dr. Zhiqun Lin
School of Materials Science and Engineering
Georgia Institute of Technology

Dr. Nancy Kelley-Loughnane, Co-Advisor
Air Force Research Laboratory, Directorate of Human Performance
Wright Patterson AFB

Dr. Ken Gall
School of Materials Science and Engineering
Georgia Institute of Technology

Dr. Valeria Milam
School of Materials Science and Engineering
Georgia Institute of Technology

Date Approved: May 6, 2014

Dedicated to my loving family

ACKNOWLEDGEMENTS

I would like to express my gratitude to Prof. Vladimir V. Tsukruk for giving me the opportunity to join his research group, for believing in me, for giving me his generous advice, inspiring guidance and encouragement throughout my research during these past five years. His passion for the research through the hard work and natural curiosity taught me a valuable life lesson that devoted effort will always be rewarded and recognized. His effort and influence helped me to carry a fruitful research as a part of Air Force Center of Excellence (CoE) on Bio-nano-enabled Inorganic/Organic Nanostructures and Improved Cognition (BIONIC) Program. Prof. Vladimir V. Tsukruk's encouragement fostered me to be recognized as an outstanding graduate student in polymer science and engineering. I will always cherish this learning experience for the rest of my life. I would also like to show my special thanks to my co-advisor, Dr. Nancy Kelley-Loughnane, for her helpful feedback, significant and constructive suggestions, and every effort she made to help me with the NRC fellowship preparation. I would like to acknowledge all the committee members Prof. Valeria Milam, Prof. Zhiqun Lin, and Prof. Ken Gall for their insightful discussions and suggestions, and kind willingness to be a part of my dissertation committee.

Our collaborators from Tufts University and Air Force Research Laboratory played a critical role in this work. In particular, I would like to thank Dr. Svetlana Harbaugh for her guidance, expertise in Microbiology and significant effort in discussion of my research data. Also I acknowledge Prof. David L. Kaplan, Dr. Rosella Callabrese for their help, expertise in silk material and assistance in the research discussion.

A good support system is important in fostering the great outcome, so for that I am thankful to former and current members of SEMA group. Particularly, I would like to thank Dr. Veronika Kozlovskaya, Dr. Olga Shchepelina for their constant support and guidance. I would also like to thank former lab members Jessica Carter, Dr. Tobias Koenig, as well as current members Dr. Chunhong Ye, Dr. Marius Chyasnavichyus, Rattanon Suntivich for their help and technical support.

Financial support from the grants FA9550-11-1-0233 and FA9550-09-1-0162 (BIONIC Center) from Air Force Office of Scientific Research is gratefully acknowledged.

TABLE OF CONTENTS

ACKNOWLEDGEMENTS ..... **iv**
LIST OF TABLES ..... **x**
LIST OF FIGURES ..... **xi**
SUMMARY ..... **xvi**
1 CHAPTER. INTRODUCTION **1**
1.1 Background 1
1.1.1 Biological and biomimetic means of cell protection 2
1.1.2 Cell Membrane Structure and Composition 3
1.1.3 Cell wall composition of bacterial cells 4
1.1.4 Cell wall composition of yeast cells 5
1.1.5 Design criteria for cell surface modification 6
1.2 Methods for cell protection and cell surface engineering 7
1.2.1 Sol-gel silica immobilization 8
1.2.2 Synthetic bulk hydrogels 10
1.2.3 Protein bulk hydrogels 12
1.2.4 Peptide bulk gels 14
1.2.5 Ultrathin coatings and shells 16
1.3 Biological detection techniques and biosensors 22
1.3.1 Non-cell-based chemical detection 22
1.3.2 Cell-based chemical detection 25
1.4 Design of the whole cell-based biosensor 26
1.4.1 Criteria for cell-immobilization matrix 27
1.4.2 Criteria for cell immobilization techniques 27
1.4.3 Multiplex cell arrays 28
1.5 Motivation 30
2 CHAPTER. RESEARCH GOALS, OBJECTIVES, AND DISSERTATION OVERVIEW ... 34

2.1 Goals 34
2.2 Objectives 36
2.3 Organization and composition of dissertation 40

3 CHAPTER. EXPERIMENTAL DETAILS 46

3.1 Fabrication of nanoscale shells 46

3.1.1 Model capsules based on hydrogen-bonding 46

3.1.2 Model capsules based on pH-responsive polymer 47

3.1.3 Model capsules based on hydrophobic interactions of silk protein 48

3.1.4 Labeling of polymers with fluorescent dyes 49

3.1.5 Synthesis of silk ionomers (system#1 and system#2) 50

3.2 Microbial cells 51

3.2.1 *S. serevisiae* yeast transgenic cells 52

3.2.2 *E. coli* and *B. subtilis* transgenic bacterial cells 52

3.3 Cell nano-coatings 53

3.3.1 Coatings based on hydrogen-bond interactions 53

3.3.2 pH-sensitive coatings 54

3.3.3 Pure silk fibroin protein coatings 54

3.3.4 Ionomeric silk coatings 55

3.4 Immobilization of cells using inkjet printer technology 55

3.4.1 Silk multilayered pads 55

3.4.2 Bacterial cells embedded in silk multilayered pads 56

3.5 Characterization techniques 56

3.5.1 Confocal Laser Scanning Microscopy (CLSM) 57

3.5.2 Atomic Force Microscopy (AFM) 57

3.5.3 Scanning Electron Microscopy (SEM) 58

3.5.4 Fluorescence recovery after photobleaching (FRAP) method 59

3.5.5 Cell viability tests and activation of green and red fluorescent proteins (GFP, RFP)…….. 60

3.5.6 Z-potential and Dynamic Light Scattering (DLS) 62

3.5.7 Attenuated Furrier Transform Infrared Spectroscopy (AFT-IR) 63

4 CHAPTER. MICROCAPSULES AND CELL COATINGS BASED ON HYDROGEN-BONDED TANNIC ACID ASSEMBLIES 64

4.1 Introduction 64

4.2 Experimental details 65

4.3 Results and discussion 65

4.3.1 pH-Responsive microcapsule reactors with different polymer counterparts 65

4.3.2 Reducing properties of TA and growth of gold NPs 76

4.3.3 Mechanical properties of shells 77

4.3.4 Permeability of shells 77

4.3.5 Enhanced cytocompatibility of hydrogen-bonded coatings 79

5 CHAPTER. PH-RESPONSIVE MICROCAPSULES AND CELL COATINGS 86

5.1 Introduction 86

5.2 Experimental details 87

5.3 Results and discussion 88

5.3.1 pH-responsive volumetric changes of microcapsules 88

5.3.2 Calculations of the mesh size in hydrogel network 89

5.3.3 Mechanical stability of shells as a function of pH 92

5.3.4 Cells encapsulated in pH-responsive shells and effect of the coating on cell function 94

6 CHAPTER. SILK-ON-SILK BIODEGRADABLE MICROCAPSULES AND CELL COATINGS 100

6.1 Introduction 100

6.2 Experimental details 103

6.3 Results and discussion 103

6.3.1 Fabrication of pure silk fibroin microcapsules by dehydration with methanol 103

6.3.2 Morphological features and permeability of capsules 106

6.3.3 Fabrication of biodegradable silk fibroin coatings on cells 109

6.3.4 Effect of silk coatings on cell function 117

7 CHAPTER. IONOMERIC SILK SHELLS WITH TAILORED CHEMISTRY OF INTERACTIONS AS MEANS TO MODULATE CELL FUNCTIONS 120

7.1 Introduction 120

7.2 Experimental details 120

7.3 Results and Discussion 123

7.3.1 Interactions during LbL self-assembly of SF polyelectrolytes 123

7.3.2 Viability studies of microbial cells engineered with silk polyelectrolyte shells 125

7.3.3 Adsorption of silk polyelectrolytes at cell surfaces 128

7.3.4 Morphologically distinct behavior of bacterial cells encapsulated in silk polyelectrolyte shells 130

7.3.5 Functionality of bacterial cells encapsulated in silk polyelectrolyte shells 134

8 CHAPTER. FABRICATION OF CELL ARRAYS EMBEDDED IN MULTILAYERED SILK HYDROGELS USING INKJET-PRINTING TECHNIQUE 139

8.1 Introduction 139

8.2 Experimental details 140

8.3 Results and discussion 141

8.3.1 Fabrication and stability of cell arrays embedded in silk multilayered pads 141

8.3.2 Biocompatibility of inkjet printing technique for fabrication of cell-based sensors 147

8.3.3 Activation of cells with target analyte after short-term and long-term storage 148

8.3.4 Fabrication of dual cell arrays 151

9 CHAPTER. GENERAL CONCLUSIONS AND BROADER IMPACT 153

9.1 General conclusions and discussion 153

9.2 Significance, broader impact and outlook 158

10 CHAPTER. DISSEMINATION OF WORK 163

REFERENCES 167

LIST OF TABLES

Table 4.1 Permeability of PEI-(TA/PVPON-55)$_4$, PEI-(TA/PVPON-360)$_4$, PEI-(TA/PVPON1300)$_4$ capsules to FITC-labeled dextrans with different molecular weight and at pH 6 and pH 9……..……...……75

LIST OF FIGURES

Figure 1.1 Structure and composition of the cell wall, plasma membrane (PM) and outer membrane in Gram positive bacterial cells (a), Gram negative bacterial cells (b) and eukaryotic cells (c).[18,19,20] 2

Figure 1.2 Cell protective barriers occurred in Nature and synthetic forms of cell protection: microencapsulation in bulk gel beads (a), sol-gel immobilization on the top of the substrate (b); engineering cell surfaces with thin conformal shells (c). 7

Figure 1.3 Schematic representation of a cell incorporated in an endosome-like lipid vesicle within a surrounding nanostructured lipid/silica droplet deposited on glass substrate (a). SEM image of the lipid-silica hemisphere confining *S. aureus* cell (b).[49] 9

Figure 1.4 Alginate microbeads with human adipose-derived stem cells incorporated (a); Live/dead staining of cells within a single microbead ("red" - dead cells, "green" - dead cells) (b).[72] 13

Figure 1.5 Aligned monodomain peptide amphiphile gels. Phase image of human mesenchymal stem cells (hMSCs) preferentially aligned along the string axis (a). Fluorescence image of calcein-stained hMSCs cultured in the aligned PA gel (b).[94] 15

Figure 1.6 SEM image of a protein structure containing a high-density *S. cerevisiae* cell population (a). SEM image of confined colony in microfluidic droplet (b). Viability dye assays of *S. cerevisiae* cells displayed that the majority of cells that divide into dense populations remained viable (dark gray = viable, light gray = apoptotic) (c). 16

Figure 1.7 LbL assembly of oppositely charged polycations and polyanions components with added nanostructures (nanotubes and nanoparticles) onto living cells. 17

Figure 1.8 Polycations with enhanced cytocompatibility can be designed by tailoring the structure of PLL-g-PEG copolymers (a). Confocal and bright field micrographs of pancreatic islets stained with calcein AM (viable) and ethidium homodimer (nonviable) after incubation with poly(L-lysine) copolymer with variable degrees of PEG grafting (scale bar, 50 μm). Confocal micrographs overlaid on bright-field images of islets coated using PLL copolymer and fluorescein-labeled alginate (F-Alg) with eight bilayers (b).[108] 19

Figure 2.1 Several types of novel compositions and morphologies in LbL shells for cell surface engineering. 34

Figure 2.2 The motivation, goals, and specific areas of interest for task 1. 36

Figure 2.3 The motivation, goals, and specific areas of interest for task 2. 38

Figure 3.1 CLSM images of a capsule before bleaching, after and recovered (a). Recovery curves of fluorescence obtained for capsules with different composition (b). 59

Figure 4.1 General schematics of the LbL (TA/non-ionic polymer) capsules formation based on hydrogen-bonding. The CLSM image of PEI-$(TA/PVPON)_3$ capsules in aqueous solution (a), inset shows silica templates; SEM image of PEI-(TA/PVPON) dried capsules (b). 66

Figure 4.2 Typical AFM topography (left) and phase images (right) of PEI-$(TA/PVPON)_4$ capsules prepared from PVPON (Mw =1,300 kDa) (a). Z-scale is 100 nm for topography images. Section analysis of the PEI-$(TA/PVPON\text{-}1300)_4$ capsule (b). 67

Figure 4.3 Evolution of zeta-potential during deposition of PEI-$(TA/PVPON)_3$ multilayers on surfaces of silica particles. 69

Figure 4.4 Confocal images of (TA-PVPON-55)4 capsules at pH 5 (a) and pH 10 (b) and PEI-$(TA\text{-}PVPON\text{-}55)_4$ at pH 5 (c) and pH 10 (d). Scale bar is 5 μm. 70

Figure 4.5 ATR-FTIR spectra of PEI-$(TA/PVPON\text{-}55)_5$ films deposited on silicon crystal from 0.01M phosphate buffer solutions at pH 5 and exposed to pH 9. 72

Figure 4.6 Confocal micrographs of PEI-$(TA/PVPON\text{-}55)_4$ capsules in phosphate buffer solution at pH 6 (top images) and at pH 9 (bottom images) exposed to FITC-dextran solution with Mw = 4000 (a, d), Mw = 70 000 (b, e), Mw = 500 000 (c, f). Scale bar is 4 μm. 74

Figure 4.7 The TEM image of PEI-$(TA/PVPON\text{-}55)_3$-Au hollow capsule (a) with the particle size distribution (b) and the UV-vis spectrum of PEI-$(TA/PVPON\text{-}55)_3$-Au capsule solution (c). The EDX data for the PEI-$(TA/PVPON\text{-}55)_3$-Au capsules (d). 76

Figure 4.8 Diffusion coefficient of FITC as a function of number of layers for PEI-primed hydrogen-bonded, pure hydrogen-bonded and electrostatically-assembled shells. 78

Figure 4.9 Formation of TA/PVPON shells on yeast cell surfaces (a). Confocal image of yeast cells encapsulated with PEI-$(TA/PVPON)_3$ shell before yEGFP expression (b). TEM images of freeze-dried bare (c) and PEI-$(TA/PVPON)_6$ -coated (d) yeast cells. 79

Figure 4.10 3D topographical AFM images of PEI-(TA/PVPON-360)n hollow shells with n=3 (a), n=4 (b), n=5 (c), and n=6 bilayers (d). Scale is 500 μm x 500 μm x 50 nm. 80

Figure 4.11 Zeta-potential after deposition of a single layer with PEI-$(TA/PVPON\text{-}360K)_3$ shells at pH 6 for two types of yeast cells (haploid YPH499 and diploid YPH501) 81

Figure 4.12 Bioreduction of resazurin from its oxidized blue form (left) to its pink colored, fluorescent intermediate resorufin (right) (a); Comparison of cell viability rates between control cells, $(TA/PVPON)_n$, PEI-$(TA/PVPON)_n$ and $(PAH/PSS)_n$ coated cells (b). 82

Figure 4.13 Expression of yEGFP from control (a), PEI-$(TA/PVPON)_3$- (b) and $(PAH/PSS)_3$-coated cells (c). Inset shows a transmittance optical image of the same area for (c). Scale bars are 5 μm. (d) Comparison of the yEGFP fluorescence intensity from control cells and PEI(TA-PVPON)- or (PAH/PSS)-coated cells after 16 hours. 83

Figure 4.14 Growth of PEI-$(TA/PVPON)_{0,(3),(4)}$-coated cells after yEGFP expression was induced (a). Confocal microscopy images of PEI-$(TA/PVPON)_3$-coated cells after 10 hours (b) and 46 hours (c) of the yEGFP expression. 84

Figure 5.1 Formation of cross-linked PMAA-co-NH_2 hydrogel microcapsules via LbL self-assembly on sacrificial silica cores. 87

Figure 5.2 ATR-FTIR spectra of uncross-linked (solid line) and cross-linked for 40 minutes (dashed line) $(PMAA\text{-}co\text{-}NH_2)_5$ microcapsules (pH 3.5). 88

Figure 5.3 Thickness and microroughness of cross-linked for 40 minutes $(PMAA\text{-}co\text{-}NH_2)_5$ capsules in swollen state at wide pH range. Inset shows distorted capsule during AFM scanning at pH 7.0. 90

Figure 5.4 Reversible changes of $(PMAA\text{-}co\text{-}NH_2)_5$ capsules in aqueous solution at pH 3.0 (a), pH 8.0 (b) and pH 3.0 (c). SEM (d) and AFM in liquid state (e) images of hydrogel capsules. Surface morphology of hydrogel shells in dry state (f). 91

Figure 5.5 Elastic moduli for uncross-linked capsules with different molecular weight of PVPON component and for capsules cross-linked for 20, 30 and 40 minutes(a); Elastic moduli of swollen $(PMAA\text{-}co\text{-}NH_2)_5$ microcapsules cross-linked for 40 minutes as a function of pH (b). 93

Figure 5.6 Assembly of pH-responsive hydrogel shells on cells surfaces. 94

Figure 5.7 Cell viability rates of $(PMAA\text{-}co\text{-}NH_2)_5$ –coated cells with or without crosslinking agent (a); and as a function of bilayer composition (5, 7, and 9 bilayers) after 2 and 4 hours incubation with resazurin assay (b). 95

Figure 5.8 Zeta-potential evolution after deposition of PVPON and PMAA-co-NH_2 layers onto surface of yeast cells. 96

Figure 5.9 $(PMAA\text{-}co\text{-}NH_2)_9$ coated yeast cells at pH 5.0 (a), and pH 7.0 (b). Growth kinetics of (PMAA-co-NH_2) coated yeast cells with different shell thicknesses in media adjusted to pH 5.0 and pH 7.0 (c). 50% growth time for bare and encapsulated cells at pH 5.0 and pH 7.0 (d). 97

Figure 5.10 Yeast cells coated with $(PMAA\text{-}co\text{-}NH_2)_7$ expressing yEGFP while growing in media at pH 7 (a). Kinetics of yEGFP expression (b). 98

Figure 6.1 Preparation of "silk-on-silk" capsules. The plot shows the shell thickness and microroughness of the microcapsules as a function of the number of silk deposition steps. 104

Figure 6.2 ATR-FTIR spectra of $(silk)_5$ film deposited on ATR Si crystal by spin assisted LbL and $(silk)_5$ shells cast on the surface of ATR Si crystal showing all major bands for ordered silk secondary structures. 105

Figure 6.3 AFM image of dried (silk) 5 capsules (z-range=100 nm) (a). CLSM image of $(silk)_5$ capsules in aqueous solution (b). High magnification AFM image of the dried $(silk)_5$ capsule (z-range=80 nm) (c). AFM 3D image of a $(silk)_8$ shell (z-range=100 nm) (d). 106

Figure 6.4 Silk-on-silk LbL deposition to form silk II rich structure on the surface of the yeast cells, followed by expression of yEGFP. Followed by gradual biodegradation and internalization of silk proteins and returning to the bare state without coatings. 109

Figure 6.5 CLSM (a) and SEM (b) images of yeast cells encapsulated in silk-on-silk shells. ζ-potential of yeast cells after deposition of each silk layer (e.g., Silk-1,Silk-2) and treatment with K^+ phosphate buffer (c). 110

Figure 6.6 Viability rates of yeast cells encapsulated in silk shells treated with 0.03 M phosphate buffres that were assessed with Live/Dead (a) and bioreduction of resazurin (b) assays. 112

Figure 6.7 Viability rates yeast cells encapsulated in silk shells treated with 0.1 M phosphate buffers that were assessed with Live/Dead (a) and bioreduction of resazurin (b) assays. 113

Figure 6.8 Comparative thickness of 10 layers of silk-on-silk films in dry state as a function of treatment. 114

Figure 6.9 Comparison of SEM images between yeast cells encapsulated in $(silk)_8$ shells during salting-out with 0.03 M K+ phosphate buffer (pH 5.3) (a) and control (non-treated) cells (b); AFM images showing surface morphology of bare yeast cells (c, d) and cells encapsulated in $(silk)_8$ shells (e, f). 116

Figure 6.10 Growth kinetics (a) and expression of yEGFP (b) of yeast cells encapsulated in 6 or 8 layers of silk ($(silk)_6$ and $(silk)_8$, respectively). 117

Figure 6.11 Biodergadation and internalization of silk protein shells inside of yeast cells during cell growth. 119

Figure 7.1 Chemical scheme for creating silk intermediate (a), and silk polyelectrolytes (b). 121

Figure 7.2 Thickness of 4 and 1 bilayered film in dry state after dip-assisted self-assembly of silk polyelectrolytes as a function of charge density, degree of PEGylation, length of PEG side chains, and interactions involved in the film self-assembly for system 1(a) and system 2(b). 123

Figure 7.3 Viability of bacterial cells encapsulated in 4 bilayers of silk polyelectrolyte shells (system 1) assembled through pure electrostatic (SF-PL/SF-PG) and hydrogen-bonded ((SF-PL-PEG/SF-PG)pH4) interactions assessed with resazurin test (a) and MTT test (b). 125

Figure 7.4 Viability rates for bacterial cells encapsulated in 4 bilayers of silk polyelectrolyte shells (system 2) assembled through week ionic interactions (SF-PL/SF-PG), partially screened ionic interactions (SF-PL-PEG/SF-PG) and ionic interactions assembled on silk-primed layers ((silk)-(SF-PL/SF-PG)). Viability was assessed with resazurin test (a) and MTT test (b). 127

Figure 7.5 Changes in zeta-potential values after adsorption of a single layer during LbL self-assembly of silk polyelectrolytes on two types of bacterial cells (*E. coli* and *B. subtilis*). Strong electrostatic interactions can be observed with highly-charged silk polyelectrolytes (a), and pure hydrogen-bonded interactions can be distinguished for PEG graft copolymer with protonated SF-PG silk polyelectrolytes (b). 128

Figure 7.6 Changes in zeta-potential values after adsorption of a single layer during LbL self-assembly of silk polyelectrolytes on two types of bacterial cells (*E. coli* and *B. subtilis*). Weak electrostatic interactions can be observed with low-charge density silk polyelectrolytes (a) and PEG-screened silk polyelectrolytes (b). 130

Figure 7.7 *B. subtilis* cells encapsulated in 4 bilayers of SF-PL/SF-PG shells (a) and SF-PL-g[9]-PEG/SF-PG shells (b). Confocal (i), SEM (ii, iii) and AFM (iv) imaging of cells-in-shells structures demonstrate distinct morphological features. 131

Figure 7.8 *E. coli* cells encapsulated in 4 bilayers of SF-PL/SF-PG shells (a) and SF-PL-g[9]-PEG/SF-PG shells (b) in comparison to control non-encapsulated cells (c)..... 132

Figure 7.9 *B. subtilis* cells encapsulated in silk polyelectrolyte shells of low charge density SF-PL/SF-PG (a) and PEGylated silk block copolymers SF-PL-co-PEG/SF-PG (b). 134

Figure 7.10 Kinetics of GFP expression in *E. coli* (a) and *B. subtilis* (b) bacterial cells encapsulated in SF-PL/SF-PG and SF-PL-PEG/SF-PG shells. Confocal images of B. subtilis cells encapsulated in SF-PL/SF-PG (c) and SF-PL-PEG/SF-PG (d) shells after incubation in cell culture medium supplemented with 5 mM of theophylline for 1 hour (i) and 6 hours (ii). 136

Figure 7.11 Kinetics of GFP expression in *E. coli* (a) and *B. subtilis* (b) cells as a function of shell stracture. 137

Figure 8.1 Schematics of formation of cell-based biosensor assemblies on hard and flexible substrates utilizing inkjet printer, and working principle of cells responding to the presence of target analytes in dual cell arrays..... 142

Figure 8.2 Optical images of $(SF\text{-}PL/SF\text{-}PG)_5$ dot arrays before deposition of cells as a large view area and a single dot (a). Optical images of sandwich arrays of $(SF\text{-}PL/SF\text{-}PG)_3$-*E coli* cells-$(SF\text{-}PL/SF\text{-}PG)_3$ constructs where cells have been injected in the middle of multilayers (b). 3D AFM images of a typical $(SF\text{-}PL/SF\text{-}PG)_3$ dot (c) and $(SF\text{-}PL/SF\text{-}PG)_3$-cells-$(SF\text{-}PL/SF\text{-}PG)_3$ sandwich structure (d). 143

Figure 8.3 AFM images of encapsulated *E. coli* in $(SF\text{-}PL/SF\text{-}PG)_1$ (a) and $(SF\text{-}PL/SF\text{-}PG)_3$ (b) multilayered stacks. 144

Figure 8.4 Stability of $(SF\text{-}PL/SF\text{-}PG)_3$-*E.coli*-$(SF\text{-}PL/SF\text{-}PG)_3$ sandwich structure during incubation in SMM cell medium for 0 min (a), 30 min (b) and 14 hours (c). Thickness of the structure with respect to the incubation time (d). 145

Figure 8.5 Live/Dead staining of *E.coli* cells injected on PS-coated glass substrate (control sample) (a) and *E. coli* cells sandwiched in $(SF\text{-}PL/SF\text{-}PG)_3$-cells-$(SF\text{-}PL/SF\text{-}PG)_3$ stacks (b). (i- live staining, ii- dead staining, iii- transmittance image). 148

Figure 8.6 Activation of RS-GFP construct in *E. coli* cells with target analyte after short (a) and long-term storage (b,c). Confocal images have been collected from individual pads (a, b) and array of sandwich structures (c). Capturing has been performed at 1 hour, 2 hour, 3 hour and 5 hour time points during incubation (b). Large scale view represents RS activation at 3 hour time point (c). Legend: i- GFP/FITC band pass filter, ii- transmittance image, iii- overlapped image. 150

Figure 8.7 Confocal images representing kinetics of RS activation for two types of *E. coli* cells sensitive to theophylline (expressing GFPa1) and IPTG (expressing TurboRFP). Legend: i – GFP/FITC band pass filter, ii – Rhodamine/CY3 band filter, iii- transmittance image overlapped with i and ii. 152

SUMMARY

Cell-surface engineering has been attracting increased interest in the field of biotechnology, tissue engineering, cell therapy, or biosensors/bioelectronics. Thin nanocoatings or sometimes referred as nanoshells allow for modifying and controlling variety of cell properties, specifically retardation of cell division or growth, masking immunological properties, providing chemical and mechanical resistance to external stressors, and ability to further functionalize shells in order to guide cells attachment, their proliferation and function in artificial environment.

Bottom-up approach, utilizing layer-by-layer (LbL) assembly of wide variety of different components (synthetic and natural polyelectrolytes, nanoparticles, and other nano-structures) has been introduced and elaborated to modify cell surfaces. Despite successful examples of the LbL-based cell encapsulation with polyelectrolytes, cytotoxicity of their polycation components possesses severe limitations for this approach. Additionally, by constructing rigid non-permeable shells can suppress the essential properties of cells.

In this view, the goal of this research is to explore the formation of cyto-compatible ultrathin coatings from synthetic and natural polymers through utilization of non-cationic counterparts, with possibility to actively control cell division, provide protection from external environment, and temper shell properties in order to elicit or change specific cell response. Cyto-compatible shells based on hydrogen-bonded LbL-assembly, lightly cross-linked pH-sensitive hydrogels and hydrophobically driven assembly of natural polymers have been explored in this research demonstrating significantly higher viability rates and

preserved cell function in comparison to traditional electrostatically assembled polymer shells known to date. Specifically, we have proven that:

- Hydrogen-bonded nanoshells assembled on cells demonstrated higher porosity and diffusion compared to polyelectrolyte shells, and hence facilitated transfer of nutrients/waste with possibility to control cell division by increasing number of layers;
- Viability of encapsulated cells proven to be comparable with non-encapsulated cells by eliminating polycationic pre-layer making cells wrapped in pure easy-to-break and immunologically masked hydrogen-bonded shells;
- Cell division of cells encapsulated in pH-sensitive hydrogel nanoshells was shown to be controlled by change in pH granting active control over cell function;
- Cells encapsulated in silk fibroin nano-shells demonstrated comparable to non-encapsulated cells viability and preserved function with complete intracellular bio-degradation of protein shell overtime in comparison to simple rupture of synthetic shell;
- While encapsulation of bacterial cells in silk polyelectrolyte shells showed adverse effect of strong charge density polycations, cells encapsulated in PEG-functionalized silk polyelectrolytes with variable degree of PEGylation resulted in high viability rate, which gives the cells the possibility to be immunologically-invisible for prolonged period of time.
- Finally, fabrication of multiplexed cell arrays immobilized in silk hydrogel matrix using inkjet printing demonstrated rapid and relatively easy process of constructing cell-based array biosensors with multiple target analytes.

1 CHAPTER

INTRODUCTION

1.1 Background

Biologically inspired materials are designed in an effort to mimic essential elements, properties, and processes naturally occurring in biological organisms.[1,2,3,4] For example, recent innovations in biomedical field allowed surface modification of implanted biomaterials to overcome nonspecific protein adsorption *in vivo*, precise immobilization of signaling groups on the surfaces, development of synthetic materials with controlled properties for drug and cell carriers, biologically inspired materials that mimic natural processes, built-in programmable biodegradation profiles, or sophisticated three-dimensional (3D) supramolecular architectures for diagnostics, healing, immobilization, implantation, and tissue regeneration.[5,6] A number of biomaterials have traditionally been used for biomedical applications, where the need for enhanced *in vivo* survival rate of implanted materials must be combined with mimicry of biological recognition processes to achieve immunosuppression.

Recently, however, developments in micro- and bioelectronics such as cell-based biosensors, thermal and chemical sensors, bio-mimicking devices, and biochip technologies have emerged.[7,8,9,10,11,12,13,14,15,16,17] Long-term viability, functionality, and sustainability of cells in artificial environment (frequently aggressive) such as inorganic electrodes, dry environment under direct light illumination, or synthetic cytotoxic matrices are essential for many of these developments. An important difference is that the biomedical applications typically rely on using much more sensitive mammalian cells, which often require only temporary immunosuppressive protection and selective affinity. In contrast, many

bioelectronic applications utilize much more robust microbial cells (fungi, bacteria, or algae) that with proper engineering of cell surfaces with biomimetic coatings can attain long-term viability under hostile physical and chemical conditions.

1.1.1 Biological and biomimetic means of cell protection

All biological organisms ranging from the simplest unicellular to the most complex multicellular have essential means to isolate their internal cellular components from the external chemical and physical environment. This cellular protection allows a cell to maintain a distinct internal chemical environment, provides mechanical support, maintains osmotic pressure, regulates transport of biomolecules and ions in and out of the cell, and provides a means for assembly and communication with other cells. The basic component of cell protection in all organisms is a cell membrane that is comprised of a bilayer of amphiphilic molecules (Figure 1.1).[19,20] Beyond the cell membrane, many types of cells including both eukaryotes and prokaryotes (respectively defined as cells with and without a

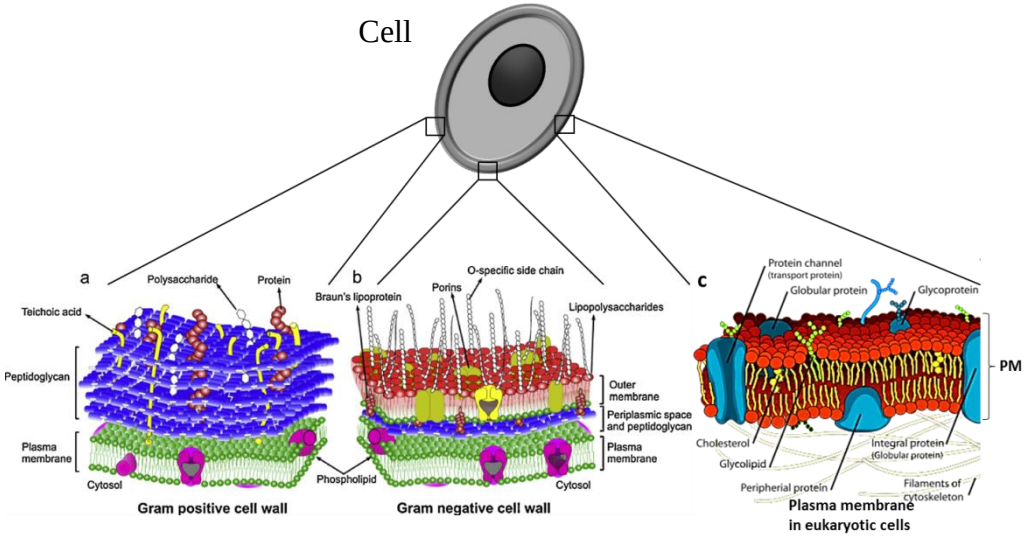

Figure 1.1 Structure and composition of the cell wall, plasma membrane (PM) and outer membrane in Gram positive bacterial cells (a), Gram negative bacterial cells (b) and eukaryotic cells (c).[18,19,20]

membrane enclosed nucleus) have additional means of protection, namely a cell wall. In the next section, basic introduction on the composition and structure of cell membranes and cell walls will be discussed in order to derive the criteria for biomimetic strategies.

1.1.2 Cell Membrane Structure and Composition

The cell membrane serves as a selective barrier sensitive to the chemical/biological environment and mechanical stresses. Because of their construction and composition, cell lipid membranes provide the cell with an extensive framework within which components (e.g., membrane proteins) can control intercellular interactions, selective adhesion, and mass transport.[18,19] However, supported by the intracellular skeleton, these very thin (around 5 nm) lipid membranes play a role in the protection of the cell interior from only very modest disturbances because of their extremely low mechanical strength and shear resistance.

Mammalian cells are separated from the external matrix by a thin, fragile, yet flexible plasma membrane (PM) that is only 5 to 10 nm thick. The membrane is held together as a cohesive sheet by lipid-protein assemblies consisting of a bimolecular layer of amphipathic lipids (phosphoglycerines, sphingosine-based lipids, glycolipids, and cholesterol), serving primary as a structural backbone and the barrier to prevent random movements of water-soluble materials into and out of the cell.[18] The two leaflets of the bilayer are composed of different types of lipids and different ratio of lipid/protein composition in respect to the type of the cell (cartilage, muscle, liver etc.) and the state of the cell (malignant vs. healthy). Many cellular activities, including signal transduction, cell division, energy transduction, and other various intracellular interactions rely on maintaining a dynamic fluid membrane in order to keep components mobile and capable of coming together to engage in many types of transient interactions.

In contrast, the microbial single-cell organisms utilized in many biotechnology applications including both prokaryotes (bacteria) and eukaryotes (fungi, algae) differ considerably from mammalian cells in their structure and composition. These cells show much higher resilience and hence can tolerate harsh artificial environments. Generally microbial cells are much smaller (usually 1-2 μm for bacterial and 4-8 μm for yeast cells) as compared to mammalian cells (usually >10 μm), shape persistent, and overall are less susceptible to mechanical stresses. A critical component of these cells is the presence of relatively thick and robust protective walls composed of different biomolecular elements (Figure 1.1).

1.1.3 Cell wall composition of bacterial cells

For bacterial cell survivability the presence of the robust but selectively permeable walls in additional to lipid membranes is critically important. Grown microbial cells possess cell walls with fungi, algae and gram-positive bacteria having thicker walls and gram-negative bacteria having thinner cell wall surrounded by an outer membrane (Figure 1.1).[18,20] There are significant differences in the cell wall structure and composition among the microbial cells themselves, which varies additionally based on the cell's growing stage (germinating, outgrowing and vegetative forms). As the cell matures over the time there is a higher complexity and increasing rigidity of the cell membrane and the wall that is built up, which prepares the cell to be more resilient to the external stresses. These robust cell walls mitigate further processing steps under unfriendly conditions such as cell surface functionalization, cell immobilization, and engineering into artificial media.

The cell wall is the exterior layer, fairly rigid and much stronger than a lipid membrane that usually lies outside of the lipid membrane (Figure 1.1). It is one of the most important prokaryotic structures because it supports the shape of the cell, helps to protect the cell from

osmotic lysis and toxic substances, and it can contribute to pathogenicity. Gram-positive bacteria, named due to the ability to retain the crystal violet stain, have a relatively thick (20-80 nm) homogeneous layer of peptidoglycan (murein) and large amounts of teichoic acids that tether underlying cell membrane with the cell wall. In contrast, gram-negative bacteria, which cannot retain the crystal violet stain, lack teichoic acids and contain only one or two sheets of 2-7 nm peptidoglycan layer covered by a 7 to 8 nm thick outer membrane containing lipopolysaccharides and lipoproteins that are covalently joined to the underlying peptidoglycan layer (Figure 1.1).[20] These layers enhance the mechanical robustness of cell shape, control intracellular transport, support the shape and membrane integrity, promote the biofilm formation, and control the surface attachment. The geometry, structure and specific interactions among glycoprotein, lipoprotein and lipopolysaccharide molecules create a unique selectively permeable barrier restricting the entry of antibiotics and toxic substances, protecting pathogenic bacteria from hostile environment, or eliciting an immune response from the host.[20]

1.1.4 Cell wall composition of yeast cells

The yeast cell walls are chemically simpler than bacterial peptidoglycan. In *Saccharomyces cerevisiae* yeast cells, the cell wall contains β(1→3)-D-glucan, β(1→6)-D-glucan, chitin, and mannoproteins.[21] The polysaccharides appear to have a structural function, whereas the mannoproteins may act as "fillers" and are important for controlling the permeability of the cell wall.[22] All components of the wall are integrated by covalent cross-linking, which provide essential rigidity and a continuous phase to the cell wall material. It has been suggested that only compounds of molecular weight smaller than 700 Da are capable of diffusing freely through the rigid walls of *S. cerevisiae* yeast cells after their maturity.[23]

Because of its rigidity, the cell wall determines the persistence of the cell shape, protect cells from excessive mechanical stresses, and helps to maintain the cell morphogenesis.

Overall, the presence of elaborate and mechanically robust cell walls enhances the survival ability of microbial cells in hostile environments.[23] Fabrication of biomimetic synthetic walls and protective media for cell entrapment holds numerous advantages to develop semipermeable and robust artificial constructs capable for protecting cells in artificial environment while allowing passage of essential nutrients and signaling cues, all critical for cell integration and functioning in a device-based environment. Even if in most of these approaches chemical composition and organization of natural protective cell walls are not directly matched, their major properties and functions are mimicked in different manners.

1.1.5 Design criteria for cell surface modification

It is critically important to mimic essential properties of the extracellular matrix (ECM) with ability to create soft but mechanically-robust, porous but semipermeable with ligand-gated selectively permissive artificial membrane/scaffold that would not interfere with biological functions of the cell. Additionally, to mimic sophisticated intelligence of a plasma membrane (PM) in order to engage specific cellular interactions (cell adhesion, cell migration, cellular differentiation, cell growth, morphogenesis and overall survivability), biochemical signals in the form of certain peptide sequences needed to be dynamically present either at the cell surfaces or extracellularly in ECM to provide healthy microenvironment for proper maintenance of a cell biological function. For example, a cell-binding site that contains the sequence arginine-glycine-aspartic acid (RGD) plays a major role in cell attachment and signal transduction at the early stages of cell differentiation in human mesenchymal stem cells, which however has to be down-regulated in order to support

correct pathway for chondrogenesis.[24] In other cases, incompatibility of cells with host immune system during transplantation/injection, occurs specifically due to the presence of cell-bound compliment regulator biomolecules. Hence, conjugation of biomolecules to biomaterials, specifically those with low-molecular weight and immunogenicity, can be used to avoid the potential cell-damaging and pro-inflammatory effects.[25]

1.2 Methods for cell protection and cell surface engineering

Many traditional methods for cell encapsulation, coating, or entrapment within synthetic polymer or silica hydrogels have been investigated as a means to create protective local environments for cells and cell colonies (Figure 1.2). Microencapsulation in macro scale gel beads,[26,27,28] emulsification,[29] micro-cell encapsulation using microfluidic devices,[30] discontinuous gradient density centrifugation,[31] formation of injectable bulk gels or sol-gel

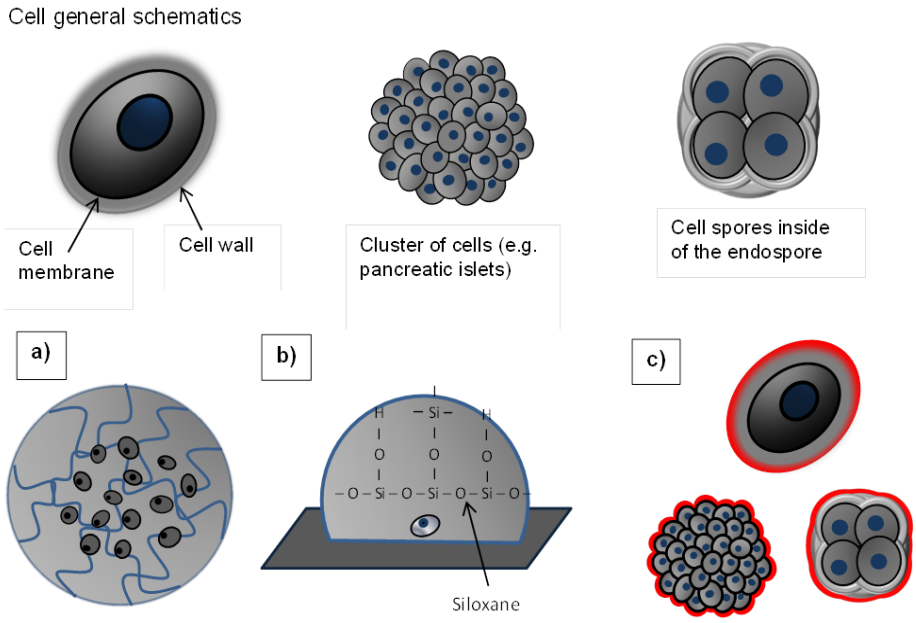

Figure 1.2 Cell protective barriers occurred in Nature and synthetic forms of cell protection: microencapsulation in bulk gel beads (a), sol-gel immobilization on the top of the substrate (b); engineering cell surfaces with thin conformal shells (c).

matrices and templates[32] have all been utilized and studied as methods to entrap and protect cells for different applications.

1.2.1 Sol-gel silica immobilization

Alkoxide-based sol-gel silica offers a number of advantages as an immobilization platform for biosensors owing to superior mechanical strength, chemical inertness, hydrophilic nature, and optical transparency (Figure 1.2).[33,34,35.36] However, the hydrolysis and condensation reactions during the encapsulation process usually require acidic or basic catalysts, with the former favoring the formation of a silica network characterized by high porosity with small pores. Since the process requires the use of harsh acidic or basic conditions, the sol-gel entrapment of biosystems is rather challenging. Enzymes may denature during formation of by-products (alcohol) in the gelling solutions, so that most of their activity can be lost upon confinement in sol-gel silica matrices.[37] Additionally, the masking of critical protein active sites might occur.[38]

Despite these challenges successful entrapment of microbial cells (*S. cerevisiae*, *S. aureus* and *E. coli*) has been demonstrated by dip-coating in cross-linkable silica solution.[39,40] An aqueous route for synthesis of silica monoliths that uses sodium silicate as a precursor has been developed for more friendly immobilization of biological entities.[35] The approach avoids generation of alcohol and, at the same time, allows encapsulation to be carried out at appropriate neutral pH to preserve biological activity. However, even in this two-step method that makes the process more compatible with enzymes, the enzymatic activity may be only partially retained. The overall shape and appearance of various cells and their clusters can be preserved after encapsulation by the siliceous membranes as has been demonstrated for human fibroblasts by Carturan *et al*.[33]

Using an alternative approach of combining silica and organic materials, immobilization of several bacteria cells has been successfully demonstrated.[41,42] Entrapment of bacterial and yeast cells in hybrid sol-gel matrices which combines synthetic and natural polymers such as alginate, peptides, phospholipids, and polysaccharides has been widely utilized[43,44,45,46,47,48] In the case of cell immobilization with phospholipids, as structure-directing agents, the cell surfaces organize multilayered phospholipid vesicles that help to relieve drying stresses (Figure 1.3).[48] These inorganic-organic matrices maintain cell viability, addressability and accessibility under dry conditions and enable stand-alone cell-based sensing. Complex cellular shapes can be also captured by silica biocomposites and fine details can be further preserved by calcination which, however, results in cell fragmentation and lysis. [41,49] Additionally, since bacteria in silica gels are entrapped in a confined space, their collective behavior (known as "quorum sensing") might be disrupted which leads to programmable cell death.[50] Overall, sol-gel encapsulation provides the opportunity to control the density of homogeneously dispersed immobilized bacteria cells. However retaining the long-term viability and proper functioning of encapsulated cells remains a great challenge.

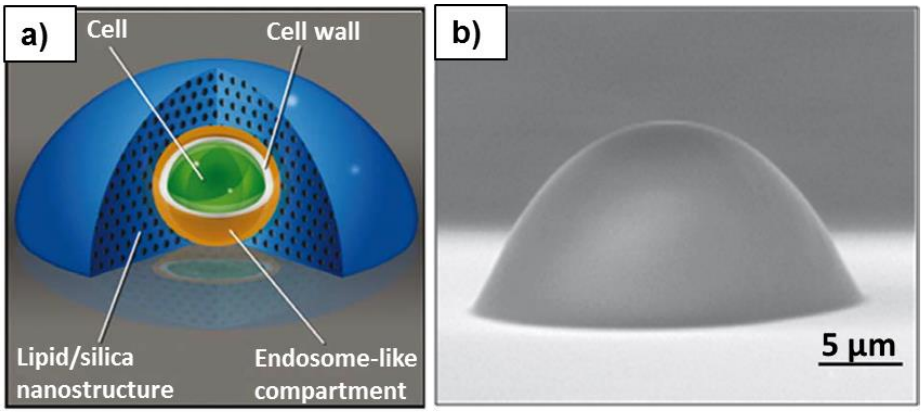

Figure 1.3 Schematic representation of a cell incorporated in an endosome-like lipid vesicle within a surrounding nanostructured lipid/silica droplet deposited on glass substrate (a). SEM image of the lipid-silica hemisphere confining *S. aureus* cell (b).[48]

1.2.2 Synthetic bulk hydrogels

Polymer hydrogels are widely utilized for cell surface engineering owing to a faster processing time, better control over hydrogel chemistry and properties, cell-friendly functionalities and potential for controlled biodegradation.[51] Usually these hydrogels are loosely cross-linked polymer networks that are insoluble but highly swellable in an aqueous medium and if made from stimuli-responsive materials, can rapidly respond to changes in the external environment.[52,53] Hydrogels based on poly(lactic acid), poly(ethylene)glycol (PEG), poly(vinyl alcohol), meth(acrlylates), poly(N-vinylpyrrolidone), or their co-modified macromers offer spatial and chemical control for cell encapsulation.[54,55,56,57,58] By creating complex heterogeneous hydrogels with segments of hydrophilic and hydrolytically degradable groups, with adjustable degree of crosslinking, the relevant macroscopic properties such as swelling rate, mechanical properties, diffusion and degradation profile can be controlled over a wide range to mimic the native extracellular matrix. When applied to cells, PEGylation procedure (formation of PEG coatings, or other biocompatible polymers) has the additional benefit of concealing surface structures that would otherwise trigger the activation of cascade reactions from the immune system and therefore protect encapsulated cells from both humoral and cellular host immunity.[59,60]

Typically, (meth)acrylate- functionalized biological monomers will react to form gels that cells can degrade through secretion of enzymes, and often the released products have a potent effect on the activity and function of the cells.[62] This ability is important for controlled protection of encapsulated cells during implantation followed by programmed hydrogel biodegradation to complete integration in a biological environment. It has been demonstrated that high molecular weight hyaluronans can provide initial structural support

and were degraded later during migration of cells after wound healing events.[61] The low molecular weight fragments can be internalized to influence cell proliferation, matrix secretion, and gene expression. For example, by tuning the chemistry of dimethacrylated tri-block copolymer (polycaprolactone-b-poly(ethylene glycol)-b-polycaprolactone (PEG-CAP-DM), the degradation of PEG-based hydrogels can be controlled to accommodate growth of the extracellular matrix.[62]

Regular synthetic polymers lack any selected recognized functionality, and at best, facilitate non-specific interactions (e.g., charged-driven protein adsorption) that can be exploited with limited control of specificity.[62] Hence, the interest in development of hybrid gels with multifunctional monomers where one group is capable of polymerizing and the other group is capable of selective conjugation to drug, peptides, or protein is essential for creating matrices to promote efficient cell survival, proper morphogenesis and immobilization.[51,63] The bioactive molecules of interest can be either permanently linked or released over time through degradable linkers, depending on the requirements of the application. An example of this type of approach includes the tethering of transforming growth factor beta (TGFβ) to hydrogels through polymerization of monoacrylated PEG conjugates, which were found to increase production of extracellular matrix by smooth muscle cells.[64] Other examples of inserting biofunctionality in naturally antifouling PEG hydrogels include conjugation of acrylate with peptide sequences, specifically those that promote cell adhesion such as the tripeptide RGD sequence, and other integrin-binding chemokines to support attachment, migration and cell differentiation in three-dimensional structure.[65,66,67]

Despite the success in cell protection, growth and directed cell morphogenesis with hybrid hydrogel matrices, the processing conditions are frequently far from physiological

conditions and detrimental to the encapsulated cells and accompanying proteins. The gelation process, which is usually initiated by harsh external stimuli (low/high pH, salt, temperature, or light) during chemical of physical polymerization, may be toxic to cells.[51] Other disadvantages of synthetic hydrogels may include low mechanical strength that pose significant difficulties in handling and long-term stability[68], and uncontrollable and/or slow degradation that ultimately leads to mass loss under harsh conditions.[69]

1.2.3 Protein bulk hydrogels

Naturally forming hydrogels prepared from extracellular matrix proteins such as collagen, fibrin, laminin, gelatin, or polysaccharides such as alginate[70,71,72,73,74,75] or hyaluronic acid[76] have become alternative choice of hydrogel matrices for less intrusive cell encapsulation.[77,78] Naturally derived materials offer a versatile alternative to synthetic silica and synthetic polymer hydrogels due to a chemical nature more akin to the extracellular matrix structure, which enables the encapsulated cell population to grow, proliferate and exhibit phenotypes more similar to those under in vivo conditions.[79]

Significant efforts have been devoted to demonstrate successful encapsulation of not only bacterial but also more environment-prone mammalian cells in alginate-derived microbeads (Figure 1.4). The successful encapsulation of probiotic microorganisms (such as bifidobacteria),[80,81,82] red blood cells with hemoglobin release,[83] pancreatic islets for post-transplantation studies,[84,85] adipose stem cells,[71] hepatocytes with assessment of proliferation and protein secretion[86] have been reported to date. However, optimization of the encapsulation procedure for long-term cell viability and mechanical robustness as well as controlled cell release still remains challenging.[87] Since a majority of chemical crosslinks and reactive functional groups are cytotoxic and result in non-injectable coagulated gels,

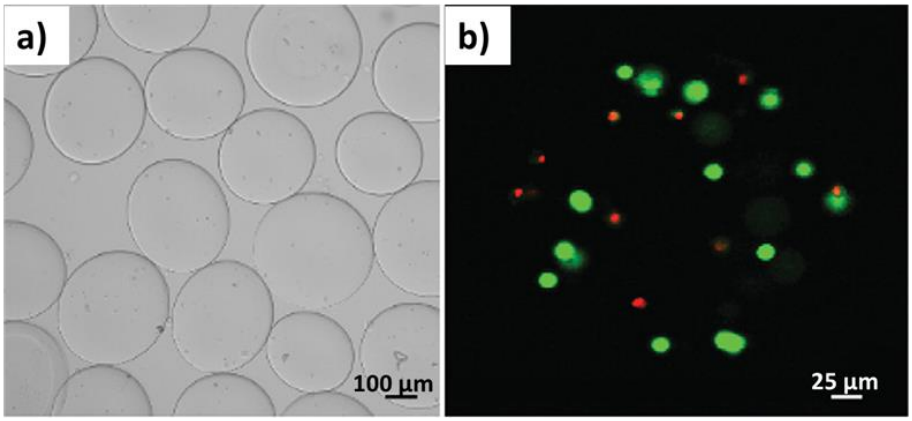

Figure 1.4 Alginate microbeads with human adipose-derived stem cells incorporated (a); Live/dead staining of cells within a single microbead ("red" - dead cells, "green" - dead cells) (b).[71]

physical hydrogels are preferred for many biomedical applications in order to temporary encapsulate multiple cell lines. These hydrogels are also readily injectable for noninvasive cell implantation applications.[88]

Encapsulation of cells in microbeads composed of crosslinked natural gels with relatively small dimensions is considered to be critical for controlling cell release as a result of enzymatic activities.[89,90] It is suggested that a well-defined number of cells and their colonies can be encapsulated in microscopic beads with dimensions of several hundred microns which are appropriate for the synthesis of injectable materials. Special attention must be paid to controlled release of cells from such alginate microbeads by designing more efficient biodegradable pathways with faster release of cells without compromising their ultimate function.[91] In a recent study, Leslie *et al* have suggested smaller crosslinked alginate microbeads with diameter below 200 µm for the implantation of viable stem cells with controlled number of cells and pre-programmed cell release.[92] These engineered microbeads were explored to encapsulate rat adipose stem cells. Gradual cell release over

many days with retained ability for differentiation after release was successfully demonstrated.

1.2.4 Peptide bulk gels

Peptide-based materials for cell encapsulation represent another type of biomimetic matrices. These matrices were designed with several classes of self-assembling peptide materials, including peptide amphiphiles, Fmoc-peptides, self-complementary ionic peptides, and hairpin peptides.[93] Due to their amphiphilic nature, the peptides assemble into a variety of supramolecular nanostructures such as spheres, cylinders, and tubes which resemble fiber-like natural materials and hybrid membranes or enclosed sacs.[94,95] The advantage of using such small molecules is their potential for full and fast degradability and formation of shear-thinning gels that can be effectively injected as low-viscosity liquids. Additionally, cell-binding epitopes as bioactive sequences can be incorporated into peptide matrices to control adhesive and cell-differentiation properties. Cellular chambers, pores, channels, and microcapsules of different shapes can be also fabricated from protein hydrogels by using various microprinting and lithography approaches and these designed structures have been exploited for their loading capacity.[96,97,98]

A more complex and efficient architecture that has recently been reported is the development of lyotropic liquid crystalline peptide amphiphile that assemble as a nanofiber network forming aligned gels.[93] The monodomain gels were formed by inducing a thermally triggered dehydration of peptide amphiphiles into two-dimensional sheets followed by cooling when molecular sheets break into large bundles of aligned nanofibers, which can be formed into long, highly-aligned constructs (Figure 1.5). The resulting structured gels were

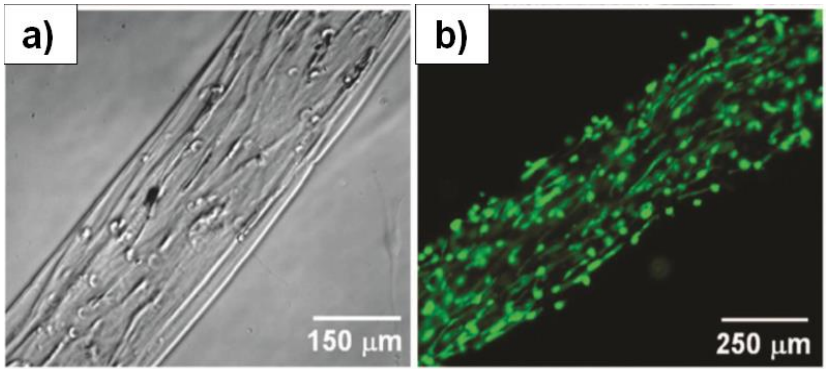

Figure 1.5 Aligned monodomain peptide amphiphile gels. Phase image of human mesenchymal stem cells (hMSCs) preferentially aligned along the string axis (a). Fluorescence image of calcein-stained hMSCs cultured in the aligned PA gel (b).[93]

capable of encapsulating and aligning cells with potential for directional guidance to facilitate axon regeneration across the damaged nerve.

Another example of two-component protein hydrogels based on proline and tryptophan-rich residues was shown to support differentiation and morphogenesis of several cell lines due to injectable and self-healing properties of fast-gelling hetero-domains.[88] These macroscopic heterogels may be particularly beneficial because the engineered peptides are recognized in the in vivo environment by additionally incorporating cell-binding domains more than a conventionally synthesized material. Furthermore, the enzymatic breakdown of protein heterogels into amino acids provides the ease for body to be able to use them as building blocks in cellular metabolism. Alternatively, protection of probiotic microorganisms with protein encapsulation has been demonstrated for oral delivery.[99,100] Picot *et al* have developed methods for encapsulation of bifidobacteria in insoluble whey protein capsules. Microcapsules were formed by spray-drying and emulsion processes. Encapsulation of bacteria resulted in increased survivability of bacteria under extreme conditions such as digestive environments.[101]

An interesting example of biocompatible 3D isolation chambers from protein hydrogels for confinement of microbial cells and their colonies has been demonstrated by Harper *et al* (Figure 1.6).[102] These microchambers can be fabricated from biocompatible precursors and under biocompatible conditions thus facilitating functioning of cells inside of these enclosures. These closed hydrogel structures can be used for physical protection of cells from hostile environment allowing cells to grow and function inside of closed microscopic space. These chambers from protein hydrogels are shape-persistent and biocompatible and, furthermore, capable of preserving their shape even during cell growth and external deformations.

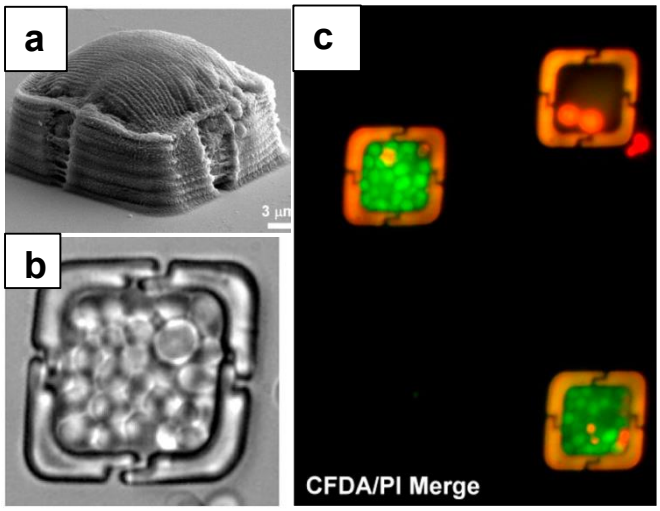

Figure 1.6 SEM image of a protein structure containing a high-density *S. cerevisiae* cell population (a). SEM image of confined colony in microfluidic droplet (b). Viability dye assays of *S. cerevisiae* cells displayed that the majority of cells that divide into dense populations remained viable (green = viable, red = apoptotic) (c).

1.2.5 Ultrathin coatings and shells

Cell surface engineering using bottom-up assembly of ultrathin conformal soft shells has been introduced to overcome some of the issues prominent in bulk cell encapsulation with hydrogel media. Loss of cellular activity after bulk and microgel encapsulation,

inflammatory host immune response, transport limitations of nutrients and signaling molecules, and void volume restrictions remain significant challenges for traditional approaches.[103] In order to minimize these challenges, conformal ultrathin (2-100 nm) protective soft shells with different morphologies, various compositions, and intermolecular interactions that facilitate fast transport and provide robust mechanical properties have been introduced and elaborated (Figure 1.7).

1.2.5.1 Coatings based on polyelectrolytes

Over the past two decades LbL assembly has emerged as a powerful and versatile bottom-up approach for engineering diverse organized films with microstructure, morphology, composition, biological, mechanical, and chemical properties readily tailored through cell-friendly assembling routines.[104,105,106] Well established LbL assembly procedures for cell

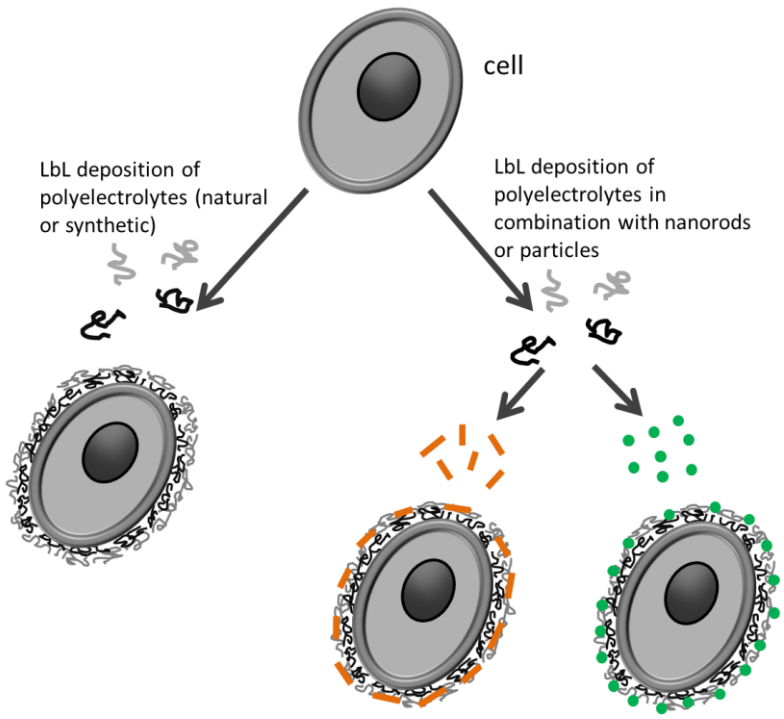

Figure 1.7 LbL assembly of oppositely charged polycations and polyanions components with added nanostructures (nanotubes and nanoparticles) onto living cells.

encapsulation include multiple steps of sequential deposition of "monolayers" of oppositely charged components onto the negatively charged cell surface. This sequential addition of material provides the ability to fabricate multilayered ultrathin soft shells with pre-defined number of layers (hence thickness) from a wide range of different components (including polyelectrolytes, proteins, and nanoparticles) (Figure 1.7).

Assembled through traditional alternating LbL assembly, ultrathin multilayered films are clearly different from naturally occurring cell membranes yet may be designed to confer similar protective and transport functions.[107] Through incorporation of naturally occurring polymers,[108,109] proteins,[110,111] nucleic acids,[112,113] liposomes,[114] biologically active nanoparticles,[115] or polymers with bioactive motifs[116] LbL shells provide wide opportunities for cell surface engineering.[107] Other advantages of this approach include formation of compliant coatings with disregard of the cell/cell complexes shape, precise control of the coating thickness, variable porosity and hence mass transport, tailored mechanical resistance and elasticity, and wide tunability of coating functionalities and properties.[104,117,118,119,120] The ability to tailor transport and mechanical properties of these synthetic walls is of particular importance for encapsulation of living cells as cell viability and long-term shelf life critically depends on the diffusion of nutrients and waste release through the artificial polymer membrane.

The poly(allylamine hydrochloride)/poly(styrene sulfonate) (PAH/PSS) LbL films are the mostly explored polyelectrolyte pair that were initially exploited to encapsulate cells.[121,122,123,124] PSS/PAH assemblies were shown to exhibit pH-controlled responsive changes in size and porosity at extreme acidic and alkaline conditions.[125,126] Despite

successful examples of the LbL-based cell encapsulation with polyelectrolytes, cytotoxicity of high-charge density polycation components has proven to be significant which undermines this approach as a routine tool in cell surface engineering.[103,127] Moreover, the sensitivity of mammalian cells to polycations is more prominent compared to microbial cells since they lack effective cell wall machinery that helps cells to withstand membrane disruption.

Indeed, the cationic materials adsorbed on cell membranes during LbL assembly of PSS-PAH (and similar) polyelectrolyte shells can cause pore formation followed by cell damage as has been demonstrated by leaking of lactose dehydrogenase.[103] On the other hand, decreasing molecular weight of polycationic chains mitigates cell membrane disruption and facilitates the LbL shell formation without adverse effect on cell functioning. Furthermore, the cytotoxicity of these LbL shells can be significantly reduced by reducing cationic content

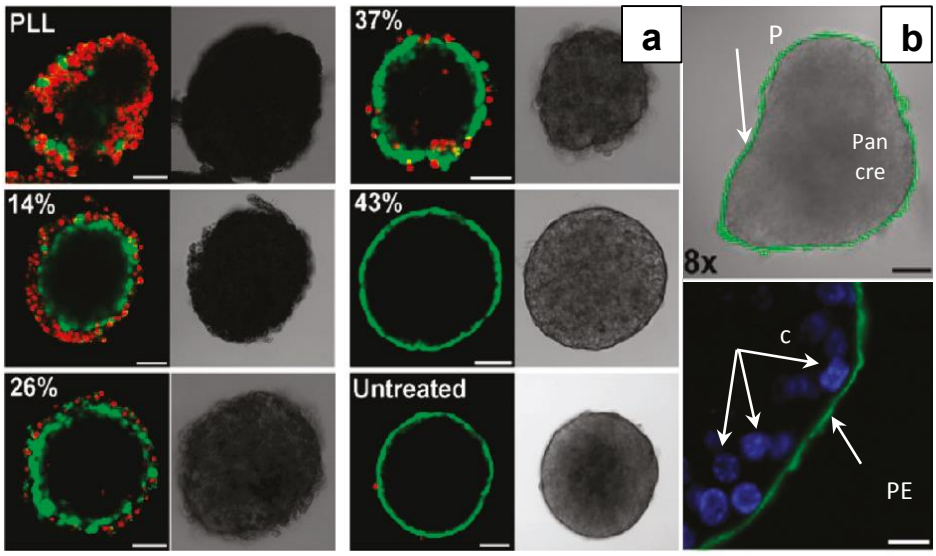

Figure 1.8 Polycations with enhanced cytocompatibility can be designed by tailoring the structure of PLL-g-PEG copolymers (a). Confocal and bright field micrographs of pancreatic islets stained with calcein AM (viable) and ethidium homodimer (nonviable) after incubation with poly(L-lysine) copolymer with variable degrees of PEG grafting (scale bar, 50 μm). Confocal micrographs overlaid on bright-field images of islets coated using PLL copolymer and fluorescein-labeled alginate (F-Alg) with eight bilayers (b).[107]

or by using cells with developed walls. For instance, the dramatic reduction in the cytoxicity can be achieved by decreasing the polycation charge density through proper grafting of PEG chains (Figure 1.8).[103,107] LbL shells from certain PEG-containing components have been shown not to interfere significantly with the viability of pancreatic islets. Composition, reactivity, thickness, and mechanical properties of such nanocomposite shells can be readily tailored by changing composition.

On the other hand, it seems that the viability of cells encapsulated in traditional LbL shells with significant cationic content is significantly higher if shells are assembled on more mature, stationary-phase cells, when they are functionally equivalent to spores. At this stage, matured cells drastically reduce their metabolic activity and hence increase their resistance to many environmental stresses.[128,129] However, the functionality of cells at this stage becomes very limited and thus the applicability of these protected cells for biosensing applications can be limited.

Introduction of metallic nanostructures into LbL shells is a well-known reinforcing approach in LbL technology.[104,130,131,132,133] Such tactic has been reported for LbL-modified cells as an effective way to increase shell strength, enable cell conductivity, make cell magnetic, and control shell permeability. Inorganic nanostructures usually form dense and robust monolayers on bacterial cells with grafting density controlled by the LbL assembly procedure.[134,135] Proper placement of usually toxic nanoparticles on the outside of functionalized shells or within LbL shells prevents or limits their adverse effect on cell function.[128] Silica nanoparticles inside LbL shells were shown to very modestly affect cell growth.[136,137] Carbon nanotubes and graphene flakes have been incorporated in LbL shells to improve robustness and induce conductivity of modified cells without compromising cell

viability.[138,139] Finally, magnetic nanostructures have been utilized in LbL shells to enable the placement and controlled flow of magnetically modified cells with external magnetic field without significant effect on mature cells with already hardened walls.[124,140]

1.2.5.2 Coatings based on hydrogen-bond interactions

Hydrogen-bonded LbL structures represent new opportunities for cell-friendly LbL shells of "soft" type with more cell-compatible components and assembly procedure (Figure 1.9). The advantage of having such LbL shells assembled via non-covalent hydrogen-bonding interactions is that their micromechanical properties can be well controlled with change in pH, light conditions, salt concentration, or temperature.[141,142,143,144] However, many of the hydrogen-bonded LbL shells studied to date have demonstrated to be unstable under certain conditions during cell encapsulation procedures that compromise mid-term stability of these shells and hence must be specifically addressed.[118] On the other hand, by adjusting conditions these shells can be controllably disassembled thus facilitating pre-programmed degradability.

The hydrogen-bonded LbL shells based on biocompatible FDA-approved functional polymers such as PEG and poly-lactic acid (PLA) might be of interest for cell surface engineering.[103,5] Another example of a non-toxic and biocompatible component is poly(N-vinylpyrrolidone) (PVPON) that can facilitates the conversion of hydrogen-bonded LbL shells to ultrathin hydrogel shells with responsive, low-fouling or/and biodegradable properties.[145] Even though, the formation of robust microcapsules based on weak hydrogen bonded interactions between several polymer compounds have been successfully established, attempts to realize this concept on living cells has never been

demonstrated.[144,118,146] Successful cells surface engineering with hydrogen-bonded LbL shells based on tannic acid (TA) assemblies will be discussed in detail in Chapter 4.

1.3 Biological detection techniques and biosensors

Rapid and accurate detection and identification of chemical and biological agents (analytes) in laboratory and field situations is a particularly important goal across the many fields.[147, 148] The recognition of analyte by the receptor usually proceeds with generation of measurable signal that can be processed by different sensing methods, such as electrical, gravimetric, or optical.[147] Optical methods in general are desirable for many sensing applications because of the potential for high sensitivity, good selectivity, rapidness of analysis, portability of instrumentation, and overall cost-effectiveness.[147] There are two most common types of optical methods: Colorimetric or fluorescence-based. Colorimetric sensors detect the change in color of a pigment upon interaction with an analyte vapor or solution. Fluorescence-based sensors rely on either quenching or onset of fluorescent signal in the presence of analyte.

1.3.1 Non-cell-based chemical detection

Many environmental and medical diagnostics that have been developed for detection of analytes range from direct optical detection, such as microscopy, to optical signal transduction of chemical or electrochemical processes. Flow cytometry, elastic-scattering-based detection of particles, surface plasmon resonance (SPR),[149] Raman spectroscopy, Fourier transform IR, Foster resonance energy transfer method, immunoassay analysis,[150,151] nucleic-acid-based assays[152] and biological culture sampling, all have been undertaken towards developing biochemical sensors and sensor arrays to identify the presence of dangerous substances.

Flow cytometry typically involves the laser illumination of individual particles traveling in a liquid stream and the detection of the resulting elastic scattering and fluorescence in order to detect and discriminate one type of particle from another type of particle. Because this method requires modification of sample particles with fluorescence-enhanced chemicals and can only perform in liquid flows, the sampling of aerosolized biological agents is rather less specific. With native fluorescence of individual biological particles, an elastic-scattering-based detector can be equipped with stealth UV-lasers to discriminate fluorescence of biological agents from background aerosols, as well as scattering patterns based on particle shape.[153,154] This instrument was referred as the fluorescence aerodynamic particle sizer (FLAPS).

Foster resonance energy transfer analysis, Raman spectroscopy, and Fourier transform infra-red spectroscopy, are all good candidates for biological/nonbiological discrimination of aerosols and even for classification of agents into likely subgroups, such as bacteria, viruses, etc. Although these techniques are characterized as the rapid and non-destructive analysis methods to probe organic and/or inorganic compounds in small samples without any need for cumbersome preparations, it requires extensive reference database to cross-validate analyte targets, and gives poor analytical results due to excessive fluorescent background. Additionally, these are quite bulky and expensive equipment to be used for portable screening in field applications. Non-destructive ultra-sensitive surface enhanced Raman scattering (SERS) analysis technique can be applied to trace and fingerprint the molecules of interest with exceptional sensitivity due to amplified Raman intensity occurred at nanoscale surface roughness.

Culture tests were the mainstay of diagnostic testing developed for the identification and confirmation stages of a biodetection system.[155] Culture can be used not only to provide some initial confirmation of the suspected agent type (by selection of a compatible culture medium) but also to establish the viability of the suspect agent sample.[148] Despite the wealth of information obtainable from culture, and accuracy of the test, the results can often take days to acquire, and require highly trained personnel.[155] Culture-independent tests (nucleic-acid-based assays based on polymerase-chain reaction (PCR), immunoassays with fluorescent-antibody-based stain, such as Enzyme-linked Immunosorbent Assay (ELISA)) are usually faster than culture and, in some cases, can provide more types of information. However, the results provided by culture-independent assays can give artificial increases or decreases due to variations in test performance, and hence pose challenges in interpreting data.[155] In addition, performance characteristics of culture-independent tests are variable and different from those of culture.[155]

While some of the methods provide high sensitivity and specificity, they suffer from costly sample and/or substrate preparation, design of aptamers, requirement for labeling with fluorescent probes (usually with high quantum yield), long turnaround and elaborate characterization that also requires highly-trained personnel, high signal-to-noise ratio background, high limits of detection (LOD) or a *priori* knowledge of the agent characteristic properties. Others offer fast qualitative and quantitative results with minimal sample preparation, however, suffer from low specificity and sensitivity. In general, there is a tradeoff between the speed/cost of the assay and its specificity/sensitivity.

1.3.2 Cell-based chemical detection

Cell-based sensors typically rely on activation of the riboswitch constructs which are regulatory RNAs located in the 5'-untranslated region of messenger RNA (mRNA) sequence. Riboswitches are composed of two structural domains: an aptamer domain that binds to a small molecule with specificity, and an expression platform that controls the expression of a downstream gene via conformational changes that are induced by ligand (target analyte) binding to the aptamer. Cell-based biosensors pre-programmed with engineered reporter-gene constructs offer exceptional specificity, controlled response and significant signal amplification which can be used for detection, identification and tracking the molecules of interest (analyte). The recognition of analyte is monitored by optical colorimetric read-out assay method: detection and quantification of fluorescence signal and its intensity, which are corresponding to the sensitivity and concentration of the molecule of interest. Ideally, with proper genetic modification, cells can be used to survey the library of different classes of small molecules: the hazardous chemicals, pesticides, explosives, or other warfare agents[156], chemical/biological agent analogs, indicators of human activity, and toxins. With traditional sensors (most chromatography methods), the detection of specifically small molecules (Mw less than 1 kDa) is unattainable due to their poor selectivity or non-specific binding which leads to inaccurate detection of analyte. For example, in enzyme-based sensors designed to monitor inhibition of esterases by various neurotoxins, the sensitivity can be very high (able to detect 10^{-10} M), but specificity is very poor, as there are many other substances (from carbamates to heavy metals) that also inhibit these enzymes.[157]

The advantage of exploiting cells over the traditional sensors is their innate ability to bind the analytes with exceptional specificity and sensitivity and to report this binding via internal amplification mechanism. Another benefit of using cells is that there is no need to use the external energy to power the production of the signal.[158] Self-powered built-in generator utilizes the machinery already present in nature that can be activated as soon as the cell senses the presence of analyte. Additionally, by constructing genetic logic circuits within the cells, the resulting signal can be enhanced and amplified to the extent when it is possible to detect the traces of the chemical of interest with precise accuracy. Moreover, in connection with portable fluorometer platforms, cell-based biosensors can be used in field applications for real-time detection of analyte or even remotely survey the area from the distance.

1.4 Design of the whole cell-based biosensor

Cell-based sensors enable long endurance, persistent monitoring with a low false-positive rate. The enzymological studies of the riboswitch construct in cells have been implemented at Air Force Research Laboratory, our collaborators. The studies included extensive search of the aptamer libraries and the selection of the best chromophore and the recognition element of the small target molecules. The best constructs have been passed to us to perform encapsulation and immobilization studies of cells in synthetic and natural polymer coatings to determine the best cytocompatible protective matrix, as well as to study the length of cells storage in confined conditions, viability studies, and efficiency of the encapsulated cell-based sensors in terms of onset of signal transduction, signal amplification and efficiency of the coating to facilitate in the diffusion of the analytes.

1.4.1 Criteria for cell-immobilization matrix

Immobilizing cells in a biocompatible matrix allows for cells protection from non-specific chemical molecules that can hurdle the function of the sensor construct in the cells. The polymer matrix should also provide an easy diffusion of chemical analytes and create the favorable conditions for cells to grow. Hence, biocompatible polymers both synthetic and natural that rely only on hydrogen-bond and hydrophobic interactions can be applied to serve as a matrix for cells.

Assembling robust, gel-like LbL shells without cationic components to reduce shell cytotoxicity, with open, loose physical and chemical crosslinking network to facilitate transport of large biomolecules, with nanoscale thickness (10-100 nm) comparable to the cell membrane/wall width to make intra-extra cellular component exchange easier, with chemical and mechanical properties closely matching to those of cell walls to reduce mismatching stresses, and with potential biodegradability all are the major criteria for this task.

1.4.2 Criteria for cell immobilization techniques

Inkjet printer systems (both piezoelectric and thermoelectric) demonstrated exceptional applicability in depositing various biomolecules onto target substrates with little or no reduction of their bioactivity. [159,160,161] Single microbial and mammalian cells, and bio-inks, where natural and synthetic physical hydrogels, polymer/hydrogel precursors are combined with living cells and natural protein solutions can be deposited to form a scaffold followed by cell printing to form 3D constructs.[162-168]

1.4.3 Multiplex cell arrays

Whole-cell biosensors designed with the aid of inkjet-assisted printing represents a versatile tool for rapid and high throughput microfabrication process of multi-cell arrays immobilized in cell-preserved matrix. Cells can be preprogrammed for identification of the specific chemical of interest, and printed in the assigned rows for detection of multiple chemical compounds. Biosensors based on both eukaryotic and prokaryotic systems were envisaged for screening of chemical and biological toxins, which not only allow the detection of a wide range of toxic chemicals with the same sensitivity level as chemical sensors, but also can indicate the type of biological activity involved.[169] Particularly, the information on the effects of the tested compound such as gene expression, metabolic activity, viability, bioavailability, toxicity and genotoxicity can only be sensed and reported by live cells. Furthermore, the use of live cells allows for reagent-free, non-destructive, real-time monitoring of biological effects as they develop.

Biochips designed on the basis of bacterial cells have many advantages. They are readily obtainable, easy to grow and maintain, can be genetically tailored to emit the desired signal in the presence of the specific target compound (analyte) or specific environmental conditions, covering the broad range of toxic elements. Additionally, microbial cells are more robust and less sensitive to physical and chemical environment, and hence can be manipulated in the way to construct multiplexed patterns.

Several recent reports have presented the fabrication of single-strain cell biosensor arrays immobilized onto biocompatible synthetic or natural hydrogel substrates using inkjet technology.[170, 171, 172, 173] The next step would be the construction of whole-cell multiplex arrays, where cells are originally transfected with target-specific reporter gene and

assembled in the multilayered matrix that not only protects cells from non-specific environmental stresses but also supports long-term ability of cells to function. Inkjet–assisted technique for the construction of such complex cell-based sensors would offer real time fabrication of robust multicomponent patterning with controlled 3D spatial and temporal arrangement of several biocomponents, which could be accomplished by optimizing the amount of material necessary for robust scaffolds and cell matrix constructs.[174]

1.5 Motivation

In order to overcome some of the issues prominent to bulk cell encapsulation, cell surface engineering using bottom-up assembly with ultrathin conformal soft shells seems to be the best choice. Loss of cellular activity after bulk and microgel encapsulation, random cell entrapment, transport limitations of nutrients and signaling molecules through rigid bulk volume, limited process scalability and no control of the cell growth remain significant challenges for these traditional approaches.[103] In order to minimize these challenges, conformal ultrathin (2-100 nm) protective soft shells with different morphologies, various compositions, and intermolecular interactions that facilitate fast transport and provide robust mechanical properties have been introduced and elaborated with LbL approach. The advantages of this approach include conformal coating of complex shapes, a precise control of the shell thickness, variable porosity and mass transport, enhanced mechanical resistance, and wide tunability of membrane functionalities and properties. [104,117,118,120,175] The ability to tailor transport and mechanical properties of these synthetic walls is of particular importance for encapsulation of living cells as cell viability and long-term shelf life critically depends on the diffusion of nutrients and waste release through the artificial polymer membrane.

Despite successful examples of the LbL-based cell encapsulation with polyelectrolytes, cytotoxicity from their polycation components poses severe limitations for this approach as a routine tool in cell surface engineering.[103] Moreover, the sensitivity of mammalian cells to polycations is more prominent compared to microbial cells since they lack effective cell wall machinery that helps cells to withstand membrane disruption.

Hydrogen-bonded LbL structures represent new opportunities for cell-friendly LbL shells of "soft" type with more cell-compatible components and assembly procedure. The advantage of having such LbL shells assembled via non-covalent hydrogen-bonding interactions instead of traditional polyelectrolyte shells is that their micromechanical properties can be well controlled by changing pH, ionic strength, salt concentration, or temperature.[53,144,176] However, many of the hydrogen-bonded LbL shells studied to date have been demonstrated to be unstable under certain conditions during cell processing that compromise mid-term stability of these shells and hence must be specifically addressed.[118] On the other hand, by adjusting conditions these shells can be controllably disassembled thus facilitating pre-programmed degradability.

Formation of stimuli sensitive conformal hydrogel shells as protective coatings provides an additional advantage. Along with highly permeable network state allowing the passage of nutrients and target analytes, this hydrogel material can mediate the cell function/activity while inducing changes in conformational transitions in shell network. Intracellular biomolecular delivery of drugs using masked pH-responsive compounds has been widely utilized,[177] while using pH triggered release of proteins in cell detachment has started to gain great attention recently.[178] LbL shells reported to date have not proven to be robust under variable environmental conditions and not capable of significant and controlled variations of their state. Thus, synthetic nanoshells currently play a passive role in cell growth, interactions, and function, and no examples of responsive synthetic nanoshells which can serve as an active barrier/coating to control cell function in biosensing devices have been reported to date. Hence, it appears to be rewarding to design and demonstrate active control of cell activity with responsive conformal shells.

While encapsulation of a wide variety of cell types in a range of natural and synthetic polymers has been demonstrated, the successful encapsulation of living cells in protein shells represents a particularly unique challenge for various biotechnology applications. The motivating factors for this effort include the ability to reengineer the surface of the cell with proteins allowing for direct control of interactions with the extracellular environment and to create more biocompatible encapsulants for applications involving long-term *in vivo* implantation, prolonged shelf life under ambient conditions, or building artificial cell walls for nutrients storage.

Recently, developments in micro- and bioelectronics such as cell-based biosensors, thermal and chemical sensors, biomimicking devices, and biochip technologies have emerged.[15,179,180,181,182,183] Demands for long-term cell viability, functionality, and sustainability in artificial environment (hostile nature) such as inorganic electrodes or synthetic cytotoxic matrices are important for many of these developments. Robust living cell-based biosensors with long-term shelf life can show high real-time sensitivity detection in response to a target analyte,[184] protection from *ex vivo* environment,[185] and preserved viability/activity. Motivation factors behind encapsulation of living cells in protein shells also include the ability to reengineer the surface of the cell with proteins allowing for control of interactions with *ex vivo* environment, such as immobilization on patterned synthetic surfaces,[186,187] controlled adhesion of coated cells on surfaces with different affinities,[188] or guided/directed location and growth of cells.[189]

The excellent mechanical properties, availability, and biocompatibility of silk proteins have made them attractive candidates for biomedical and biotechnology applications.[190,191] Silk microparticles and microgels are excellent candidates for delivery platforms, composite

materials, and cell encapsulation. However, to date, only a few examples of utilizing silk for the fabrication of microgels as cell entrapment platforms have been introduced,[192,193] while no focus on formation of conformal thin silk shells has been addressed due to potentially toxic processing conditions necessary to induce stable protein shells. Hence, to develop processing conditions utilizing all-aqueous solutions necessary for adsorption of silk proteins on cell surfaces and to stabilize silk proteins in order to create robust conformal LbL shells seems to be rewarding. Biocompatible, slowly degradable, ultrathin, but highly robust, porous silk shells with tunable thickness and controlled permeability might be of interest for tissue implantation, biotechnology, biosensors application where selective adhesion to various substrates, selective transport of target analytes, sustainability under excessive mechanical stresses, osmotic pressure, or external field is critically important.

2 CHAPTER

RESEARCH GOALS, OBJECTIVES, AND DISSERTATION OVERVIEW

2.1 Goals

The goal of this research is the understanding of interfacial interactions and organization of natural and synthetic macromolecules at the cell surfaces during cell surface engineering. The idea behind this project was to design the most cytocompatible coatings (shells) through careful selection of chemical interactions applied in creating of LbL shells at the cell surface (Figure 2.1). Out of the number of non-specific interactions, shells assembled through multiple sites of hydrogen-bonded interactions seem to overcome the cytotoxicity, the major drawback of shells assembled through electrostatic (ionic) interactions, specifically with high charge density polycations.

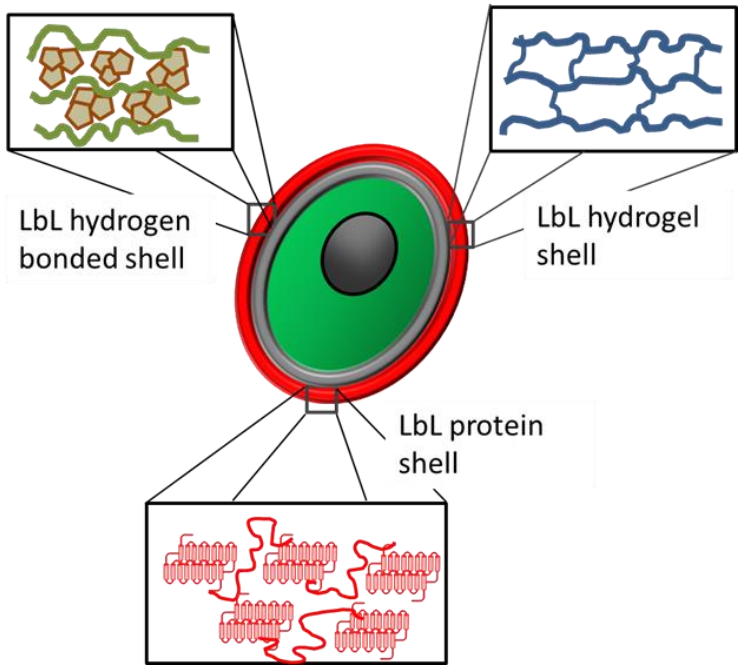

Figure 2.1 Several types of novel compositions and morphologies in LbL shells for cell surface engineering.

These nanoscale coatings assembled through sequential deposition of hydrogen-rich and hydrogen-deprived species, as well as through hydrophobic interactions between biocompatible synthetic and natural polymers including proteins, will be compared and contrasted in terms of cells survivability, onset of replication and ability to respond to environmental cues with traditionally used polyelectrolyte shells that rely on electrostatic interactions. The criteria for novel cytocompatible shells are to support long-term activity/function of encapsulated cells and to not interfere with essential properties of the cells. Hence, the diffusion kinetics and permeability limits must be assessed and tuned in order to create semipermeable coatings designed to allow nutrients, analytes and waste to freely exchange through the shell and block an entry of toxic elements. Soft coatings that are compatible with essential elements of the cell surface, namely its structure, composition, elasticity, and morphology, have the potential to increase cell stability in a hostile environment without compromising sensing ability. It is critically important to mimic essential properties of the ECM and to create soft biointerfaces which are mechanically-robust but semipermeable, ultrathin but stable, diverse in chemical composition but cytocompatible, and which ultimately do not interfere with biological functions of the cell.

Ability of microbial cells to interact with coatings and respond to the changes caused by conformational changes in polymer material induced by environmental shift in either pH, temperature, or light represents additional means to control the behavior of cells when complex cells-in-shells assemblies are used in cell-based bioelectronics. The ultimate goal of this project is to design an efficient long-term protection of cells from *ex vivo* environment by utilizing non-cytotoxic or natural biopolymers (proteins) that provide selective permeability to target analytes. Once the suitable coatings are identified, a prototype of cell-

based biosensor will be fabricated when cells arrays would be immobilized in the user-defined multilayered matrix assembled trough inkjet-assisted deposition of chemically-modified silk.

2.2 Objectives

In this comprehensive study, the two major tasks will be accomplished through the following specific *technical objectives*. Details regarding the two specific tasks to be addressed are described in detail below and are summarized in Figures 2.2 and 2.3.

Task 1:

- *Study the self-assembly of hydrogen-bonded LbL shells between natural polyphenol (tannic acid, TA) and neutral polymer (poly-(N-vinylpyrrolidone, PVPON) where essential properties (stability to pH, temperature changes, porosity, permeability, elastic properties and build-up of the shells) will be addressed in order to probe the robustness of the hydrogen-bonded TA-based coatings on cells.*

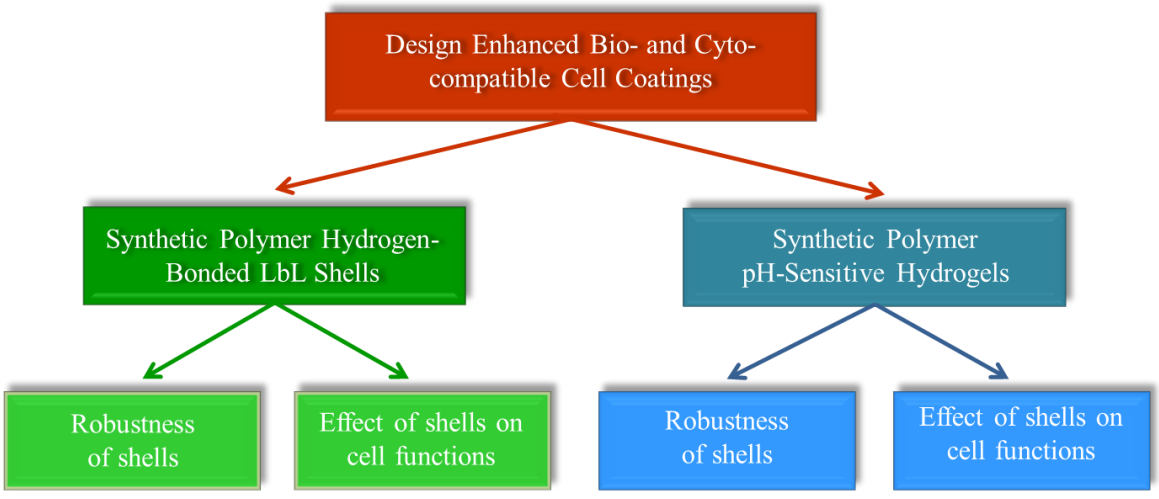

Figure 2.2 The motivation, goals, and specific areas of interest for task 1.

- *Study the survivability and post-entrapment activity/function of encapsulated cells by exploring formation of protective coatings with cytocompatible polymer shells based on hydrogen-bonded interactions between TA and PVPON. Study the post-encapsulation viability rates and ability of cells to express fluorescent biomarker (green fluorescent protein, GFP). We expect to see enhanced viability from hydrogen-bonded system compared to electrostatically assembled system due to the absence of polycationic polymers.*
- *Design and study essential properties (volume changes, degree of crosslinking, mechanical robustness) of cytocompatible hydrogel shells sensitive to external changes in pH. This will allow for on-demand regulation of function/activity of encapsulated cells through stimuli-responsive protective coating.*

***Task 2**:*

- *Design, optimize deposition conditions for cells, create and study physical properties (porosity, mechanical stability, pH stability) of pure silk fibroin shells by utilizing sequential LbL assembly of silk protein layers when random coils are transitioned into β-sheets after absorption of each layer.*
- *Design and optimize conditions to fabricate cytocompatible coatings for cells by utilizing sequential LbL assembly of chemically-modified silk with oppositely-charged poly-amino acids (A.A.) of various degree of derivation to emphasize the importance of chemical interactions involved in creating biocompatible shells.*

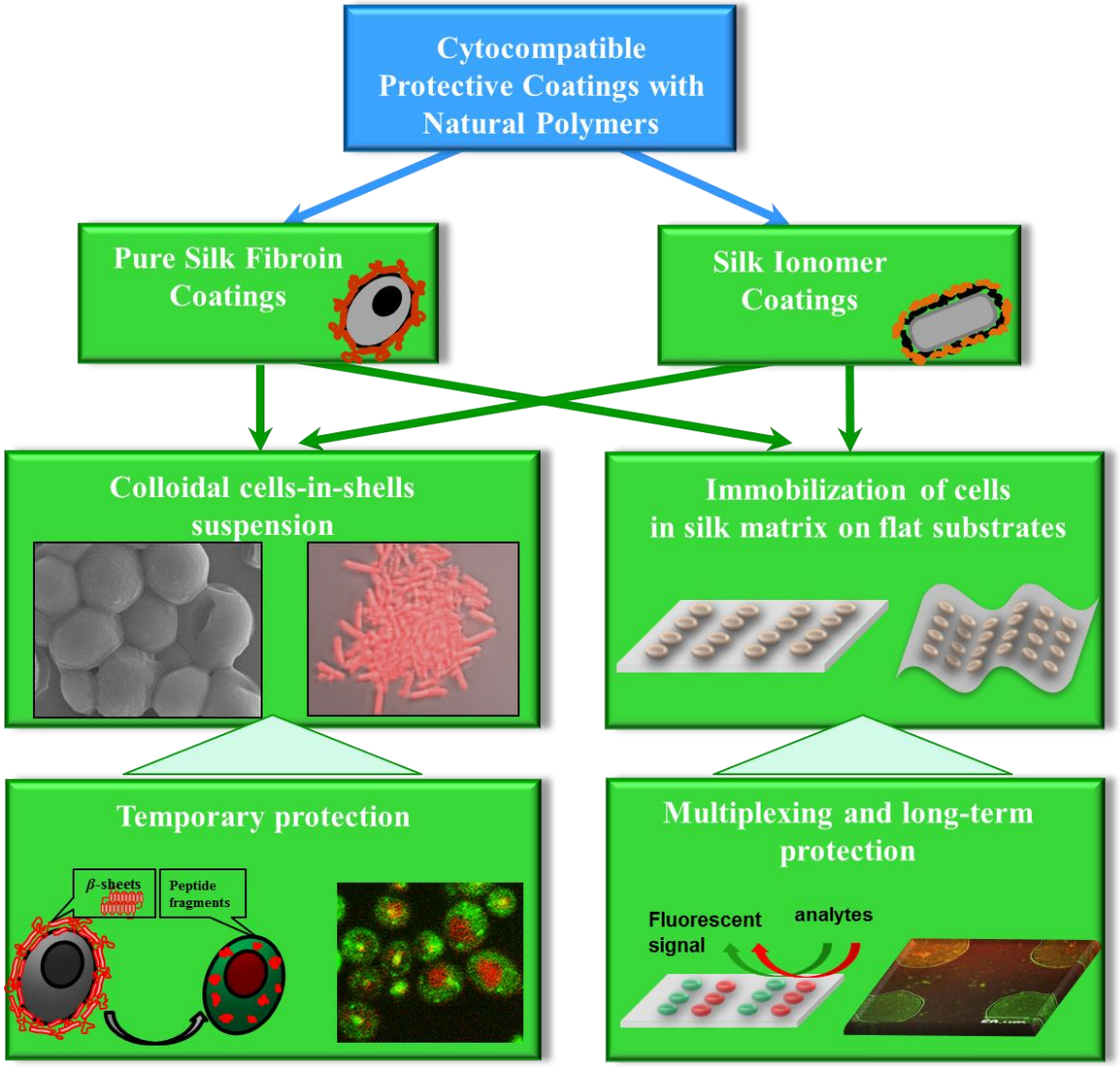

Figure 2.3 The motivation, goals, and specific areas of interest for task 2.

- *Fabricate cell arrays with two distinct reporter constructs (expressing GFP and RFP) immobilized in the multilayered silk matrix by utilizing inkjet printer, and demonstrate effectiveness of silk-based matrix to protect cells against harsh environment conditions and serve as the hydrogel matrix capable to hold, support and prolong cells function.*

The study of interfacial organization and interactions between cell surface and protective coating material (whether synthetic or natural) will help to understand the effect of material properties on the function of the cell as a response-mediated highly sensitive device. Bio-inspired materials with tunable bio- and physicochemical properties provide an indispensable platform to actively control and support cell functionality *in vitro* and *in vivo*. Cell surface engineering with application of various cytocompatible protective, mediating, functionalized media comprised of inorganic, polymeric, and biological shells dramatically increase cell viability and stability in synthetic environment as well as expand their applicability in biomedical, biotechnology, and bioelectronics fields.

2.3 Organization and composition of dissertation

Chapter 1 is a critical review of issues and state of the art research related to current cell surface modification and encapsulation techniques with different materials including synthetic and natural polymers. The differences in cell architecture between mammalian and microbial cells as well as within microbial cells themselves play a major role in assessing the appropriate method of encapsulation, as well as the biocompatibility of the material, and more precise what types of interaction forces involved in the assembly of protective layers direct the cytocompatibility of the coating. Hydrogen-bonded LbL structures represent new opportunities for cell-friendly LbL shells of "soft" type with more cell-compatible components and assembly procedures. The advantage of having such LbL shells assembled via non-covalent hydrogen-bonding interactions instead of traditional polyelectrolyte shells is that their micromechanical properties can be well controlled by changing pH, ionic strength, salt concentration, or temperature.[53,167] This provides tailoring of the pore sizes, porosity and degradability of shells for efficient diffusion of nutrients and chemical cues to and waste products from the cells,[194] as well as on-demand degradability of the shells. Also, discussed are the methods and criteria for immobilization of cells in biocompatible hydrogel matrix using inkjet assisted printing to serve as an efficient colorimetric biosensor.

Chapter 2 is a concise description of the goals and technical objectives of the work presented in this dissertation. Furthermore, it provides a brief overview of the organization of the dissertation, with brief descriptions of the contents of each chapter.

Chapter 3 discusses the experimental techniques and materials that played a critical role in the studies presented in this dissertation. It includes synthesis of pH-responsive PMAA-co-

NH_2 co-polymer, extraction of silk fibroin protein from the silk cocoons, labeling of polymers with fluorescent tags, fabrication of hollow microcapsules and formation of shells-on-cells coatings of various compositions. The choice of microbial cells that can respond to the presence of model analytes was also presented in this chapter. Characterization techniques include atomic force microscopy for observing topography of the cell surfaces, estimation of roughness and measuring micromechanical properties of the shells; confocal laser scanning microscopy for observing the presence of fluorescently-tagged LbL shells and for imaging cells expressing GFP or RFP after encapsulation; scanning electron microscopy for visualization of cells-in-shells; UV-Vis and fluorometer for assessing the viability tests and kinetics of GFP and RFP intensity that relied on progressive detection of fluorescence; zeta-potential for monitoring absorption of polymer layers and estimation of pKa at different pH; attenuated total reflectance Fourier transform infrared spectroscopy for monitoring the appearance of chemical groups after crosslinking; ellipsometry measurements for estimation of the thickness of LbL films. The chapter also introduces the fluorescence recovery after photobleaching technique that measures the diffusion coefficient through the capsule shell.

Chapter 4 relates to the detailed study of the hydrogen bonded model microcapsules based on tannic acid (TA) and polymer counterpart, as well as formation of TA-based LbL shells on yeast cells. Binding of tannic acid with several synthetic polymers has been shown to be pH-stable within a wide range from pH 2 to pH 10 with permeability properties inversely proportional on molecular weight in contrast to vast majority of hydrogen-bonded LbL shells based on poly(carboxylic acids).[145] Elastic compliance of shells, estimated with SFS at nanoscale level was measured to be ~3 MPa, which is several folds higher than Young's modulus of healthy cell membranes, and hence can restrict cell growth and reproduction.[195]

High biological activity of tannic acid including antioxidant, antimicrobial, and anticarcinogenic properties can be screened by other shell components providing protection from oxidative damage.[196]

Cell surface engineering with hydrogen-bonded LbL shells based on tannic acid as a critical component was demonstrated to preserve long-term survivability of the encapsulated cells with cell viability reaching 79% in contrast to ~20% viability for conventional PSS/PAH shells assembled on younger cells.[197] Stable *true hydrogen bonded* LbL shells can be assembled by eliminating prime poly(ethylene imine) (PEI) layer with viability rates reaching 94% for the comparable number of bilayers.[127] The study discusses the possible origins of high cytocompatibility of hydrogen-bonded shells, with focus on shell permeability studies, morphology and thickness of shells, structure and mechanical compliance of shells, effect of cationic pre-layer on viability of cells.

Beyond cell viability, the activity of cells in response to inducer molecules that simulated biosensing routine was shown to be higher for cells encapsulated in hydrogen-bonded LbL shells compared to electrostatically-assembled LbL shells.[127,197] Depending on the thickness of the shell, their chemical composition, and the nature of interactions within the shell, delay in cell growth to varying degrees was studied.

Ultrathin hydrogel shells with highly permeable network state offer unique properties controlled by the crosslinking density and pH-responsive behavior.[146] **Chapter 5** reports on the design and fabrication of lightly cross-linked LbL hydrogel microcapsules based on amine-functionalized poly(methylacrylic acid) (PMAA-*co*-NH_2).[198] Shells contained a low fraction of cross-linkable amine groups (17%) facilitated a highly swollen state in aqueous

environment. *S. cerevisiae* yeast cells encapsulated in such pH-responsive synthetic nanoshells assembled in sequential adsorption of PMAA-co-NH2 and neutral polymer via hydrogen-bonding demonstrated high viability rate indicating bio-compatibility of synthetic shells that allowed exchange of nutrients in and waste out of cells through the porous shells. Such high survivability level of encapsulated cells was attributed to the high compliance of the porous hydrogel shells and very minor content of a cationic component.

The study provides calculations on cross-linking degree and molecular weight between points of cross-links as a function of time during cross-linking procedure that explained more than 3 fold increase in capsule size at different pH conditions. Measurements of the thickness of the shells network as a function of pH, mechanical compliance and effect of pH on elastic modulus, pH-driven changes in shell topography demonstrated highly swollen nature of PMAA-*co*-NH_2 hydrogel system. Study of the cell growth was demonstrated to be mediated by the pH sensitive transitions occurring in the polymer material, which however did not influence cells function to produce GFP. We proposed that pH-responsive LbL shells can be used as active barrier for controlling the growth behavior of encapsulated cells. The ability to manipulate perceptible response from the cells by keeping them in "dormant" conditions (constrained replication) for extended time can be rewarding for biosensing applications with consistent long-term performance.

Chapter 6 describes the formation of biocompatible silk fibroin microcapsules with tunable shell thickness and controlled permeability.[199] "Silk-on-silk" LbL assembly was accomplished by dehydrating absorbed silk macromolecules with methanol to induce transitions from random coils to β-sheet-rich structure. The silk microcapsules demonstrated

good stability and high permeability which was readily controlled by the thickness of the silk shells.

Our study demonstrated that stable silk fibroin protein shells can be locked in at the cell surfaces by inducing secondary transition from Silk I to β-sheet-rich Silk II by salting-out in a proper ionic mixture complemented with shear-thinning effect.[200] Gentle ionic treatment allowed stabilization of the protein shell structure and did not compromise the cell function/activity, as was indicated by fast response from encapsulated cells. The study described the effect of ionic molarity and choice of the kosmotropic ions used to precipitate silk fibroin proteins on cell viability/function and effectiveness to produce stable silk shells. Very high viability rates (up to 97%) along with preserved metabolic activity of "silked" cells were achieved by matching extracellular conditions in molar concentrations. The process of precipitation of proteins by salting-out demonstrated formation of highly porous and ultrathin silk nanoshells, which are rarely achieved with synthetic polymer shells. The capability of cells to replicate was also studied in order to assess the robustness of the silk shells and the mechanism of biodegradation.

Chapter 7 reports on importance of chemical interactions involved in the assembly of cytocompatible coatings based on chemically modified silk protein with variable degree of derivation. Additionally, it describes the differences in shells morphology and cells-in-shells behavior as ionic charges involved in LbL assembly progressively got screened by poly(ethy-leneglycol) (PEG). The most cytocompatible LbL shells were demonstrated to be with highly modified (9% mol of PEG) silk fibroin poly-L-Lys ionomer when assembly was carried out via hydrogen-bonded interaction with protonated silk fibroin poly-L-Glu ionomer. The viability of cells encapsulated in this type of shells reached ~95%. Reduction

in cationic charges in silk ionomer with PEG block copolymer was demonstrated to significantly increase cytocompatibility of LbL shells reaching ~88% survivability rate compared to ~30% rate of cells-in-shells assembled through ionic pairing.

In **Chapter 8**, we demonstrated the feasibility of piezoelectric inkjet printer to fabricate cell arrays imbedded in silk multilayered structures. A prototype version of the cell-based biosensor arrays was envisioned with two types of reporter element (GFP and RFP) that were printed in arrays on variety of substrates (glass and polyethylene terephthalate). Transgenic cells embedded in silk matrix structures were capable of fast detection of the model analyte even after a long-term storage (2 months). Assembled in layered structures made from silk functionalized with positively- and negatively-charged natural polyelectrolytes, silk hydrogel matrix served as a substrate for printed cells securing and sealing them from external environment. It also provided robust and net-like structure for fast growing cells once the favorable conditions are present.

Finally, **Chapter 9** provides general conclusions for the overall work in the dissertation with a specific focus on impact and future directions.

3 CHAPTER

EXPERIMENTAL DETAILS

The following chapter is intended to provide a brief description and experimental details for the techniques and instruments used throughout this work.

3.1 Fabrication of nanoscale shells

The bulk of this research relies on fabrication on mono-dispersed model capsules on sacrificial silica templates that are matched in size to the cells we explored in this project. For this reason, a detailed description of the experimental procedures used in our lab for the formation of hollow capsules, measurements of essential physical properties are given in the following chapters.

3.1.1 Model capsules based on hydrogen-bonding

Hollow shells have been constructed on sacrificial spherical silica templates of 3.4 μm size according to established procedure.[201] Briefly, 0.5 mg mL^{1} polymer solutions were prepared by dissolving polymers in 0.01M sodium phosphate buffer with pH adjusted to 5, except for PEI, which was dissolved in 0.1 M NaCl with pH adjusted to 7. Typical deposition time was 15 min followed by three rinsing steps in phosphate buffer solution (0.01 M, pH=5) to remove excess of polymer. The hydrogen-bonded multilayers of (TA/neutral polymer) were deposited onto silica microparticles or planar silicon substrates by two routes. In the first route, a pre-layer of branched-PEI was adsorbed first followed by alternate adsorption of (TA/PVPON) multilayer starting with TA. In the second route, direct deposition of (PVPON/TA) multilayer was performed on particulate or planar substrates at pH = 2 starting from a neutral polymer. For particle suspensions, after each deposition step they

were settled down by centrifugation at 2000 rpm for 2 min to remove the excess of polymer. Deposition, rinsing and re-suspending steps were performed on a VWR analog vortex mixer at 2000 rpm. To etch out silica cores, the microparticles with the deposited multilayers were exposed to 8% hydrofluoric acid solution (HF) overnight followed by dialysis in ultra-pure water for 36 h with repeated change of water.

3.1.2 Model capsules based on pH-responsive polymer

In order to fabricate cross-linked hydrogel shells based on amine-functionalized poly-(methacrylic acid), PMAA-co-NH_2), a copolymer was synthesized using bulk copolymerization of a monomer of metharcylic acid (MAA) and a monomer, N-(tert-butoxycarbonylaminopropyl) methacrylamide (t-BOCAPMA). Briefly, 8.7 mL (100 mmol) of MAA and 658 mg (2.9 mmol) of t-BOCAPMA were mixed in a round-bottom flask. The solution was deoxygenated by bubbling with nitrogen for 30 min. After that, the mixture was heated to 45°C and stirred. Then, 40mg (0.25 mmol) of AIBN was added to the flask, and the reaction mixture was stirred under nitrogen atmosphere for 3 h. The reaction was terminated after 3 h by pouring the mixture into a 10-fold excess volume of diethyl ether. The precipitated copolymer was dissolved in tetrahydrofuran and precipitated in hexane. After a repeated precipitation step, the copolymer was dried in vacuum. t-Boc protecting groups were hydrolyzed by treating the copolymer with 1 M HCl in methanol for 100 h. Solutions of the deprotected copolymers were dialyzed against nanopure water using a Slide-A-Lyzer dialysis cassette (Thermo Scientific) with a molecular weight cutoff of 10 kDa and lyophilized. The molecular weight of PMAA-co-NH_2 was determined using GPC (Waters, 717 plus) equipped with a HPLC pump (Waters, 1515) at flow rate of 1 mL/min in THF at

25°C and three columns (guard and two PLgel 5 μm MIXED-C columns). The Mw of the resultant amino-containing copolymer was determined to be 14 kDa (PDI = 1.4).

Hydrogen-bonded LbL shells were deposited on a sacrificial silica cores starting from PVPON followed by PMAA-co-NH_2 until the desired thickness was achieved. The deposition time for each layer was 15 min under gentle shaking at 250 rpm using a vortex-shaker (VWR analog vortex). After each deposition, particles were centrifuged at 2000 rpm for 2 min and washed with 0.01 M phosphate buffer solution three times.

To prepare cross-linked capsules, silica particles with five polymer bilayers were introduced into the solution of EDC (5 mg/mL, 0.01 M phosphate buffer at pH 5.0) for 20, 30, and 40 min with consecutive washing in phosphate buffer solution at pH 6.0 for at least 1 h to remove coupling agent, reaction byproducts, and the PVPON layer. Un-cross-linked PVPON component and silica material were removed and dissolved in 8% aqueous hydrofluoric acid (HF) for 4 h with gentle shaking in the vortex to remove the sacrificial template and release hollow capsules. Exhaustive dialysis against nanopure water adjusted to pH 3.5 was performed for the next 72 h to remove any traces of HF. Dialysis of hydrogel capsules was performed in 1 mL Float-A-Lyzer dialyzing cassettes with 20 kDa cutoff pore size cellulose ester membranes.

3.1.3 Model capsules based on hydrophobic interactions of silk protein

Silk was obtained from *Bombyx mori* silkworm cocoons as previously reported.[202,203] Briefly, cocoons were boiled for 20 min in an aqueous solution of 0.02 M Na 2 CO 3 and then rinsed thoroughly with distilled water to extract the glue-like sericin proteins. The extracted silk fibroin was dissolved in 9.3 M LiBr solution at 60 ° C for 4 h, yielding a 20%

(w/v) solution. The solution was dialyzed against Nanopure water using Slide-a-Lyzer dialysis cassettes (molecular weight cutoff (MWCO) 3500, Pierce) at room temperature overnight to remove the LiBr. The dialysate was centrifuged three times, each at 20°C for 20 min, to remove impurities and the aggregates that occurred during dialysis. The 8% (w/v) dialysate solution was filtered just prior to use using 0.4 μ m glass-fiber syringe filters.

Silk solution was further diluted with Nanopure water to obtain 0.1% (w/v) solution. Silica particles were dispersed in silk solution and silk protein monolayer was allowed to absorb during mild agitation at 15 rpm for 15 minutes. Next, particles were re-dispersed first in Nanopure water to remove unbound silk proteins; centrifuged down to remove supernatant; then re-dispersed in 50% methanol solution followed by centrifugation and re-dispersion in 100% methanol solution to gradually induce transitions from random coils to β-sheets. To etch out silica cores, the microparticles with the deposited multilayers were exposed to 8% hydrofluoric acid solution (HF) overnight followed by dialysis in ultra-pure water for 36 h with repeated change of water.

3.1.4 Labeling of polymers with fluorescent dyes

Synthesis of PVPON-co-Alexa532. Amino-containing copolymer PVPON-co-NH_2 (4.2% on NH_3) was reacted with Alexa Fluor532 carboxylic acid succinimidyl ester fluorescent dye in methanol overnight in the dark to produce Alexa Fluor 532–PVPON fluorescently tagged polymer.[204] The Alexa Fluor 532–PVPON was exhaustively dialyzed against deionized water for 5 days. The dialysis was completed after no fluorescence was detected in the dialysis water. The dialyzed polymer solution was lyophilized, and solution of Alexa Fluor 532–PVPON (0.2 mg/mL, 0.01M Na phosphate buffer, 0.1M NaCl, pH6) was allowed to absorb as the last layer on cells.

Synthesis of PMAA-co-Alexa568. Accordingly, PMAA-co-Alexa568 was synthesized when Alexa Fluor568 carboxylic acid succinimidyl ester was reacted with PMAA-co-NH_2 (17% of NH_3). Fluorescently-labeled PMAA-co-Alexa568 was deposited as a top layer (0.2 mg/mL, 0.01 M phosphate buffer, pH 4.5).

Synthesis of Silk-co-Alexa532. Aqueous solution of silk (0.2% w/v) was combined with aqueous solution of Alexa Fluor532 (N -hydroxysuccinimidyl ester) fluorescent dye in a 15:1 ratio. The mixture was kept in a cold water bath overnight with slow stirring to produce silk-co-Alexa532 fluorescently labeled silk. The solution of silk-co-Alexa532 was exhaustively dialyzed against Nanopure water for 4 days using Slide-a-Lyser dialysis cassettes to remove any unbound fluorescent dye and was used directly on the top of the pre-formed silk shells.

Synthesis of SF-Lys-co-DyLight550. SF-Lys protein (2 mg/mL in PBS, pH 7.4) was reacted with DyLight NHS ester 550 in conjugation buffer according to the manufacturer's protocol. Fluorescently-labeled conjugated protein was further purified with dye removal columns and applied as a top layer on cells.

3.1.5 Synthesis of silk ionomers (system#1 and system#2)

Poly(amino acid)-modified silk materials were obtained using previously published methods that involve diazonium activation of the abundant tyrosine side chains in the SF chains, followed by chemical linking with polylysine or polyglutamic acid.[205] The SF was extracted from *Bombyx mori* cocoons according to established procedure.[206] For system#1, initially lower molecular weight of SF was obtained by boiling silk for 60 min followed by enriching SF in carboxyl content; then, one of the silk-poly(amino acid)-based ionomers (silk fibroin-

poly-L-Glutamic acid, SF-PG) was obtained by grafting poly-Glutamic acid (M_w=15 kDa) on SF to achieve a high content of carboxyl group. SF-PL represents the SF modified with poly-L-Lysine (M_w=15 kDa) to enrich the amine group content. Further modification of SF-PL with poly-ethylene glycol (PEG, M_w=5 kDa) side chains of different grafting density was performed to obtained branched SF-PL-co-$(PEG)_5$ and SF-PL-co-$(PEG)_9$ polymers. For system#2, initially silk was boiled for 5 min to obtain higher molecular weight of SF followed by modifying SF with shorter chains of poly-amino acids. SF-PL and SF-PG were obtained by grafting poly-L-Lysine (M_w=1 kDa) and poly-L-Glutamic acid (M_w=1 kDa) directly to tyrosine residues on SF. Additionally, copolymer PL-co-PEG (M_w=2.6 kDa) was grafted to silk fibroin tyrosine residues to obtain SF-PL-co-PEG.

3.2 Microbial cells

Genetically-modified microbial cells utilized in our study have been generously provided by collaborators from Air Force Research Laboratory (WPAFRL, Dayton, OH).[207,208] For all of the experiments, variety of microbial cells (spore-forming Gram-positive *B. subtilis* and non-spore-forming Gram-negative *E. coli* cells) have been transfected with a riboswitch construct containing an aptamer and a reporter domains (GFP or RFP plasmids). Galactose-sensitive yeast cells expressing yeast enhanced green fluorescent protein (yEGFP) and theophylline-activated synthetic riboswitch expressing green or red fluorescent proteins (GFP, or RFP) in bacterial cells were used for monitoring and quantitative analysis of cell activity after the encapsulation process.

3.2.1 *S. serevisiae* yeast transgenic cells

The *S. cerevisiae* YPH501 diploid yeast strain expressing a plasmid encoding yEGFP as a biomarker was used for this study.[127,197] Cells were cultured in synthetic minimal medium (SMM) supplemented with 2% raffinose solution. Yeast cells were grown at 30°C in a shaker incubator (New Brunswick Scientific) with 220 rpm to bring them to an early exponential phase when optical density reached 0.4-0.5 a.u. based on a 0-2 scale (absorbance was measured at 600 nm on a GE cell calculator).

3.2.2 *E. coli* and *B. subtilis* transgenic bacterial cells

BL21 *E. coli* cells (from Novagen) in this study were transformed with plasmids containing synthetic riboswitch constructs. Theophylline riboswitch (clone 12.1) [207,208] was placed either upstream of the sequence encoding a new fluorescent protein (GFPa1) from *Amphioxus* within pSAL vector (pSAL:RS12.1GFPa1His), or upstream of DsRed encoding sequence within pSAL vector (pSAL:RS12.1DsRed). In 1012 WT *B. subtilis* cells (from Novagen), riboswitch was placed upstream of pHT01:RSE_sfGFP plasmid vector. All types of bacterial cells were cultured in Luria-Bertani (LB) broth supplemented with 10 μg/mL of ampicillin (for *E. coli*) and 10 μg/mL of chloramphenicol (for *B. subtilis*). Cells were grown at 37ºC in a shaker incubator (New Brunswick Scientific) with 220-240 rpm to bring them to an early exponential phase when optical density reached 0.3-0.5 a.u. based on a 0-2 scale (absorbance was measured at 600 nm on a GE cell calculator). Expression from GFPa1 was measured at λ_{ex}=515 nm (λ_{em}=488 nm) and RFP at λ_{ex}=543 nm, λ_{em}= 592 nm on a spectrofluorophotometer (Shimadzu RF 5301 PC) and optical density at λ=600 nm was collected on cell calculator (from GE) over the course of cell study (48-56 h).

3.3 Cell nano-coatings

Nano-thin (3-30 nm) shells were assembled on cell surfaces of different types of microbial cells (*S. cerevisiae, E. coli, B. subtilis*). The sequential LbL assembly was employed for encapsulation of individual cells to form variable number of bilayers of pure hydrogen-bonded TA-based shells, lightly cross-linked hydrogel shells based on amine-functionalized PMAA-co-NH_2 copolymer, pure silk fibroin shells and silk ionomer shells according to the same procedure described earlier for the formation of microcapsules. Before deposition of LbL shells cells were harvested in 2 mL centrifuge tubes and washed three times with phosphate buffer (0.01 M, in 0.1 M NaCl, pH 5).

3.3.1 Coatings based on hydrogen-bond interactions

Pure hydrogen-bonded and PEI-primed LbL coatings were assembled on surface of yeast cells. For PEI-primed shells, first, a precursor, was allowed to adsorb onto yeast cell membrane from 0.5 mg/mL aqueous solution (0.1 M NaCl, pH 7) for 15 min followed by the LbL deposition of hydrogen-bonded TA/PVPON layers from solutions of the same concentrations dissolved in 0.01M phosphate buffer and 0.1MNaCl at pH 6.[197] For pure hydrogen-bonded LbL shells, TA was absorbed first followed by deposition of PVPON until the desired number of layers was achieved.[127] During LbL deposition, cells were re-dispersed in the appropriate solution by gentle shaking (at 225 rpm) for 15 minutes. After deposition of each layer, cells were collected in a pellet by centrifugation and washed three times with phosphate buffer. To visualize the polyelectrolyte membrane in CLSM, Alexa Fluor 532–PVPON was used during the deposition of the outermost (TA/PVPON) bilayer. All solutions were filter-sterilized with polystyrene non-pyrogenic membrane systems (0.22 mm pore size) (Corning filter system) before applying to the cells.

3.3.2 pH-sensitive coatings

Consecutive layers of PVPON and PMAA-co-NH_2 were assembled onto yeast cell walls from 0.5 mg/mL aqueous solutions (0.01 M phosphate buffer, pH 3.5) for 15 min until the desired number of bilayers was achieved.[198] Followed deposition of shells cross-linking was performed for 40 min with 1-ethyl-3-(dimethylaminopropyl) carbodiimide hydrochloride (EDC) (5 mg/mL, 0.01 M phosphate buffer, pH 5). During deposition and cross-linking, cells were re-dispersed by gentle rotation at 60 rpm at ambient conditions. After each deposition step, cells were collected into the pellet by centrifugation at 2000 rpm for 2 min and washed two times with phosphate buffer (0.01 M, pH 3.5) to remove the PVPON layer and residual cross-linking agent.

3.3.3 Pure silk fibroin protein coatings

Silk layers (designated as $(silk)_n$, where n denotes the number of layers) were allowed to absorb on cell surfaces from aqueous solution (1 mg/mL , pH 5) for 10 min by gentle rotation at 35 rpm.[200] After deposition of silk, cells were collected by centrifugation at 1000 rpm and washed with Nanopure water to remove any unbound silk protein, followed by incubation in Na^+ or K^+ phosphate buffer solutions (0.03 M pH 5.5, or 0.1 M pH 5.5) for 10 min. To induce transition of silk fibroin from random coil to β-sheet cells were incubated by vigorous shaking on Vertex (1000 rpm). The final washing was done in Nanopure water, after which the next deposition step of silk was performed. The formation of stable silk-on-silk shells around cells was induced by an all-aqueous salting-out process after deposition of every silk layer.

3.3.4 Ionomeric silk coatings

Silk ionomers (system#1 and system#2) were used to assemble pure ionomer and PEG-modified LbL coatings on bacterial cells (*E. coli* and *B. subtilis*). Deposition started from either SF-PL or SF-PL-PEG ionomer solution (1 mg/mL, in 0.05M Na phosphate buffer, pH6) followed by deposition of SF-PG (1 mg/mL in 0.05M Na phosphate buffer, pH6) for 10 minutes at 20 rpm on a rotating stage until desired number of bilayers was reached. After a monolayer of each ionomer was absorbed, two brief washing steps (0.05 M phosphate buffer, pH6) were performed to remove unbound protein molecules with centrifugation at 2,000 rpm for 2 minutes. Encapsulated cells were stored in the fridge at 4°C unless further studies of cell viability, activation of riboswitch or zeta-potential measurements were performed.

3.4 Immobilization of cells using inkjet printer technology

Piezoelectric system, JetLab II inkjet printer (MicroFab Technologies), was used for all experiments with 50 μm nozzle diameters for all materials and cell suspensions. Piezo-actuation of solutions produced the microdroplets on demand having a diameter of ~50 μm and volume of 70 pL injected at a speed of 2-3 m/s.

3.4.1 Silk multilayered pads

Silk ionomer multilayers (1 mg/mL in Na phosphate buffer, pH 5.5) were printed on hydrophobic glass substrates in alternate fashion starting from SF-PL layer followed by SF-PG layer constituting 1 bilayer structure until desired number of silk bilayers was achieved. Multilayered structures were printed as 20x20 circular dots arrays each dot having a diameter of ~100 μm and separated by ~150 μm.

3.4.2 Bacterial cells embedded in silk multilayered pads

In order to create biosensor arrays (8x8, 20x20), high concentration of *E. coli* cell suspensions (>5×10^8 cells/mL) were injected on the top of 3 bilayer silk structure followed by sealing cells with additional 3 bilayer structure of silk (3 bl-cells-3 bl). Cells containing two reporter elements (GFP and RFP) were kept in M9CA medium to preserve cells function and optimize printing conditions. Upon printing, cells were kept at 4°C up to 2 months to check their responsive function. Activation of RS in GFP-caring cells was performed with 2.5 mM and 5 mM of theophylline (0.05 M Na phosphate, pH 6) and activation of RS in TurboRFP-caring cells was performed with 0.5 mM and1 mM of IPTG (DI water) after 2 days (short term storage) and after 3 months (long term storage), respectfully.

3.5 Characterization techniques

This research is highly dependent on the application of a wide range of characterization techniques for the comprehensive study of physical and chemical properties of shells with different materials, as well as the cytocompatibility of polymer coatings and overall behavior of cells-in-shells assemblies. A variety of techniques were used to determine detailed information about the structure and behavior of the polymer coatings and their effect on cells function. The accurate characterization of the polymer material and model structures assembled from different polymers is an extremely critical part of this research and therefore the techniques used to do this will be discussed in detail with an emphasis on particular methods that are important for the work described.

3.5.1 Confocal Laser Scanning Microscopy (CLSM)

Confocal images of microbial cells encapsulated with different composition of shells and hollow capsules based on the same shell composition were obtained on Zeiss LSM 510 system, which is an inverted microscope equipped with Ar laser (Ex=488 nm) and He-Ne laser (Ex=543 nm). Emission from GFP and RFP was visualized with 515 nm and 560 nm band-pass filters, respectively. All fluorescently-labeled shells were excited with He-Ne laser (Ex=543 nm) and visualized with 560-590 nm band-pass filter.

To investigate capsule permeability to FITCl-labeled dextrans of different weight, a drop of a dispersion of hollow capsules was added to several Lab-Tek chambers, which were then half-filled with water and then mixed with FITC-dextran solutions in water (1mg/mL). CLSM images of the capsules were taken after 15 min and averaged for 20 individual capsules. Capsules appear dark when the hydrodynamic radius of dextran is comparable or greater than the pore size of the capsules ("close" state). When the dextran is able to penetrate through the capsule shell, capsules appear green ("open" state). Hence the pore size can be determined by the nominal hydrodynamic radius of the impenetrable dextran.

3.5.2 Atomic Force Microscopy (AFM)

Surface morphology of the hollow capsules and cells covered with different type of LbL shells was examined using atomic force microscopy (AFM). AFM images were collected using a Dimension-3000 (Digital Instruments) microscope in the ''light'' tapping mode (resonant frequency 100-500 kHz) at 90° scanning direction using silicon V-shape cantilevers having a spring constant of 46 N/m for dry capsules and 0.046 N/m for swollen capsules. Tapping mode AFM allows for the high resolution imaging of soft polymeric and biological samples without damage to tip or sample since contact with the surface is

minimized. Liquid cell was used for AFM scanning in water according to the well-established procedure.[209] For capsule sample preparation, a drop of capsule suspension was placed onto a pre-cleaned silicon wafer and dried in air prior to AFM imaging. For film thickness measurements the capsule single wall thickness was determined as half of the height of the collapsed flat regions of dried capsules bearing analysis from NanoScope software to generate height histograms.

Imaging of cells was performed on gluteraldehyde-fixed (GA, 4% v/v in water) cells. Prior to AFM scanning, cells have been extensively washed in Nanopure water and air-dried on silicon substrates. Surface roughness was estimated as Rq value from 300x300 nm box of a 1x1 μm scanned area.

AFM nanomechanical measurements of capsules in the swollen state were performed separately at different pH values by collecting 16 x 16 point arrays of force-distance curves for at least 5-6 capsules to ensure representative results. The spring constants of the cantilevers were determined by their thermal resonance frequency spectra. The tip radius was estimated by scanning 5 nm gold nanoparticle standards and performing deconvolution calculation using custom-made MMA processing software. Data processing and evaluation of the adhesion distribution were performed using the Sneddon's model. The indentation depth was limited to 2÷10 nm to avoid plastic deformation.

3.5.3 Scanning Electron Microscopy (SEM)

Scanning electron microscopy (SEM) (Hitachi-S-3400-II system) was used to investigate overall morphology of microcapsules and assembly behavior of cells-in-shells. Samples of capsules or cells were drop casted on silicon wafers, air-dried and sputtered with ~10 nm

film of gold, then imaged with an operating voltage of 5-10 keV. Before imaging, cells were fixed with a 4% gluteraldehyde buffered solution (0.1 M Na^+ phosphate buffer, pH 7.4).

3.5.4 Fluorescence recovery after photobleaching (FRAP) method

Experiments on permeability are performed using CLSM.[210] Briefly, photobleaching of fluorescent molecules (fluorescein isothiocyanate), (FITC) inside the TA/PVPON capsules with 4, 5 and 6 bilayers is performed by combining 100 µL of hollow capsules solution with 200 µL of 1 mg/mL FITC solution. Mixture is allowed to settle down in a Lab-Tek chamber glass cell for three hours before starting the experiment. Laser beam (488 nm) is focused within a region of interest (ROI) inside a capsule, and pulsed at 100% intensity to photobleach the dye molecules (Figure 3.1a). Each experiment is started with 3 pre-bleached image scans followed by 25-35 bleach pulse exposures of 3 ms each within ROI. The bleaching time can be adjusted to ensure complete photobleaching of FITC inside the capsule. The fluorescence recovery is monitored by capturing 30 scans of 3 ms exposure at 3% laser intensity. The recovery is considered complete when the intensity of the

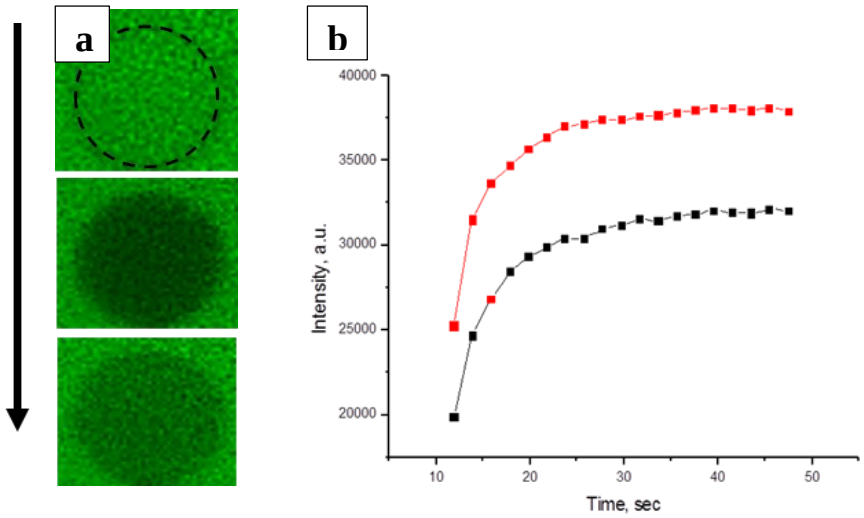

Figure 3.1 CLSM images of a capsule before bleaching, after and recovered (a). Recovery curves of fluorescence obtained for capsules with different composition (b).

photobleached region stabilized. The quantitative analysis was performed using ImageJ software, and curve-fitting is conducted in Origin (Figure 3.1b). The recovery curve of the fluorescence intensity $I(t)$ as a function of time t can be fit by:

$$I = I_0\left(1 - e^{-At}\right) \quad (1)$$

where I and I_0 are the equilibrium and initial fluorescence intensities, respectively. The coefficient A is related to the diffusion coefficient, D, according to:

$$A = 3D/rh \quad (2)$$

for FITC diffusion through a spherical wall with radius r and thickness h.

In the solution, (1) obeys Fick's law and can be written as:

$$dc/dt = -A\left(c - c_0\right) \quad (3)$$

where c and c_0 are the concentrations inside and outside the capsules, respectively, and $c \sim I$. A typical fit of the recovery curve is obtained using (1) and the coefficient A can be deduced from the fitting.[211,212,213]

3.5.5 Cell viability tests and activation of green and red fluorescent proteins (GFP, RFP)

Single point assays of viability or cytotoxicity are not sufficient to determine mechanism of toxicity. Hence, several cytotoxicity assays kits were performed to predict effect of coatings and encapsulation procedures on cells. Tests were performed immediately after encapsulation process with Live/Dead, MTT and rezasurin assay kits according to

manufacturer's protocols (Promega). Live/Dead viability kit provides two different nucleic acid stains to rapidly distinguish live bacteria with intact plasma membranes from dead bacteria with compromised membranes. Cells were stained according to the manufacturer's protocol. Representative images were collected with Zeiss 510 LSM using a band-pass filter λex/em = 488/505 and λex/em = 543/560 nm for detection of FITC and rhodamine, respectively. Confocal micrographs were analyzed with Zen2009 software to quantify the number of pixels corresponding to fluorescent emission from live (green) and dead (red) cells.

Rezasurin test estimates the number of viable cells in the cell medium serum. The assay is based on the ability of living cells to convert a redox dye (resazurin) into a fluorescent end product (resorufin). Viable cells retain the ability to reduce resazurin into resorufin. Nonviable cells rapidly lose metabolic capacity, do not reduce the indicator dye, and thus do not generate a fluorescent signal. For rezasurin-based assay, fluorescence from rezarufin was measured at λ=585 nm (λex = 560 nm) on a spectrofluorophotometer (Shimadzu RF 5301 PC) after incubation for 2, 4 and 6 h.

The mitochondrial MTT assay brings the predictive data to distinguish mitochondrial dysfunction from other cytotoxic effects. MTT assay is based on the differential measurement of biomarkers associated with changes in cell membrane integrity and cellular ATP levels. The MTT assay involves the conversion of the water soluble MTT (3-(4,5-dimethylthiazol-2-yl)-2,5-diphenyltetrazolium bromide) to an insoluble formazan. The formazan is then solubilized with DMSO, and the concentration determined by optical density at 570 nm on (Schimadzu UV-2450) spectro-photometer.

Kinetics of GFP and TurboRFP intensities in bacterial cells were performed on spectro-fluoro-photometer (Schimadzu RF 5301 PC) with Ex/Em=480/510 nm (for GFP), and Ex/Em=560/585 nm (for TurboRFP) after 0, 2, 4, 6, 8 and 24 hours. Activation of RS was done with theophylline (2.5 mM or 5 mM in 0.05M Na phosphate buffer, pH6) or IPTG (0.5 mM or 1 mM, DI water) while incubating in M9CA medium. Activation of GFP in yeast cells was induced with galactose (2%) while incubating in SMM medium.

3.5.6 Z-potential and Dynamic Light Scattering (DLS)

Zeta-potential was used to determine the surface charge of the coatings after deposition of each layer. This technique is extremely sensitive for observing interactions between absorbed polyelectrolytes and colloidal surfaces. It also can be used as a metric for determining if proper surface functionalization has been achieved when exchanging polyelectrolytes. Zeta-potential measurements were obtained on Zetasizer Nano-ZS equipment (Malvern). Each value was made at ambient conditions at 25°C by averaging three independent measurements of 35 sub-runs using the Smoluchowski model. Polystyrene disposable Zeta-potential cuvettes (Malvern) were utilized. The same instrument was also used for dynamic light scattering measurements of the silk particles using disposable polystyrene 1.5 mL microcuvettes (PlastiBrand, Germany). Silk solution was mixed with potassium phosphate of different molarities in volumetric ratios of 1:6 using a pipette. Measurements were made with the 173° backscatter detector using refractive indices of 1.33 and 1.6 for buffer and protein solutions respectively. These measurements provided the hydrodynamic diameter of the silk at different pH values as the transition from random coils to β-sheets was induced at low and high pH values.

3.5.7 Attenuated Furrier Transform Infrared Spectroscopy (AFT-IR)

Chemical signature peaks and their shifts were performed to obtain the information on chemical interactions involved during LbL assembly. Measurements were performed on hollow capsules using a Bruker FTIR spectrometer Vertex 70 equipped with a narrow-band mercury cadmium telluride detector and a rectangular trapezoidal Si crystal according to a procedure established in our group. Spectra were collected at 1 cm^{-1} resolution, and the number of averaged scans was 120. Aqueous solutions of capsules were spin-coated on ATR crystal for 30 seconds (RPM = 3,000).

4 CHAPTER

MICROCAPSULES AND CELL COATINGS BASED ON HYDROGEN-BONDED TANNIC ACID ASSEMBLIES

4.1 Introduction

Hollow microcapsules can be produced by the layer-by-layer (LbL) assembly onto colloid cores with charged polyelectrolytes and/or charged inorganic nanoparticles followed by subsequent decomposition of cores.[214,215] Properties of polyelectrolyte multilayer LbL microcapsules can be well controlled by changing various parameters, including pH, ionic strength, salt concentration, temperature, light, and magnetic field.[216,217] The micromechanical properties of bare or functionalized with microparticles LbL microcapsules were shown to be varied in a wide range via selection of polymers and fabrication conditions.[218,219]

Hydrogen-bonded LbL materials present new opportunities for LbL-fabricated shells, which, otherwise, could be more difficult to realize. Most of hydrogen-bonded systems studied to date have been demonstrated to be unstable and dissolve under physiological conditions thus facilitating degradability but compromising mid-term stability.[118,144] Their properties offer fabrication of nano- and micro-containers responsive in biologically and physiologically relevant pH range under mild environmental conditions. Thus, the hydrogen-bonded LbL assembly of films and shells in water allows incorporating uncharged biocompatible functional polymers within the LbL film such as poly(ethylene oxide) (PEO), known to be resistant to protein and lipid adsorption, which is crucial for use in biomedical applications.

4.2 Experimental details

Information regarding the fabrication of hollow capsules based on hydrogen-bonded assembly of two-component hydrogel materials: multi-phenol tannic acid (TA) and several hydrophilic polymers (poly(N-vinylpirrolidone) (PVPON), poly(N-vinylcaprolactam) (PVCL), and poly(N-isopropylacrylamide) (PNIPAM)), the responsive properties of the (TA/neutral polymer) capsules, synthesis of in-situ gold nanoparticles within the shells, encapsulation of yeast cells with pure and PEI-primed hydrogen-bonded shells, as well as the characterization through Zeta-potential, AFM, SEM, ATR-FTIR spectroscopy and cell viability studies can be found in Chapter 3.

4.3 Results and discussion

4.3.1 pH-Responsive microcapsule reactors with different polymer counterparts

Model hollow shells of TA/PVPON multilayers with different molecular weight of PVPON have been produced according to the established procedure.[145] Figure 4.1 depicts overall principles of the microcapsule design exploited in this work. The shell fabrication was applied to silica spherical templates. Two routes of the multilayer formation were explored in this study. The silica surfaces can be pre-coated with poly(ethyleneimine) (PEI) layer to ensure good adhesion of the following (TA/polymer) LbL multilayer to the particle surfaces. In the other route, we employed the direct formation of the (polymer/TA) LbL multilayers on silica surfaces through hydrogen-bonding interactions of PVPON, PVCL or PNIPAM components with the hydroxyl-terminated silica surface.[220]

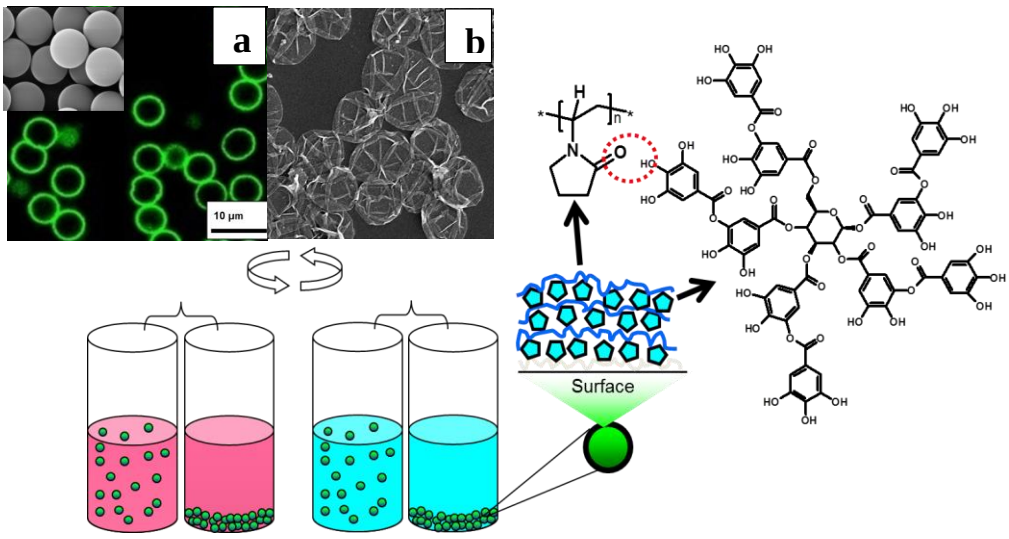

Figure 4.1 General schematics of the LbL (TA/non-ionic polymer) capsules formation based on hydrogen-bonding. The CLSM image of PEI-$(TA/PVPON)_3$ capsules in aqueous solution (a), inset shows silica templates; SEM image of PEI-(TA/PVPON) dried capsules (b).

We were able to successfully fabricate TA-based LbL hollow capsules at pH=5 (0.01 M) with all non-ionic polymers used in this work. Figure 4.1a demonstrates that robust and well-separated TA/PVPON hollow capsules with no sign of capsule aggregation can be produced after completely etching out silica cores. After being placed on a silicon wafer, the capsules have been collapsed upon drying with many random folds caused by local instabilities and wrinkling due to capillary forces acting on the microcapsules (Figure 4.1b).

The surface morphology of the obtained capsules was analyzed with AFM (Figure 4.2). The AFM analysis of the dried hollow TA/PVPON capsules shown in Figure 4.2 revealed a grainy surface morphology of the folded shells in all three studied TA/PVPON systems. The microroughness of 5.6±0.3 nm, 5.2±0.3 nm and 5.4±0.2 nm was measured for different capsules when the molecular weight of PVPON was 55 000 Da, 360 000 Da and 1,300 kDa, respectively (here and below measured at 1×1 mm^2 areas). These values are higher than

common values for ionic-based LbL films (usually below 1 nm) and reflect local aggregation of the polymer components.[221,222] In fact, hydrogen bonded multilayers are usually reported to have higher microroughness of several nanometres with the values dependent on fabrication conditions.[223] AFM images obtained with the higher magnification demonstrate the presence of larger TA/PVPON domains of aggregated polymer layers (close to 100 nm) regardless of the molecular weight of PVPON component.

We explored the effect of molecular weight of a neutral polymer, i.e., PVPON or PVCL, on the properties of the (TA/non-ionic polymer) multilayers assembled at pH=5. Interestingly, the change in the molecular weight from 55 kDa to 1,300 kDa resulted in a doubled bilayer thickness of a single TA/PVPON wall and increased from 1.0±0.1 nm to 2.2±0.2 nm, respectively. AFM analysis of the domains revealed a slight increase in the domain height in the case of higher molecular weight of PVPON from 5±2 nm for the $(TA/PVPON\text{-}55)_4$ to

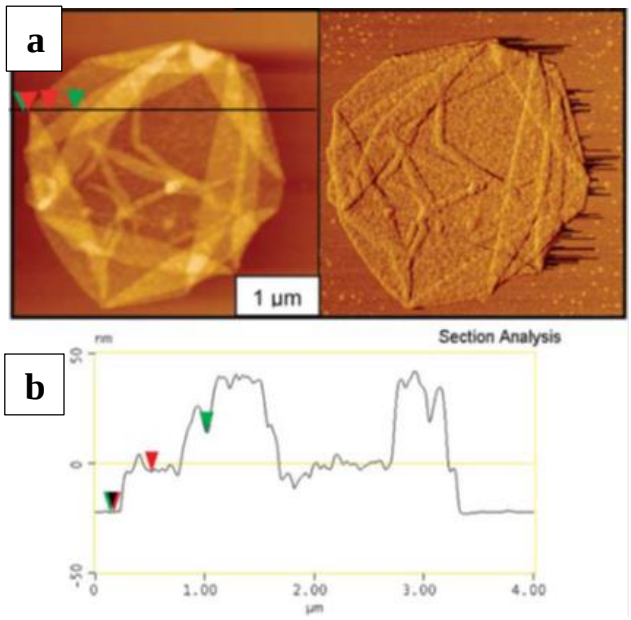

Figure 4.2 Typical AFM topography (left) and phase images (right) of $PEI\text{-}(TA/PVPON)_4$ capsules prepared from PVPON (Mw =1,300 kDa) (a). Z-scale is 100 nm for topography images. Section analysis of the $PEI\text{-}(TA/PVPON\text{-}1300)_4$ capsule (b).

8±2 nm for the $(TA/PVPON\text{-}360)_4$ and to 8±2 nm for the $(TA/PVPON\text{-}1300)_4$. These results reflect the increase in the overall thickness for TA/PVPON systems, probably due to an increased amount of binding sites for longer PVPON chains.

We pursued the fabrication of TA-based hydrogen-bonded capsules at a slightly acidic pH=5 to design shells with pH responsive properties stable under biologically relevant conditions. It is worth mentioning that in the case of planar films it is important to ensure the pH-stability of the pre-layers used to enhance the initial adsorption. In some cases, weakened interactions of the enhancing pre-layer and the substrate can result in the detachment of the multilayer from the substrate leading to wrong conclusions about the multilayer pH-stability.

The deposition of TA/PVPON multilayers was performed at pH=5 onto silica particles pre-coated with PEI. Typically, 1.2±0.8 nm of PEI was adsorbed under these conditions. The strong interaction of the first TA layer with PEI is facilitated via ionic pairing of positively charged PEI (pKa=9.5 for primary amines, pKa=7 for secondary amines) with slightly negatively charged phenolic groups of TA. Although the estimated pKa values for phenolic groups is reported to be in the pH region from 5 to 8.5, the increased ionization of TA phenol groups was also reported in the vicinity of positively charged polyelectrolyte chains.

Figure 4.3 demonstrates the evolution of the surface charges of capsules during LbL formation of $PEI\text{-}(TA/PVPON\text{-}55)_3$ on silica particles. After PEI deposition, the zeta-potential of the capsules switches from 56±2 mV for silica surface due to ionized silanol groups (pK_0 and pKa of surface silanol groups are 2–3 and 9.1–9.4, respectively) to +40±4 mV due to adsorbed positively charged polycation chains. Such surface charge reversal is typically observed in electrostatic LbL assembly of oppositely charged polymers at surfaces.

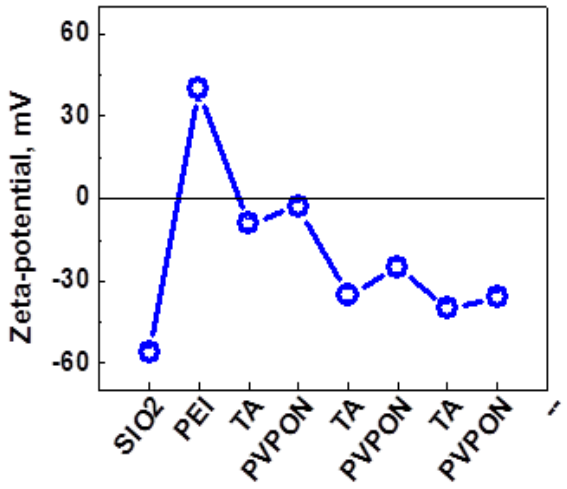

Figure 4.3 Evolution of zeta-potential during deposition of PEI-(TA/PVPON)$_3$ multilayers on surfaces of silica particles.

However, in contrast to the regular LbL assembly of conventional polyelectrolytes, the LbL formation of the following hydrogen- bonded TA/PVPON is characterized by the overall negative zeta-potential throughout the entire multilayer formation due to the ionized phenolic groups of TA molecules.

During the deposition steps of PVPON component, the decrease in the negative value of the zeta-potential was observed to be -6 mV. Similar oscillations of the zeta-potential within negative values were reported for hydrogen-bonded multilayers of poly(carboxylic acid)s[224,225] and were explained by the shifting of the effective slip plane, at which electrophoretic mobility and the zeta-potential is measured, away from the surface. Such a shift occurs due to immobilization of water associated with the polymer loops when uncharged polymer adsorbs onto a charged surface. On the other hand, the absence of the charge reversal along with the presence of negative surface charge throughout the entire deposition allows a good stability of the particle suspension and prevents it from severe

aggregation. The charge mediated stability of the polymer-coated particles is crucial for the fabrication of well-separated capsules.

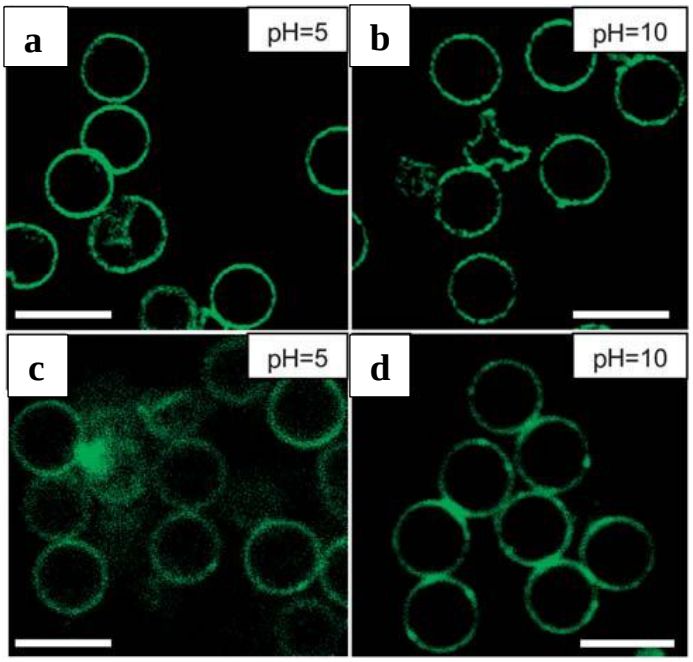

Figure 4.4 Confocal images of (TA-PVPON-55)4 capsules at pH 5 (a) and pH 10 (b) and PEI-(TA-PVPON-55)$_4$ at pH 5 (c) and pH 10 (d). Scale bar is 5 μm.

In the second route, direct deposition of the PVPON/TA LbL multilayers onto silica surfaces without a PEI-treatment was performed at pH=2. In this case, PVPON was adsorbed first because of hydrogen bonds formed between protonated silanols of the silica surface and carbonyl groups on PVPON chains.[220,226] When hollow PEI-(TA/PVPON)$_3$ or (PVPON/TA)$_3$ capsules were transferred from pH=5 to pH=10, no capsule dissolution was observed (Figure 4.4). There was also no distinctive change in the capsule diameter. For instance, PEI-(TA/PVPON)$_3$ capsules exhibited the diameter of 2.8±0.2 mm at pH=5 and 2.9±0.2 mm at pH=10 (Figures 4.4a,b). The hydrogen-bonded capsule shells did not show pH-dependent swelling typical for the polyelectrolyte capsules under conditions when charge balance within a shell is disturbed. In such a case, the excess of either charge is

introduced within the shell under extreme pH close to p*K*a values of the polyelectrolytes. The observed phenomenon can be explained by the fact that TA is a small and relatively rigid molecule with permanent molecular dimensions unable to swell upon the pH changes unlike flexible and long-chain synthetic poly(carboxylic acid)s.[227,228]

Such high pH-stability seems surprising especially if we consider the p*K*a of TA is in the range from pH=5 to pH=8.5. Quick disassembly of the hydrogen-bonded PMAA/PVPON or PAA/PVPON usually occurs when such multilayers are brought to pH close to a p*K*a value of the ionizable counterpart.[144] On the other hand, increased association strength of hydrogen-bonded components due to cooperative hydrophobic interactions was observed for higher molecular weights of a polymer component. This effect resulted in overall increase of the film pH-stability and a shift of a critical dissolution pH to higher pH values.[229]

The emerging negative charges in response to pH increase were observed for PEI-$(TA/PVPON)_3$ capsules composed from PVPON with Mw=55 kDa. The magnitude of the negative surface charge of the PEI-(TA/ PVPON) capsules increased after their exposure to the basic pH and became 55±2mV at pH=9 versus 36±2mV at pH=6 reflecting the appearance of ionized phenolic groups within the capsule shells. However, it is evident that the magnitude of such increase is lower when PVPON with higher molecular weight was used for the capsule shell fabrication. This difference is probably reflective of better negative charge screening by longer PVPON chains and consistent with the thicker TA/PVPON-1300 shells with the same number of deposited layers. The better charge screening, in turn, can be due to a suppressed ionization because of a larger number of binding sites in the case of longer PVPON chains.[229]

To understand if any compositional changes occur within the shell upon the pH change from pH=5 to pH=9, in situ ATR-FTIR experiments were additionally performed. For these measurements, the PEI-(TA/PVPON)$_5$ LbL films were built on a silicon crystal in a flow-through cell, and their pH-triggered changes were monitored in real-time (Figure 4.5). The important feature of the ATR-FTIR technique is its ability to monitor individual components of the layered films with very few layers and track compositional changes by following the characteristic functional groups.

Figure 4.5 demonstrates that the FTIR spectrum of the LbL film at pH=5 is similar to that at pH=9 with four major absorbance bands which are easily resolved. The O–H stretching frequencies for the phenolic groups are located in the 3180–3400 cm^{-1} region.[230] An adsorption band at 1718 cm^{-1} is associated with C=O stretching vibration of the ester groups in TA molecule and a strong adsorption band at 1654 cm^{-1} originates from stretching vibrations of carbonyl groups of the pyrrolidone ring[231] overlapped with the stretching

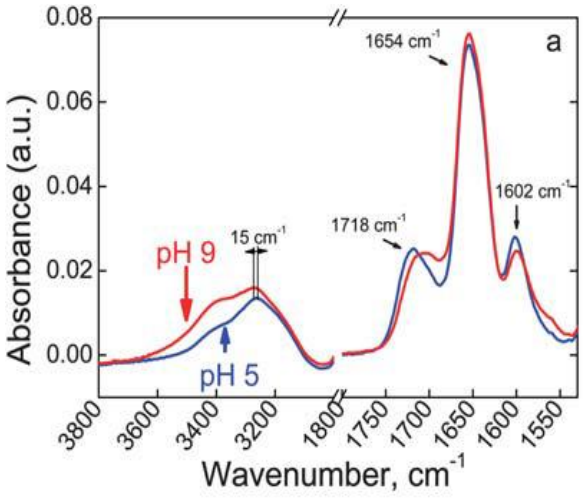

Figure 4.5 ATR-FTIR spectra of PEI-(TA/PVPON-55)$_5$ films deposited on silicon crystal from 0.01M phosphate buffer solutions at pH 5 and exposed to pH 9.

vibrations from TA aromatic rings.[232] Another absorption peak of aromatic ring stretch vibrations appears at ~1602 cm^{-1}.[232]

In our experiments, the peak at 1718 cm^{-1} shifted to 1704 cm^{-1} along with the O–H stretch band shift from 3258 cm^{-1} to 3273 cm^{-1} when the $(TA/PVPON)_5$ LbL film was exposed to pH=9. These changes reflect the disruption of hydrogen-bonds of carbonyl and hydroxyl groups in LbL multilayers. As known, such a disruption causes a displacement of the frequencies of the stretch absorption of the carbonyl towards lower wavenumbers up to 20 cm^{-1} while in the case of hydroxyl groups such shift occurs upwards up to 300 cm^{-1}.[233] Importantly, the presence of the adsorption band at 1654 cm^{-1} at both pH=5 and pH=9 indicates that there is no PVPON released from the film upon the pH change. The observed high capability of TA/PVPON films to withstand an internal ionization within the multilayer can be explained by the ability of TA to form intra-molecular hydrogen bonds. Such stabilizing effect can be enhanced with the increase of a number of participating phenolic units.

Hydrogen-bonded shells demonstrated pH-dependent permeability properties to FITC-labeled dextrans, which can be additionally regulated by MW of the counter-part polymer (Figure 4.6). The capsule permeability was monitored by using FITC-dextrans of various molecular weights as a fluorescent probe. Capsules were considered impermeable for the probe if the ratio of intensities from capsule interior to bulk solution was less than 0.5 during 15 min after the fluorescent probe solution was mixed with capsules. Table 1 compares the permeability of the dextrans through the TA/PVPON shells made of various molecular weight PVPON polymers.

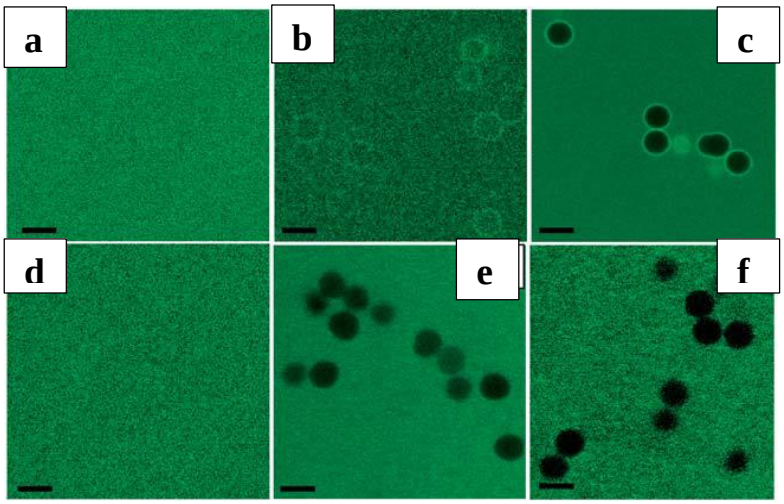

Figure 4.6 Confocal micrographs of PEI-$(TA/PVPON\text{-}55)_4$ capsules in phosphate buffer solution at pH 6 (top images) and at pH 9 (bottom images) exposed to FITC-dextran solution with Mw = 4000 (a, d), Mw = 70 000 (b, e), Mw = 500 000 (c, f). Scale bar is 4 μm.

Figure 4.6 shows that the $(TA/PVPON\text{-}55)_4$ shells exposed to pH=6 demonstrate a highly permeable, ‘‘open’’ structure for the dextrans of up to 250 kDa, being ‘‘closed’’ only for the dextran with Mw=500 kDa (Figures 4.6a,b). High molecular weight permeants (Mw > 500 kDa) are rejected by the $(TA\text{-}PVPON\text{-}55)_4$ capsules at pH=6, which is close to the fabrication conditions of the shells when they bear some negative charge (Figure 4.6c). The dextran permeability through the shells decreased with stronger bound multilayers of the $(TA/PVPON\text{-}360)_4$ and $(TA/PVPON\text{-}1300)_4$. In those cases, the shells were capable of excluding dextrans of Mw < 40 kDa (Table 1). These results correlate well with the data on the thicker shells of $(TA/PVPON\text{-}360)_4$ and $(TA/PVPON\text{-}1300)_4$ compared to that of TA/PVPON-55.

The permeability of dextrans through the shells decreased when pH was switched from slightly acidic pH 6 to basic pH 9 (Table 1). This permeability profile is in contrast to previously studied permeability of TA/PAH or TA/PDDA ionically paired multilayer LbL capsules which showed the lowest permeability in the pH region from 5 to 7.[234] Figure 4.6

illustrates that the $(TA/PVPON\text{-}55)_4$ capsules became impermeable for the dextran of 70 kDa when pH was changed from 6 to 9 (Figures 4.6b and 4.6e, respectively).

Under basic pH conditions similar trend of the decreased dextran permeability was observed when PVPON with Mw=55 kDa was changed to that with Mw=360 kDa or Mw=1,300 kDa (Table 1). In the case of ionically paired TA/PAH or TA/PDDA capsules, the pH-dependent permeability was attributed to slow dissolution of the capsules under basic pH. However, in the case of the hydrogen-bonded TA/PVPON capsules stable within $2 < pH < 10$ range, the observed decrease in the shell permeability most probably reflects structural changes within the capsule shells. We suggest that the phenomenon is related to the disruption of intra-molecular hydrogen bonds of TA molecules at basic pH as discussed above.

Table 4.1. Permeability of $PEI\text{-}(TA/PVPON\text{-}55)_4$, $PEI\text{-}(TA/PVPON\text{-}360)_4$, $PEI\text{-}(TA/PVPON\text{-}1300)_4$ capsules to FITC-labeled dextrans with different molecular weight and at pH 6 and 9.

	TA/PVPON-1300kDa		**TA/PVPON-360kDa**		**TA/PVPON-55kDa**	
Dextran Mw, kDa	**pH 6**	**pH 9**	**pH 6**	**pH 9**	**pH 6**	**pH 9**
4	+	–	+	+	+	+
10	+	–	+	+	+	+
20	+	–	+	–	+	+
40	–	–	+	–	+	+
70	–	–	–	–	+	–
150	–	–	–	–	+	–
250	–	–	–	–	–	–

4.3.2 Reducing properties of TA and growth of gold NPs

The chelating and reducing properties of TA were used to produce gold nanoparticles (NP) within the hydrogen-bonded TA/PVPON shells. Mono-dispersed gold NPs with narrow size distribution and average size of 4 nm were analyzed with TEM, as well as the presence of gold was confirmed with EDX, and absorbance spectra at 530 nm in PEI-(TA/PVPON55)$_3$-Au capsules solution (Figure 4.7). By increasing MW of polymer counterpart, the broader distribution of gold NPs diameter was observed (~8±5 nm for PVPON-360kDa). This attributes to increased amount of TA/PVPON present in shells wall (or thicker shell wall), and hence more available reducing sites on tannic acid resulting in larger nanoparticles produced. With increasing MW of PVPON to 1,300 kDa, two distribution peaks of NPs with average size of 3±1 nm and 10±2 nm were analyzed. Non-ionic polymer serves as a capping agent, stabilizing NPs and not allowing them to aggregate, which responsible for small size

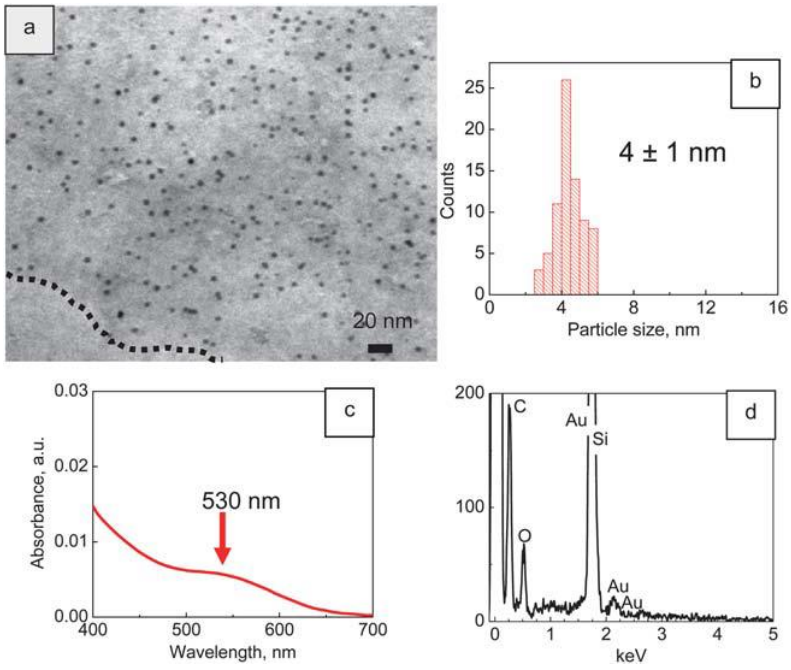

Figure 4.7 The TEM image of PEI-(TA/PVPON-55)$_3$-Au hollow capsule (a) with the particle size distribution (b) and the UV-vis spectrum of PEI-(TA/PVPON-55)$_3$-Au capsule solution (c). The EDX data for the PEI-(TA/PVPON-55)$_3$-Au capsules (d).

NPs. At the same time, increased amount of TA/PVPON allows for efficient reducing of gold by higher amount of phenolic groups of TA available to produce larger size NPs.

4.3.3 Mechanical properties of shells

The average elastic modulus of the PEI-(TA/PVPON-55) shell in water was determined to be 0.2–0.4 MPa, a common value for highly compliant densely cross-linked gel materials.[195] The values measured for TA/PVPON is much lower than that for traditional LbL shells in the swollen state (hundreds MPa). The increase of the molecular weight of the PVPON component from 55 to 1300 kDa promotes chain entanglements and intermixing that causing significant stiffening of LbL shells with the elastic modulus rising from 0.2 to 0.45 MPa for PEI-free LbL shells. Moreover, adding a PEI prime layer to the core before LbL shell assembly dramatically affects the growth and aggregation state of hydrogen-bonded multilayers which consequently results in dramatically stiffer, thicker, and rougher shells with the elastic modulus reaching 4.3 MPa for high molecular PVPON component. Assembling a cationic primary layer and variation of molecular weight of polymer layers allows for control the thickness and the stiffness of the capsule shell which is crucial for the potential applications in drug release and sensor platforms.

4.3.4 Permeability of shells

Permeability of a small molecule (fluorescein isothiocyanate, FITC) through PEI-$(TA/PVPON)_n$ model shells using FRAP method was performed to model the permeability of nutrients through the shells (see Experimental Section 3 for detail, Figure 6.5). In this technique, polymeric hollow microcapsules serve as model system to evaluate and compare permissive properties as a function of shell structure. Since basic nutrients (glucose, essential amino acids) and inducer molecules (e.g., galactose, Mw=180 Da) are comparable in size

with FITC molecules (Mw=380 Da), we suggest that these molecules will also be able to freely pass through the shell membrane and be available for proper cell function.

As demonstrated by a graph from Figure 4.8, the permeability through hydrogen-bonded shells is dramatically higher than for PAH/PSS shells of comparable number of bilayers with diffusion coefficient reaching $D=8\times10^{-12}$ cm^2s^{-1} which is almost five times higher than that known for traditional LbL shells. The diffusion coefficient decreases with increasing number of bilayers which implies the diffusion limiting permeation. The observed difference for diffusion coefficients between PAH/PSS and TA/PVPON shells can be attributed to loose, nano-porous morphology of the TA/PVPON LbL multilayers, a characteristic feature of hydrogen-bonded systems. These results support our suggestion on the highly permeable structure of hydrogen-bound shells exploited here which is critical for the transport of nutrients towards coated cells.

Moreover, our results on polysaccharides diffusion across LbL shells suggested the threshold of the shell permeability between 20 and 40 kDa under the experimental conditions.[145]

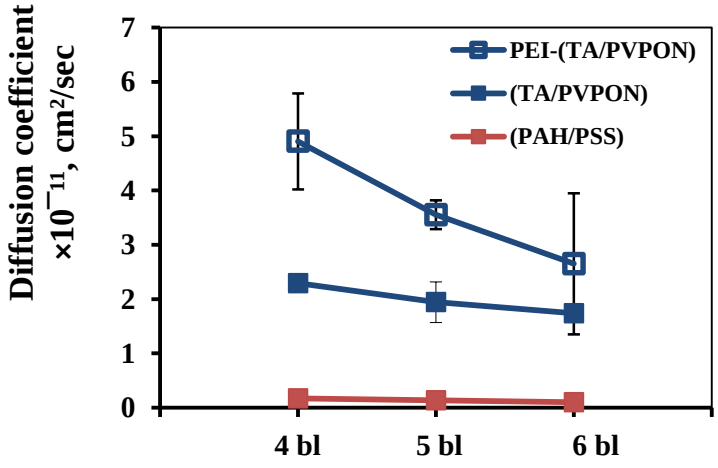

Figure 4.8 Diffusion coefficient of FITC as a function of number of layers for PEI-primed hydrogen-bonded, pure hydrogen-bonded and electrostatically-assembled shells.

Considering reported size of the FITC-dextrans of 1.5 and 2.2 nm, respectively, the mesh size of the $(TA/PVPON)_4$ network can be estimated to be within this range under these assembling conditions. Indeed, the AFM analysis of the shells confirmed grainy surface morphology and the microroughness of 3 nm (within 1×1 μm^2), well exceeding microroughness of 0.5 nm for uniform, smooth PSS/PAH coatings without any pores presented.

4.3.5 Enhanced cytocompatibility of hydrogen-bonded coatings

S. cerevisiae yeast cells were sequentially coated with $(TA/PVPON)_n$ LbL shells through hydrogen-bonding between hydroxyl groups of TA and carbonyl groups of PVPON under deposition conditions which preserved cell integrity and functioning.[197] TA possesses antioxidant and antibacterial properties and can inhibit radical-induced oxidation thus

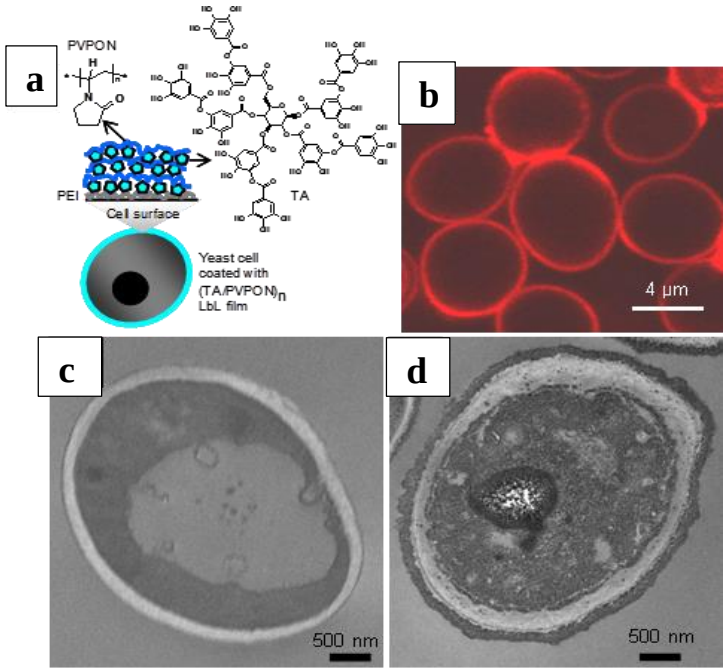

Figure 4.9 Formation of TA/PVPON shells on yeast cell surfaces (a). Confocal image of yeast cells encapsulated with PEI-$(TA/PVPON)_3$ shell before yEGFP expression (b). TEM images of freeze-dried bare (c) and PEI-$(TA/PVPON)_6$ -coated (d) yeast cells.

providing for enhanced cell viability. Figure 4.9a illustrates the LbL assembly of hydrogen-bonded shells around living cells.

The successful formation of the shells around the cells was initially confirmed by confocal microscopy. Figure 4.9b demonstrates homogeneous fluorescence from AlexaFluor532-fluorescently tagged PVPON confirming formation of the polymer membrane. TEM analysis further confirms the CLSM data and demonstrates the integrity of the cell membrane upon adsorption of the PEI-(TA/PVPON)$_6$ hydrogen-bonded shell (Figure 4.9c).

AFM images show highly textured porous surface morphology of the films (Figure 4.10). The average TA/PVPON bilayer thickness from AFM cross-sections was 4.0±0.2 nm which is as twice as high compared to that of the film adsorbed from aqueous solutions (1.7±0.2 nm). This difference for the film formed under higher salt conditions is characteristic for

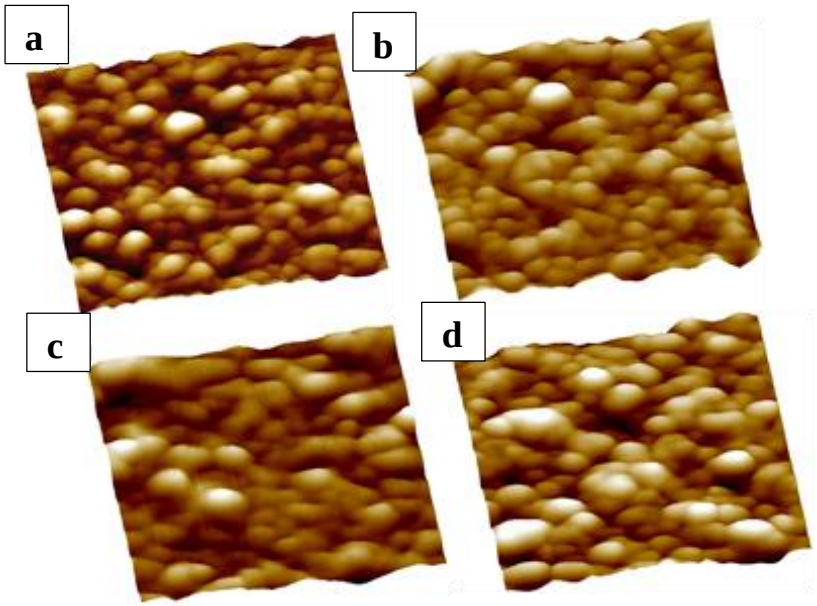

Figure 4.10 3D topographical AFM images of PEI-(TA/PVPON-360)n hollow shells with n=3 (a), n=4 (b), n=5 (c), and n=6 bilayers (d). Scale is 500 μm x 500 μm x 50 nm.

the hydrogen-bonded LbL assembly and results from charge screening and decreased polymer solubility.

To assure the neutrality of the encapsulated yeast cells, we performed zeta-potential measurements as a function of the number of deposited layers for both haploid and diploid cells (Figure 4.11). As confirmed by these measurements, the initial negative charge of the cell membrane was partially neutralized after deposition of the precursor PEI layer, and was completely neutralized after 3-4 layer deposition on cell surface, making cells completely neutral.

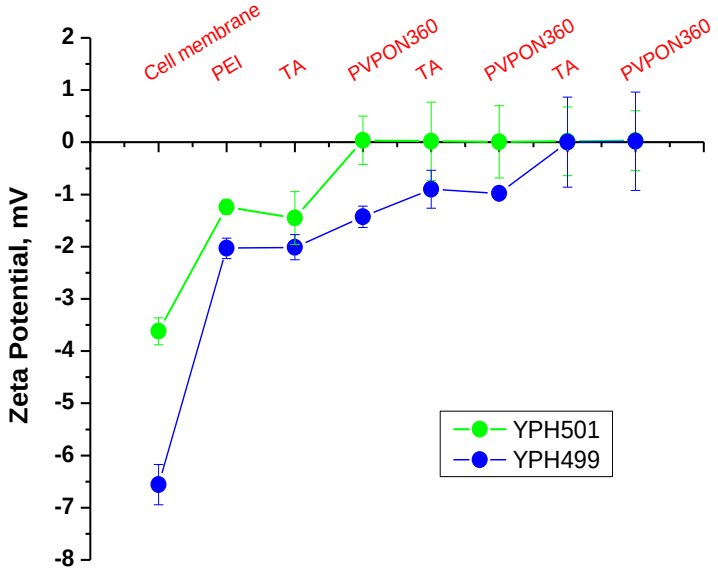

Figure 4.11 Zeta-potential after deposition of a single layer with PEI-(TA/PVPON-360K)$_3$ shells at pH 6 for two types of yeast cells (haploid YPH499 and diploid YPH501) .

The viability of cells with different LbL shells was assessed with the resazurin assay. As schematically shown in Figure 4.12a, bio-reduction of resazurin by reducing enzyme cofactors in viable cells results in the conversion of the resazurin oxidized blue form to its pink fluorescent intermediate, resorufin. The absence of such cofactors in dead cells leads

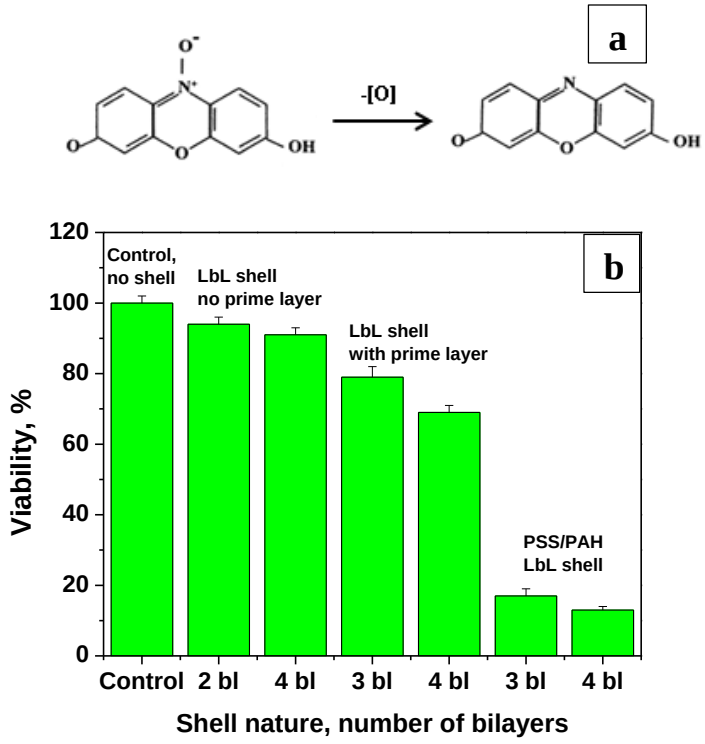

Figure 4.12 Bioreduction of resazurin from its oxidized blue form (left) to its pink colored, fluorescent intermediate resorufin (right) (a); Comparison of cell viability rates between control cells, (TA/PVPON)n, PEI-(TA/PVPON)n and (PAH/PSS)n coated cells (b).

conversion and no fluorescence can be detected. The cells coated with the $(TA/PVPON)_n$ layers showed high viability up to the thickest shells studied here (Figure 4.12b).[127] Unlike the PAH/PSS, hydrogen-bonded shells exert a minor, 5%, cytotoxicity with each following bilayer. We attribute the initial decrease in cell viability in case of PEI-$(TA/PVPON)_n$ shell to the PEI pre-layer. Notably, assembly of 3- and 4-bilayer PEI-(TA/PVPON) LbL shells maintained high viability up to 79% in contrast to traditional polyelectrolyte (PAH/PSS) shells (Figure 4.12b). Indeed, 3 and 4 bilayers of ionic (PAH/PSS) shell caused up to 88% of cell death which is consistent with the PAH/PSS cytotoxicity vastly reported in literature. Moreover, truly hydrogen-bonded $(TA/PVPON)_n$ shells resulted in even more dramatic improvement in viability reaching level of 94% (Figure 4.12b).

Cell surface engineering with hydrogen-bonded shells supported important functional ability of yeast cells to produce a reporter protein (yEGFP) in response to an inducer molecule (Figure 4.13). Confocal fluorescence microscopy of control and PEI-$(TA/PVPON)_3$ or $(PAH/PSS)_3$ –coated cells showed that hydrogen-bound shells do not interfere with the yEGFP expression, and fluorescence emission from the cells can be easily observed (Figure 4.13b). By contrast, no fluorescence from $(PAH/PSS)_3$ coated yeast cells can be detected that indicates suppression of the yEGFP-reporter function of cells coated with PAH/PSS multilayers (Figure 4.13c). The same surface area observed under transmission mode

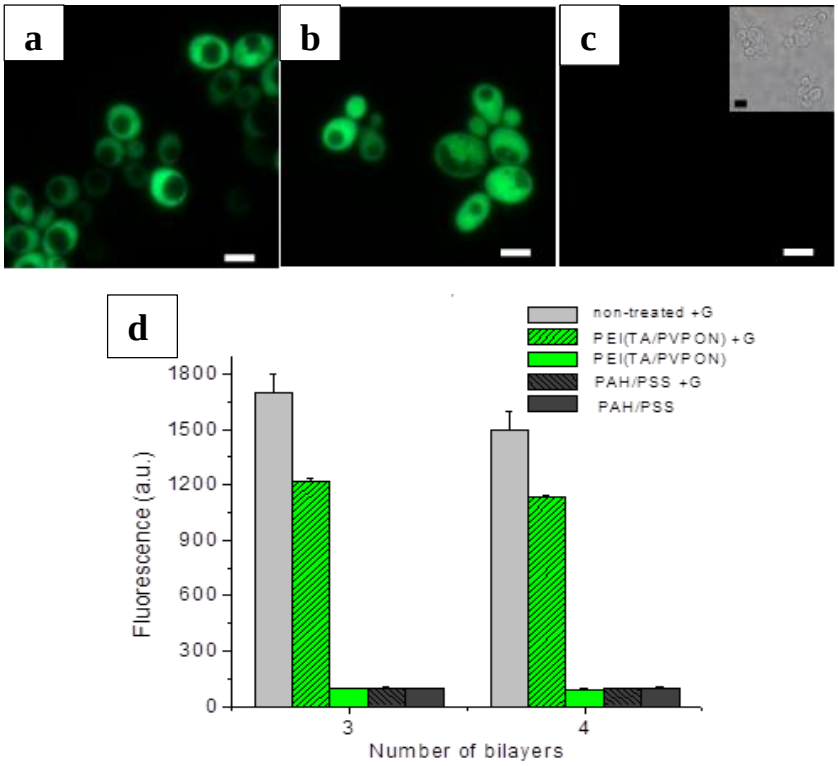

Figure 4.13 Expression of yEGFP from control (a), PEI-$(TA/PVPON)_3$- (b) and $(PAH/PSS)_3$-coated cells (c). Inset shows a transmittance optical image of the same area for (c). Scale bars are 5 µm. (d) Comparison of the yEGFP fluorescence intensity from control cells and PEI(TA-PVPON)- or (PAH/PSS)-coated cells after 16 hours.

revealed the presence of the $(PAH/PSS)_3$-coated cells (Figure 4.13c, inset). Moreover, continuous monitoring of the yEGFP fluorescence from coated yeast cells after induction of

the reporter protein expression showed that gradually increased fluorescence can be detected from the coated cells. For comparison, the fluorescence intensity from 4-bilayer (TA/PVPON) coated cells was almost 13 times higher than that from $(PAH/PSS)_4$-coated cells indicating dramatic difference in activities of these counterparts (Figure 4.13d).

Preserved cell function and viability is indicated by their ability to bud after cellular surfaces were modified with the LbL shells. Figure 4.14a demonstrates the characteristic S-shaped cell growth of control cells and PEI(TA/PVPON)-coated cells. During the initial lag phase the rate of growth, or cell division, is slow in all cases. Red fluorescence in confocal images

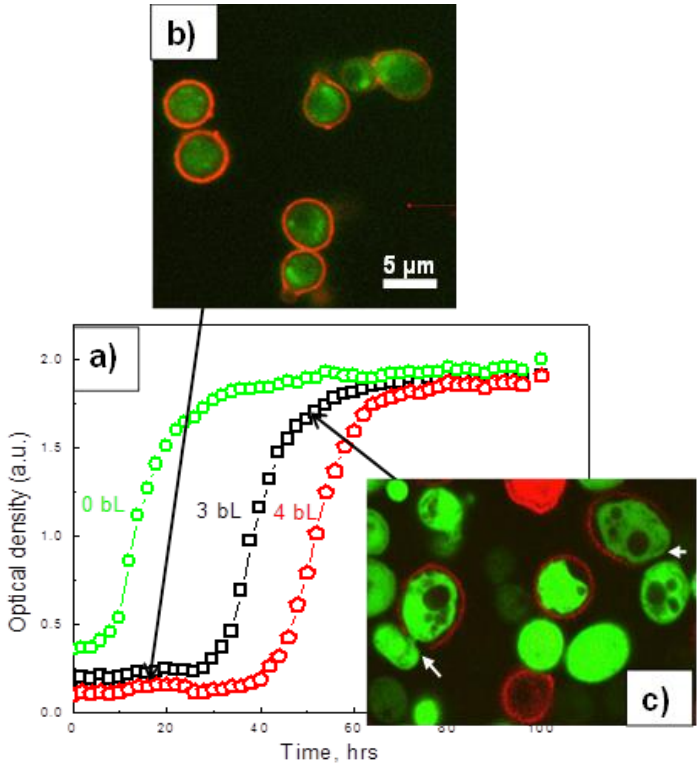

Figure 4.14 Growth of PEI-$(TA/PVPON)_{0,(3),(4)}$-coated cells after yEGFP expression was induced (a). Confocal microscopy images of PEI-$(TA/PVPON)_3$-coated cells after 10 hours (b) and 46 hours (c) of the yEGFP expression.

of the PEI-$(TA/PVPON)_3$-coated cells taken in the lag phase witnesses a homogenous polymer coating around cells (Figure 4.14b). Moreover, the green fluorescence from the

yEGFP-reporter produced by the yeast cells confirms that this functional capacity of the cells was not adversely influenced by the shell presence. This stage is followed by the exponential growth mode when cell division accelerates and a unicellular organism duplicates, i.e., one cell produces two in a given period of time (see divided cells as indicated by arrows in Figure 4.14c). During this phase very rapid multiplying of yeast cells is observed by reading absorbance (optical density) at 600 nm. The exponential phase then proceeds to a stationary phase when there is no discernible change in cell concentration.

While original yeast cells go into the exponential phase after eight hours duplicating every four hours (data not shown), there is a delay of the exponential phase for the (TA/PVPON)-coated cells which is dependent on the thickness of the polymer coating (Figure 4.14b). Confocal imaging of the PEI(TA/PVPON)$_3$-coated cells before the stationary phase revealed that during exponential growth coated cells are able to break the polymer shell suggesting that the coating delays but does not suppress cell division (Figure 4.14c). This is similar to polycation/ polyanion coatings and is due to comparable rigidity of the TA/PVPON coatings which exhibit Young's modulus of 1.8±0.4 GPa in dry state (buckling test[235]), similar to that of the PAH/PSS system (1–4 GPa)[236].

5 CHAPTER

PH-RESPONSIVE MICROCAPSULES AND CELL COATINGS

5.1 Introduction

Numerous stimuli-responsive surfaces and interfaces were developed by introducing ionisable groups into the backbones.[237,238] Another approach to produce stimuli-responsive material involves the formation of gels by physical and/or chemical cross-linking, or by supramolecular association of molecular chains dispersed in solvents.[239, 240] Hydrogels are of particular interest since their porous net-like structure is filled with a large amount of water, which resembles biological structures. (LbL) approach represents alternative way of creating stimuli-responsive multilayer systems in which chemical species with opposite charges, hydrogen-bonding interactions, or combination of thereof are assembled in alternating fashion.[104,105,241] In particular, a lot of attempts have been undertaken to use ultrathin LbL nanoshells for controlled encapsulation of cells in order to create protected cells and cell assemblies, fabricate cell replica, biosensing arrays, and to mediate transport properties.[108,122,146,242,243,123,244,245]

However, LbL shells reported to date were not proven to be robust under variable environmental conditions and be capable of significant and controlled variations of their state. Thus, currently synthetic nanoshells play a passive role in cell growth, interactions, and functioning. No examples of responsive synthetic nanoshells which can serve as active barrier/coating to control cell functionality in biosensing devices have been reported to date.

In this work, we describe a facile strategy for the design of robust but pH-responsive and compliant one-component LbL nanoshells based upon cross-linkable, hydrogel PMAA

copolymer for rendering the cell function and the rate of proliferation which can be controlled by conformational changes in nanocoatings in response to pH. High viability rates of encapsulated cells, which reaches 90%, was related to the elastic nature of cross-linked and highly porous hydrogel shells with thickness of a few tens of a nanometer and very minor content of a cationic component. In this strategy, the incorporation of small amount of amine functional groups into the backbone of responsive PMAA component allowed us to create strong amide bonding using zero-length coupling agent of 1-ethyl-3-(3-dimethylaminopropyl)-carbodiimide (EDC) without adverse effect on cell viability.

5.2 Experimental details

Detailed experimental procedure on formation of model hollow capsules and LbL deposition on yeast cells can be found in Experimental section, while the simplified schematic drawing and chemicals used in the LbL films are outlined in Figure 5.1.

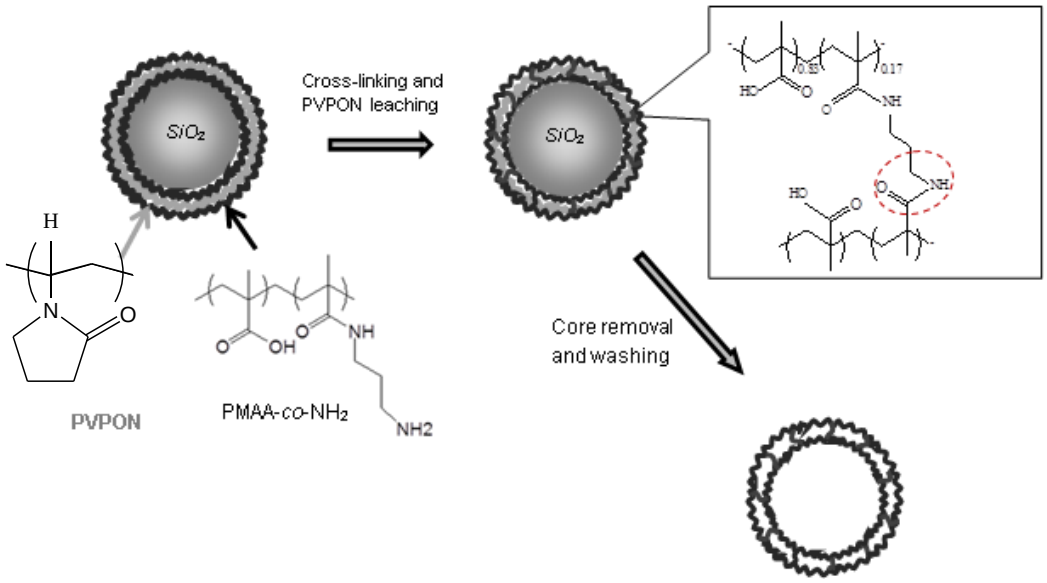

Figure 5.1 Formation of cross-linked PMAA-co-NH_2 hydrogel microcapsules via LbL self-assembly on sacrificial silica cores.

5.3 Results and discussion

5.3.1 pH-responsive volumetric changes of microcapsules

Chemical composition of cross-linked single-component PMAA-*co*-NH_2 capsules (Figure 5.1) was confirmed with ATR-FTIR measurements before and after the crosslinking reaction. Figure 5.2 demonstrates ATR-FTIR spectra of the uncross-linked and cross-linked capsules. In both spectra, there are two broad absorption peaks between 3000 cm^{-1} and 3500 cm^{-1} which are characteristic of N-H stretching in primary amines.[246] The NH_2 wagging vibrations are also present at 680 cm^{-1} for both types of capsules. The very distinct sharp peak centered around 1456 cm^{-1} in the cross-linked spectrum can be assigned to C-N stretching and N-H bending and provides the necessary evidence for peptide bonding.[247] The presence of this peak is a distinctive feature of amide bonding associated with EDC crosslinking within the PMAA-*co*-NH_2 shell. It is worth mentioning that the second distinctive peak centered at ~1303 cm^{-1} was also observed and can be attributed to a complex

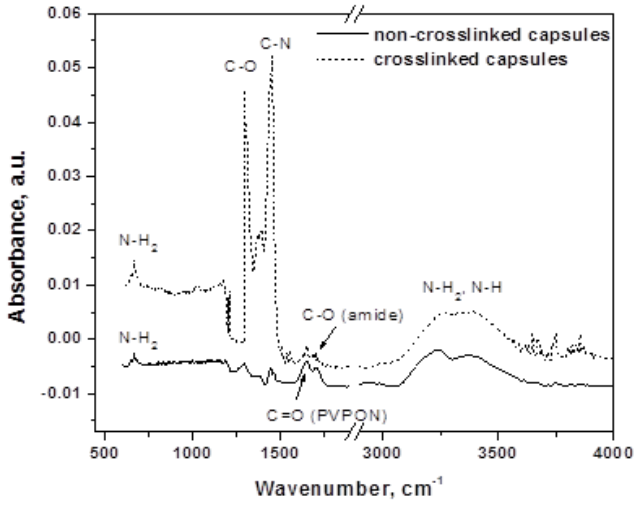

Figure 5.2 ATR-FTIR spectra of uncross-linked (solid line) and cross-linked for 40 minutes (dashed line) (PMAA-co-NH_2)$_5$ microcapsules (pH 3.5).

mixing of C-N stretching, N-H bending, and C-H deformation of amide III from peptide bonding.[248] From the intensity of both peaks it can be inferred that carboxylic groups were activated during the coupling process.

In the FTIR spectrum for uncross-linked capsules there were two broad closely placed peaks in the range of 1625 – 1770 cm^{-1}. The 1720 cm^{-1} peak is related to protonated carboxylic groups[233] and the 1660 cm^{-1} peak is associated with C=O stretching vibrations in PVPON.[225] After crosslinking, both peaks were diminished indicating that a significant amount of PVPON was released (peak 1660 cm^{-1}) and the contribution of carboxylic groups was reduced. In addition to this peak, closely placed minor absorption peaks at 1560 – 1565 cm^{-1} can be associated with additional N-H bending from the amide II band.[248, 249] These data confirmed the formation of partially cross-linked one-component (PMAA-*co*-NH_2)$_5$ shells upon activation with a coupling agent. The large fraction of residual non-reacted carboxylic groups remain free and thus provided sites for the reversible conversion from the protonated to ionized form when exposed to higher pH values responsible for the significant swelling of capsules as discussed below.

5.3.2 Calculations of the mesh size in hydrogel network

Single component PMAA-co-NH_2 capsules with reversible swelling we obtained using mild concentrations of zero-length coupling agent (EDC, 5 mg/mL) and by reducing the time of crosslinking (40 min). The optimal time for crosslinking within copolymerized PMAA multilayers was specifically set for the lowest possible value to achieve stable capsules with minimum exposure to a highly reactive coupling agent which generates toxic byproducts during the reaction.[250] On average, the time of crosslinking reported in the literature was much higher, reaching 13 hours.[220,251,231]

The molecular weight between crosslinks, *Mc*, was determined from the equilibrium swelling data. The calculations yielded *Mc*=9,500 Da or about 99 monomeric units between the crosslinks, a very low crosslinking density which facilitated a high swelling ratio. Thus, with 17% of amine content, on average, every sixth unit of the PMAA-*co*-NH_2 chains was amine-functionalized, out of which only every sixteenth unit of the polymer backbone was actually cross-linked.

The analysis of shell thickness and microroughness of crosslinked $(PMAA\text{-}co\text{-}NH_2)_5$ capsules in dry and swollen states revealed that in the swollen state microcapsules were ~ 25% thicker (25.5 ± 0.9 nm) at low pH as compared to the same capsules in dry state (18.9 ± 1.1 nm). As demonstrated by AFM measurements, below the critical pH point of PMAA (deprotonation of carboxylic groups) the capsule thickness was in the range of 22.6 – 24.0 nm. Increasing pH resulted in a gradual increase in the capsule thickness to 44.1 ± 5.1 nm at pH 6.0 followed by a sharp drop to around 3 nm above pH 6.5 (Figure 5.3). Above pH

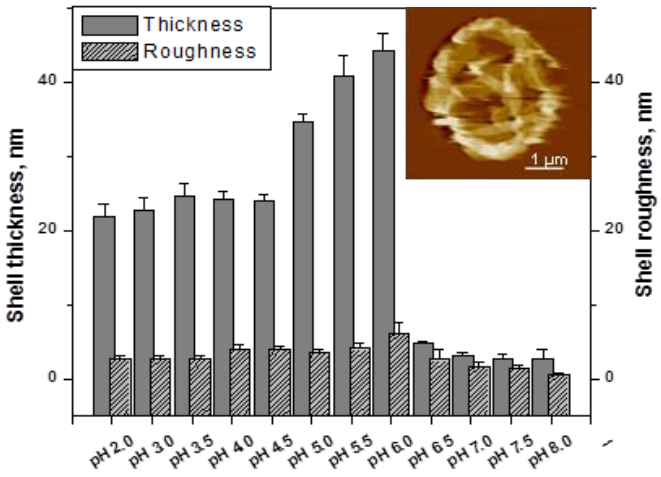

Figure 5.3 Thickness and microroughness of cross-linked for 40 minutes $(PMAA\text{-}co\text{-}NH_2)_5$ capsules in swollen state at wide pH range. Inset shows distorted capsule during AFM scanning at pH 7.0.

6.5, capsules exhibit sharp volume phase transition caused by deprotonation of carboxylic segments and collective diffusion of solvent molecules into the bulk of polymer shells resulting in dramatic decrease in the nanoshell thickness. As a result, increased build-up of osmotic pressure results in disruption of LbL shells under these conditions as confirmed by direct in-liquid AFM imaging.

Sharp changes in the surface charges and volume transitions in different types of solvents (Nanopure water and SMM media) were confirmed with CLSM and ζ-potential measurements. The highest amplitude of charge changes was observed in pure water, when ζ-potential was gradually dropping from a positive value (+12 ± 1.6 mV at pH 3.0) to a negative value (-68 ± 1.2 mV at pH 6.5). Although in cell media capsules went through similar charge changes, the amplitude of such changes was less pronounced: from +4.8 ±

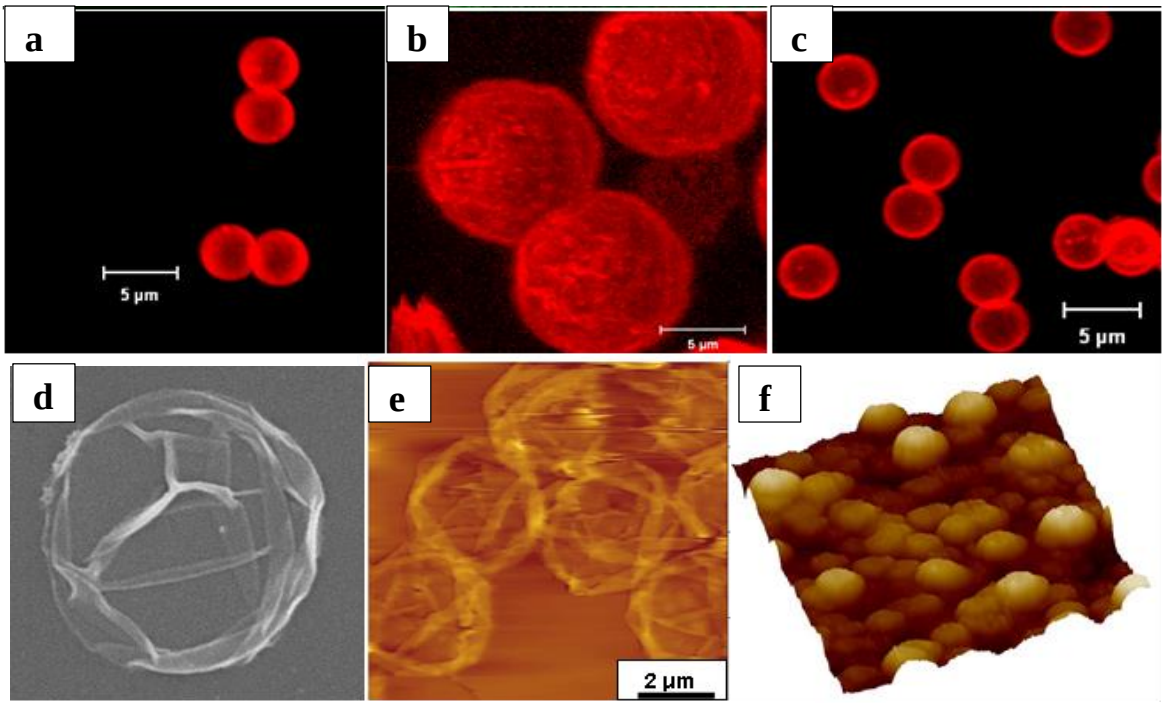

Figure 5.4 Reversible changes of $(PMAA\text{-}co\text{-}NH_2)_5$ capsules in aqueous solution at pH 3.0 (a), pH 8.0 (b) and pH 3.0 (c). SEM (d) and AFM in liquid state (e) images of hydrogel capsules. Surface morphology of hydrogel shells in dry state (f).

0.4 mV at pH 3.0 to -25.2 ± 1.3 mV at pH 7.5. Smaller drop in ζ-potential amplitude can be associated with hydrodynamically larger molecules present in the media (amino acids) that are trapped within the proximity of the polymer loops.[225] On the other hand, the media contains a number of essential amino acids which affect overall ionic strength of the solution. Hence, there is a significant ionic screening of the electrostatic repulsions between charges of equal sign. [252]

Confocal images of hollow cross-linked (PMAA-*co*-NH_2)$_5$ capsules showed dramatic changes in the capsule diameter which accompanies changes in the surface charges discussed above (Figure 5.4). Below pH 5.0 hollow capsules of 3.4 ± 0.5 μm in diameter were close to the size of original silica templates. Above pH 5 capsules began to swell and reached their maximum swelling at pH 7.5 with capsule diameter of 10.5 ± 0.2 μm in case of pure water and 9.6 ± 0.4 μm in SMM media. Reversibility of dimensional changes was confirmed by multiple cycling between low and high pH values.

5.3.3 Mechanical stability of shells as a function of pH

The studies of localized mechanical properties of capsules using surface force spectroscopy (SFS) have revealed distinct changes in the capsule elasticity as a function of pH, crosslinking time and Mw of the buffer polymer layer. If comparing crosslinking time, elastic modulus of (PMAA-*co*-NH_2)$_5$ shells incubated in the solution of EDC for 20 min was four-folds lower (0.76 ± 0.13 MPa) compared to the same shells incubated for 40 min (3.1 ± 0.4 MPa). If comparing Mw of the counterpart polymer, shell prepared with highest Mw of PVPON (1,300 kDa) were 25% stiffer compared to shells prepared with PVPON of 55 kDa.

Young's modulus of 3.2 – 4.3 MPa at low pH is typical for partially swollen hydrogel elastomers.[253,254] With increasing pH of the solution above *pK*a, the elastic modulus decreases by two orders of magnitude to ~20 kPa, this is a characteristic of a weakly cross-linked and highly swollen hydrogel material (Figure 5.5). Decreased stiffness of the cross-linked (PMAA-*co*-NH_2)$_5$ capsules correlates well with remarkable swelling within the same range of pH 5.5 – 6.5 and provides means for dramatic stretching of thin shells. Such softening is caused by deprotonation of the acidic groups within PMAA polymer chains and repulsive charge-charge interactions.

Overall, dramatic changes observed in the shell thickness, microroughness, and elasticity at the p*K*a of PMAA copolymer can all be associated with increased deprotonation of unbound PMAA-*co*-NH_2 carboxylic groups when Coulombic interactions cause electrostatic repulsion produced within the network.[220,255] At p*K*a, dissociation of unbound carboxylic groups on the network chains increases the charge density on the network to the highest

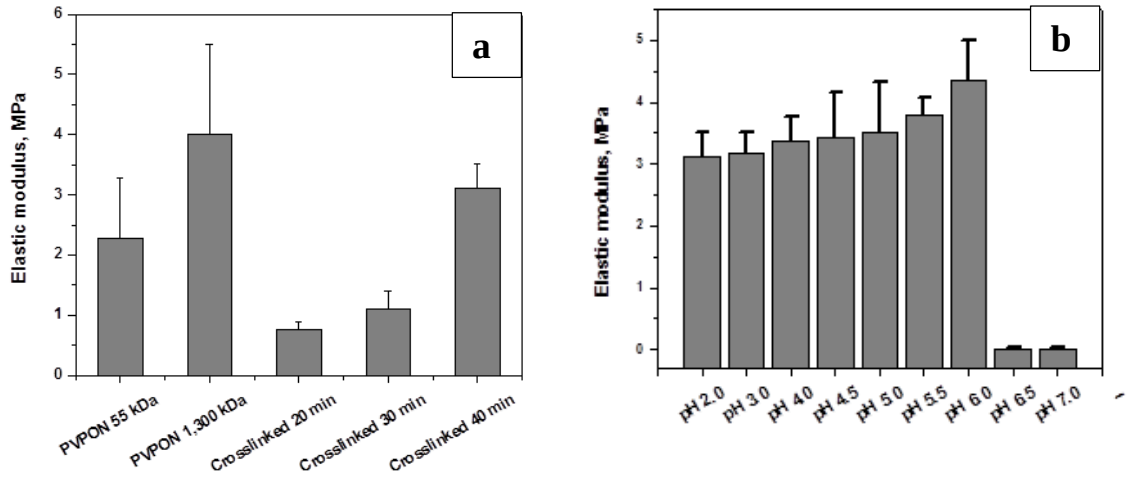

Figure 5.5 Elastic moduli for uncross-linked capsules with different molecular weight of PVPON component and for capsules cross-linked for 20, 30 and 40 minutes(a); Elastic moduli of swollen (PMAA-co-NH_2)$_5$ microcapsules cross-linked for 40 minutes as a function of pH (b).

degree. The increase in mobile counterion content increases the internal osmotic pressure, which induces the swelling of hydrogel until the network chains reach a maximum of ionization. On the other hand, the lateral stretching within the points of entanglements plays a role in increased swelling, thus making capsule walls thinner. Overall, swelling in a wide pH range seems to occur in two-stages: (1) at the acidic conditions (pH 3.0 – 5.5) PMAA-modified shells are modestly swollen, uniform, and stiffer due to limited uptake of water molecules into partially hydrophobic shells and (2) exponential increase in capsule diameter (more than 3-fold) and decrease in shell thickness and stiffness occurring above pH 5.5 all are due to the increased ionization of PMAA segments, that results in lateral stretching and dramatic shell thinning limited by crosslinking sites. Finally, at pH > 7.0 partial disintegration of capsules begins to occur, which progresses at even higher pH.

5.3.4 Cells encapsulated in pH-responsive shells and effect of the coating on cell function

Hydrogel shells were assembled on yeast cell surfaces according to the procedure described in Experimental section (Figure 5.6). *S. cerevisiae* yeast cells coated with PMAA-*co*-NH_2 shells and treated with EDC for different time periods showed excellent viability despite the presence of highly reactive crosslinking agent.

As evidenced from live-dead staining test, cell viability rate was in the range of 90 ± 1.3% for cells treated with EDC for 40 minutes, and slightly decreased to 85 ± 2.4% when the time

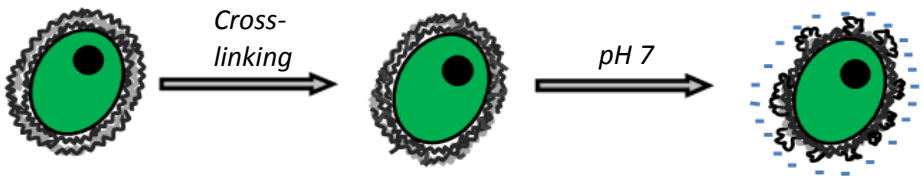

Figure 5.6 Assembly of pH-responsive hydrogel shells on cells surfaces.

of exposure to EDC was increased up to 3 hours (Figure 5.7). With increasing number of layers, hence increasing thickness of the shell, the viability of cells only slightly decreased to 82% for 9 bilayer shells. The difference in viability rates appears to be not significant with increased time of exposure, which might be crucial for biocompatibility of the current procedure to produce highly stable synthetic shells. We suggest that very low cytotoxicity

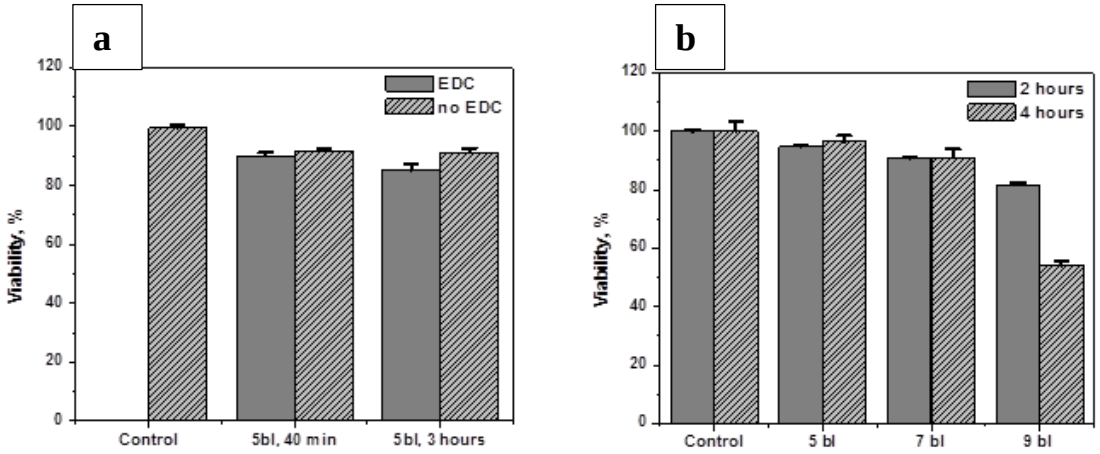

Figure 5.7 Cell viability rates of $(PMAA\text{-}co\text{-}NH_2)_5$ –coated cells with or without crosslinking agent (a); and as a function of bilayer composition (5, 7, and 9 bilayers) after 2 and 4 hours incubation with resazurin assay (b).

of (PMAA-*co*-NH_2)-based shells fabricated here in comparison with traditional electrostatically assembled shells with cationic components arises from the nature of intermolecular bonding in hydrogen bonded shells and highly permeable network morphology after removal of PVPON component.

The viability observed here is very high compared to common LbL encapsulation. The toxicity of cationic components of traditional LbL shells towards a variety of cell types has been well documented and mainly associated with charge reversal at cell membranes.[103, 256] We suggest that very low cytotoxicity of (PMAA-*co*-NH_2)-based shells fabricated here in

comparison with traditional electrostatically assembled shells with cationic components arises from the nature of intermolecular bonding in hydrogen bonded shells and highly permeable network morphology after removal of PVPON component. Indeed, shells fabricated in this study contain a very low fraction of amine groups which does not exceed few volume percent in a highly swollen, lightly cross-linked shells.

In order to evaluate surface potential during LbL assembly, we performed ζ-potential measurements after deposition of each layer (Figure 5.8). As confirmed by these measurements, initial negative charge of the cell membrane (-28.5 mV) was partially neutralized to -9.9 mV after deposition of neutral polymer (PVPON) and oscillated within overall negative range (-10 – -13 mV) in contrast to drastic positive-negative variations in conventional polyelectrolyte membranes. Hence, the absence of positive charges in shells prevents the excessive death of the encapsulated cells.

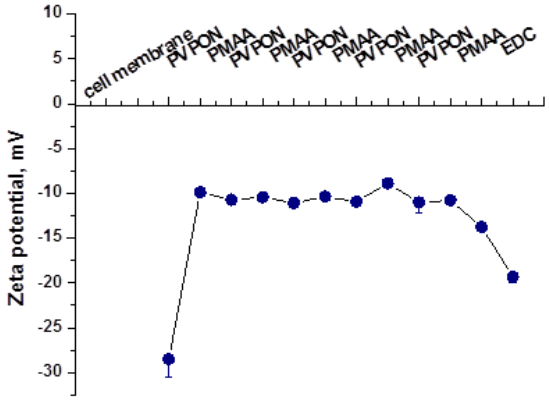

Figure 5.8 Zeta-potential evolution after deposition of PVPON and PMAA-co-NH_2 layers onto surface of yeast cells.

pH-responsive hydrogel shells assembled on cell surfaces stayed intact and permanently attached to the cells after gradual change in pH from 5 to 9 (Figure 5.9 a, b). In this experiment, we observed that even at pH 9.0, the shells (labeled with dye) demonstrated compliance to the cell surfaces without any indication of swelling, which was observed for hollow capsules (Figure 5.4). Strong attachment of the LbL shell to the cell wall was probably due to multiple ionic interactions, hydrogen bonding, and chemical crosslinking.[257,259] Since cell walls are rich in amine-bearing ligands, strong tethering between polymer shells and cell walls can easily occur during incubation period with a crosslinking agent.

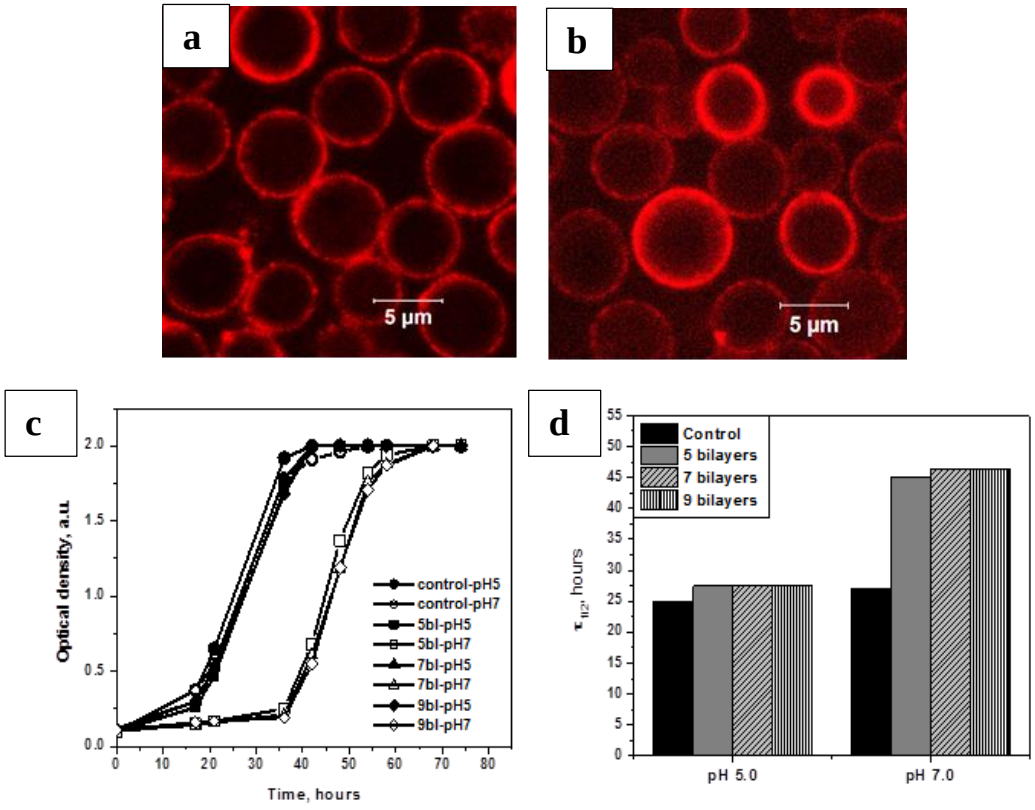

Figure 5.9 $(PMAA\text{-}co\text{-}NH_2)_9$ coated yeast cells at pH 5.0 (a), and pH 7.0 (b). Growth kinetics of $(PMAA\text{-}co\text{-}NH_2)$ coated yeast cells with different shell thicknesses in media adjusted to pH 5.0 and pH 7.0 (c). 50% growth time for bare and encapsulated cells at pH 5.0 and pH 7.0 (d).

Significant effect of pH-responsive behavior of LbL shells on the cell growth and function was observed when encapsulated cells were allowed to grow in media adjusted to pH 5 and pH 7 (below and above pKa for PMAA) (Figure 5.9 c, d). The formation of budded daughter cells and expression of yEGFP was monitored until the stationary phase has reached its plateau at 48 hours for pH 5.0 and 72 hours for pH 7.0 (Figure 5.9 c). As observed, the growth of bare cells was not affected by pH with the half-time of the growth cycle close to 25 hours in both cases. In contrast, all encapsulated cells showed dramatic change in a growth mode at pH 7. For cell encapsulated with different shell thicknesses, budding and replication was delayed by about 24 hours with half-time growth close to 47 hours (Figure 5.9 d). Independent studies confirmed tolerance of bare *S. cerevisiae* yeast cells to alkali conditions with growth behavior and expression rate of yEGFP remaining intact. Strong fluorescence coming from yEGFP expression was observed when cells were grown in the presence of 2% galactose at both pH 5.0 and 7.0 with hydrogel shell still present after 17 hours of yEGFP induction (Figure 5.10). Gradual increase of yEGFP expression was observed for the cells coated with 5, 7, and 9 bilayers.

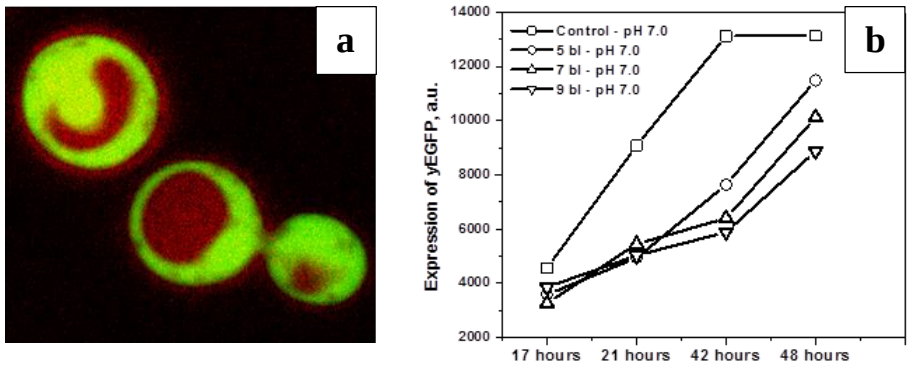

Figure 5.10 Yeast cells coated with $(PMAA\text{-}co\text{-}NH_2)_7$ expressing yEGFP while growing in media at pH 7 (a). Kinetics of yEGFP expression (b).

Such a strong effect of the presence of (PMAA-*co*-NH_2) shells on the functionality of encapsulated cells at higher pH can be associated with pH-caused changes in the state of free carboxylate groups and shell thickness. Progressive deprotonation above pH 5.0 increases the degree of ionization and drives surface potential to increased net negative charge. Increased thickness of the shells at pH 7.0 should result in a reduced transport of nutrients thus delaying the cell growth. Indeed, in our recent study of hydrogen-bonded shells, we observed dramatic, many-fold reduction of the diffusion across shells with increasing thickness.[127] Indeed, as was observed in our recent studies, the shell thickness increase results in the replication onset postponed by many hours.[145]

The formation of pH-sensitive LbL shells directly on the cell surfaces allowed the control of cell growth by variation in pH without affecting cell function as indicated by stable yEGFP expression. By keeping encapsulated cells at physiologically relevant conditions (pH 7.0), we were able to postpone the replication process without inhibition of biosensing activity of the cells. The ability to manipulate perceptible response from the cells by keeping them in "dormant" conditions (constrained replication) for extended time can be rewarding for biosensing applications when the early onset of cell growth can compromise the long-term performance. In this sense, our pH-responsive LbL shells behave as an active barrier that controls the growth behavior and the function of cells.

6 CHAPTER

SILK-ON-SILK BIODEGRADABLE MICROCAPSULES AND CELL COATINGS

6.1 Introduction

Silks are proteins produced naturally by silkworms and spiders and are known as a biocompatible, biodegradable, and extraordinarily robust biomaterial frequently utilized in biomaterial composites.[260,261] The versatility of silk proteins, along with their favorable characteristics, and potential for processing in aqueous solution under ambient conditions make silk-based materials excellent candidates for biomedical applications such as drug delivery systems and scaffolds for tissue engineering.[262] A variety of materials can be produced from silk proteins including fibers,[263,264] capsules,[265,266] particles,[267] films,[268,269,270] foams,[271] and gels.[272]

In particular, recent developments in biomedical fields have made clear the need for drug delivery systems with the capability to accurately target and deliver payloads with one of the popular design being thin film microcapsules.[273,274] Microcapsules and microparticles prepared from silk fibroin (from *B. mori*) are excellent candidates for biomedical delivery platforms. Moreover, silk demonstrates excellent mechanical properties (high elastic modulus, elongation to break and toughness)[275] and remarkable optical properties such as near-perfect transparency in the visible range.[260] Silk based materials have also been demonstrated to stabilize the activity of enzymes and biomolecules in harsh environments, allowing for the potential to deliver treatments that may otherwise quickly lose efficacy. However, to date only few examples of utilizing silk for the fabrication of microcapsules via interfacial adsorption of protein have been reported by Hermanson et al.[265,266]

Silk fibroin, has been successfully used for cell encapsulation. Silk-based materials have been exploited for tissue engineering scaffolds and matrices due to their biodegradation, biocompatibility, excellent mechanical properties, and versatility in further functionalization.[276,277,278,279,280,281,282,283284,285] Due to long-term stability and low inflammatory or immune response *in vivo*, a number of mammalian cells and tissues were encapsulated in silk scaffolds. For example, by systematically changing silk material concentration during extraction and processing, cartilage cells were encapsulated in silk hydrogels with the full maintenance of cell viability. [276, 286]

Another example of successful *in situ* gelation and cell entrapment was reported by synthesizing ionomer-functionalized silk biopolymers and mixing them in equal amounts in the presence of fibroblast cells at physiologically relevant conditions in order to produce instant hydrogels with entrapped cells. By taking advantage of genetically engineered silk-elastin polymers that undergo sol-to-gel transitions within minutes, injectable matrices can be used for delivery of cell-based therapeutics.[287] Such hydrogels were proven to be viable scaffolds for the *in vivo* chondrogenesis if stimulated by growth factors but were unfavorable for the diffusion of the produced extracellular matrix proteins due to limited flexibility of the hydrogel scaffold and free volume into which extracellular proteins could be deposited. Large volumes and limited porosity of bio-enabled hydrogels are the major obstacles for cell-based therapeutics or bio-sensing applications when rapid responsiveness of the encapsulated cells should be attained.

The formation of ultrathin silk coatings on cell surfaces has never been explored despite the fact that robust silk films have been widely demonstrated. [132,268,288,289] In this context, layer-by-layer (LbL) self-assembly has been explored not only between oppositely-charged

polyelectrolytes, but also in hydrogen-bonded or hydrophobic systems.[104,105] These nanoshells efficiently reduce material volume while retaining the presence of the protective coating, [103,107,127,145,197] create semipermeable artificial membranes for the efficient exchange of nutrients and signaling molecules and efficiently release waste products. Moreover, these coatings might inhibit molecular recognition [135,290,291] or guide the delivery of the cargo.[244,292,295]

The transition of a random silk fibroin that is soluble in water (silk I) to a highly stable and organized structure that is insoluble in water (silk II), which is required to form stable silk matrices, can be accomplished by several processing methods including dehydration by using organic solvents, surfactants, initiators or crosslinking agents, or physical factors (shear, sonication, temperature).[282,296,298,299,300] It also has been shown that the extent of protein aggregation can be controlled by the concentration of kosmotropic salts or ions.[296] However, despite prior investigations on bulk hydrogelation of native silk fibroin by salting-out processes [192,296,] and examples of stable microgels and thin films,[282,298,299,300] no attempts directed at exploiting silk fibroin for surface cell engineering have been reported.

In this work, we developed the technique to fabricate biocompatible, monodisperse, highly porous silk microcapsules with ultrathin and tunable shell thickness and controlled permeability, as well as stable silk nanoshells around living *S. cerevisiae* yeast cells without compromising their viability. The nanoshells facilitated initial protection of the cells and allowed them to function in encapsulated state for some time period, afterwards being completely biodegraded and consumed by the cells. In contrast to a traditional methanol treatment, a gentle ionic treatment suggested here stabilizes the shell silk fibroin structure but does not compromise the viability of the cells, as indicated by the fast response of the

encapsulated cells, with an immediate activation by the inducer molecules. Extremely high viability rates (up to 97%) and preserved activity of encapsulated cells were facilitated by cytocompatibility of the natural proteins and the formation of highly porous shells in contrast to traditional polyelectrolyte-based materials. Moreover, in a high contrast to traditional synthetic shells, the silk proteins are biodegradable and can be consumed by cells at a later stage of growth, thus releasing the cells from their temporary protective capsules.

6.2 Experimental details

Detailed experimental procedure on formation of silk-on-silk microcapsules and silk nanothin shells adsorbed on cell surfaces can be found in Chapter 3. We utilized surface microscopy (AFM), SEM, confocal microscopy, zeta-potential and ellipsometry measurements to characterize physical properties of capsules and shells, as well as the cytotoxicity measurements to assess the effect of the silk protein shells and adsorption procedure on function of cells.

6.3 Results and discussion

6.3.1 Fabrication of pure silk fibroin microcapsules by dehydration with methanol

We utilize one-component "silk-on-silk" LbL technique to fabricate biocompatible microcapsules stabilized by physical crosslinks (β-sheets) and hydrophobic–hydrophobic interactions during dehydration with methanol (Figure 6.1). In the first step, silk protein molecules were deposited from aqueous solution onto the silica cores to form protein monolayer, followed by washing in water and redispersion in methanol to induce formation of β-sheet-rich structure of the absorbed silk protein and to stabilize adsorbed silk layer, thus resulting in robust LbL films stabilized by physical crosslinks (β-sheets) and hydrophobic-

hydrophobic interactions.[268,301] The next silk layer was further deposited in the same way and the procedure was repeated multiple times. The silk microcapsules formed here demonstrated good stability and high permeability, which was readily controlled by the thickness of the capsule shell.

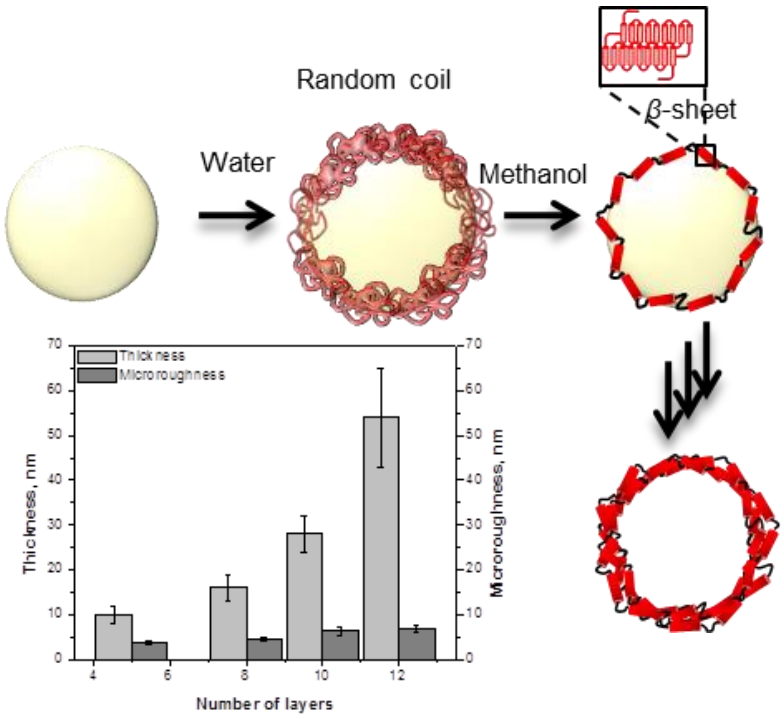

Figure 6.1 Preparation of "silk-on-silk" capsules. The plot shows the shell thickness and microroughness of the microcapsules as a function of the number of silk deposition steps.

Zeta-potential measurements were performed to confirm deposition of silk protein. After deposition of the first layer of silk the surface charge of silica particles significantly reduced from –90.0 ± 7.0 mV to –46.0 ± 4.0 mV. This indicates that the deposition of the first silk layer was a result of electrostatic interactions between the charged silica surface and protein moieties. In addition, strong hydrogen bonding promoted adhesion of water-soluble silk to the silica surface.

Moreover, the increase in the shell thickness was confirmed with cross-sectional AFM analysis after each processing step. The shell thickness determined this way increased stepwise from 10 ± 2 to 54 ± 11 nm which is a critical confirmation of an organized LbL assembly with the average increment close to that known for a single silk monolayer for planar LbL films (around 5 nm).

To verify the secondary structure of silk layers after core removal, ATR-FTIR spectra of hollow silk capsules and silk layers that were deposited on silicon wafer and not treated with HF were compared (Figure 6.2). Both spectra demonstrate a characteristic amide I band (1660–1700 cm^{-1}) which corresponds to the C = O bond in the silk backbone coupled to the N–H bending and C = N stretching modes.[302] Second, the major peak centered at 1623 cm^{-1} is attributed to crystalline β-sheets in both spectra. Deconvolution of the spectra of a silk film gives two peaks centered at 1688 and 1623 cm^{-1} and associated with β-sheets and two

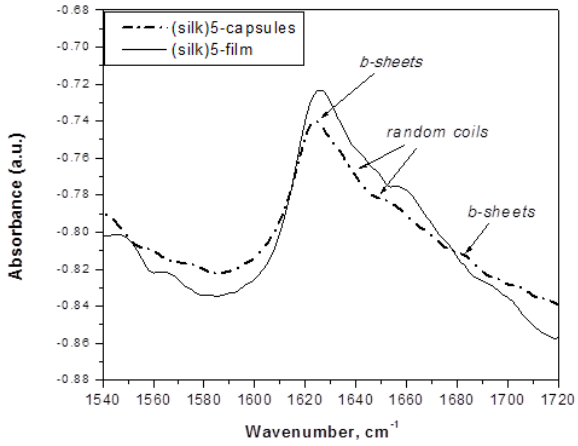

Figure 6.2 ATR-FTIR spectra of $(silk)_5$ film deposited on ATR Si crystal by spin assisted LbL and $(silk)_5$ shells cast on the surface of ATR Si crystal showing all major bands for ordered silk secondary structures.

bands at 1645 and 1661 cm^{-1} attributed to random coils (Figure 6.2). Methanol treatment during capsule preparation induced the conformational transition from silk I to silk II by dehydration, which promotes the formation of a hydrogen bonding network and β-sheet formation.

6.3.2 Morphological features and permeability of capsules

Figure 6.3 demonstrates AFM and CLSM images of the resultant hollow $(silk)_5$ microcapsules. The confocal image shows that all capsules are very uniform in size with the average diameter of 3.5 ± 0.1 μm as defined by the original core (Figure 6.3b). After being placed on a silicon wafer, the capsules have been collapsed upon drying with many random folds caused by local instabilities and wrinkling due to capillary forces acting on the

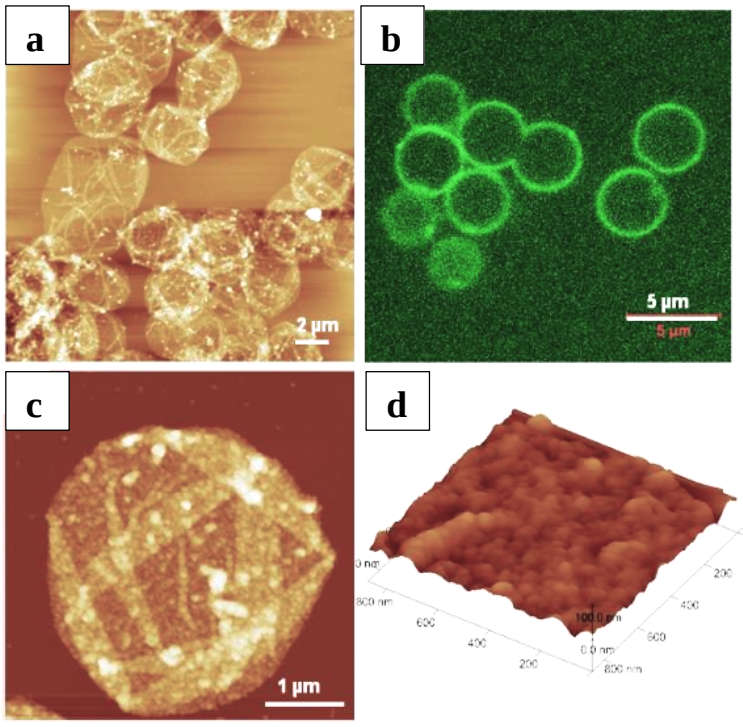

Figure 6.3 AFM image of dried (silk) 5 capsules (z-range=100 nm) (a). CLSM image of $(silk)_5$ capsules in aqueous solution (b). High magnification AFM image of the dried $(silk)_5$ capsule (z-range=80 nm) (c). AFM 3D image of a $(silk)_8$ shell (z-range=100 nm) (d).

microcapsules.[145] Non-linear shell thickness growth starting from 2 nm per layer for the 5-layer silk capsules increased to 4.5 nm per layer for the 12-layer silk capsules indicating interpenetration and free diffusion of silk molecules during deposition, which is common for exponentially grown LbL films. (Figure 6.3) With each deposition silk molecules do not only absorb on the top of the outmost layers, but also penetrate within already deposited layers, resulting in dramatic shell thickness growth. The high-resolution AFM analysis of the dried hollow silk capsules revealed the grainy texture of the folded shells which correspond to the known grainy morphology of silk nanolayers partially converted into a silk II ordered structure (Figure 6.3d). The microroughness of different capsules was found to be between 3.8 and 7 nm for LbL shells with different numbers of layers, which is higher than common values for ionic-based LbL films (usually below 1 nm) and reflect local aggregation of the silk II structure. [221,222] In the case of silk LbL assembly on silica colloids, the surface roughness increased dramatically for higher number of layers. Such an increase in surface microroughness is consistent with steady development of domain morphology which is caused by the unique multidomain composition and formation of β-sheets. In spin-assisted assembly, the silk molecules are forced to stretch along the substrate surface. We suggest that, in contrast, during LbL assembly on colloids, the molecules freely interdiffuse resulting in increase of β-sheet content and enhancement of inter-molecular interactions.

A highly grainy surface morphology and microroughness suggest a potentially porous morphology of the LbL shells. Thus, CLSM was performed to analyze the permeability properties of the silk capsules by using fluorescein isothiocyanate (FITC)-labeled dextrans of various molecular weights as a fluorescent probe. $(Silk)_5$ shells demonstrate a very "open" structure for the dextrans of up to 500 kDa, being "closed" only for the highest molecular

weight dextran of 2,000 kDa. This indicates the highly permeable, porous nature of silk-on-silk capsules. Considering the reported hydrodynamic diameters of the 500 kDa and 2000 kDa FITC-dextrans of 22.9 and 31.8 nm, respectively, the mesh size of the $(silk)_5$ network can be estimated to be around 25 nm under these assembly conditions, which is much larger than the regular porosity of common LbL shells. Shell permeability can be finely tuned with increasing number of layers. Silk shells with 12 layers are permeable only for dextrans with a molecular weight of 70 kDa, meaning that the threshold of the shell permeability is between 70 and 150 kDa. The reported hydrodynamic diameters of these FITC-dextrans are 5.8 and 9.6 nm, respectively.[303] The mesh size of the $(silk)_{12}$ shells was reduced to around 7 nm. Silk shells at given conditions allow control of the permeable/non-permeable state for molecular weight from as low as 70 kDa to as high as 1500 kDa thus facilitating a loading ability for large macromolecules.

Compared to other types of multilayer LbL capsules, such as hydrogen-bonded[144,145] and polyelectrolyte-based[304], silk-on-silk microcapsules demonstrated significantly different properties. Such a difference can be related to a different secondary structure of silk proteins as determined by supramolecular interactions such as hydrogen bonding between amine and carboxylic groups and π-stacking between aromatic rings.[305] As known, methanol promotes β-sheet formation at the expense of α-helices due to dehydration of the α-helices.[306] Using this effect, the assembly of recombinant spider-silk proteins at an emulsion interface has been used to form microcapsules, 3 to 80 microns in size.[265,266] In this technique the emulsion interface is used to orient peptide sequences in the adsorbed polypeptide and subsequently immobilize the peptide chains by non-covalent interactions. Emulsion interfaces induce self-assembly of silk proteins into predominantly β-sheet configurations,

resulting in a mechanically stable thin polymer shell. Although this method is fast and produces robust microcapsules, it requires transfer from the emulsion into a single-phase aqueous solution. The emulsion-based technique is limited in producing capsules with precisely controlled diameters, pore size and permeability. In contrast, LbL-based silk capsules have tunable permeability, which can be achieved simply by changing the number of deposited silk layers as well as highly monodispersed dimensions easily variable from 100 nm to 100 μm.

6.3.3 Fabrication of biodegradable silk fibroin coatings on cells

In order to minimize cytotoxicity and avoid prolonged exposure of the cells to potentially toxic processing conditions, we explored the formation of stable silk shells produced by an all-aqueous salting-out process induced by a kosmotropic phosphate buffer. In order to assess the effect of salts on the viability of yeast cells and to optimize molar concentrations,

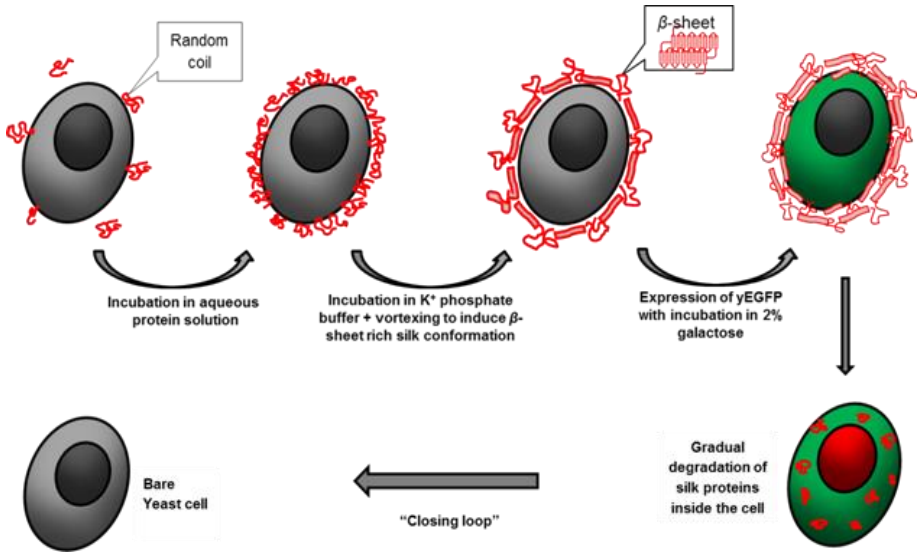

Figure 6.4 Silk-on-silk LbL deposition to form silk II rich structure on the surface of the yeast cells, followed by expression of yEGFP. Followed by gradual biodegradation and internalization of silk proteins and returning to the bare state without coatings.

we performed LbL encapsulation of *S. cerevisiae* yeast cells in locked in silk shells induced by treatment with sodium phosphates, potassium phosphates, or phosphates supplemented with calcium chloride. Stable silk protein shells can be locked in at the cell surfaces by inducing secondary transition from water-soluble Silk I to non-soluble β-sheet-rich Silk II by salting-out in a proper ionic mixture complemented with shear-thinning effect (Figure 6.4).[200]

The formation of stable silk shells was evident as strong fluorescent emission (red) was observed around the periphery of yeast cells with confocal microscopy imaging as well as with SEM (Figure 6.5a,b). It also confirms the integrity of the silk coatings and the formation of stable silk nanoshells via the salting-out process by a moderately strong K^+ phosphate buffer and preservation of non-soluble silk nanoshells.

Successful assembly of silk LbL shells was also monitored by measuring ζ-potential after deposition and the salting-out procedure (Figure 6.5c). Control yeast cells possessed strong

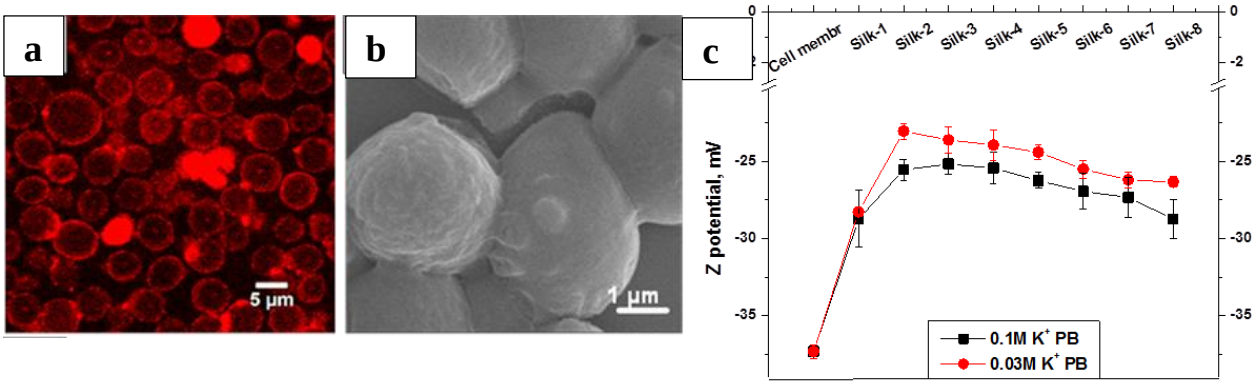

Figure 6.5 CLSM (a) and SEM (b) images of yeast cells encapsulated in silk-on-silk shells. ζ-potential of yeast cells after deposition of each silk layer (e.g., Silk-1,Silk-2) and treatment with K^+ phosphate buffer (c).

negative ζ-potential of -38 mV. After assembly of silk proteins, ζ-potential was reduced to the range of -22 to -28 mV regardless of the molarity of potassium phosphates (0.1M or 0.03M) or number of deposition cycles, suggesting the stabilization of protein shells by salts and accumulation of silk on the cell surfaces.

Figure 6.6 demonstrates the viability of encapsulated cells in response to the treatment with different salts or the traditional methanol cure (control sample). With the control specimen, even a low methanol concentration and brief washing steps (5-10 sec), which are necessary to induce β-sheet conformations, result in a significant reduction of cell viability (below 40%) that confirmed incompatibility of the traditional methanol treatment with cell surface engineering (Figure 6.6a). Negative controls were assessed to determine the viability of yeast cells incubated in the solutions of phosphate buffers with different ionic strengths (0.1M or 0.03M). These results show that salts alone do not compromise cell activity, since bare cells demonstrated 100% viability and metabolic activity. On the other hand, after encapsulation and treatment with phosphate buffers the viability rate varied depending on the strength of molarity and the type of buffer. Potassium phosphate at physiologically relevant conditions (0.03 M, pH 5.3 for yeast cells) promoted higher cell viability rates in comparison to sodium phosphate of the same molarity or potassium phosphate of a higher molarity (0.1 M, pH 5.3).

Alternatively, a live-dead assay (Figure 6.6a) or a bioreduction assay of resazurin (Figure 6.6b) complemented each other, showing excellent viability rates: 97% (live-dead test) and about 92% (resazurin test) for cells encapsulated in 8 layers of silk nanoshells. In contrast, viability rates for cells encapsulated in silk shells with the same composition of layers but incubated in higher molarity of phosphates (0.1 M) were moderately reduced to 80% (live-

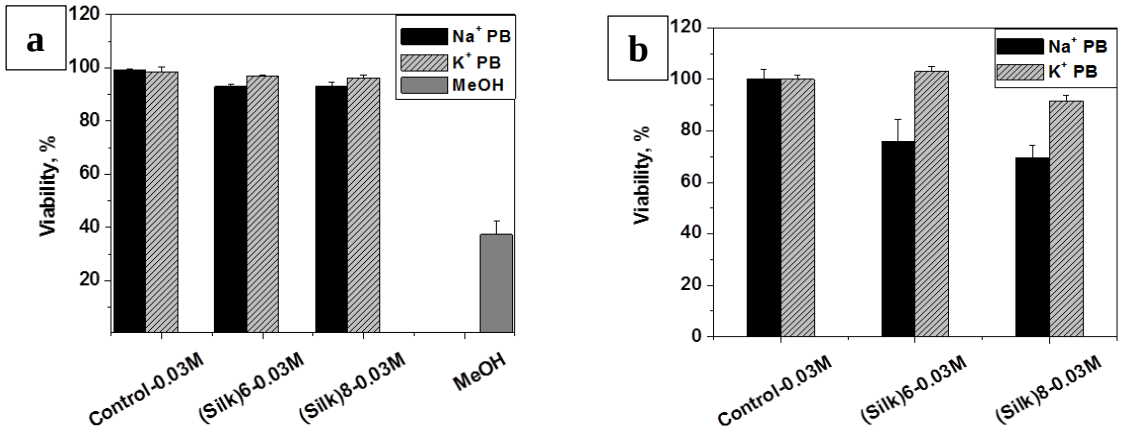

Figure 6.6 Viability rates of yeast cells encapsulated in silk shells treated with 0.03 M of phosphate buffers that were assessed with Live/Dead (a) and bioreduction of resazurin (b) assays.

dead test) or 67% (resazurin test). The difference in viability rates can be explained by the nature of susceptibility testing. While general survivability of cells is represented by live-dead test, the level of metabolic activity of viable cells is assessed by bio-reduction of resazurin, where the function/activity of even membrane-preserved cells could be significantly affected. Hence, assessment with two independent cytotoxicity assays allowed us to demonstrate not only high survivability rate (97%) of silk-modified cells using physiologically relevant salt treatment, but also showed consistent and significant retention of metabolic activity after the process of encapsulation (92%). With increased concentration of phosphate buffers during incubation (0.5 M, pH5.3), significant aggregation of cells was observed, indicating limiting conditions of the salting-out process and the need for a moderate strength molarity of phosphate buffers.

In vivo studies suggested that Ca^{2+} ions (strong kosmotrope) play an important role in stabilizing the silk fibroin protein in order to yield proper folding of the protein and to obtain

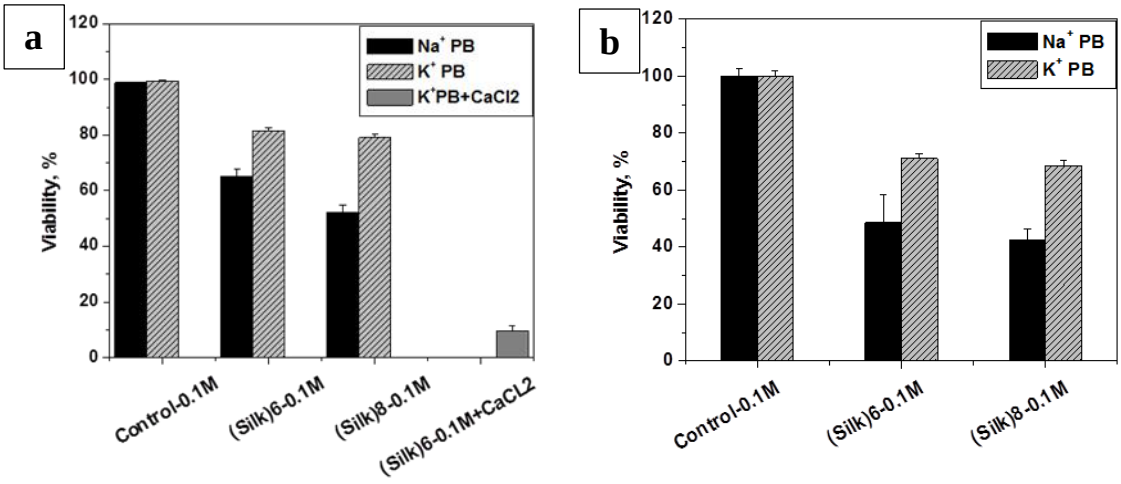

Figure 6.7 Viability rates yeast cells encapsulated in silk shells treated with 0.1 M of phosphate buffers that were assessed with Live/Dead (a) and bioreduction of resazurin (b) assays.

the silk II conformation.[88, 307] However, the effect of calcium ions even in low concentrations (0.05 M) supplemented with either K^+ or Na^+ phosphates had an adverse effect on cell viability and resulted in significant reduction of viability rates to 9.5%. Hence, the formation of stable silk nanoshells on cell surfaces was limited to the salting-out process induced by phosphate buffers (either Na^+ or K^+). Even though Na^+ and K^+ ions are placed next to each other in the Hofmeister series and are roughly neutral, with the former being a very weak kosmotrope and the later a weak chaotrope, it can be assumed that Na^+ along with phosphate (very strong kosmotrope) can efficiently stabilize proteins or membranes and strengthen hydrogen bonding and hydrophobic interactions during the salting-out process. However, viability rates were significantly lower compared to K^+ phosphate after encapsulation in silk nanoshells and incubation in a Na^+ phosphate buffer of comparable molarity (Figure 6.7). On the other hand, combination of potassium with the phosphate

anion demonstrated the most cytocompatibility, where the metabolic activation in addition to the high viability of encapsulated cells has been preserved.

Such behavior can be caused by matching extracellular conditions of potassium ions (0.03 M, pH 5.3), which correlates well with intrinsic conditions essential for active transport across the cell membrane and hence for preservation of metabolic activity of the cells.[19] Alternatively, potassium is found to be significantly less efficient in binding affinity to protein surfaces containing COO^- groups than Na^+.[308] Protein hydrophilic domains can be impaired by Na^+, which can destabilize the proteins and lead to their unfolded structure and thus reduced cell viability.[308] Pairing a chaotropic cation (K^+) with a kosmotropic anion (HPO_4^{2-}) is responsible for the preferential hydration of the protein, which enables enhanced water-protein interactions.[309]

To evaluate the thickness of silk films and to proof the concept that silk secondary structure transition is indeed induced by salting-out process, silk protein was absorbed (0.1% aqueous

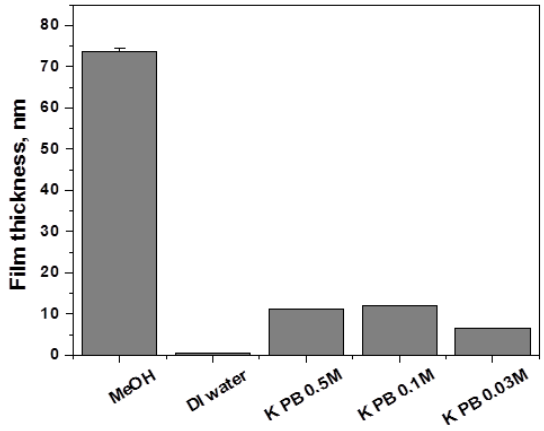

Figure 6.8 Comparative thickness of 10 layers of silk-on-silk films in dry state as a function of treatment.

solution) on pre-cleaned silica substrates using dip-assisted methodology. Pre-cut freshly cleaned silicon wafers were alternatively immersed into the solution of silk followed by washing in either of the buffer solutions. After deposition of silk for 10 min substrates were immersed in the solutions of K^+ phosphate buffers of different strength (0.03M, 0.1M, or 0.5M, pH 5.5) followed by brief washing in Nanopure water, after which the deposition process of silk was repeated. Estimation of thickness in dry state was performed after formation of 10 layers of silk using Ellipsometer (Figure 6.8) The resulting high retention of silk materials showed that even lower molarities of K^+ phosphate buffer promoted silk film stabilization lower but comparable than that of the traditional methanol treatment. Based on these measurements, we optimized the conditions for gentle and cell-friendly stabilization of silk shells by salting-out in 0.03 M potassium phosphate buffer (pH 5.3).

AFM and SEM analysis confirms the formation of uniform silk coatings on cells (Figure 6.9). Increased aggregation of silk shells and a net-like appearance are characteristics of these shells a modest increase in microroughness from 1.5 nm (within 1x1 μm^2 area) for bare cells to 3.5 nm for cells encapsulated in $(silk)_8$ shells (Figure 6.9). Fine domain texture for silk shells is typical for silk materials with a significant amount of β-sheets, which are aggregated in nanoscale domains.[199] A highly grainy surface morphology suggests a potentially porous morphology of the silk shells. The pore sizes might possibly reach 20 nm as was measured for similar silk microcapsules after methanol treatment.[199] The high permeability of the silk shells is essential for transporting the nutrients and for the proper response to physiological changes.

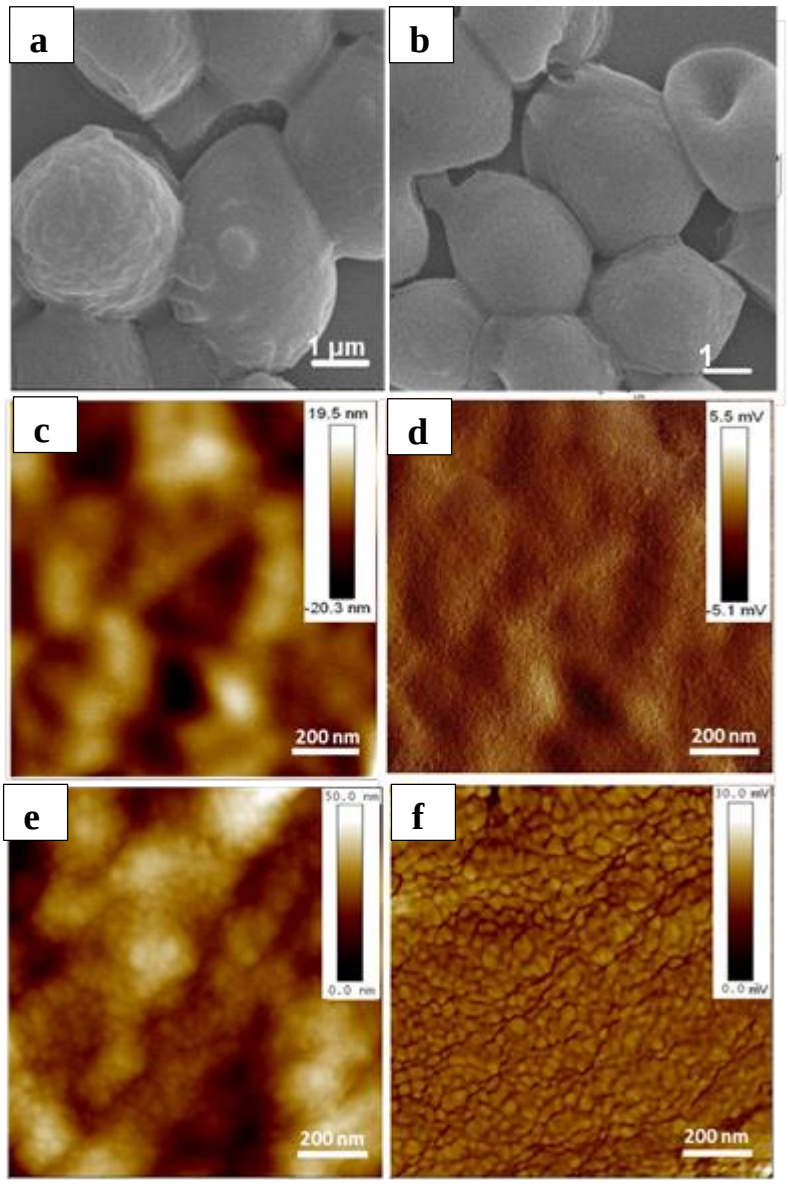

Figure 6.9 Comparison of SEM images between yeast cells encapsulated in $(silk)_8$ shells during salting-out with 0.03 M K+ phosphate buffer (pH 5.3) (a) and control (non-treated) cells (b); AFM images showing surface morphology of bare yeast cells (c, d) and cells encapsulated in $(silk)_8$ shells (e, f).

6.3.4 Effect of silk coatings on cell function

The ability of cells to bud (produce daughter cells) after the process of encapsulation was not affected and showed no changes in the ability of cells to replicate, with a small delay (by two hours or about 10% change) in reaching the maximum rate of log phase. Additionally, it has also been demonstrated the non-cytotoxic nature of silk nanoshells compared to synthetic composites. Accumulation of yeast enhanced green fluorescent protein (yEGFP) production in response to the inducer molecule further confirmed weakly affected cell function with insignificant (only a few hours) lag (Figure 6.10).

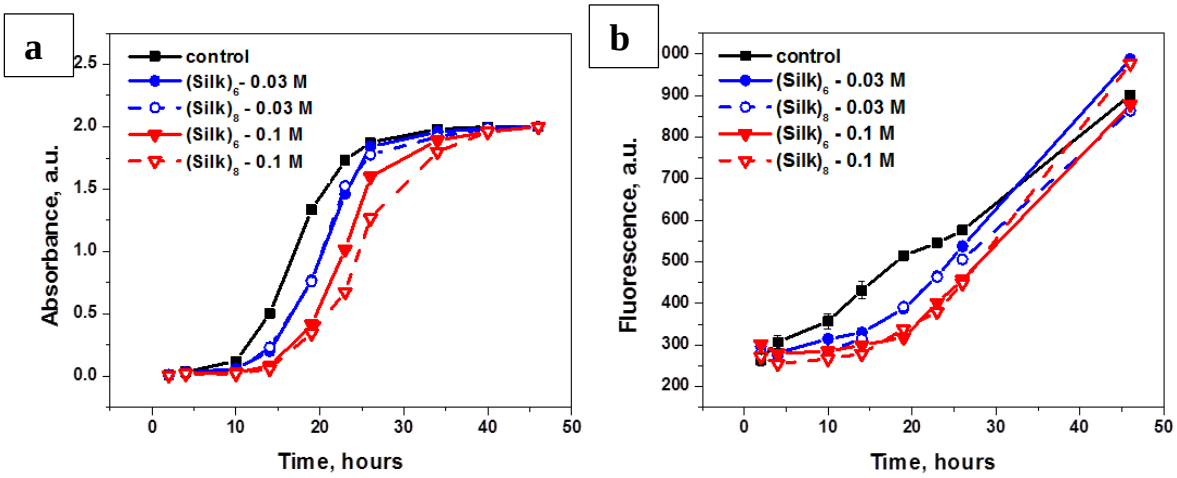

Figure 6.10 Growth kinetics (a) and expression of yEGFP (b) of yeast cells encapsulated in 6 or 8 layers of silk ($(silk)_6$ and $(silk)_8$, respectively).

A minimal delay in reaching the stationary phase and unaltered yEGFP expression suggests that silk shells can efficiently preserve inherited functionality of cells in contrast with cells encapsulated in synthetic polymer shells. In comparison to polymer nanoshells, these "silked" cells demonstrated significantly higher response rates and shorter lag times.[197] A relatively fast response to the inducer molecules and as a result, synthesis of the yEGFP,

demonstrates the integrity and unaltered functionality of encapsulated yeast cells, and it can be considered as proof of preserved metabolic activity. Factors such as high biocompatibility of the salting-out process of silk protein along with high porosity of the shells might be responsible for higher viability and unaltered cellular function, which are rarely achieved with synthetic polymer shells.[197]

The confocal images taken after encapsulation and throughout the log phase at different times displayed a gradual change in "silked" cell morphology (Figure 6.11). Immediately after encapsulation, the red fluorescent silk shell is clearly observed as a thin red shell surrounding the peripheral part of the cell (Figure 6.11). During cell maturation after incubation in media supplemented with yEGFP inducer molecules (12 hours), it appears that the labeled protein diffuses through the periphery of the cell.

In contrast to synthetic polymer shells that shown to be slowly degraded extracellularly, silk protein coatings go through fast biodegradation intracellularly. The process of fast degradation begins not until the cells reach mid of the log phase in their growth behavior at the expense of partial degradation of silk during exocytosis of waste products (mainly CO_2, and ethyl alcohol). Under these conditions silk protein undergoes structure transition to β-sheet secondary structure. Along with active extracellular enzymatic activity, cells might further promote digestion of silk protein, and endocytosis of degraded protein fragments (Figure 6.11). Particularly, a higher concentration of residuals from labeled silk was found to be accumulated after 25 hours in the cell vacuole, a type of lysosome responsible for recycling of misfolded proteins and storing the waste (Figure 6.11). Thus, after initially serving as protective nanoshell, silk coating undergoes fast biodegradation and digestion, leaving behind mature cells with full functionality and no trace of the initial shell. Hence,

the biodegradable silk nanoshells can be considered as an efficient way to provide short-term protection for the cells during implantation without affecting their metabolic activity.

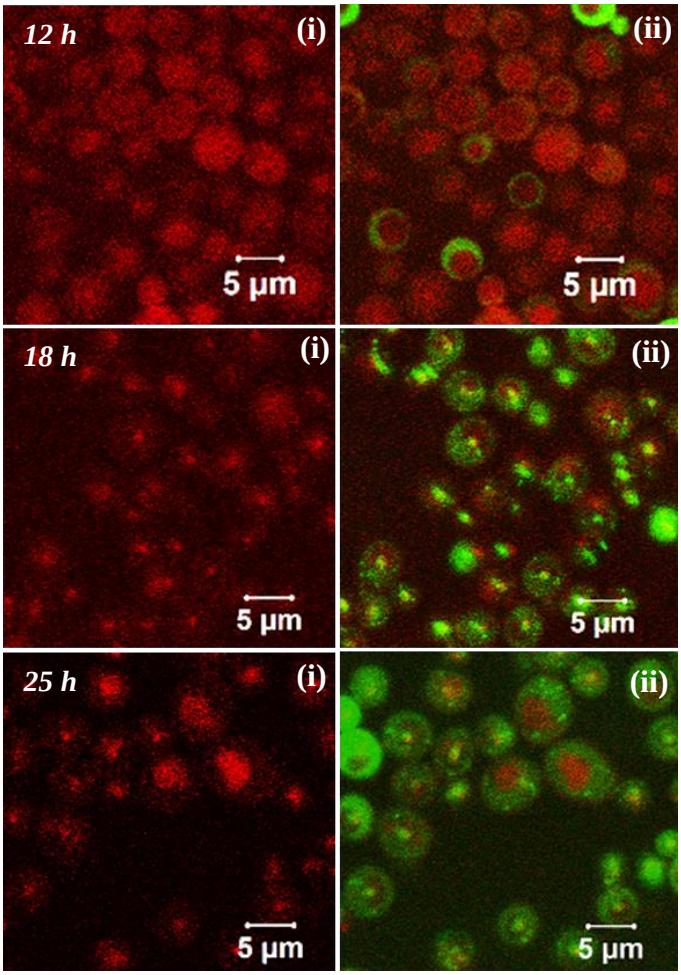

Figure 6.11 Biodergadation and internalization of silk protein shells inside of yeast cells during cell growth. Legend: i-Rhodamine/CY3 bandpass filter; ii-overlap of GFP/FITC and Rhodamine/CY3 bandpass filters.

7 CHAPTER

IONOMERIC SILK SHELLS WITH TAILORED CHEMISTRY OF INTERACTIONS AS MEANS TO MODULATE CELL FUNCTIONS

7.1 Introduction

Chemical modification of SF with charged amino-acids allows for exploring new properties of silk-based materials with enhanced mechanical stiffness and tailored protein absorption.[298] The grafting density, the length and the conformation of charged amino acids attached to the backbone of the silk protein, overall charge net of poly-electrolytes and interactions involved in the self-assembly significantly influence the protein adsorption during the LbL film growth and hence affect the properties of silk-functionalized surfaces. When we consider the cell coatings based on the self-assembly of modified proteins, the cytocompatibility has to play a major factor in assessing LbL shells as effective means for protection of bioactivity of encapsulated cells. Hence, proper tailoring of polyamino acids into the backbone of silk macromolecule with the right degree of functionalization and length of amino acid side chains should be attained in order to balance the formation of robust shells and at the same time not impose toxicity from polycationic part.

7.2 Experimental details

Detailed experimental procedure on the synthesis of silk polyelectrolytes has been described in Experimental section including LbL deposition on bacterial cells, and viability assay tests while the simplified schematic drawing and chemicals used in the LbL shells are outlined in Figure 7.1.

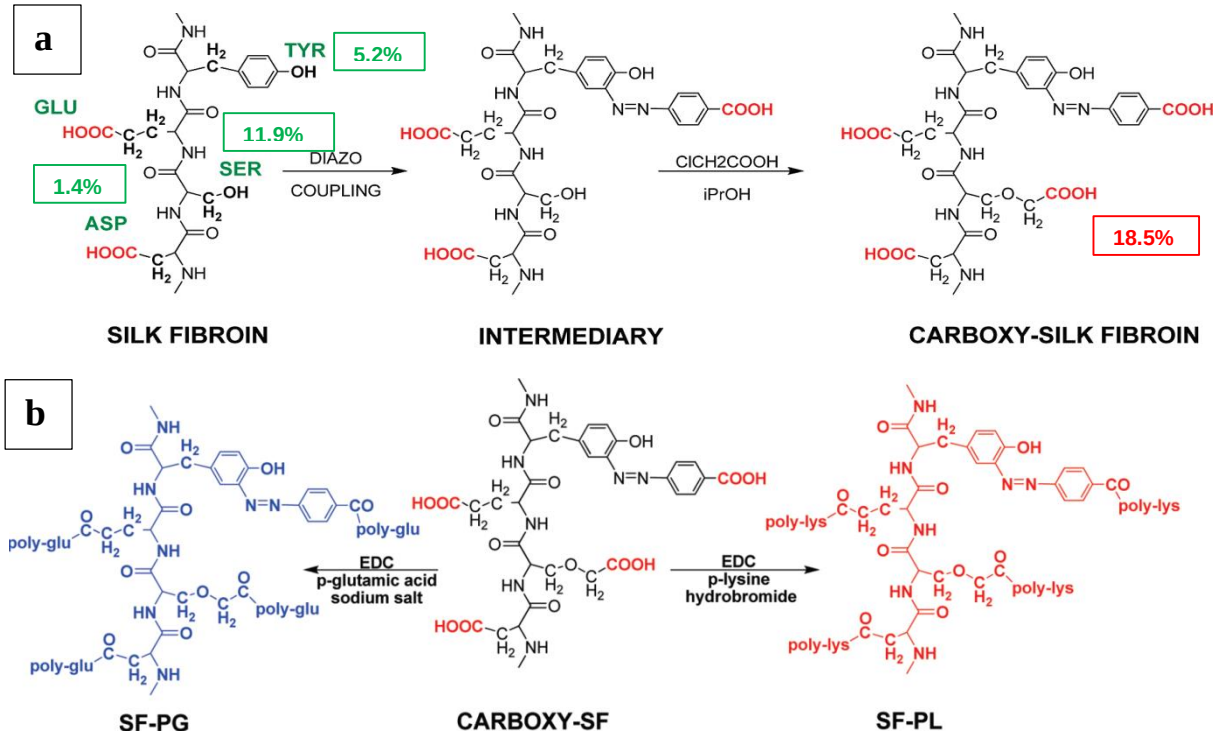

Figure 7.1 Chemical scheme for creating silk intermediate (a), and silk polyelectrolytes (b).

Silk ionomers were obtained from Prof. D. L. Kaplan group and used as received. Reconstituted silk fibroin (SF) protein was modified with polyamino acids (poly-L-Lys and poly-L-Glu) to obtain naturally-derived silk polyelectrolytes of two types: with high and low charge density silk ionomers. System 1 was synthesized to obtain a high degree of derivation of silk ionomers with long chains of polyamino acids grafted to the tyrosine (Y) and serine (S) residues of SF, namely SF-(Y,S)-PL and SF-(Y,S)-PG silk ionomers.[205] Alternatively, system 2 was synthesized to obtain a lower charge density of ionomers with short chains of polyamino acids (degree of polymerization *n*, *n*=20) grafted to S residues of SF (SF-(S)-Lys_{20} and SF-(S)-Glu_{20} silk ionomers). Specifically, system 1 was obtained when potentially lower molecular weight of silk fibroin (60 min boiling time) was first enriched with carboxyl content followed by chemical modification with carbodiimide-mediated coupling to attach

high molecular weight natural polyelectrolytes (M_w=15 kDa, PDI=2.5). The intermediate step of enriching the silk fibroin with carboxylate groups allowed to increase the reactive sites for further conjugation of charged polyelectrolytes to the backbone of SF (up to 18% of modified amino acids out of the total number of residues in SF), which would allowed efficient charge-charge interactions during layer-by-layer adsorption of proteins. In turn, system 2 was synthesized when initially higher molecular weight of SF (5 min boiling time) was chemically modified with low molecular weight polyelectrolytes (M_w=1 kDa) attached to S residues that accounted for 11.9% of the total amino acids.[310,311]

As was previously demonstrated, grafting of poly-(ethylene glycol) (PEG) can reduce cytotoxicity of polycations.[103,244,] Here, to improve biological compatibility of shells assembled at cell surfaces, several PEG-grafted silk copolymers were obtained. Graft (*g*) copolymer SF(Y,S)-PL-*g*[*D*]-PEG was synthesized by conjugation PEG (Mw=5 kDa, PDI=2.5) to a high charge density SF-PLys silk ionomer with variable degree of grafting ratio, designated as *D*. Degree of grafting refers to the percentage of PEG groups grafted to a poly-lysine side chain. On the other hand, block copolymer SF(S)-PL-*co*-PEG was synthesized by conjugation poly-L-lys_x-PEG_n (Mw=2.6 kDa, x=10, *n*=22) to S residues selectively on the backbone of SF (Figure 7.1).

^{1}HNMR analysis confirmed successful modification of silk ionomers with PEG groups for both types of copolymers. Specifically, graft SF(Y,S)-PL-*g*-PEG copolymer was produced with 4 mol% and 9 mol% degree of PEG conjugation (SF(Y,S)-PL-*g*[*4*]-PEG and SF(Y,S)-PL-*g*[*9*]-PEG), that corresponds to on average of 5 and 11 PEG chains of high molecular weight (Mw=5 kDa) attached to a single poly-lysine side chain, respectively. The degree of derivation for SF-(S)-Lys_{10}-*co*-PEG_{22} block copolymer was calculated to be 0.5 mol%, and

can be reported in terms of side chains grafted to SF molecule as ~ 27 out of reported ~ 5,300 amino acid residues in a single SF molecule extracted from silk cocoons in a similar way.[310]

7.3 Results and Discussion

7.3.1 Interactions during LbL self-assembly of SF polyelectrolytes

Assembly of a pair of polyelectrolytes carried by attractive forces between oppositely charged species is significantly affected by the charge density and structural architecture of the polymers. Ellipsometry measurements of 4 bilayered film structures with variable charge density, length of PEG and grafting architecture of silk copolymers were performed in order to assess the shell thickness during deposition of silk copolymers at cell surfaces. Figure 7.2 represents comparison of the film thicknesses for two systems of silk polyelectrolytes adsorbed on planar substrates during dip-assisted deposition. As expected, high charge density polyelectrolytes with longer chains of amino acids demonstrated strong absorption

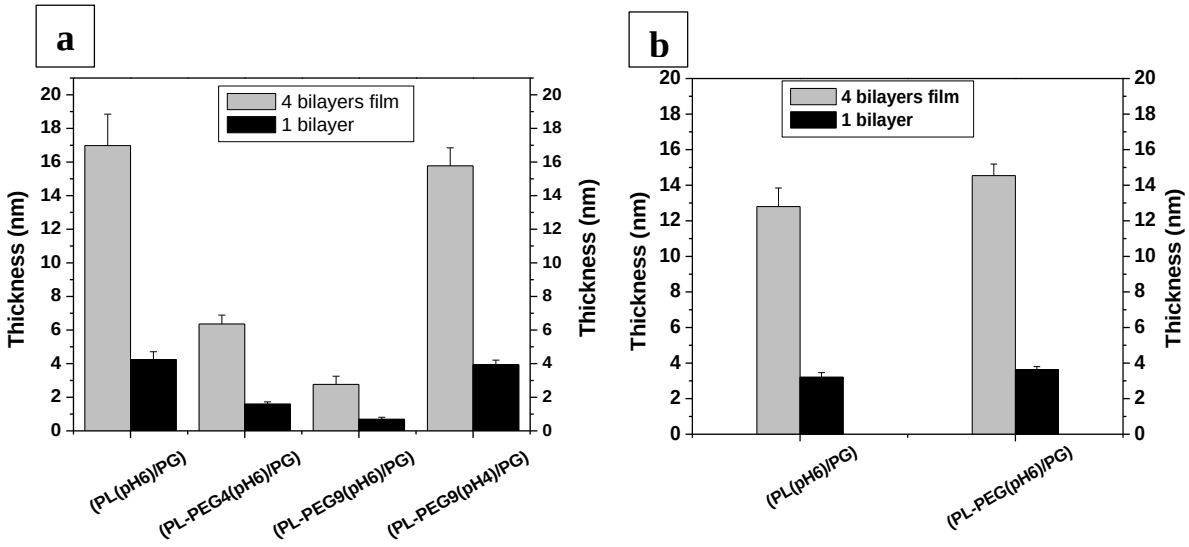

Figure 7.2 Thickness of 4 and 1 bilayered film in dry state after dip-assisted self-assembly of silk polyelectrolytes as a function of charge density, degree of PEGylation, length of PEG side chains, and interactions involved in the film self-assembly for system 1(a) and system 2(b).

of SF ionomers at pH 6 with 4.2±0.5 nm thickness per single bilayer. Low charge density SF polyelectrolytes with short chains of amino acids demonstrated reduced accumulation of macromolecules during self-assembly of $(SF\text{-}PL/SF\text{-}PG)_4$ film at pH6 with 3.2±0.3 nm thickness per 1 bilayer. PEGylated silk graft block-copolymers consistently gave us hindered adsorption of monolayers during self-assembly with SF-PGlu polyelectrolyte, specifically when the deposition was performed at pH6. By increasing the grafting ratio of PEG chains the potential for electrostatic interactions necessary to drive film assembly is hindered by steric effect of highly hydrated long chains of polyether (5 kDa) that tend to obtain a globular conformation at pH 5.5. Consistently, graft copolymer with 11 PEG side chains (SF-PL-*g*-[*9*]-PEG) gave us the lowest film thickness with 0.7±0.1 nm bilayer thickness. In order to restore the assembly of LbL films with highly PEGylated silk copolymers, we switched the nature of interactions between polyelectrolytes from electrostatic to hydrogen-bonded. By lowering the pH just below the pKa for glutamic acid (pKa=4.07) we relied on interactions between hydrogen donor specie (protonated state of SF-PG silk) and its counter-specie hydrogen acceptor (polyether SF-PL-*g*[*9*]-PEG). The film thickness of hydrogen-bonded self-assembled silk polyelectrolytes at pH4 demonstrated significant increase in macromolecules absorption on planar substrates with 4±0.3 nm bilayer thickness (Figure 7.2a).

Self-assembly of silk polyelectrolytes with short side chains maintained good adsorption of macromolecules at pH6 when both species have effective counter-charges necessary to drive film assembly based on charge-charge interactions (Figure 7.2b). Interestingly, films assembled with PEG block co-polymer demonstrated statistically similar values for the

thickness with non-PEGylated silk polyelectrolytes due to the minor content of short PEG chains conjugated to the silk backbone (paired t-test, $p>0.05$).

The effect of silk polyelectrolytes was assessed on two types of bacterial cells: Gram-negative (ex. *E. coli*) and Gram-positive (ex. *B. subtilis*) cells. Even though both types of the cells have the same rod-shape appearance, the cell structure differs significantly in terms of cell wall/membrane architecture.[312] Because of the striking variance in physical nature of the cell surfaces the adsorption of silk polyelectrolyte may provoke the distinct changes in the cell survivability, their behavior and overall appearance of cells-in-shells assembly.

7.3.2 Viability studies of microbial cells engineered with silk polyelectrolyte shells

Viability of cells encapsulated in silk polyelectrolyte shells was assessed independently with two assay tests to confirm the effect of silk polyelectrolytes on cells activity (Figures 7.3, 7.4). Bioreduction of resazurin assay was used immediately after the encapsulation to test

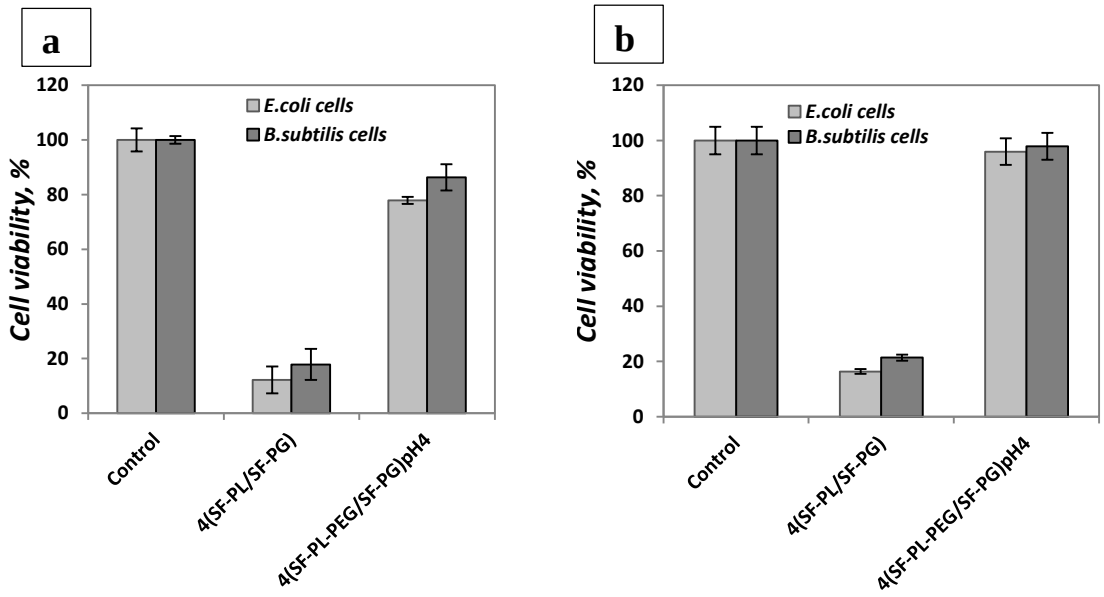

Figure 7.3 Viability of bacterial cells encapsulated in 4 bilayers of silk polyelectrolyte shells (system 1) assembled through pure electrostatic (SF-PL/SF-PG) and hydrogen-bonded ((SF-PL-PEG/SF-PG)pH4) interactions assessed with resazurin test (a) and MTT test (b).

the susceptibility of bacterial cells to the processing conditions and the exposure to silk copolymers. The results were confirmed with formazan-based (MTT) cell proliferation assay after incubation in cell culture medium for 24 hours (Figure 7.3a,b). To be noted, MTT assay test gave us 4-18% higher values compared to resazurin-based test due to the distinct nature involved in the bioactivity of the specific enzymes and the prolonged time used to assess cellular metabolic activity. Consistently, *B. subtilis* cells on average demonstrated 3-5% higher viability rates regardless of more receptive nature of their cell walls to chemical agents.

As demonstrated, cells encapsulated in four bilayer-shells using highly-charged silk polyelectrolytes (system 1, 4(SF-PL/SF-PG)) showed reduced viability rates in the range of 12-16% (for *E. coli* cells) and 17-21% (for *B. subtilis* cells) compared to the hydrogen-bonded shells made of the same number of bilayers (4(SF-PL-PEG/SF-PG)pH4) with viability rates in the range 77-95% (for *E.coli*) and 86-97% (for *B. subtilis*). It has already been confirmed by the work from other groups specifically on larger size eukaryotic cells that in part high charge density polycations elicit cytotoxicity due to nonspecific formation of the pores in the plasma membrane that can also depend on the size and the conformation of the polymers used for the cell coatings.[103,107] Bacterial cells are known for their resilience to the external perturbations in the local environment, including minor disruptions in the plasma membrane, and denaturing non-essential proteins or membrane lipids. The fact that high charge silk polyelectrolyte shells have significant effect on microbial metabolic behavior and inhibition of growth (at least within the first 24 hours) confirms adverse effects of electrostatically driven self-assembly of silk copolymers with high molecular weight of polyamino acids even on microorganisms. On the other hand, hydrogen-bonded assembly

of SF-PL-*g*-[*9*]-PEG PEGylated copolymer with its protonated counter-part SF-PG has no effect on microbial activity, making these shells cytocompatible.

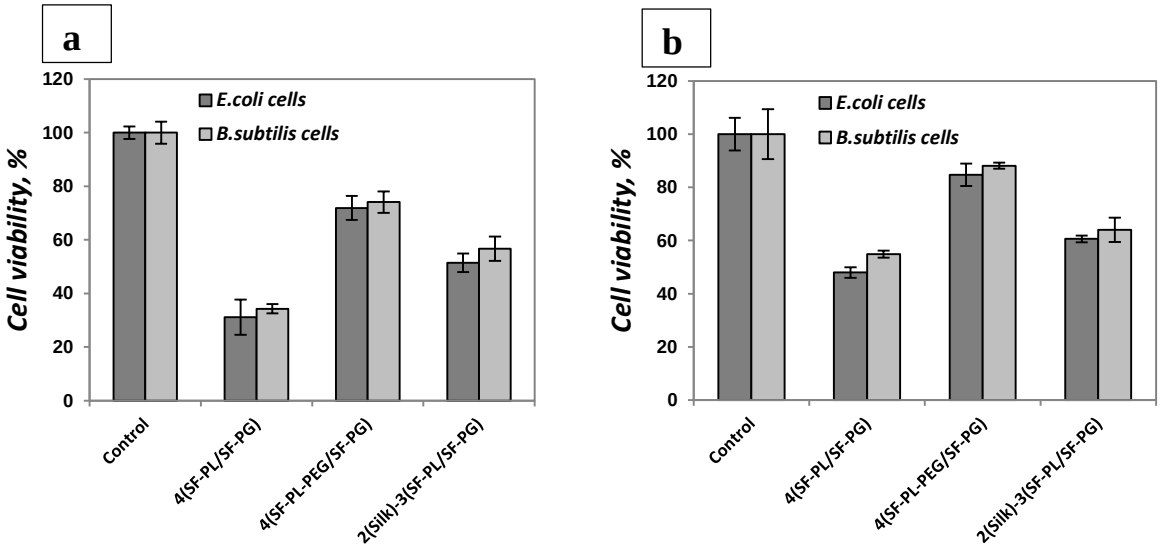

Figure 7.4 Viability rates for bacterial cells encapsulated in 4 bilayers of silk polyelectrolyte shells (system 2) assembled through week ionic interactions (SF-PL/SF-PG), partially screened ionic interactions (SF-PL-PEG/SF-PG) and ionic interactions assembled on silk-primed layers ((silk)-(SF-PL/SF-PG)). Viability was assessed with resazurin test (a) and MTT test (b).

Viability studies of bacterial cells encapsulated in low charge density silk polyelectrolytes (system 2) demonstrated significantly higher rates (paired t-test, $p>0.05$) (Figure 7.4a,b). Bacterial cells encapsulated in 4-bilayer LbL shells using silk copolymers with short amino acids had viability rates in the range of 31-45% for *E. coli* and 34-54% for *B. subtilis*, respectively. Cells encapsulated in silk shells assembled with PEGylated block copolymer had viability rates in the range 71-84% for *E. coli* and 74-88% for *B. subtilis*, respectively emphasizing the effect of decreasing the charge density of polycation with PEG grafts. Not surprisingly, lower grafted silk polyelectrolyte shells with short side chains (system 2) demonstrated higher viability rates compared to higher grafted silk polyelectrolyte shells with higher molecular weight side chains (system 1), which is consistent with previous

reports on inverse correlation between M_w and charge density with cell toxicity.[107,313] The cytotoxic effect of polycations can be significantly reduced by adsorbing buffer layers to shield the cell surface from conformational changes induced by amino groups in polycations.[103,244] Bacterial cells primed with two silk fibroin layers prior to adsorption of silk polyelectrolytes showed significantly higher viability rates in the range of 51-60% for *E. coli* cells and 56-63% for *B. subtilis* cells, respectively. The data suggest that toxicity originates during direct contact of polycations with cell membranes as a result of enhanced interfacial contact with amino-groups.

7.3.3 Adsorption of silk polyelectrolytes at cell surfaces

Deposition of silk polyelectrolytes was monitored by measuring zeta-potential after adsorption of a single layer during LbL deposition of silk shells. Figure 7.5 represents changes in the surface charge acquired as a result of non-covalent interactions (either ionic or hydrogen-bonded interaction forces) between silk proteins of different composition. An example of pure electrostatic interactions between highly charged silk polyelectrolytes is

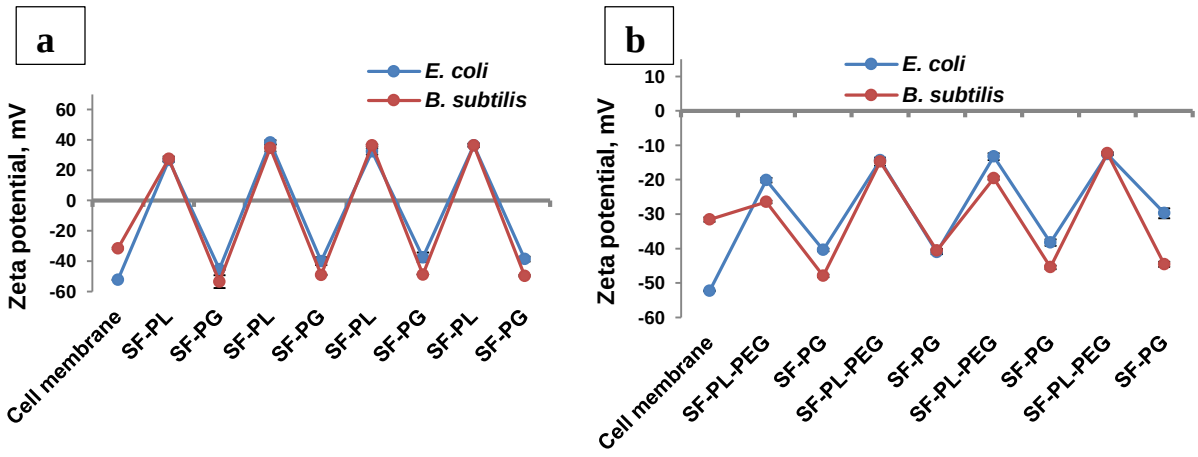

Figure 7.5 Changes in zeta-potential values after adsorption of a single layer during LbL self-assembly of silk polyelectrolytes on two types of bacterial cells (*E. coli* and *B. subtilis*). Strong electrostatic interactions can be observed with highly-charged silk polyelectrolytes (a), and pure hydrogen-bonded interactions can be distinguished for PEG graft copolymer with protonated SF-PG silk polyelectrolytes (b).

represented in Figure 7.5a, where efficient charge reversal can be observed with the adsorption of strongly induced charges of silk ionomers at pH 5.5. With highly PEGylated silk polyelectrolyte (SF-PL-g[9]-PEG(5)) the assembly of silk shells was carried at pH4 to promote hydrogen-bonded interactions with a protonated counter-part specie, SF-PG (Figure 7.5b). Since the assembly was relying on hydrogen bonding between ether groups of PEG chains and carboxylate groups of SF-PG chain the charge reversal was hindered suggesting that significant number of un-protonated polyglutamic acid side chains was responsible for negative values of surface charges and overall good colloidal stability of cells-in-shells structures. The self-assembly of protein macromolecules can be more complex since the folding of the protein into secondary and tertiary structures can be induced by many factors, specifically non-covalent interactions including Van der Waals and hydrogen bond forces. However, the degree of modification of silk proteins was significant and beyond the appearance of pure protein macromolecule, the effect of intramolecular forces can be minor.

Assembly of silk polyelectrolytes with low charge density at surfaces of bacterial cells demonstrated minimal effect of side chains mainly due to the short length of polylysine and polyglutamic acids (n=20). The surface charges were alternated in negative values for the first two bilayers, then appeared to have positive values for the last two bilayered structures (Figure 7.6a). The adsorption of silk polyelectrolytes with low grafting density and short side chains based on pure electrostatic interactions seem to compete with protein self-folding into the secondary and tertiary structures as less steric hindrance from charged amino acids pose any constrain to form a 3D structure. With PEGylated silk polyelectrolyte proteins, the effect of charge-charge interactions was even more diminished suggesting that other non-covalent interactions (Van der Waals, hydrogen bonded, hydrophobic interactions) play

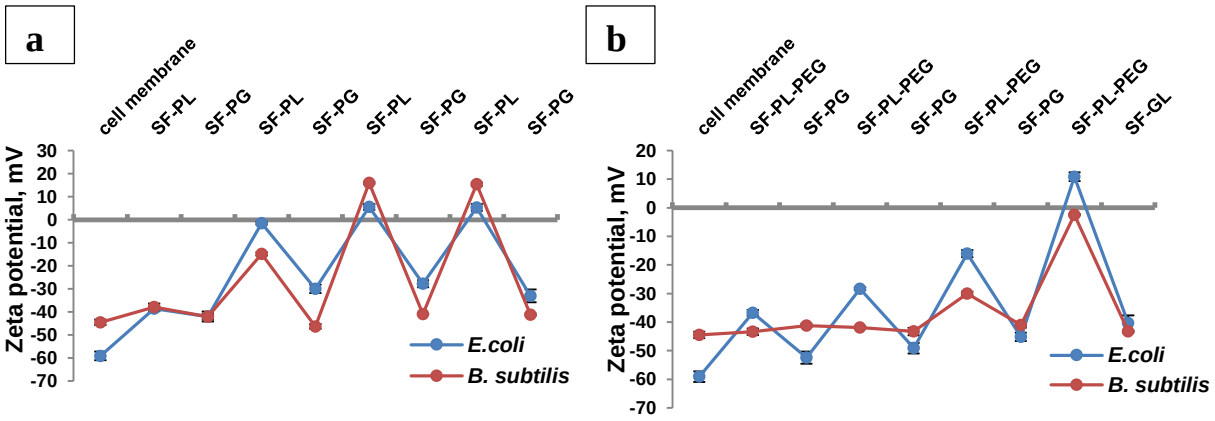

Figure 7.6 Changes in zeta-potential values after adsorption of a single layer during LbL self-assembly of silk polyelectrolytes on two types of bacterial cells (*E. coli* and *B. subtilis*). Weak electrostatic interactions can be observed with low-charge density silk polyelectrolytes (a) and PEG-screened silk polyelectrolytes (b).

more significant role during self-assembly of silk protein shells (Figure 7.6b). Consistently, Gram-positive bacterial cells were demonstrated significantly lower values of zeta-potential compared to Gram-positive cells.

7.3.4 Morphologically distinct behavior of bacterial cells encapsulated in silk polyelectrolyte shells

The nature of chemical interaction that governed the adsorption of silk polyelectrolyte films had major effect on morphological appearance and aggregation behavior of cells-in-shells assemblies. Figures 7.7, 7.8 represent confocal and SEM images illustrating distinct changes in surface morphology of bacterial cells encapsulated in high charge density polyelectrolyte $(SF\text{-}PL/SF\text{-}PG)_4$ shells (Figures 7.7a, 7.8a) and hydrogen-bonded (SF-PL-g[9]-PEG/SF-$PG)_4$ shells (Figures 7.7b, 7.8b). As shown on the figure the aggregation of cells during LbL deposition of electrostatically-assembled shells was induced by highly-charged nature of polyelectrolytes. The size of cell agglomerates ranged between 20 to 50 μm for *B. subtilis*

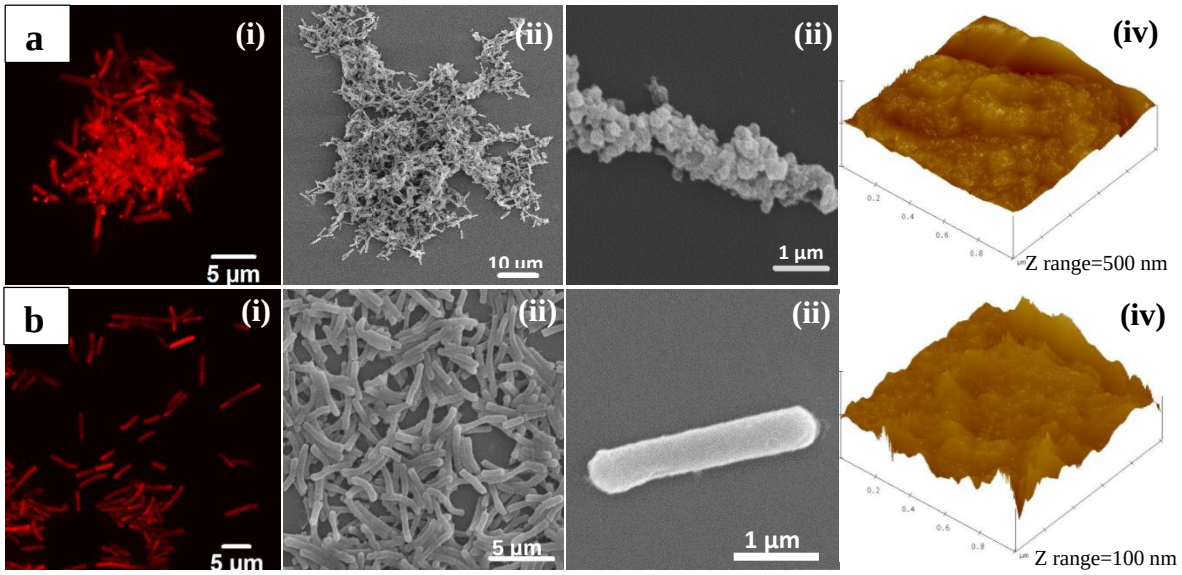

Figure 7.7 *B. subtilis* cells encapsulated in 4 bilayers of SF-PL/SF-PG shells (a) and SF-PL-g[9]-PEG/SF-PG shells (b). Confocal (i), SEM (ii, iii) and AFM (iv) imaging of cells-in-shells structures demonstrate distinct morphological features.

cells (Figure 7.7a), and between 60 to 100 µm for *E. coli* cells, emphasizing the significance of cell surface structure and composition that can influence the adsorption of protein macromolecules and drive assembly process towards aggregation. The distinct feature of Gram-negative bacteria cells (ex. *E. coli*) is the presence of lipopolysaccharide outer membrane. The large complex molecule is anchored to the underlying peptidoglycan cell wall and has a polysaccharide chain extending outward from the cell surface. The abundance of these side chains makes the cell surface look like the high density protrusions. In contrast, Gram-positive bacteria (ex. *B. subtilis*) have thick peptidoglycan cell wall consisting of sugars and amino acids that forms a mesh-like layer outside of the cell membrane. While more structurally flat surfaces promote formation of uniform layers of protein polyelectrolytes films, the architecturally-rough cell surfaces may contribute to the significantly higher surface roughness of the protein layers. Specifically, increased roughness was characteristic to the silk LbL shells assembled through electrostatic

interactions when adsorption of proteins with high-charge density favors globular conformation and can not produce optimized electrostatic attraction.[314]

Functionalization with silk polyelectrolyte macromolecules (specifically with high charge density and bulky side chains) at cell surfaces tailors conformational changes of proteins to the extent resulted in unbound amino acid residues that are available for the contact with incoming proteins of opposite charge. As a consequence, further intermixing of proteins may induce protein aggregation and formation of nanoparticles that abundantly decorated the surface of the cells and involved in the creation of cell aggregates. In contrast, hydrogen-bonded shells showed well-dispersed homogeneous suspension of cells-in-shells structures with no evidence of aggregation of PEGylated silk protein polyelectrolytes (Figures 7.7b, 7.8b). Conformational changes induced by hydrated chains of high molecular weight PEGs may be responsible for extended conformation of silk polymers that promote formation of

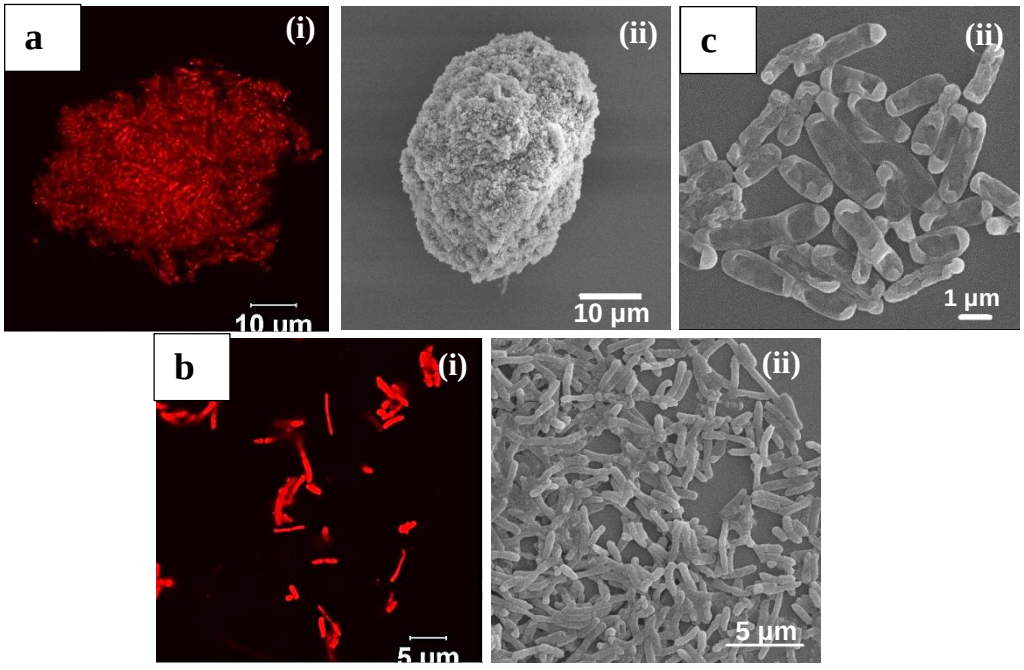

Figure 7.8 *E. coli* cells encapsulated in 4 bilayers of SF-PL/SF-PG shells (a) and SF-PL-g[*9*]-PEG/SF-PG shells (b) in comparison to control non-encapsulated cells (c). Confocal (i) and SEM (ii) images demonstrate morphological behavior of shells.

smoother LbL films. Assessment of surface roughness by atomic force microscopy confirmed elevated values for highly-charged silk polyelectrolyte shells in both types of bacterial cells with Rq=13.7±2 nm and 17.5±4 nm, respectively for *B. subtilis* and *E. coli* cells. In contrast, hydrogen-bonde d shells assembled at bacterial cell surfaces demonstrated significantly smoother film structure with Rq=5.4±0.9 nm and 7.4±2 nm for *B. subtilis* and E. coli cells, accordingly. Interestingly, the immobilization of the silk protein shells (regardless of the nature of the interactions involved in the shell assembly) at cell surfaces provided the structural robustness to the cells against the external perturbations (high or low pressure), which can be evidenced from SEM micrographs. Cells encapsulated in protein shells had distinct rod-shape appearance compared to non-encapsulated cells that have been pressurized and appeared compressed under high vacuum (Figure 7.8c).

Silk shells assembled at cell surfaces using low charge density polyelectrolytes (system 2) demonstrated reduced aggregation of cells-in-shells behavior with significantly less surface roughness compared to the high-charge density polyelectrolyte shells (Figure 7.9). In this case, the complexation of silk protein macromolecules during shell assembly is reduced due to less effect from short charged side chains when electrostatic attractions are failed in favor to hydrogen-bonded, Van der Waals and hydrophobic interactions. The values for the roughness varied significantly with respect to the nature of the silk protein shells and the type of cells. Morphologically more flat bacterial cells (*B. subtilis*) had a surface roughness of 3.8±0.8 nm (in dry collapsed state), while more rough cells (*E. coli*) had a surface roughness of 5.15±0.8 nm. During encapsulation with low-charge density silk polyelectrolyte shells, roughness increased to 6.9±0.8 nm and 8.2±1.5 nm for *B. subtilis* and

E. coli cells respectively, whereas for PEGylated silk shells the roughness decreased accordingly to 5±1 nm and 5.6±0.6 nm.

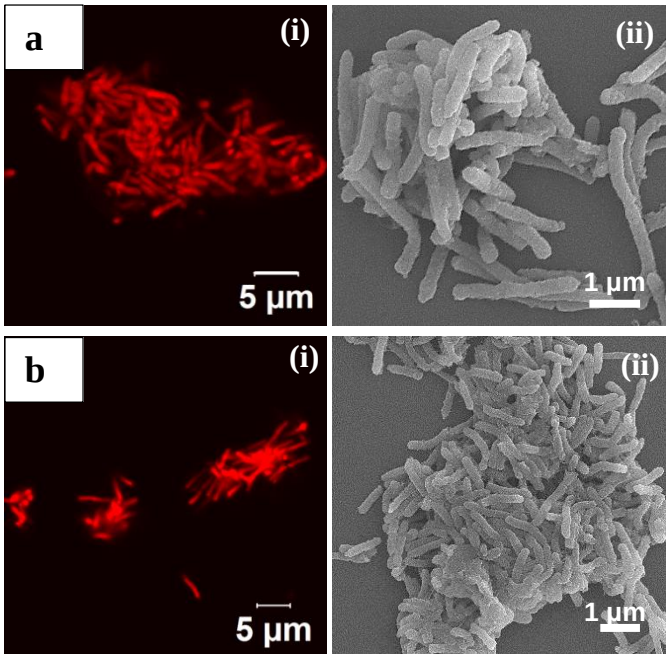

Figure 7.9 *B. subtilis* cells encapsulated in silk polyelectrolyte shells of low charge density SF-PL/SF-PG (a) and PEGylated silk block copolymers SF-PL-co-PEG/SF-PG (b). Legend: i – confocal, ii – SEM imaging.

7.3.5 Functionality of bacterial cells encapsulated in silk polyelectrolyte shells

Ability of cells to function along with toxicity results provide important information regarding the cytocompatibility of engineered coatings. For many applications involving integration of cells into scaffolds or immobilization of cells into the active platforms, the robustness of protective coatings play significant role. Here, the functional capacity of cells to respond to the analyte molecules after encapsulation in silk polyelectrolyte shells has been probed. Depending on the chemical composition of the shells and the type of genetic construct associated with the analyte recognition, bacterial cells responded differently to the presence of theophylline (analyte). Figure 7.10a,b represents kinetics of GFP expression

during incubation of encapsulated cells (both *E. coli* (a) and *B. subtilis* (b)) in the cell culture medium supplemented with 5 mM of theophylline (DMSO). Importantly, the analytical recognition constructs were cell-specific demonstrating *E. coli* as the most efficient cellular platform for recognizing, processing and activating the fluorescent signal, as a part of riboswitch construct, in response to the target analyte. Consistently, they had the most dynamic signal amplification with exponential growth of fluorescent protein intensity.

Overall, cells encapsulated in high charge density silk polyelectrolytes had lower intensity rates compared to more cytocompatible hydrogen-bonded shells with high degree of grafting density of PEGs regardless of the cell type (Figure 7.10a,b). The apparent difference in intensity levels was significant at least during the first seven hours of monitoring the fluorescence ($p>0.01$). This trend is not surprising owing to the fact that strong polycationic polymers (regardless of the nature) impose cytotoxicity to the functionalized cells, which correlates linearly with the grafting density of charged groups and length of the polycationic side chains.[103] In our case, cells encapsulated in silk polyelectrolyte shells assembled through attractive forces of high-charge density silk polymers had significantly reduced viability rates, and as the result, low fluorescence intensities associated with intracellular recognition and processing of the analyte molecules. In contrast, cytocompatible hydrogen-bonded shells assembled through interactions between highly-grafted PEGylated silk and its protonated counterpart SF-PG supported cellular activity and demonstrated comparable level of induced fluorescence.

With respect to the stability of engineered shells, the robustness of hydrogen-bonded shells started to deteriorate during 6 hours of incubation of cell suspensions in rich media under vigorous rotation (220 rpm). As shown on the micrographs, the absence of the fluorescently-

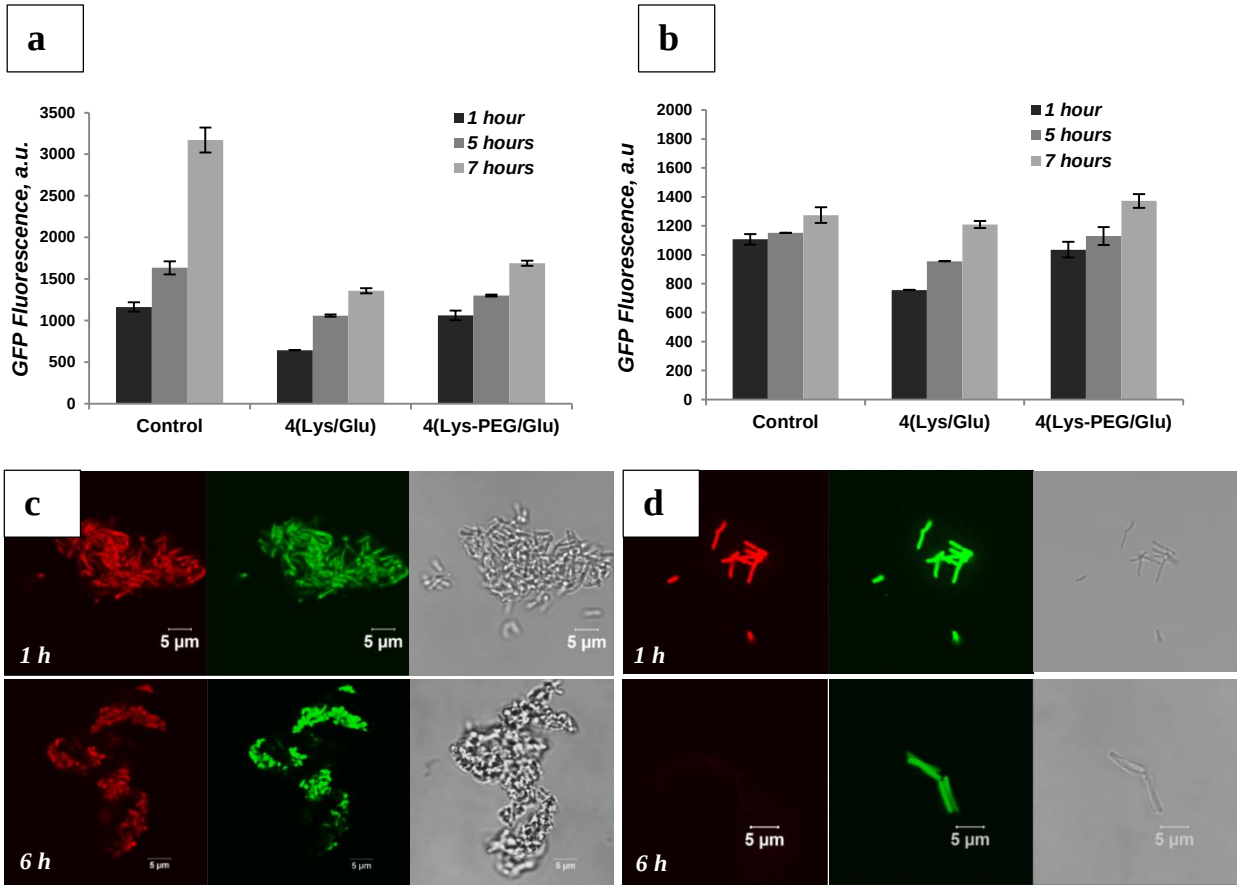

Figure 7.10 Kinetics of GFP expression in *E. coli* (a) and *B. subtilis* (b) bacterial cells encapsulated in SF-PL/SF-PG and SF-PL-PEG/SF-PG shells. Confocal images of *B. subtilis* cells encapsulated in SF-PL/SF-PG (c) and SF-PL-PEG/SF-PG (d) shells after incubation in cell culture medium supplemented with 5 mM of theophylline for 1 hour and 6 hours.

labeled red shells was observed at 6 hour mark (Figure 7.10d). In contrast, during comparable time frame, strongly-bound polyelectrolyte silk shells demonstrated significant robustness and were tethered to the cells as the existence of the red fluorescence associated with labeled shells was overlapped with green fluorescence coming from the GFP-producing cells (Figure 7.10c). Bonding forces involved in the construction of hydrogen-bonded shells can be easily broken during culturing cell-in-shells suspensions at 37°C in concentrated cell medium rich in amino acids and salts under constant rotation. In contrast, the grouped behavior of cells promoted by stronger forces of electrostatically-assembled silk

polyelectrolytes aided in slowing the dissolution of polymer shells even during vigorous cell culturing.

Silk polyelectrolyte shells with low charge density and short chains demonstrated higher levels of fluorescence intensity in comparison to high charge density silk polyelectrolyte shells (Figure 7.11). Cells encapsulated in shells assembled with PEG block copolymer (SF-PL-co-PEG/SF-PG) demonstrated even higher levels of GFP fluorescence for both types of the cells emphasizing the negative effect of polycationic silk electrolytes on functionality of cells. Consistently, if cells were primed with two layers of silk fibroin prior to encapsulation with low charge density of polyelectrolytes (2(silk)-3(SF-PL-co-PEG/SF-PG) shells), the capacity of cells to respond to the effector cues was not inhibited. The GFP fluorescence showed comparable levels of intensity as for cells encapsulated with low charge density silk polyelectrolytes.

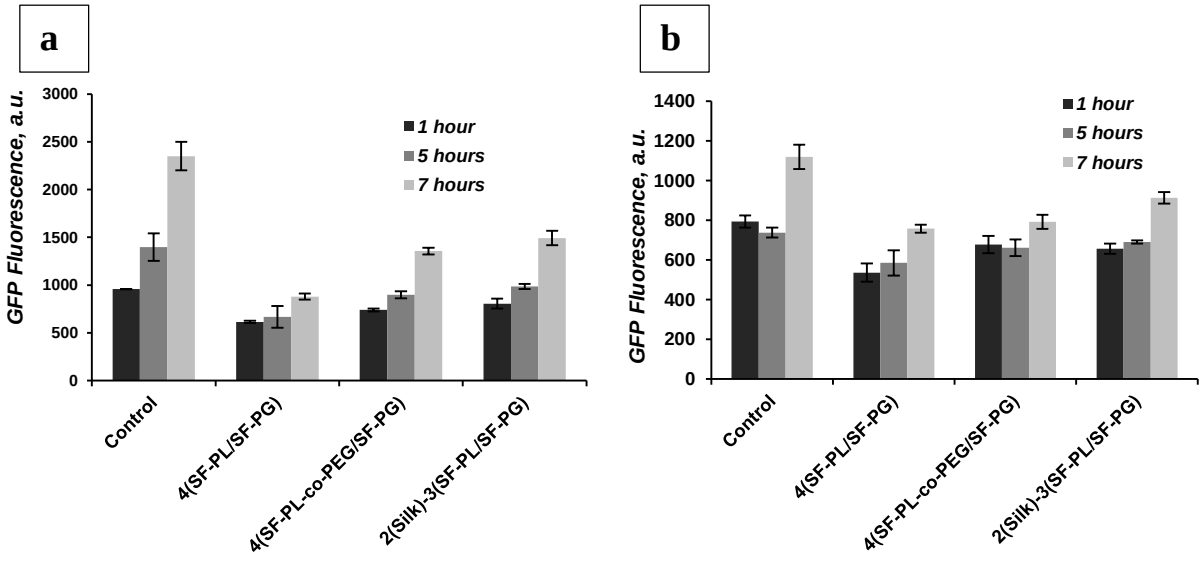

Figure 7.11 Kinetics of GFP expression in *E. coli* (a) and *B. subtilis* (b) cells as a function of shell stracture.

The viability rates were consistent with the rates of cell functionality in terms of the potential of cells to respond to the target analyte when the small molecules have to bind to the aptamer domain and turn "ON" the expression of GFP. The cell functionality studies confirmed that the nano-thick shells did not restrict the diffusion of theophylline, and the ability of cells to respond to the presence of analyte was more as a factor of polycationic component in the assembly of LbL shells. Cationic silk polyelectrolytes and subsequently electrostatically-driven assembly of silk shells played a major role in nominal production of GFP signal as the cells had to recover first from transient destruction in the cell membrane caused by binding of polylysine chains in silk fibroin ionomers to the cell membrane. The recovery of bacterial cells is much higher compared to any eukaryotic cells and probably why the activity of cells (intensities of GFP fluorescence) is significant after only one hour of exposure to theophylline. On the other hand, minor inclusions of polycationic components of small molecular weight can promote stability of LbL shells and restrict the cell growth and binary division. Hence, by tailoring the extend of charge density of polycations, the grafting density and the structure of copolymers with PEG side chains we can engineer the proper cytocompatible cell coatings with properties mandated by the application field.

8 CHAPTER

FABRICATION OF CELL ARRAYS EMBEDDED IN MULTILAYERED SILK HYDROGELS USING INKJET-PRINTING TECHNIQUE

8.1 Introduction

LbL fabrication represents one of the approaches for assembling and engineering complex 3D constructs in the field of bioengineering applications. Commercial and modified inkjet printer systems demonstrated that various biomolecules can be deposited onto target substrates with little or no reduction of their bioactivity. DNA and other oligonucleotides biochips, enzyme patterns, protein and antigen arrays can be generated using commercially available thermal inkjet printers.[315,316,317] Originally, started from simple printing of very robust microbial cells, the concept of delivering viable cells to the exact positions was extended to more sensitive mammalian cells that retain their viability and full ability to function throughout the printing process.[318,319,320,321] Later, envisioned by ability of inkjet printers to carry multiple bioink cartridges, the simplified versions of living tissue analogs and tissue networks were constructed for tailor-made drug and chemical screening, drug efficacy, chemical and biological toxicological evaluations, regenerative medicine, and basic cell biology. Bioinks, such as natural and synthetic physical hydrogels, polymer/hydrogel precursors combined with living cells and natural protein solutions can be deposited first to form a scaffold followed by cell printing to form 3D constructs.[162,163,164,165,166,167,322] Recently, it has been demonstrated with piezo-electronic inkjet printing that hierarchical cell manipulation allows for the fabrication of heterogeneous 3D human micro-tissues controlled at the single-cell layer level.[323] Sequential printing of two the most common cell types in the liver (hepatocytes and endothelial cells) and two the most abundant extracellular matrix

proteins (fibronectin and gelatin) enabled formation of simplified 3D-liver structures that demonstrated functions similar to other 3D organ tissue constructs for high-throughput drug evaluations.[323]

Piezoelectric inkjet printing demonstrates feasibility to fabricate non-cell-based biosensors that works as colorimetric sensor strips based on inhibition of protein activity by several neurotoxins. Bioactive sensor was realized with immobilization of acetylcholinesterase (AChE) enzyme that was sandwiched between two biocompatible silica layers and deposited onto paper substrate using inkjet printing.[324] The sensor was able to identify paraoxon and aflatoxin with detection limit on nano-scale level even after storage for 2 months at 4 °C.

In this chapter, we address complex inkjet printed cell reporter systems. Using careful alignment of jets facilitated the formation of multilayered silk protein hydrogel pads to immobilize injected bacterial cells. These patterns were followed by sealing the cells with multilayered silk films to generate robust complexes that demonstrated biocompatibility for long-term cell preservation and rapid onset of bio-sensitivity for screening target analytes. The whole-cell multiplex arrays demonstrated a prototype of biosensor that has potential for high-throughput chemical/ pharmaceutical screening, environmental monitoring and food safety, among others.

8.2 Experimental details

Fabrication of cell-based biosensor arrays using a JetLab piezoelectric inkjet printer platform with detailed description on materials used and step-by-step procedure can be found in the Experimental section. Transgenic *E. coli* cells with two reporter systems GFPa1 and TurboRFP have been used to construct multiplexed cell arrays when bacterial cells sensitive

to the presence of theophylline (expressing GFPa1) and IPTG (expressing TurboRFP) have been printed in alternate rows in the middle of silk multilayered structures.

8.3 Results and discussion

8.3.1 Fabrication and stability of cell arrays embedded in silk multilayered pads

In cell-based sensor platforms, immobilization of non-adherent cells is of particular interest for sustained monitoring of perturbations in the environment either in lateral flow or dip probing approaches. The choice of biopolymer matrix for immobilization of cells is defined by cytocompatibility, long-term stability and compatibility with inkjet dispersing technique. Silk fibroin functionalized with poly-amino acids proved to be a cytocompatible platform, whose mechanical strength, porosity and biodegradability can be tailored. The excellent mechanical compatibility of silk fibroin protein network (Young's modulus, E=6.4 ± 1.2 MPa at pH 7) with the mechanical stiffness of cell envelope of several bacterial strains (Gram-negative, *E. coli*, E=3.0 ± 0.6 MPa[325], and Gram-positive, *B. subtilis*, E=30 MPa[326]), and slow biodegradability makes silk substrates usful for immobilization and long-term protection of bacterial cells. The requirement for fabrication of silk matrices prior to injection of *E. coli* cells was further confirmed in control experiments, when cells injected on glass substrates were spread and later washed away from the substrate after 20 minutes incubation in cell medium solution.

LbL approach was used to first print several bilayers (bl) of silk ionomer films as a cushioning matrix to alleviate mechanical stresses during printing of cells followed by injection bacterial cells and finally, sealing the cells with the same number of silk ionomer bilayers to construct silk-cells-silk sandwich structures (Figure 8.1). Stable multilayered silk

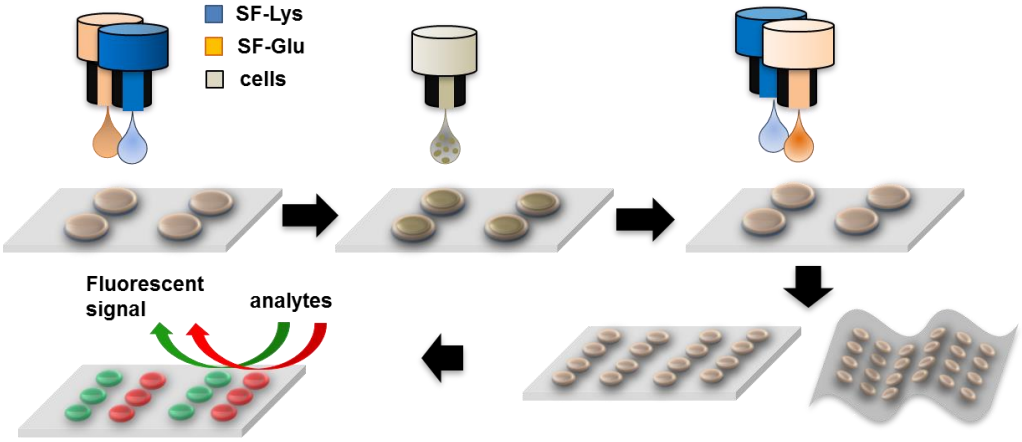

Figure 8.1 Schematics of formation of cell-based biosensor assemblies on hard and flexible substrates utilizing inkjet printer, and working principle of cells responding to the presence of target analytes in dual cell arrays.

ionomer films were constructed by sequential LbL injecting of positively-charged silk ionomer solution (SF-PL) followed by negatively-charged silk ionomer solution (SF-PG) comprising 1 bilayer structure $(SF\text{-}PL/SF\text{-}PG)_1$ with possibility to construct up to 5 bilayer silk substrates. [205,298] Due to strong charge-charge interactions between positively-charged and negatively-charged silk ionomers, the structures demonstrated robustness and shape stability even after incubation in cell medium for more than 24 hours. Stable multilayer stacks of silk ionomers were printed on two types of transparent substrates: hard - glass, and flexible – polyethylene terephthalate, (PET) without washing steps between the injected layers. By optimizing the concentration of injected solutions the quality of dots was improved and a complete and even layering of silk material was achieved. The average diameter of the printed dots was about 100 μm and these features sizes were significantly affected by the viscosity (concentration) of injectable solutions and the hydrophobicity of the substrate. The high quality of multilayered silk stacks was achieved with 1 mg/mL concentration of silk ionomer solutions dissolved in Na^+ phosphate buffer (pH 5.5) printed

on precoated polystyrene (PS) film (2 μm) or standard hydrophilic glass substrates (glass coverslips) to decrease de-wetting phenomena during the formation of the silk films.

Multilayer $(SF\text{-}PL/SF\text{-}PG)_5$ stacks 600 nm thick (measured as printed in the center) were optically transparent (Figures 8.2a). By injecting cell suspension of high concentration ($>5\times10^8$ cells/mL), even coverage of a high density cells (data) was achieved on silk pads that reduced the transparency of the silk arrays (Figure 8.2b). Reconstructed 3D atomic force microscopic image of a typical $(SF\text{-}PL/SF\text{-}PG)_5$ silk pad revealed a concave profile of a circular shaped dot of about 100 μm in size with a deep depression in the center (600±100 nm) and elevated edges (1,000±130 nm), useful as cup-like structure for depositing and holding the cells (Figure 8.2c). Based on the thickness of the SF-Lys/SF-Glu bilayers from

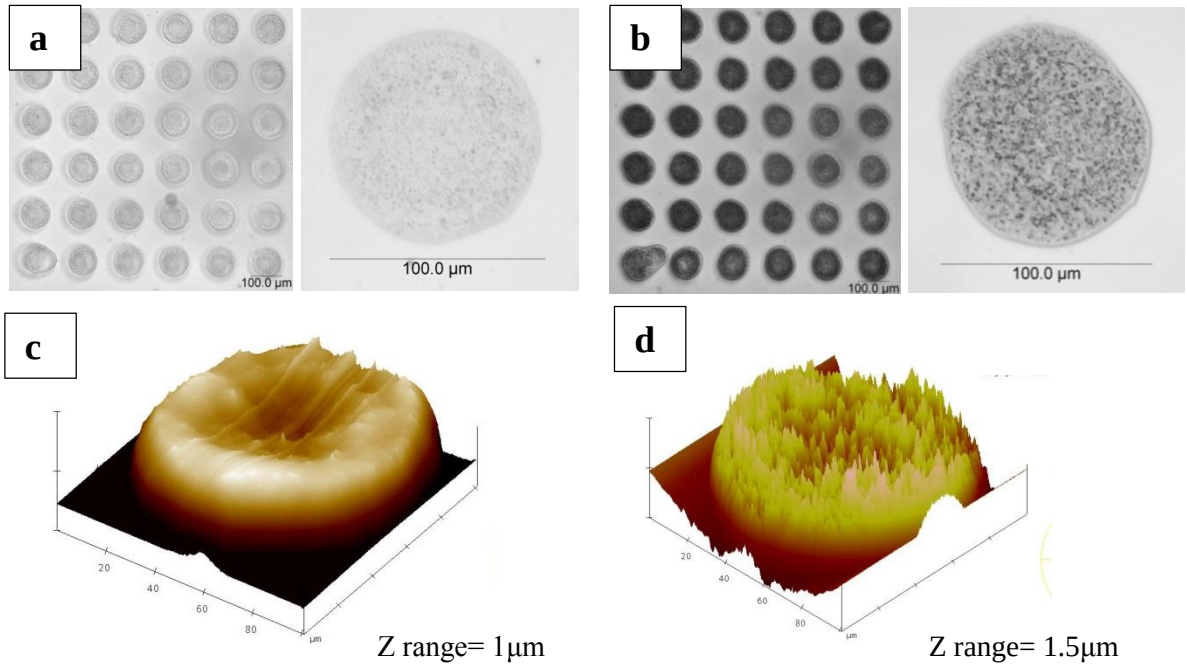

Figure 8.2 Optical images of $(SF\text{-}PL/SF\text{-}PG)_5$ dot arrays before deposition of cells as a large view area and a single dot (a). Optical images of sandwich arrays of $(SF\text{-}PL/SF\text{-}PG)_3$-*E coli* cells-$(SF\text{-}PL/SF\text{-}PG)_3$ constructs where cells have been injected in the middle of multilayers (b). 3D AFM images of a typical $(SF\text{-}PL/SF\text{-}PG)_3$ dot (c) and $(SF\text{-}PL/SF\text{-}PG)_3$-cells-$(SF\text{-}PL/SF\text{-}PG)_3$ sandwich structure (d).

our previous research, where on average each bilayer was estimated to be 53±10 nm (after release of unbound silk material during incubation in cell medium), we chose to encapsulate cells in 3 bilayer sandwich systems that allowed for the construction of robust protective matrices while also providing fast diffusion of target analyte molecules through 150 nm film.

Figures 8.2c,d represent reconstructed 3D images of a typical multilayered stack with *E. coli* cells immobilized in the middle layer of 3 bl – cells – 3 bl sandwich system and analyzed by AFM and confocal software, respectively. According to both images, printed constructs retained concave shape with the height of the matrix reaching 2 μm at the edges and 1.5 μm in the center. AFM imaging confirmed the uniform seeding of bacterial cells throughout the surface of the sandwich structure once the cells were injected from the nozzle (Figure 8.3). The thickness of the 1 bl – cells — 1 bl sandwich structure was 785 ± 110 nm and the surface

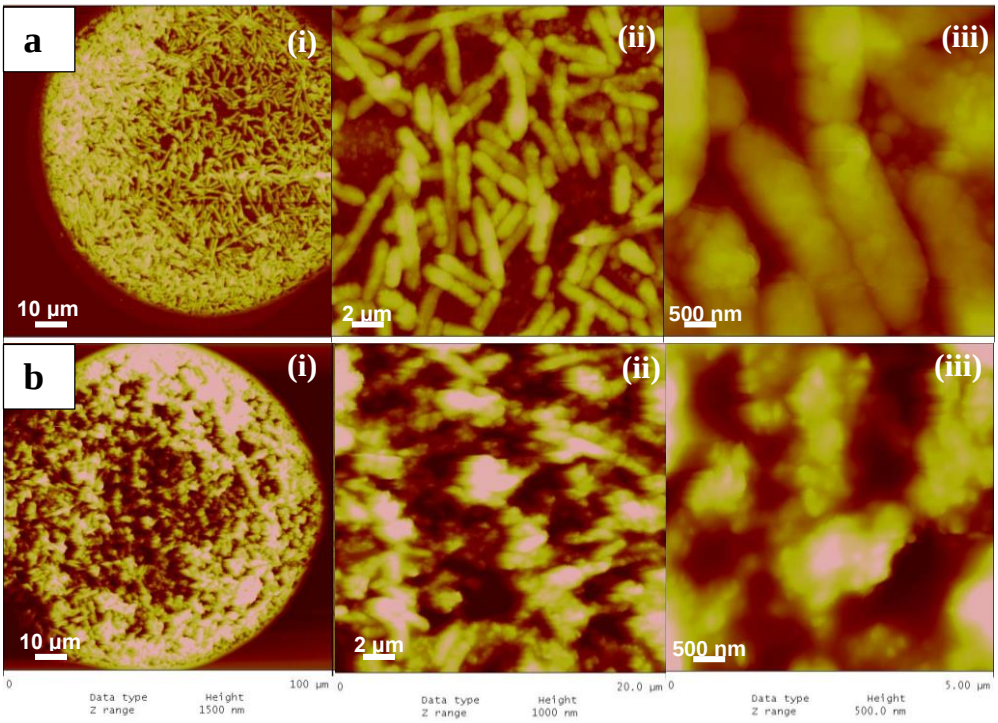

Figure 8.3 AFM images of encapsulated *E. coli* in $(SF\text{-}PL/SF\text{-}PG)_1$ (a) and $(SF\text{-}PL/SF\text{-}PG)_3$ (b) multilayered stacks. Z-scale: 1.5 μm in (i), 1 μm in (ii) and 0.5 μm in (iii).

roughness of was 234 ± 70 nm, measured after printing (before incubation in cell medium) (Figure 8.3a). By injecting more layers on the top of the cells, the topography defined by the rod shape of bacterial cells become less pronounced suggesting complete sealing of cells (Figure 8.3b). Accordingly, the thickness of the 3 bl –cells–3 bl sandwich system increased to 1124 ± 200 nm and the surface roughness remained on the same scale (232 ± 60 nm), suggesting that the morphology coarseness of the multilayered sandwich structure was defined mainly by the presence of cells.

The stability of silk multilayered sandwich structures was assessed by incubation in synthetic minimal medium (SMM). Figures 8.4a-c represent AFM images of a typical (SF-PL/SF-PG)$_3$-cells-(SF-PL/SF-PG)$_3$ sandwich structure in the dry state before (a) and after incubation in SMM media at 37°C for 30 minutes (b) and 14 hours (c), and Figure 8.4d reflects changes of thickness as a function of incubation time. The multilayered structures demonstrated the robustness of the ionomeric silk network, as the shape of the circular

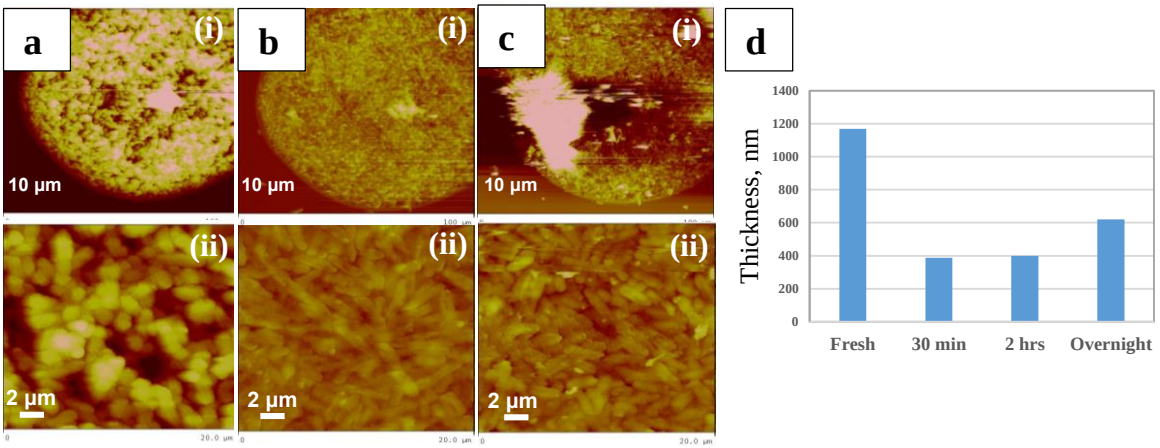

Figure 8.4 Stability of (SF-PL/SF-PG)$_3$-*E.coli*-(SF-PL/SF-PG)$_3$ sandwich structure during incubation in SMM cell medium for 0 min (a), 30 min (b) and 14 hours (c). Thickness of the structure with respect to the incubation time (d). Z-scale: 1.5 µm in (i), 1 µm in (ii).

multilayered structures was unchanged and the cell density appeared to be constant (Figures 8.4a-c). At the same time, the thickness of the structures decreased significantly from initial 1100 nm to 380 nm (after 30 minutes incubation time) and remained at the same level for the first 2 hours of incubation time, however increased by 50% to 620 nm after 18 hours. The initial drop in thickness was associated with the release of unbound protein molecules from the multilayered stacks as the result of elimination of intermediate rinsing steps. At the same time, the cell density was not affected by the removal of excess components, as it appeared that the number of cells had not significantly changed.

Stoichiometrically-equal in charged groups silk poly-ionomers were assembled through strong cooperative electrostatic interactions as the pH of the ionomers solutions was set apart from the isoelectric points so that proteins were sufficiently charged under the experimental conditions. Moreover, ionically-paired multilayered silk protein stacks behaved as hydrogel networks, increasing in thickness and demonstrating swelling up to 50% after incubation in cell medium for 18 hours, which accommodated successful cell proliferation. Limited intermixing of silk protein derivatives during inkjet-assisted LbL assembly occurred as a result of fast radial solvent evaporation and small volume solvent casting, yielding the formation of complex structures of loops and folds in addition to tertiary and quaternary structures of ionomeric proteins. After removal of unbound macromolecules that provided free volume for swelling, the resulted cross-linked silk networks were stable enough in low-ionic-strength media due to cooperative interactions of loops and entanglements between layered proteins. Additionally, the cells deposited in the middle behave as crosslinks to provide stability to multilayers during swelling in cell medium.

8.3.2 Biocompatibility of inkjet printing technique for fabrication of cell-based sensors

Viability of *E. coli* cells was assessed immediately after printing in order to check the feasibility of inkjet-assisted printing for cell-based sensors. Figures 8.5a and 8.5b demonstrate Live/Dead staining of *E. coli* printed directly on glass substrate (control sample) and in the middle of 6 bl silk structures (3 bl-cells-3 bl sample), respectively. Green fluorescent images represent viable cells as cell-permeable green dye penetrates all cells, and red fluorescent images represent potentially dead cells as otherwise non-permeable red dye breaches only cells with damaged cell wall/membrane. According to the staining results, after injection, cells appeared to be damaged as indicated by the presence of red fluorescent dye that matched the position of green-labeled cells. Even ejection of the cells in silk pads designed to alleviate mechanical stresses associated with jet printing did not aid in reducing the impact of the physical forces. Cells experienced strong shear stresses during injection through the nozzle and pressure during deposition on the substrate. Analysis of the cell suspension droplet showed that the droplets having diameter of 52 μm and volume of 70 pL were injected at a speed of 2-3 m/s, which corresponded to the shear stresses up to 300 kPa (or 3 atm). Apparently, mechanical stiffness of bacterial envelope (3 MPa) was enough to withstand the shear forces through the jet nozzle, however was not sufficient to bear the physical stresses at the impact with the substrate.[327] Additionally, cells can be susceptible to transient piezo actuation (1 kHz) during ejection that can be critical to cell wall integrity.[328] Propidium iodide, red fluorescent dye, which has a hydrodynamic radius of 16 Å and normally is non-cell-permeable, however diffused through the cell walls of Gram-negative bacteria in all injected cells, suggesting formation of nano-pores during either deposition of the cells or landing on the substrate. As was experimentally and theoretically

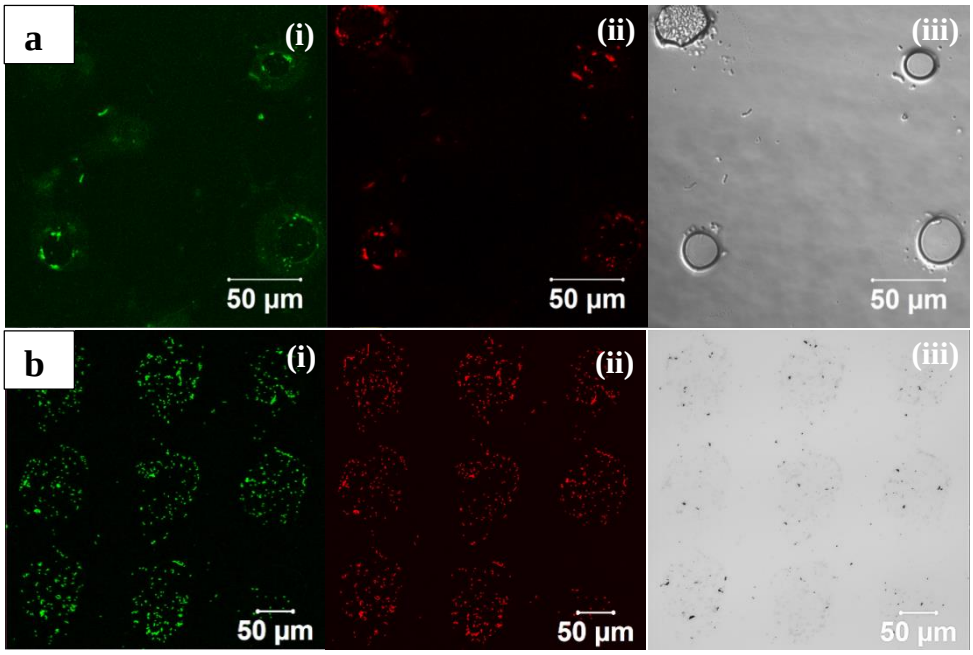

Figure 8.5 Live/Dead staining of *E.coli* cells injected on PS-coated glass substrate (control sample) (a) and *E. coli* cells sandwiched in $(SF\text{-}PL/SF\text{-}PG)_3$-cells-$(SF\text{-}PL/SF\text{-}PG)_3$ stacks (b). (i- live staining, ii- dead staining, iii- transmittance image).

analyzed in Gram-positive bacteria, formation of nanoholes in cell walls can be critical to the homeostasis of cells when the pore sizes exceeded 15-24 nm range.[329] Below that range and under certain conditions, however, bacteria may be able to recover and repair small pores in cell walls. Obviously, *E. coli* cells employed in our study had a chance to recover during incubation in cell culture medium as per stimulation with analyte molecules cells were able to respond by producing fluorescent protein in continuous manner, which is discussed below.

8.3.3 Activation of cells with target analyte after short-term and long-term storage

The ability of the cells to respond to a specific analyte is based on the engineered genetic modular signaling and sensing circuits, namely, riboswitch. Riboswitch (RS) is a cellular construct composed of an aptamer and expression platform domains. The latter controls the expression of a downstream gene via conformational changes that are induced by a ligand

binding to the aptamer domain. When riboswitch is coupled with fluorescent reporter gene, the recognition of analyte can be monitored by optical colorimetric read-out assay method: detection and quantification of fluorescence signal and its intensity, which are corresponding to the sensitivity and concentration of the molecule of interest. The advantage of exploiting cells over the traditional sensors is their innate ability to bind the analytes with exceptional specificity and sensitivity and to report this binding via internal amplification mechanism. The cells exploited in our study were transformed with theophylline responsive riboswitch coupled with GFPa1 and TurboRFP genes.[207]

The capability of cells to react on the presence of target analyte and how fast a RS can be activated after short-term (2 days, at 4°C) and long-term storage (2-3 months at 4°C) was checked with confocal microscopy. Figure 8.6a represents snap shots at different time points of the kinetics of RS activation in 3 bl sandwich systems after short-term storage. Fluorescence has been observed after 30 min of incubation in a medium supplemented with theophylline (target analyte) at different concentrations (2.5 mM and 5 mM, 0.05M NaH_2PO_4, pH 5). Cells were able to fully activate RS and express GFP within 2 hours. Moreover, when left in the medium for 24 hours, the silk protein multisystems behaved as hydrogel matrix. Over the time, soaked in water-based cell medium, the silk matrix became progressively swelled, and promoted active cell proliferation, as demonstrated by increased number of cells, and hence increased fluorescence signal generated by cells collectively. The ability of silk protein ionomers assembled in multilayer pads to swell, support full activity of bacterial cells and promote cell proliferation make them proper biocompatible substrates for the construction of cell-based biosensors.

Long-term storage of cells embedded in silk structures demonstrated full capability of cells to respond to the presence of analyte with comparable to short-term storage intensities and onset of RS activation. After storage for up to 3 months, cells were easily revived and demonstrated detectable level of GFP signal within 1 hour and a maximum intensity of GFP fluorescence after 2 hours of incubation in the medium supplemented with target analyte

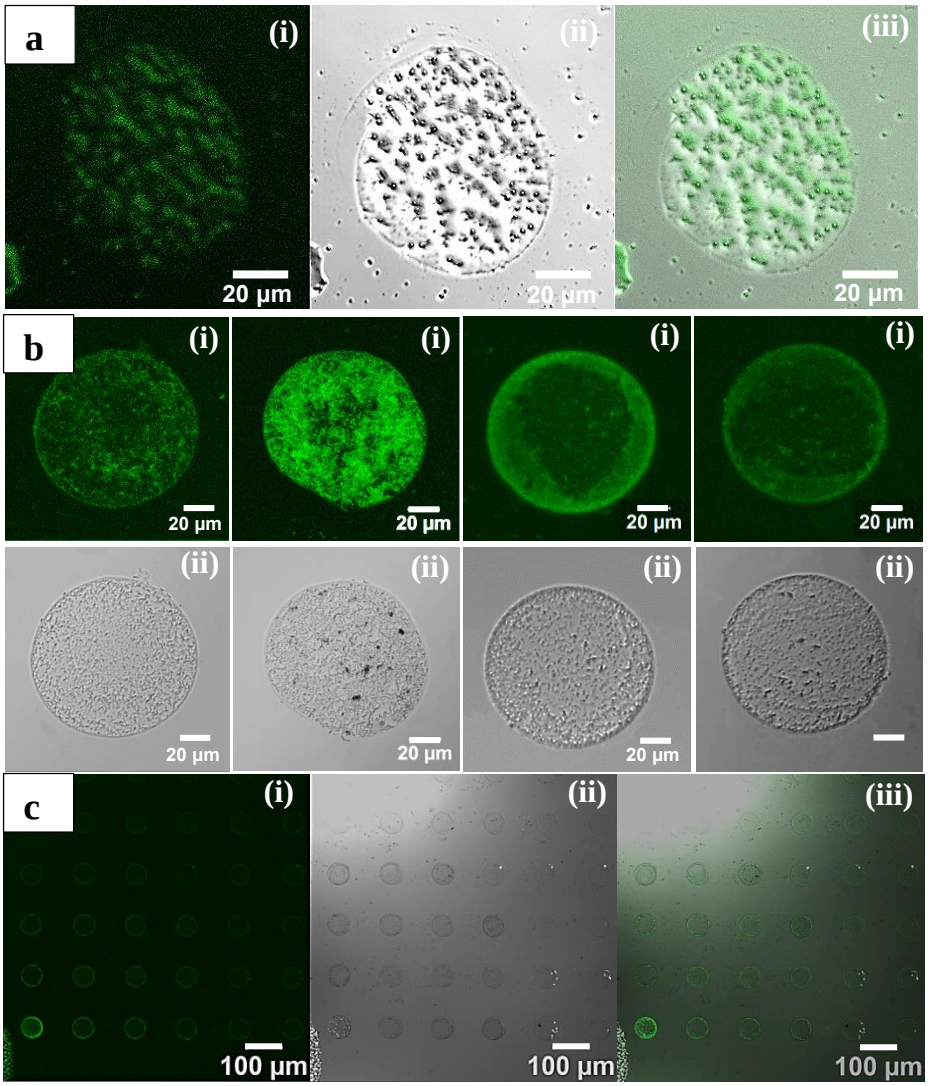

Figure 8.6 Activation of RS-GFP construct in *E. coli* cells with target analyte after short (a) and long-term storage (b,c). Confocal images have been collected from individual pads (a, b) and array of sandwich structures (c). Capturing has been performed at 1 hour, 2 hour, 3 hour and 5 hour time points during incubation (b). Large scale view represents RS activation at 3 hour time point (c). Legend: i- GFP/FITC band pass filter, ii- transmittance image, iii- overlapped image.

(Figure 8.6b). This data suggest that cells immobilized in silk matrix even for long time were capable to function and respond to the presence of analyte. Fast identification of analytes (within an hour) can be specifically beneficial for field applications when prolonged shelf-life storage is required. Linear relationship was observed for the fluorescence signal as a function of theophylline concentration, suggesting higher diffusion rates with increased concentration of analyte molecules (Figure 8.6d).

8.3.4 Fabrication of dual cell arrays

The ability of cells to specifically detect a molecule of interest out of the mixture of different chemical cues makes the cell multiplexing is an efficient tool for screening several potentially hazardous chemicals in one pot. Multiplexed arrays of cells with two reporter elements capable to detect two different analytes were constructed by immobilizing *E. coli* cells in 3 bl sandwich structures printed in the rows in alternate fashion. Figure 8.7 represents time-resolved confocal images of cell arrays sensitive to detection of theophylline (RS coupled to GFPa1) and IPTG (RS coupled to TurdoRFP). Over the time, it shows the dynamics of fluorescence intensity for both types of cells with theophylline-sensitive cells (RS-GFPa1) having a bright intensity maxima within the first two hours of incubation, and IPTG-sensitive cells (RS-TurboRFP) within 0.5-1 hours of incubation. The apparent shift was due to the subcloning in different vectors within RS construct and distinct fluorescent properties for GFP and TurboRFP proteins. With respect to the analyte concentrations, fluorescence intensities demonstrated linear relationship and time-delayed shift in fluorescence maxima suggesting slower intracellular transport kinetics with lower concentration gradients.

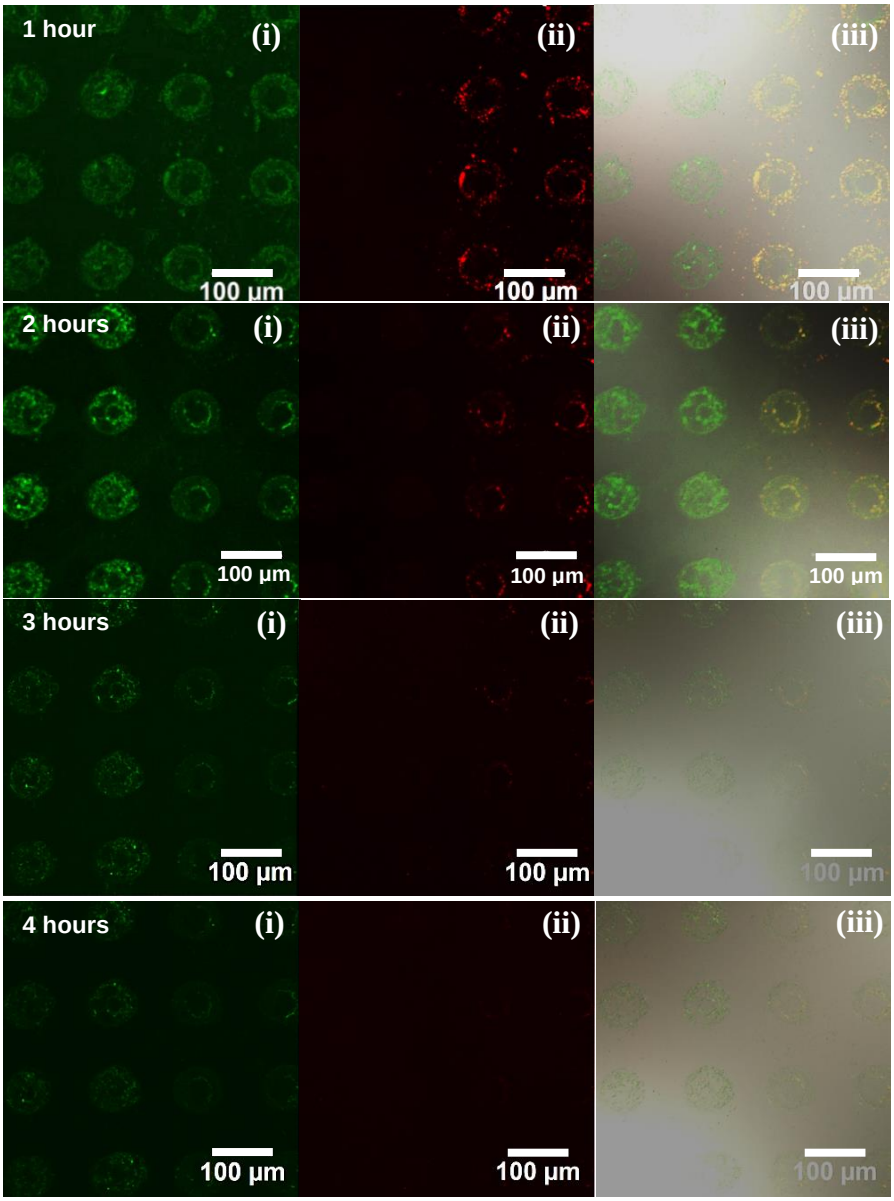

Figure 8.7 Confocal images representing kinetics of RS activation for two types of *E. coli* cells sensitive to theophylline (expressing GFPa1) and IPTG (expressing TurboRFP). Legend: i – GFP/FITC band pass filter, ii – Rhodamine/CY3 band filter, iii- transmittance image overlapped with i and ii.

Overall, fabrication of multiplexed arrays where immobilization of *E. coli* cells in silk protein hydrogels was performed utilizing piezoelectric inkjet printing platform demonstrated feasibility to construct analyte-specific cell-based biosensors.

9 CHAPTER

GENERAL CONCLUSIONS AND BROADER IMPACT

9.1 General conclusions and discussion

To generate biocompatible artificial shells during surface-assembling of molecules on cells involves the interdisciplinary technologies from chemistry, biology and materials science. Particularly, the design criteria for fabrication of cytocompatible cell coatings relies on the understanding of chemical interactions involved during the adsorption of macromolecules at the cell surface. It is critically important for the fabrication of robust protective shells to mimic the function, morphology and composition of cell membrane surfaces in order to retain cell's essential functions. Chemical functionalization of cells through specific interactions demand specialized recognition features that may confer intracellular properties incompatible with normal function of cells, hence more cytocompatible methods have to be explored. Amongst non-covalent interactions, assembly of artificial shells through hydrogen-bonding between hydrogen-acceptor and hydrogen-donor species, and through hydrophobic interactions are most promising. The advantage of having these interactions as opposed to electrostatic attractions in polyelectrolyte shells is that the cytotoxicity is directly proportional to the charge density of polycations, as well as concentration and time exposure. Hence, design and synthesis of the suitable artificial shells with high cytocompatibility should be addressed for cellular shellization specifically for biosensing applications. In this view, two types of artificial shells have been proposed in this study:

1) A detailed analysis of *synthetic coatings* based on a polyphenol component as a key element in constructing robust cytocompatible shells with antioxidant properties and tailored mechanical and transport properties to control function of encapsulated cells. Additionally,

in-depth study of *pH-sensitive synthetic shells* have been explored based on lightly cross-linked amine-functionalized polymethacrylic acid as pH-responsive specie that actively controlled cells function in response to environmental changes in pH.

2) Formation of *natural shells* based on silk fibroin proteins, both *pure* and *functionalized with polyamino acids and PEGs* to increase the robustness of protective shells and retain their cytocompatibility have been extensively studied in order to construct multilayered substrate assemblies during inkjet printing capable to protect bio-sensing cell function.

   A pioneering work on the formation of hydrogen bonded LbL shells assembled on microbial cell surfaces has been conducted in this work. *The study demonstrated the importance of avoiding cationic component, as a toxic element, in construction of nanothin shells with permeability and mechanical properties more akin to the cell membrane*. The viability studies confirmed that cytotoxicity resulted in over 80% of cell death for three bilayers of traditional PAH/PSS polyelectrolyte shells, while the same number of true hydrogen-bonded bilayers causes only 4% reduction in viability. Comparison of the diffusion coefficient for tannic acid/neutral polymer structure shell with commonly used polyelectrolyte shells showed a much higher (up to five times) values with highly grainy topography structure, which is a characteristic feature of hydrogen bonding shells.

   Most importantly, the new coating has very little effect on the sensing functionality of the cells, in which the fluorescence from GFP is increased dramatically by the introduction of galactose, whereas PAH/PSS layers cause almost complete suppression of it. Depending on the thickness of the shell, their chemical composition, and the nature of interactions within the shell, the protective shell can delay cell growth to varying degrees but does not suppress

the cell division. In fact, the cell proliferation eventually results in the budding cells rapturing the surrounding polymer shell.

In the next study of engineering pH-sensitive LbL shells assembled at cell surfaces through hydrogen-bonding between protonated states of carboxyl groups from PMAA-co-NH_2 and carbonyl groups from neutral polymer we designed biocompatible coatings with active functional properties. The advantage of assembling ultrathin hydrogel shells is their highly permeable network state, which is controlled by the crosslinking density and pH-responsive behavior. *It was found that low fraction of amine groups (17%) and low cross-linking degree facilitated formation of cytocompatible hydrogel shells with a high responsive behavior*. Yeast cells (engineered to express GFP) encapsulated in such pH-responsive synthetic nanoshells demonstrated high viability rate of around 90% indicating high bio-compatibility of synthetic shells capable of permeating nutrients and waste into and out of cells through the porous shells. Such high survivability level of encapsulated cells was also attributed to the high compliance of the porous hydrogel shells and very minor content of a cationic component.

The key discovery of this work was that cell function could be mediated by the shell pH responsive physical properties, in which by keeping encapsulated cells above the pKa of the hydrogel system, the budding and replication cycle were effectively delayed by about 24 hours as compared to encapsulated cells kept below pKa. Such a strong effect of the presence of (PMAA-*co*-NH_2) shells on the functionality of encapsulated cells at neutral pH was associated with pH-triggered changes in the state of unbound free carboxylate groups. Deprotonation of carboxylic groups above pH 5 increased the degree of ionization and resulted in the higher net negative charge for the surface potential, which lead to doubled

thickness of the shell wall. As a result of negative surface charge and increased shell thickness the transport of nutrients (amino acids, ions) was efficiently reduced thus damping the replication process. At the same time, biosensing activity of encapsulated cells was not reduced. *Cells kept in swollen-state shells had the same level of GFP intensity as was observed for the cells in the shrunken-state shells*. In this sense, pH-sensitive hydrogel shells behaved as active ultrathin barrier that can control the transport of charged molecules and ultimately the growth of encapsulated cells.

Next, the study conducted on the formation of *natural protective coatings* from silk fibroin demonstrated that cytocompatible conditions to efficiently promote adsorption of macromolecules can be carried out by salting-out in a mild concentration mixture of phosphate buffers complemented with shear-thinning effect. *Specifically, ionic treatment (0.03 M) with potassium phosphate buffer allowed stabilization of the silk fibroin protein structure without compromising the cell function/activity.* Fast response of encapsulated cells with an immediate activation and synthesis of yEGFP protein by the inducer molecules demonstrated cytocompatible conditions during silk shells assembly. *The key discovery is that high viability rate (up to 97%) of "silked" cells was achieved due to highly porous and ultrathin silk nanoshell structure, which is rarely achieved with synthetic polymer shells.* The ability of cells to bud (produce daughter cells) after the process of encapsulation was not affected with a short delay (by two hours or about 10% change) in reaching the maximum rate of log phase.

In contrast to synthetic polymer shells that shown to be slowly degraded extracellularly, silk fibroin protein coatings go through fast biodegradation intracellularly. The process of degradation begins shortly after cells reached mid of the log phase growth at the expense of

partial degradation of silk during exocytosis of waste products (mainly CO_2, and ethyl alcohol). Along with active extracellular enzymatic activity, cells might further promote digestion of silk protein shells through endocytosis of degraded protein fragments. Thus, nanothin silk coatings serve as short-term protection for encapsulated cells with full functionality and no trace of the initial shell. Hence, rapidly biodegradable silk coatings can be considered as efficient means to escape initial host immune defense during implantation/transplantation with preserved full activity of transplanted cells.

Engineering cell surfaces with natural polyelectrolytes based on silk fibroin protein can provide means to construct robust and cytocompatible coatings with distinct morphological appearance and controlled aggregation of cells-in-shells structures. We demonstrated that cytotoxicity of cell coatings was related to the charge density of polycations if shell assembly was carried through attractive forces of opposite charge in silk polyelectrolytes. The cells-in-shells assemblies showed reduced viability and functional capacity of bacterial cells along with distinct aggregation behavior of cells promoted by intermixing of proteins during LbL assembly. By grafting PEG side chains to silk backbone polycations the positive charges can be efficiently screen and hence significantly reduce the toxicity of silk coatings. *The key discovery in this work was that by switching interactions during shell assembly to hydrogen-bonding between highly PEGylated silk polycation ionomer and protonated silk polyanion ionomer the cytotoxicity of shells can be significantly decreased (only 5% reduction in viability from control). At the same time, capacity of cells to respond to the analyte detection can be protected, and distinct morphological appearance of individually-coated cells demonstrated strong colloidal stability of cell-in-shells suspensions with hydrogen-bonded LbL shells.*

Finally, based on the study of silk polyelectrolytes, we fabricated multiplexed cell-based biosensor arrays capable to detect several analytes. *The most critical finding in this study was that hydrogel matrix assembled through printing of silk ionomers served as an effective and robust substrate for immobilization and protection of cells, as well as a biocompatible hydrogel matrix that supported proliferation and function of cells in aqueous media.* Additionally, long-term storage of cells (up to 3 months) in the silk matrix did not affect ability of cells to sense and respond to the presence of analytes, and demonstrated rapid onset of activation of the riboswitch construct, and was comparable in the level of intensity to short-term cell storage. The whole-cell multiplex arrays demonstrated a possibility to fabricate a biosensor that specific for detection of several analytes, and hence has a potential for high-throughput chemical/pharmaceutical screening, environmental monitoring and food safety, among others.

The findings in this work related to fabrication strategies to obtain encapsulated cells with novel structures and functions, which can fulfill the requirements of new applications. Specifically, focus on the formation of the most biocompatible method for cellular shellization, cytocompatibility of materials involved in the designing of coatings as well as their high stability, mechanical resilience, blockage of cell cycle, prolong cell storage and ability to be surface-functionalized have been proposed and explored in this study. Prospective applications of this knowledge, as well as the perspectives of the further developments will be discussed in the following section.

9.2 Significance, broader impact and outlook

A range of cells, including bacteria, yeast, human normal and cancer cell lines, and microscopic species are intensively being used in sensing applications requiring surface

functionalization. Currently, a range of methods for endowing individual cells with microgels, polyelectrolyte coatings, hard shells, and other nanoparticle assemblies on their surfaces have been proposed, allowing such encapsulated cells to perform new functions, often very different from their original specialization. The application field usually drives the innovation criteria in the methods for cell functionalization and materials used as a way to promote specific interactions unattainable in non-encapsulated states. Here is the summary of several types of biomimetic shells with emphasis on their specific application.

Cell surface engineering with application of various cytocompatible protective and functional media dramatically increase cell viability and stability in synthetic environment and expand their applicability in biomedical, biotechnology, and bioelectronics fields. However, traditional inorganic and organic gel media do not readily support a number of modern applications because of very slow diffusion of nutrients or analytes into bulky and low porosity matrices. Individual cell encapsulation with bulky matrix is also challenging due to limitations in current fabrication methods. Slow biodegradation of these materials, high enzyme resistivity, low long term viability, slow response time, and questionable compatibility with microelectronic devices can be challenging. On the other hand, polymer and protein microgels and microbeads as media for cell entrapment has shown significant potential for cell therapy applications because of several factors related to downscaling of their dimensions.

Recently, formation of mineral shells and composite mineral-organic coatings through biomineralization process allowed to build biomimetic inorganic shells on individual living microbial cells. Among other properties, durability against harsh environments, controllability in cell cycles, long term storage and reactivity for cell-surface modification

that characterize the artificial hard shells encapsulating single living cells to form spore-like structure, called "artificial spores". Obviously, the studies involving encapsulation of simple eukaryotic cells cannot be applied to more gentle human cells due to restrict nature of hard shells. However, cells encapsulated with mineral shells show the potential for whole-cell biosensors applications, artificial spore fabrication.

Polyelectrolyte shells are a relatively new method for cellular encapsulation. Its potential has been shown in giving cells new properties, but the toxicity to many cells and specifically to mammalian cells is the major limitation on its use. Compared to polyelectrolyte shells, hydrogel shells that mimic extracellular matrix elements seem to be the most biocompatible method for cellular protection and now widely used in tissue engineering and regenerative medicine. Among other types of ultrathin shells, assembled via hydrogen-bonding from biocompatible synthetic polymers or natural materials hydrogen-bonded LbL shells can be considered as the best choice for a wide range of applications including tissue engineering, biosensing, cell-based therapies, regenerative medicine.

Based on the composition of ultrathin shells, several benefits attributed to the camouflaging shells on the outside. Protection from immune attack, oxidative damage, toxic shock, external harmful agents through active border defense have shown to be credited to ultrathin shells.[330] With a proper selection of chemical interactions, material composition and assembling conditions we can achieve dramatic increase in the viability of encapsulated cells and ultimately, increase in shells stability, mechanical robustness, and resistance to the external disturbances and aggressive environment. On the other hand, nanoscale thickness of these shells (well below 100 nm) and highly controlled permeability allow for rapid transport and exchange of external molecules, fast biodegradability, complied behavior, fast

cell release from the artificial shells at well-defined conditions associated with abrupt changes in physical properties. Hence, cells functionalized with these shells can find promising potential for biomedical applications, including cell implant protection, biosensors, cell therapy and tissue engineering.

Although the significant advances in the area of cell surface engineering have been witnessed, some challenges are still remaining. New fabrication strategies focused on encapsulated cells with novel structures and functions, which can fulfil the requirements of new applications, have to be pursued. Passive/non-selective mass transport across the artificial shell membrane, passive/non-selective adsorption and adhesion of functionalized cells, limited tunability of shell properties need specific attention for the future developments in cell-surface engineering. For the top-down approach, down-scalability of macro-encapsulation method still remains challenging that limits efficiency of implanted cells. With encapsulation of cells using bottom-up approach, innovative techniques focused on the reduction of materials use and increase of the yield of cells-in-shells assemblies have to be addressed in order to reduce cumbersome and costly processing conditions.

By introducing active biological and synthetic elements into shells such as active channels, tightly controlled pores, or by adding surface bioactive groups and recognition elements can facilitate cooperative effect in cells and adjacent regions. Importantly, symbiotic effect can be manifested by the shell material on not only functionalized cells, but also in the neighboring regions within the target organ/tissue. Shape supporting shells/films can be fabricated for 2D and 3D cells assemblies and multicellular clusters. By using advantage of self-assembly via non-specific interactions, encapsulated cells with complimentary

functionality can be heterogeneously deposited in porous, multilayered highly-organized structures to form tissue-like patches effective for tissue/organ regeneration.

Formation of actuating and reconfigurable shells, compartmentalization of encapsulated media, guided cell delivery through directed stimulation via external forces all should be considered for further exploration. Eventually, a path to assembling robust, sustainable, long-living, and functional artificial "cyborg cells", where external film-like or nanoparticulate coating deposited on living cells produces "cyborg" interface between the living human cells and non-living polymers/nanoparticles resulting in novel functionalities, which may significantly improve the use of "cyborg" cells in cell-based therapies.[331] Cell-mimicking and cell-replacing mesoscale structures can be thought and might be found in distant future beginning of a novel and emerging field of integrative nanoscience, biology and cell technology.

10 CHAPTER

DISSEMINATION OF WORK

This work has been conveyed to the scientific community by the following publications and presentations.

Publications

1. **Drachuk, I**.; Suntivich, R.; Calabrese, R.; Harbaugh, S.; Kelley-Loughnane, S.; Kaplan, D. L.; Stone, M.; Tsukruk, V. V. Inkjet printing of cell-based biosensor arrays, **2014** (in preparation).
2. **Drachuk, I**.; Calabrese, R.; Harbaugh, S.; Nancy Kelley-Loughnane, N.; Kaplan, D. L.; Stone, M.; Tsukruk, V. V. Ionomeric Silk Shells with Tailored Chemistry of Interactions as Means to Modulate Cell Function, **2014** (in preparation).
3. Suntivich, R.; **Drachuk, I**.; Calabrese, R.; Kaplan, D. L.; Tsukruk, V. V. Inkjet printing of silk nest arrays for cell hosting. *Biomacromolecules*, **2014**, DOI 10.1021/bm500027c.
4. **Drachuk, I,** Gupta, M. Tsukruk, V. V. Biomimetic Coatings to Control Cellular Function through Cell Surface Engineering., *Advanced Functional Materials* **2013**, *23*, 4437-4453.
5. **Drachuk, I.**; Shchepelina, O.; Harbaugh, S.; Kelley-Loughnane, N.; Stone, M.; Tsukruk, V. V. Cell Surface Engineering with Edible Protein Nanoshells. *Small* **2013**, *9*, 3128-3137.
6. Ye, C.; **Drachuk, I.**; Calabrese, R.; Dai, H.; Kaplan, D. L.; Tsukruk, V. V. Permeability and Micromechanical Properties of Silk Ionomer Microcapsules. *Langmuir* **2012**, *28*, 12235–12244.
7. **Drachuk, I.**; Shchepelina, O.; Lisunova, M.; Harbaugh, S.; Kelley-Loughnane, N.; Stone, M.; Tsukruk, V. V. pH-Responsive Layer-by-Layer Nanoshells for Direct Regulation of Cell Activity. *ACS Nano* **2012**, *6*, 4266–4278.
8. Ye, C.; Shchepelina, O.; Calabrese, R.; **Drachuk, I.**; Kaplan, D. L.; Tsukruk, V. V. Robust and Responsive Silk Ionomer Microcapsules. *Biomacromolecules* **2011**, *12*, 4319−4325.
9. Shchepelina, O.; **Drachuk, I.**; Gupta, M. K.; Lin, J.; Tsukruk, V. V. Silk-on-Silk Layer-by-Layer Microcapsules. *Adv. Mater*. **2011**, *23*, 4655–4660.
10. Lisunova, M. O.; **Drachuk, I.**; Shchepelina, O. A.; Anderson, K. D.; Tsukruk, V. V. Direct Probing of Micromechanical Properties of Hydrogen-Bonded Layer-by-Layer

Microcapsule Shells with Different Chemical Compositions. *Langmuir* **2011**, *27*, 11157–11165.

11. Carter, J. L.*; **Drachuk, I.***; Harbaugh, S.; Kelley-Loughnane, N.; Stone, M.; Tsukruk, V. V. Truly Nonionic Polymer Shells for the Encapsulation of Living Cells. *Macromol. Biosci.* **2011**, *11*, 1244–1253. * - *both authors contributed equally*.
12. Kozlovskaya, V.; Harbaugh, S.; **Drachuk, I.**; Shchepelina, O.; Nancy Kelley-Loughnane, N.; Stone, M.; Tsukruk, V. V. Hydrogen-bonded LbL Shells for Living Cell Surface Engineering. *Soft Matter*, **2011**, *7*, 2364-2372.
13. Kozlovskaya, V.; Kharlampieva,E.; **Drachuk, I.**; Cheng, D.; Tsukruk, V. V. Responsive microcapsule reactors based on hydrogen-bonded tannic acid layer-by-layer assemblies. *Soft Matter* **2010**, *6*, 3596–3608.

Presentations

1. **Drachuk, I**.; Harbaugh, S.; Kelley-Loughnane, N.; Stone, M.; Calabrese, R.; Kaplan, D. L.; Tsukruk, V. V. Layer-by-layer Approach for Individual Encapsulation of Cells Based on Hydrogen-bonded, Complimentary Electrostatic and Hydrophobic interactions, *ACS Spring Meeting 2014*, Dallas, TX (*Selected Oral presentation*).
2. **Drachuk, I**.; Suntivich, R.; Calabrese, R.; Harbaugh, S.; Kelley-Loughnane, N.; Kaplan, D. L.; Stone, M.; Tsukruk, V. V. Inkjet Assisted Encapsulation of Cell-Based Sensors in Silk Hydrogel Matrices, *ACS Spring Meeting 2014*, Dallas, TX (*Poster presentation*).
3. **Drachuk, I**.; Shchepelina, O.; Lisunova, M.; Harbaugh, S.; Kelley-Loughnane, N.; Stone, M.; Tsukruk, V. V. pH-Responsive Layer-by-Layer Nanoshells for Direct Regulation of Cell Activity, *ACS Spring Meeting 2014*, Dallas, TX (*Poster presentation*).
4. **Drachuk, I**.; Shchepelina, O.; Harbaugh, S.; Kelley-Loughnane, S.; Stone, M.; Tsukruk, V. V. Cell Surface Engineering with Silk Protein Nanoshells, *ACS Spring Meeting 2014*, Dallas, TX (*Poster presentation*).
5. **Drachuk, I**.; Calabrese, R.; Harbaugh, S.; Kelley-Loughnane, N.; Kaplan, D. L.; Stone, M.; Tsukruk, V. V. Shells from Ionomer Silk Derivatives and Microbial Cells Response. *ACS Spring Meeting 2014*, Dallas, TX (*Oral presentation*).

6. **Drachuk, I.**; Shchepelina, O.; Lisunova, M.; Harbaugh, S.; Kelley-Loughnane, N.; Stone, M.; Tsukruk, V. V. pH-Responsive Layer-by-Layer Nanoshells for Direct Regulation of Cell Activity, *SAIC 2012,* Atlanta, GaTech (*Poster presentation*).
7. **Drachuk, I**.; Schepelina, O.; Lin, J.; Tsukruk, V. V. Anisotropic Janus Particles, *MRS Fall Meeting 2012*, Boston, MA (*Poster presentation*).
8. **Drachuk, I**.; Harbaugh, S.; Kelley-Loughnane, N.; Stone, M.; Calabrese, R c.; Kaplan D. L.; Tsukruk, V. V. Layer-by-layer Approach for Individual Encapsulation of Cells Based on Hydrogen-bonded, Complimentary Electrostatic and Hydrophobic Interactions, *MRS Fall Meeting, 2012*, Boston, MA (*Poster presentation*)
9. **Drachuk, I.**; Shchepelina, O.; Lisunova, M.; Harbaugh, S.; Kelley-Loughnane, N.; Stone, M.; Tsukruk, V. V. pH-Responsive Layer-by-Layer Nanoshells for Direct Regulation of Cell Activity, *MRS Fall Meeting, 2012*, Boston, MA (*Oral presentation*)
10. **Drachuk, I.;** Ye, C.; Calabrese, R.; Dai, H.; Kaplan, D. L.; Tsukruk, V. V. Tunable Permeability and Micromechanical Properties of Silk Ionomeric Microcapsules for Engineering Cell Surfaces, *MRS Fall Meeting, 2012,* Boston, MA (*Oral presentation*)
11. **Drachuk, I.**; Shchepelina, O.; Tsukruk, V. V. High Permeability and Diffusion Parameters of Hydrogen-Bonded Multilayer Capsules, *ACS Fall Meeting, 2011*, Denver, CO (*Poster presentation*).
12. **Drachuk, I.**; Harbaugh, S.; Carter, J.; Shchepelina, O.; Kelley-Loughane, N.; Stone, M.; Tsukruk, V. V. Non-ionic hydrogen-bonded LbL shells with improved biocompatibility for cell encapsulation. *ACS Fall Meeting, 2011*, Denver, CO (*Oral presentation*).
13. **Drachuk, I.**; Shchepelina, O.; Gupta, M. K.; Tsukruk, V. V. Biocompatible and biodegradable silk LbL microcapsules. *ACS Fall Meeting, 2011*, Denver, CO (*Poster presentation*).

Awards

- Finalist of NRC Research Associateship Program, Air Force Research Laboratory **2014 Spring**
- American Chemical Society, *Excellence in Graduate Polymer Research*, Spring National Meeting, Dallas, TX, *Invited talk* **2014 Spring**
- *School of Materials Science and Engineering* (*MSE*), Georgia Institute of Technology, MSE Graduate Students Poster Competition, *1st Place in Biomaterials* **2013 Spring**
- *Science Applications International Corporation* (*SAIC*), Graduate Student Paper Competition, Georgia Institute of Technology, *First Finalist Award* **2012 Fall**
- *Air Force Center of Excellence* (CoE) on *Bio-nano-enabled Inorganic/Organic Nanostructures and Improved Cognition* (*BIONIC*) Scholarship, Georgia Institute of Technology and AFRL (Wright Patterson Air Force Base) **2011-2014**

REFERENCES

(1) Weibel, D. B.; DiLuzio, W. R.; Whitesides, G. M. *Nat. Rev. Microbiol.* **2007**, *5*, 209-218.
(2) Mann, S. in *Biomineralization: Principles and Concepts in Bioinorganic Materials Chemistry*, Oxford University Press, New York, NY, **2001**.
(3) Bar-Cohen, Y. in *Biomimetics: Biologically Inspired Technologies*, CRC Press, Boca Raton, FL **2006**, 2-40.
(4) Vasudev, M. C.; Anderson, K. D.; Tsukruk, V. V.; Bunning, T. J.; Naik, R. R. *ACS Appl. Mater. Interfaces* **2013**, *5*, 3983-3994.
(5) Ratner, B. D.; Bryant, S. J. *Annu. Rev. Biomed. Eng.* **2004**, *6*, 41-75.
(6) Pritchard, E. M.; Dennis, P. B.; Omenetto, F.; Naik, R. R.; Kaplan, D. L. *Biopolymers* **2012**, *97*, 479-498.
(7) Morin, S.A.; Shepherd, R. F.; Kwok, S. W.; Stokes, A. A.; Nemiroski, A.; Whitesides, G. M. *Science* **2012,** *337*, 828-832.
(8) Martinez, R. V.; Fish, C. R.; Chen, X.; Whitesides, G. M. *Adv. Funct. Mater.* **2012**, *22*, 1376-1384.
(9) Shepherd, R. F.; Ilievski, F.; Choi, W.; Morin, S. A.; Stokes, A. A.; Mazzeo, A. D.; Chen, X.; Wang, M.; Whitesides, G. M. *Proc. Natl. Acad. Sci. U.S.A.* **2011,** *108*, 20400-20403.
(10) Kreit, E.; Mathger, L. M.; Hanlon, R. T.; Dennis, P. B.; Naik, R. R.; Forsythe, E.; Heikenfeld, J. *J. R. Soc., Interface* **2013,** *10*, 20120601-20120613.
(11) Cui, Y.; Kim, S. N.; Naik, R. R.; Mcalpine, M. C. *Acc. Chem. Res.* **2012**, *45*, 696-704.
(12) McConney, M. E.; Anderson, K. D.; Brott, L. L.; Naik, R. R.; Tsukruk, V. V. *Adv. Funct. Mater.* **2009,** *19*, 2527-2544.
(13) Potyrailo, R. A.; Nagraj, N.; Surman, C.; Boudries, H.; Lai, H.; Slocik, J. M.; Kelley-Loughnane, N.; Naik, R. R. *Trends Anal. Chem.* **2012**, *40*, 133-145.
(14) Orozco, V. H.; Kozlovskaya, V.; López, B. L.; Tsukruk, V. V. *Polymer* **2010,** *51*, 4127-4139.
(15) Anderson, K. D.; Weber, R. B.; McConney, M. E.; Jiang, H.; Bunning, T. J.; Tsukruk, V. V. *Polymer* **2012,** *53*, 4686-4693.
(16) McConney, M. E.; Chen, N.; Lu, D.; Hu, H. A.; Coombs, S.; Liu, C.; Tsukruk, V. V. *Soft Matter* **2009,** *5*, 292-295.
(17) Peleshanko, S.; Julian, M. D.; Ornatska, M.; McConney, M. E.; LeMieux, M. C.; Chen, N.; Tucker, C.; Yang, Y.; Liu, C.; Humphrey, J. A. C.; Tsukruk, V. V. *Adv. Mater.* **2007,** *19*, 2903-2909.
(18) Tripathi, P.; Beaussart, A.; Andre, G.; Rolain, T.; Lebeer, S.; Vanderleyden, J.; Hols, P.; Dufrêne, Y. F. *Micron* **2012**, *43*, 1323-1330.
(19) Karp, G. in *Cell and Molecular Biology*, 4th ed., Wiley & Sons, Inc., Hoboken, NJ. **2005**, Ch. 4.
(20) Prescott, Harley, Klein's *Microbiology*, (Eds: J. M. Willey, L. M. Sherwood, C. J. Woolverton) 7th ed., McGraw-Hill, New York, NY, **2008**, Ch.3, 4.
(21) Kollar, R.; Reinhold, B. B.; Petrakova, E.; Yeh, H. J. C.; Ashwell, G.; Drgonova, J.; Kapteyn, J. C.; Klis, F. M.; Cabib, E. *J. Biol. Chem.* **1997**, *28*, 17762-17775.
(22) Lipke, P. N.; Ovalle, R. *J. Bacteriol.* **1998**, *15*, 3735-3740.
(23) Russel, A. D. *J. Antimicrob. Chemother.* **2003**, *52*, 750-763.
(24) Kloxin, A. M.; Klasko, A. M.; Salinas, C. N.; Anseth, K. S. *Science* **2009**, *324*, 59-63.
(25) Ricklin, D.; Hajishengallis, G.; Yang, K.; Lambris, J. D *Nat. Immunol.* **2010**, *11*, 785-797.
(26) Bae, K. H.; Yoon, J. J.; Park, T. G. *Biotechnol. Prog.* **2006**, *22*, 297-302.
(27) Yeh, J.; Ling, Y.; Karp, J. M.; Gantz, J.; Chandawarkar, A.; Eng, G.; Blumling III, J.; Langer, R.; Khademhosseini, A. *Biomaterials* **2006**, *27*, 5391-5398.
(28) Ghosh, K.; Shu, X. Z.; Li, B.; Sokolov, J. C.; Prestwich, G. D.; Clark, R. A. F.; Rafailovich, M. H. *Biomaterials* **2006**, *27*, 3782-3792.
(29) Koster, S.; Angile, F. E.; Duan, H.; Agresti, J. J.; Wintner, A.; Schmitz, C.; Rowat, A. C.; Merten, C. A.; Pisignano, D.; Griffiths, A. D.; Weitz, D. A. *Lab Chip* **2008**, *8*, 1110-1115.

(30) Shintaku, H.; Kuwabara, T.; Kawano, S.; Suzuki, T.; Kanno, I.; Kotera, H. *Microsyst. Technol.* **2007**, *13*, 951-958.
(31) Sefton, M. V.; May, M. H.; Lahooti, S.; Babensee, J. E. *J. Controlled Release* **2000**, *65*, 173-186.
(32) Avnir, D.; Braun, S.; Lev, O.; Ottololenghi, M. *Chem. Mater*. **1994**, *6*, 1605-1614.
(33) Carturan, G.; Dal Toso, R.; Boninsegna, S.; Dal Monte, R. *J. Mater. Chem*. **2004**, *14*, 2087-2098.
(34) Baca, H. K.; Ashley, C.; Carnes, E.; Lopez, D.; Flemming, J.; Dunphy, D.; Singh, S.; Chen, Z.; Liu, N.; Fan, H.; Lopez, G. P.; Brozik, S. M.; Werner-Washburne, M.; Brinker, C. J. *Science* **2006**, *313*, 337-341.
(35) Baca, H. K.; Carnes, E.; Singh, S.; Ashley, C.; Lopez, D.; Brinker, C. J. *Acc. Chem. Res.* **2007**, *40*, 836-845.
(36) Bhatia, R. B.; Brinker, C. J.; Gupta, A. K.; Singh, A. K. *Chem. Mater*. **2000**, *12*, 2434-2441.
(37) Badjic, J. D.; Kostic, N. M. *Chem. Mater*. **1999**, *11*, 3671-3679.
(38) Karlsson, M.; Martensson, L. G.; Jonsson, B. H.; Carlsson, U. *Langmuir* **2000**, *16*, 8470-8479.
(39) Inama, L.; Dire, S.; Carturan, G.; Cavazza, A. *J. Biotechnol*. **1993**, *30*, 197-210.
(40) Conroy, J. F. T.; Power, M. E.; Martin, J.; Earp, B.; Hosticka, B.; Daitch, C. E.; Norris, P. M. *J. Sol–Gel. Sci. Technol*. **2000**, *18*, 269-283.
(41) Coiffier, A.; Coradin, T.; Roux, C.; Bouvet, O. M. M.; Livage, J. *J. Mater. Chem*. **2001**, *11*, 2039-2044.
(42) Yu, D.; Volponi, J.; Chhabra, S.; Brinker, C. J.; Mulchandani, A.; Singh, A. K. *Biosens. Bioelectron.* **2005**, *20*, 1433-1437.
(43) Yang, S. H.; Ko, E. H.; Jung, Y. H.; Choi, I. S. *Angew. Chem. Int. Ed*. **2011**, *50*, 6115-6118.
(44) Coradin, T.; Livage, J. *J. Sol-Gel Sci. Technol*. **2003**, *26*, 1165-1168.
(45) Ren, L.; Tsuru, K.; Hayakawa, S.; Osaka, A. *J. Sol-Gel Sci. Technol*. **2001**, *21*, 115-121.
(46) Nasif, N.; Coiffier, A.; Coradin, T.; Roux, C.; Livage, J.; Bouvet, O. M. M. *J. Sol-Gel. Sci. Technol*. **2003**, *26*, 1141-1144.
(47) Ogasawara, W.; Shenton, W.; Davis, S. A.; Mann, S, *Chem. Mater*. **2000**, *12*, 2835-2837.
(48) Carnes, E. C.; Lopez, D. M.; Donegan, N. P.; Cheung, A.; Gresham, H.; Timmins, G. S.; Brinker, C. *Nat. Chem. Biology* **2009**, *6*, 41-45.
(49) Kaehr, B.; Townson, J. L.; Kalinich, R. M.; Awad, Y. H.; Swartzentruber, B. S.; Dunphy, D. R.; Brinker, C. J. *Proc. Natl. Acad. Sci. U. S. A.* **2012**, *109*, 17336-17341.
(50) Nassif, N.; Bouvet, O.; Rager, M. N.; Roux, C.; Coradin, T.; Livage, J. *Nat. Mater*. **2002**, *1*, 42-44.
(51) Nicodemus, G. D.; Bryant, S. J. *Tissue Eng., B* **2008**, *14*, 149-165.
(52) Wu, D.-Q.; Sun, Y.-X.; Xu, X.-D.; Cheng, S.-X.; Zhang, X.-Z.; Zhuo, R.-X. *Biomacromolecules* **2008,** *9*, 1155-1162.
(53) Stuart, M. C.; Huck, W.; Genzer, J.; Müller, M.; Ober, C.; Stamm, M.; Sukhorukov, G.; Szleifer, I.; Tsukruk, V. V.; Urban, M.; Winnik, F.; Zauscher, S.; Luzinov, I.; Minko, S. *Nat. Mater.* **2010,** *9*, 101-113.
(54) Williams, C. G.; Malik, A. N.; Kim, T. K.; Manson, P. N.; Elisseeff, J. H. *Biomaterials* **2005**, *26*, 1211-1218.
(55) Kretlow, J. D.; Mikos, A. G. *AIChE J*. **2008**, *54*, 3048-3067.
(56) Oh, J. K.; Drumright, R.; Siegwart, D. J.; Matyjaszewski, K. *Prog. Polym. Sci*. **2008**, *33*, 448-477.
(57) Hoffman, A. S. *Adv. Drug Delivery Rev.* **2013**, *65*, 10-16.
(58) Cushing, M. C.; Anseth, K. S. *Science* **2007**, *316*, 1133-1134.
(59) Nilsson, B.; Korsgren, O.; Lambris, J. D.; Ekdahl, K. N. *Trends Immunol.* **2009**, *31*, 32-38.
(60) Dang, T. T.; Bratlie, K. M.; Bogatyrev, S. R.; Chen, X. Y.; Langer, R.; Anderson, D. G. *Biomaterials* **2011**, *32*, 4464-4470.
(61) Toole, B. P. *Semin. Cell Dev. Biol.* **2001**, *12*, 79-87.
(62) Nuttelman, C. R.; Rice, M. A.; Rydholm, A. E.; Salinas, C. N.; Shah, D. N.; Anseth, K. S. *Prog. Polym. Sci*. **2008**, *33*, 167-179.
(63) Ratner, B.; Hoffnam, A.; Schoen, F.; Lemons, J. in *Biomaterials Science*, 2nd ed. Elsevier Academic Press, San Diego, **2004**.

(64) Mann, B. K.; Schmedlen, R. H.; West, J. L. *Biomaterials* **2001**, *22*, 439-444.
(65) Wang, X.; Heath, D. E.; Cooper, S. L. *J. Biomed. Mater. Res., A* **2012**, *100*, 794-801.
(66) Hubbell, J. A. *Curr. Opin. Biotechnol*. **1999**, *10*, 123-129.
(67) DeForest, C. A.; Anseth, K. S. *Nat. Chem*. **2011**, *3*, 925-931.
(68) Hutmacher, D.W. *J. Biomater. Sci. Polym. Ed*. **2001**, *12*, 107-124.
(69) Elisseeff, J.; McIntosh, W.; Anseth, K.; Riley, S.; Ragan, P.; Langer, R. *J. Biomed. Mater. Res.* **2000**, *51*, 164-171.
(70) Serp, D.; Cantana, E.; Heinzen, C.; Von Stockar, U.; Marison, I. W. *Biotechnol. Bioeng*. **2000**, *70*, 41-53.
(71) Lee, C. S.; Moyer, H. R.; Gittens I, R. A.; Williams, J. K.; Boskey, A. L.; Boyan, B. D.; Schwartz, Z. *Biomaterials* **2010**, *31*, 4926-4934.
(72) Moyer, H. R.; Kinney, R. C.; Singh, K. A.; Williams, J. K.; Schwartz, Z.; Boyan, B. D. *Ann. Plast. Surg.* **2010**, *65*, 497-503.
(73) Sugiura, S.; Oda, T.; Izumida, Y.; Aoyagi, Y.; Satake, M.; Ochiai, A.; Ohkohchi, N.; Nakajima, M. *Biomaterials* **2005**, *26*, 3327-3331.
(74) Tan, W.-H.; Takeuchi, S. *Adv. Mater*. **2007**, *19*, 2696-2701.
(75) Peirone, M.; Ross, C. J. D.; Hortelano, G.; Brash, J. L.; Chang, P. L. *J. Biomed. Mater. Res*. **1998**, *42*, 587-596.
(76) Burdick, J. A.; Prestwich, G. D. *Adv. Mater*. **2011**, *23*, H41-H56.
(77) Rohrich, R. J.; Sorokin, E. S.; Brown, S. A. *Plast. Reconstr Surg*. **2004**, *113*, 391-395.
(78) Kaufman, M. R.; Bradley, J. P.; Dickinson, B.; Heller, J. B.; Wasson, K.; O'Hara, C.; Huang, C.; Gabbay, J.; Ghadjar, K.; Miller, T. A. *Plast. Reconstr. Surg*. **2007**, *119*, 323-331.
(79) Bitar, M.; Salih, V.; Brown, R. A.; Nazhat, S. N. *J. Mater. Sci. Mater. Med.* **2007**, *18*, 237-244.
(80) Hansen, L. T.; Allan-Wojtas, P. M.; Jin, Y. L.; Paulson, A. T. *Food Microbiol.* **2002**, *19*, 35-45.
(81) Cui, J. H.; Goh, J. S.; Kim, P. H.; Choi, S. H.; Lee, B. J. *Int. J. Pharm.* **2000**, *210*, 51-59.
(82) Chan, E. S.; Zhang, Z. *Food Bioprod. Process.* **2002**, *80*, 78-82.
(83) Chandy, T.; Mooradian, D. L.; Rao, G. H. *Artif. Organs* **1999**, *23*, 894-903.
(84) Bratlie, K. M.; York, R. L.; Invernale, M. A.; Langer, R.; Anderson, D. G. *Adv. Healthcare Mater*. **2012**, *1*, 267-284.
(85) Hardikar, A. A.; Risbud, M. V.; Bhonde, R. R. *Transplant. Proc*. **2000**, *32*, 824-825.
(86) Haque, T.; Chen, H.; Ouyang, W.; Martoni, C.; Lawuyi, B.; Urbanska, A. M.; Prakash, S. *Biotechnol. Lett.* **2005**, *27*, 317-322.
(87) Anal, A. K.; Singh, H. *Trends Food Sci. Technol.* **2007**, *18*, 240-251.
(88) Foo, C. T. W. P.; Lee, J. S.; Mulyasasmita, W.; Parisi-Amon, A.; Heilshorn, S. C. *Proc. Natl. Acad. Sci. U. S. A.* **2009**, *106*, 22067-22072.
(89) Kong, H. J.; Kaigler, D.; Kim, K.; Mooney, D. J. *Biomacromolecules* **2004**, *5*, 1720-1727.
(90) Ashton, R. S.; Banerjee, A.; Punyani, S.; Schaffer, D. V.; Kane, R. S. *Biomaterials* **2007**, *28*, 5518-5525.
(91) Lee, K. Y.; Bouhadir, K. H.; Mooney, D. J. *Biomaterials* **2004**, *25*, 2461-2466.
(92) Leslie, S. *M.S. Thesis*, Georgia Institute of Technology, USA **2012**.
(93) Zhang, S.; Greenfield, M. A.; Mata, A.; Palmer, L. C.; Bitton, R.; Mantei, J. R.; Aparicio, C.; Cruz, M. O.; Stupp, S. I. *Nat. Mater*. **2010**, *9*, 594-601.
(94) Carvajal, D.; Bitton, R.; Mantei, J. R.; Velichko, Y. S.; Stupp, S. I.; Shull, K. R. *Soft Matter* **2010**, *6*, 1816-1823.
(95) Rozkiewicz, D. I.; Myers, B. D.; Stupp, S. I. *Angew. Chem. Int. Ed*. **2011**, *50*, 6324-6327.
(96) Takeuchi, S.; DiLuzio, W. R.; Weibel, D. B.; Whitesides, G. M. *Nano Lett.* **2005**, *5*, 1819-1823.
(97) Kaehr, B.; Shear, J. B. *J. Am. Chem. Soc*. **2007**, *129*, 1904-1905.
(98) Khripin, C. Y.; Brinker, C. J.; Kaehr, B. *Soft Matter* **2010**, *6*, 2842-2848.
(99) Heidebach, T.; Forst, P.; Kulozik, U. *Food Hydrocolloids* **2009**, *23*, 1670-1677.
(100) Chen, L.; Remondetto, G.; Rouabhia, M.; Subirade, M. *Biomaterials* **2008**, *29*, 3750-3756.
(101) Picot, A.; Lacroix, C. *Int. Dairy J.* **2004**, *14*, 505-515.

(102) Harper, J. C.; Brozik, S. M.; Brinker, C. J.; Kaehr, B. *Anal. Chem*. **2012**, *84*, 8985-8989.
(103) Wilson, J. T.; Cui, W.; Chaikof, E. L. *Nano Lett*. **2008**, *7*, 1940-1948.
(104) Decher, G.; Schelenoff, J. B. in *Multilayer Thin Films: Sequential Assembly of Nanocomposite Materials*, 2nd ed. (Eds: G. Decher and J. B. Schlenoff), Wiley-VCH Verlag GmbH & Co. KGaA, Weinheim, **2012.**
(105) Ruiz-Hitzky, E.; Ariga, K.; Lvov, Y. in *Bio-inorganic Hybrid Nanomaterials: Strategies, Syntheses, Characterization and Applications*, Weinheim: Wiley-VCH, **2008.**
(106) Jiang, C.; Tsukruk, V. V. *Adv. Mater.* **2006,** *18*, 829-840.
(107) Wilson, J. T.; Cui, W.; Kozlovskaya, V.; Kharlampieva, E.; Pan, D.; Qu, Z.; Krishnamurthy, V. R.; Mets, J.; Kumar, V.; Wen, J.; Song, Y.; Tsukruk, V. V.; Chaikof, E. L. *J. Am. Chem. Soc*. **2011**, *133*, 7054-7064.
(108) Veerabadran, N. G.; Goli, P. L.; Stewart-Clark, S. S.; Lvov, Y. M.; Mills, D. K. *Macromol. Biosci*. **2007**, *7*, 877-882.
(109) Hillberg, A. L.; Tabrizian, M. *Biomacromolecules* **2006**, *7*, 2742-2750.
(110) Mertz, D.; Vogt, C.; Hemmerle, J.; Mutterer, J.; Ball, V.; Voegel, J. C.; Schaaf, P.; Lavalle, P. *Nat. Mater*. **2009**, *8*, 731-735.
(111) Shutava, T. G.; Kommireddy, D. S.; Lvov, Y. M. *J. Am. Chem. Soc*. **2006**, *128*, 9926-9934.
(112) Liu, X. H.; Zhang, J. T.; Lynn, D. M. *Adv. Mater*. **2008**, *20*, 4148-4153.
(113) Dimitrova, M.; Affolter, C.; Meyer, F.; Nguyen, I.; Richard, D. G.; Schuster, C.; Bartenschlager, R.; Voegel, J. C.; Ogier, J.; Baumert, T. F. *Proc. Natl. Acad. Sci. U. S. A.* **2008**, *105*, 16320-16325.
(114) Michel, M.; Vautier, D.; Voegel, J. C.; Schaaf, P.; Ball, V. *Langmuir* **2004**, *20*, 4835-4839.
(115) Yoo, P. J.; Nam, K. T.; Qi, J. F.; Lee, S. K.; Park, J.; Belcher, A. M.; Hammond, P. T. *Nat. Mater*. **2006**, *5*, 234-240.
(116) Yang, S. H.; Kang, S. M.; Lee, K.-B.; Chung, T. D.; Lee, H.; Choi, I. S. *J. Am. Chem. Soc*. **2011**, *133*, 2795-2797.
(117) Hammond, P. T. *Adv. Mater*. **2004**, *16*, 1271-1293.
(118) Quinn, J. F.; Johnston, A. P. R.; Such, G. K.; Zelikin, A. N.; Caruso, F. *Chem. Soc. Rev*. **2007**, *36*, 707-718.
(119) Kinnane, C. R.; Such, G. K.; Antequera-Garcıa, G.; Yan, Y.; Dodds, S. J.; Liz-Marzan, L. M.; Caruso, F. *Biomacromolecules* **2009**, *10*, 2839-2846.
(120) Kozlovskaya, V.; Kharlampieva, E.; Erel, I.; Sukhishvili, S. A. *Soft Matter* **2009**, *5*, 4077-4087.
(121) Diaspro, A.; Silvano, D.; Krol, S.; Cavalleri, O.; Gliozzi, A. *Langmuir* **2002**, *18*, 5047-5050.
(122) Krol, S.; Nolte, M.; Diaspro, A.; Mazza, D.; Magrassi, R.; Gliozzi, A.; Fery, A. *Langmuir* **2005**, *21*, 705-709.
(123) Fakhrullin, R. F.; Zamaleeva, A. I.; Morozov, M. V.; Tazetdinova, D. I.; Alimova, F. K.; Hilmutdinov, A. K.; Zhdanov, R. I.; Kahraman, M.; Culha, M. *Langmuir* **2009**, *25*, 4628-4634.
(124) Fakhrullin, R. F.; Garcia-Alonso, J.; Paunov, V. N. *Soft Matter* **2010**, *6*, 391-397.
(125) Lewis, S. R.; Datta, S.; Gui, M.; Coker, E. L.; Huggins, F. E.; Daunert, S.; Bachas, L.; Bhattacharyya, D. *Proc. Natl. Acad. Sci. U. S. A.* **2011**, *21*, 8577-8582.
(126) Antipov, A. A.; Shchukin, D.; Fedutik, Y.; Zanaveskina, I.; Klechkovskaya, V.; Sukhorukov, G.; Mohwald, H. *Macromol. Rapid Commun*. **2003**, *24*, 274-277.
(127) Carter, J. L. Drachuk, I.; Harbaugh, S.; Kelley-Loughnane, N.; Stone, M.; Tsukruk, V. V. *Macromol. Biosci*. **2011**, *11*, 1244 –1253.
(128) Fakhrullin, R. F.; Zamaleeva, A. I.; Minullina, R. T.; Konnova, S. A.; Paunov, V. N. *Chem. Soc. Rev*. **2012**, *41*, 4189-4206.
(129) Gasch, A. P.; Werner-Washburne, M. *Funct. Integr. Genomics* **2002**, *2*, 181-192.
(130) Kulkarni, D.; Choi, I.; Singamaneni, S.; Tsukruk, V. V. *ACS Nano* **2010,** *8*, 4667-4676.
(131) Tang, Z.; Kotov, N. A.; Magonov, S.; Ozturk, B. *Nat. Mater.* **2003**, *2*, 413-418.
(132) Kharlampieva, E.; Kozlovskaya, V.; Wallet, B.; Shevchenko, V. V.; Naik, R. R.; Vaia, R.; Kaplan, D. L.; Tsukruk, V. V. *ACS Nano* **2010**, *4*, 7053-7063.
(133) Jiang, C.; Markutsya, S.; Pikus, Y.; Tsukruk, V. V. *Nat. Mater.* **2004,** *3*, 721-728.

(134) Kahraman, M.; Zamaleeva, A. I.; Fakhrullin, R. F.; Culha, M. *Anal. Bioanal. Chem*. **2009**, *395*, 2559-2567.
(135) Ai, H.; Fang, M.; Jones, S. A.; Lvov, Y. M. *Biomacromolecules* **2002**, *3*, 560-564.
(136) Yang, S. H.; Lee, K. B.; Kong, B.; Kim, J. H.; Kim, H. S.; Choi, I. S. *Angew. Chem. Int. Ed*. **2009**, *48*, 9160-9163.
(137) Wang, G.; Wang, L.; Liu, P.; Yan, Y.; Xu, X.; Tang, R.;*Chem. Bio. Chem.* **2010**, *11*, 2368-2373.
(138) Zamaleeva, A. I.; Sharipova, I. R.; Porfireva, A. V.; Evtugyn, G. A.; Fakhrullin, R. F. *Langmuir* **2009**, *26*, 2671-2679.
(139) Kempaiah, R.; Chung, A.; Maheshwari, V. *ACS Nano* **2011**, *5*, 6025-6031.
(140) Fakhrullin, R. F.; Shlykova, L. V.; Zamaleeva, A. I.; Nurgaliev, D. K.; Osin, Y. N.; García-Alonso, J.; Paunov, V. N. *Macromol. Biosci*. **2010**, *10*, 1257-1264.
(141) Xu, W.; Choi, I.; Plamper, F. A.; Synatschke, C. V.; Muller, A. H. E.; Tsukruk, V. V. *ACS Nano* **2012**, *7*, 598-613.
(142) Kodiyath, R.; Choi, I.; Patterson, B.; Tsitsilianis, C.; Tsukruk, V. V. *Polymer* **2013**, *54*, 1150-1159.
(143) Radtchenko, I. L.; Sukhorukov, G. B.; Leporatti, S.; Khomutov, G. B.; Donath, E.; Mohwald, H.; *J. Colloid Interface Sci*. **2000**, *230*, 272-280.
(144) Kharlampieva, E.; Kozlovskaya, V.; Sukhishvili, S. A. *Adv. Mater*. **2009**, *21*, 3053-3065.
(145) Kozlovskaya, V.; Kharlampieva, E.; Drachuk, I.; Cheng, D.; Tsukruk, V. V. *Soft Matter* **2010**, *6*, 3596-3608.
(146) Becker, A. L.; Zelikin, A. N.; Johnston, A. P. R.; Caruso, F. *Langmuir* **2009**, *25*, 14079-14085.
(147) Diehl, K. L.; Anslyn, E. V. *Chem. Soc. Rev*. **2013**, *42*, 8596-8611.
(148) Greenwood, D. P.; Jeys, T. H.; Johnson, B.; Richardson, J. M.; Shatz, M. P. *Proc. IEEE* **2009**, *97*, 971-989.
(149) Homola; J.; Yee; S. S.; Myszka, D. in *Optical Biosensors: Present and Future: Surface plasmon resonance biosensors* (Eds.: F. S. Ligler and C. A. R. Taitt), The Netherlands: Elsevier, Amsterdam, **2004**, ch. 7.
(150) Lequi, R. *Clin. Chem*. **2005**, *51*, 2415–2418,
(151) Van Weeman, B. K. *Clin. Chem*. **2005**, *51*, 2226-2226.
(152) Mackay, I. M. in *Real-Time PCR in Microbiology*. Portland, OR: Caister Academic, **2007**.
(153) Shelton, M. J.; Evans, S. P.; Smith, P. D.; Simpson, I. A.; Kaye, P. H.; Clarke, J. M. *Proc. SPIE* **2004**, *5617*, 284–291.
(154) Hurst, E.; Kaye, P. H.; Foot, V.; Clark, J. M.; Withers, P. B. *Proc. SPIE* **2004**, *5617*, 416–423.
(155) Cronquist, A. B.; Mody, R. K.; Atkinson, R.; Besser, J.; D'Angelo, M. T.; Hurd, S.; Robinson, T.; Nicholson, C.; Mahon, B. E. *Clin. Infect. Dis.* **2012**, *54*, S432-S439.
(156) Viveros, L.; Paliwal, S.; McCrae, D.; Wild, J.; Simonian, A. *Sens. Actuators, B* **2006**, B 115, 150–157.
(157) Ibrahim, H.K.R.; Helmi, S.; Lewis, J.; Crane, M. *Toxicol.* **1998**, *60*, 448–455.
(158) Ziegler, C. Fresenius *J. Anal. Chem.* **2000**, *366*, 552-559.
(159) Okamoto, T.; Suzuki, T.; Yamamoto, N. *Nat. Biotechnol*. **2000**, *18*, 438-441.
(160) Roda, A.; Guardigli, M.; Russo, C.; Pasini, P.; Baraldini, M. *Biotechniques* **2000**, *28*, 492-496.
(161) Roth, E. A.; Xu, T.; Das, M.; Gregory, C.; Hickman, J. J.; Boland, T. *Biomaterials* **2004**, *25*, 3707-3715.
(162) Cui, X.; Boland, T. *Biomaterials* **2009**, *30*, 6221–6227.
(163) Cui, X.; Breitenkamp, K.; Finn, M. G.; Martin Lotz, M.; D'Lima, D. D. *J. Tissue Eng., A*, **2012,** *18*, 1304-1312.
(164) Moon, S. ; Hasan, S. K.; Song, Y. S.; Xu, F.; Keles, H. O.; Manzur, F.; Mikkilineni, S.;Hong, J. W.; Nagatomi, J.; Haeggstrom, E.; Khademhosseini, A.; Demirci, U. *J. Tissue Eng., C* **2010**, *16*, 157-166.
(165) Ferris, C. J.; Gilmore, K. J.; Beirne, S.; McCallum, D.; Wallace, G. G.; Panhuis, M. *Biomater. Sci.* **2013**, *1*, 224-230.
(166) Lee, Y. B.; Polio, S.; Lee, W.; Dai, G.; Menon, L.; Carroll, R. S.; Yoo, S. S. *Exp. Neurol.* **2010**, *223*, 645-652.

(167) Arai, K.; Iwanaga,S.; Toda, H.; Genci, C.; Nishiyama, Y.; Nakamura, M. *Biofabrication*, **2011**, *3*, 1-7.
(168) Nakamura, M.; Iwanaga, S.; Henmi, C; Arai, K.; Nishiyama, Y. *Biofabrication* **2010**, *2*, 1-7.
(169) Elad, T.; Lee, J. H.; Belkin, S.; Gu, M. B. *Microb. Biotechnol.* **2008**, *1*, 137–148.
(170) Flickinger, M. C.; Schottel, J. L.; Bond, D. R.; Aksan, A.; Scriven, L. E. *Biotechnol. Prog.* **2007**, *23*, 2–17.
(171) Ivask, A.; Green, T.; Polyak, B.; Mor, A.; Kahru, A.; Virta, M.; Marks, R. *Biosens. Bioelectron.* **2007**, *22*, 1396–1402.
(172) Thirumalapura, N. R.; Ramachandran, A.; Morton, R. J.; Malayer, J. R. *J Immunol. Methods* **2006**, *309*, 48–54.
(173) Choi, W. S.; Ha, D.; Park, S.; Kim, T. *Biomaterials* **2011**, *32*, 2500-2507.
(174) Andres, C. M.; Kotov, N. A. *J. Am. Chem. Soc*. **2010**, *132*, 14496–14502.
(175) Kinnane, C. R.; Such, G. K.; Antequera-Garcıa, G.; Yan, Y.; Dodds, S. J.; Liz-Marzan, L. M.; Caruso, F. *Biomacromolecules* **2009**, *10*, 2839–2846.
(176) Radtchenko, I. L.; Sukhorukov, G. B.; Leporatti, S.; Khomutov, G. B.; Donath, E.; Mohwald, H. *J. Colloid Interface Sci*. **2000**, *230*, 272-280.
(177) Murthy, N.; Campbell, J.; Fausto, N.; Hoffman, A. S.; Stayton, P. S. *Bioconjugate Chem*. **2003**, *14*, 412–419.
(178) Gensel, J.; Borke, T.; Pérez, N. P.; Fery, A.; Andreeva, D. V.; Betthausen, E.; Müller, A. H. E.; Möhwald, H.; Skorb, E. V. *Adv. Mater*. **2012**, *24*, 985–989.
(179) Morin, S. A.; Shepherd, R. F.; Kwok, S. W.; Stokes, A. A.; Nemiroski, A.; Whitesides, G. M. *Science* **2012**, *337*, 828-832.
(180) Martinez, R. V.; Fish, C. R.; Chen, X.; Whitesides, G. M. *Adv. Funct. Mater*. **2012**, *22*, 1376-1384.
(181) Shepherd, R. F.; Ilievski, F.; Choi, W.; Morin, S. A.; Stokes, A. A.; Mazzeo, A. D.; Chen, X.; Wang, M.; Whitesides, G. M. *Proc. Natl. Acad. Sci. U. S. A*. **2011**, *108*, 20400-20403.
(182) Cui, Y.; Kim, S. N.; Naik, R. R.; McAlpine, M. C. *Acc. Chem. Res*. **2012**, *45*, 696-704.
(183) Potyrailo, R.A.; Nagraj, N.; Surman, C.; Boudries, H.; Lai, H.; Slocik, J. M.; Kelley-Loughnane, N.; Naik, R. R. *Trends Anal. Chem*. **2012**, *40*, 133-145.
(184) Harper, J. C.; Edwards, T. L.; Savage, T.; Harbaugh, S.; Kelley-Loughnane, N.; Stone, M. O.; Brinker, C. J.; Brozik, S. M. *Small* **2012**, *8*, 2743-2751.
(185) Eby, D. M.; Harbaugh, S.; Tatum, R. N.; Farrington, K. E.; Kelley-Loughnane, N.; Johnson, G. R. *Langmuir* **2012**, *28*, 10521-10527.
(186) Yang, S. H.; Kang, S. M.; Lee, K.-B.; Chung, T. D.; Lee, H.; Choi, I. S. *J. Am. Chem. Soc*. **2011**, *133*, 2795-2797.
(187) Gensel, J.; Borke, T.; Perez, N. P.; Fery, A.; Andreeva, D. V.; Betthausen, E.; Muller, A. H. E.; Mohwald, H.; Skorb, E. V. *Adv. Mater*. **2012**, *24*, 985-989.
(188) Nugaeva, N.; Gfeller, K. Y.; Backmann, N.; Lang, H. P.; Düggelin, M.; Hegner, M. *Biosens. Bioelectron.* **2005**, *21*, 849-856.
(189) De-Bashan, L. E.; Hernandez, J. P.; Morey, T.; Bashan, Y. *Water Res*. **2004**, *38*, 466-474.
(190) Altman, G. H.; Horan, R. L.; Lu, H. H.; Moreau, J.; Martin, I.; Richmond, J. C.; Kaplan, D. L. *Biomaterials* **2002**, *23*, 4131-4141.
(191) Altman, G. H.; Diaz, F.; Jakuba, C.; Calabro, T.; Horan, R. L.; Chen, J.; Lu, H.; Richmond, J.; Kaplan, D. L. *Biomaterials* **2003**, *24*, 401-416.
(192) Yucel, T.; Cebe, P.; Kaplan, D. L. *Biophys. J.* **2009**, *97*, 2044-2050.
(193) Wang, X.; Kluge, J. A.; Leisk, G. G.; Kaplan, D. L. *Biomaterials* **2008**, *29*, 1054-1064.
(194) Kretlow, J. D.; Klouda, L.; Mikos, A. G. *Adv. Drug Delivery Rev.* **2007**, *59*, 263–273.
(195) Lisunova, M. O.; Drachuk, I.; Shchepelina, O. A.; Anderson, K. D.; Tsukruk, V. V. *Langmuir* **2011**, *27*, 11157–11165.
(196) Shutava, T. G.; Balkundi, S. S.; Vangala, O.; Steffan, J. J.; Bigelow, R. L.; Cardelli, J. A.; O'Neal, D. P.; Lvov, Y. M. *ACS Nano* **2009**, *3*, 1877–1885.

(197) Kozlovskaya, V.; Harbaugh, S.; Drachuk, I.; Shchepelina, O.; Kelley-Loughnane, N.; Stone, M.; Tsukruk, V. V. *Soft Matter* **2011**, *7*, 2364–2372.
(198) Drachuk, I.; Shchepelina, O.; Lisunova, M.; Harbaugh, S.; Kelley-Loughnane, N.; Stone, M.; Tsukruk, V. V. *ACS Nano* **2012**, *6*, 4266–4278.
(199) Shchepelina, O.; Drachuk, I.; Gupta, M. K.; Lin, J.; Tsukruk, V. V. *Adv. Mater*. **2011**, *23*, 4655–4660.
(200) Drachuk, I.; Shchepelina, O.; Harbaugh, S.; Kelley-Loughnane, N.; Stone, M.; Tsukruk, V. V. *Small* **2013**, *9*, 3128-3137.
(201) Breitenkamp K.; Emrick, T. *J. Am. Chem. Soc*. **2003**, *125*, 12070–12071.
(202) Phillips, D. M.; Drummy, L. F.; Conrady, D. G.; Fox, D. M.; Naik, R. R.; Stone, M. O.; Trulove, P. C.; De Long, H. C.; Mantz, R. A. *J. Am. Chem. Soc*. **2004**, *126*, 14350-14351.
(203) Phillips, D. M.; Drummy, L. F.; Naik, R. R.; De Long, H. C.; Fox, D. M.; Trulove, P. C.; Mantz, R. A. *J. Mater. Chem*. **2005**, *15*, 4206-4208.
(204) Pristinski, D.; Kozlovskaya V.; Sukhishvili, S. A. *J. Opt. Soc. Am. A* **2006**, *23*, 2639–2644.
(205) Serban, M. A.; Kaplan, D. L. *Biomacromolecules* **2010**, *11*, 3406−3412.
(206) Murphy, A. R.; St. John, P.; Kaplan, D. L. *Biomaterials* **2008**, *29*, 2829−2839.
(207) Harbaugh, S.; Kelley-Loughnane, N.; Davidson, M.; Narayanan, L.; Trott, S.; Chushak, Y. G.; Stone, M. O. *Biomacromolecules* **2009**, *32*, 1610-1614.
(208) Lynch, S. A.; Gallivan, J. P. *Nucleic Acids Res*. **2009**, *37*, 184-192.
(209) Tsukruk, V. V.; Reneker, D. H. *Polymer* **1995**, *36*, 1791–1808.
(210) Glinel, K.; Sukhorukov, G. B.; Mohwald. H.; Khrenov, V.; Tauer, K. *Macromol. Chem. Phys.* **2003**, *204*, 1784-1790.
(211) Ibarz, G.; Dähne, L.; Donath, E.; Mohwald, H. *Chem. Mater*. **2002**, *14*, 4059-4062.
(212) Glinel, K.; Dubois, M.; Verbavatz, J.-M.; Sukhorukov, G. B.; Zemb, T. *Langmuir* **2004**, *20*, 8546-8551.
(213) Antipov, A. A.; Sukhorukov, G. B.; Donath, E.; Mohwald, H. *J. Phys. Chem. B* **2001**, *105*, 2281-2284.
(214) Antipov, A. A.; Sukhorukov, G. B. *Adv. Colloid Interface Sci*. **2004**, *111*, 49–61.
(215) Srivastava, S.; Kotov, N. *Acc. Chem. Res*. **2008**, *41*, 1831–1841.
(216) Dong, W.-F.; Liu, S.; Wan, L.; Mao, G.; Kurth D. G.; Mohwald, H. *Chem. Mater*. **2005**, *17*, 4992–4999.
(217) Kim, B.-S.; Lebedeva, O. V.; Koynov, K.; Gong, H.; Glasser, G.; Lieberwith I.; Vinogradova, O. I. *Macromolecules* **2005**, *38*, 5214–5222.
(218) Bedard, M. F.; Munoz-Javier, A.; Mueller, R.; del Pino, P.; Fery, A.; Parak, W. J.; Skirtach A. G.; Sukhorukov, G. B. *Soft Matter* **2009**, *5*, 148–155.
(219) Mueller, R.; Kohler, K.; Weinkamer, R.; Sukhorukov G.; Fery, A. *Macromolecules* **2005**, *38*, 9766–9771.
(220) Kozlovskaya V.; Sukhishvili, S. A. *Macromolecules* **2006**, *39*, 6191–6199.
(221) Markutsya, S.; Jiang, C.; Pikus Y.; Tsukruk, V. V. *Adv. Funct. Mater*. **2005**, *15*, 771–780.
(222) Jiang, C.; Markutsya S.; Tsukruk, V. V. *Langmuir* **2004**, *20*, 882–890.
(223) Kozlovskaya, V.; Kharlampieva, E.; Khanal, B. P.; Manna, P.; Zubarev E. R.; Tsukruk, V. V. *Chem. Mater*. **2008**, *20*, 7474–7485.
(224) Yang, S. Y.; Lee, D.; Cohen R. E.; Rubner, M. F. *Langmuir* **2004**, *20*, 5978–5981.
(225) Kozlovskaya, V.; Yakovlev, S.; Libera M.; Sukhishvili, S. A. *Macromolecules* **2005**, *38*, 4828–4836.
(226) Kozlovskaya, V.; Shamaev A.; Sukhishvili, S. A. *Soft Matter* **2008**, *4*, 1499–1507.
(227) Ariga, K.; Vinu, A.; Miyahara, M.; Hill J. P.; Mori, T. *J. Am. Chem. Soc*. **2007**, *129*, 11022–11023.
(228) Pristinski, D.; Kozlovskaya V.; Sukhishvili, S. A. *J. Chem. Phys*. **2005**, *122*, 0149071-0149079.
(229) Kharlampieva E.; Sukhishvili, S. A. *J. Macromol. Sci., Polym. Rev.* **2006**, *46*, 377–395.
(230) Lin-Vien, D.; Colthup, N. B.; Fateley, W. G.; Grasselli, G. G. in *The Handbook of Infrared and Raman Characteristics Frequencies of Organic Molecules*, Academic Press, Boston, **1991**, 45–57.
(231) Kozlovskaya, V.; Kharlampieva, E.; Mansfield, M.; Sukhishvili, S. A. *Chem. Mater*. **2006**, *18*, 328–336.

(232) Erel-Unal I.; Sukhishvili, S. A. *Macromolecules* **2008**, *41*, 3962–3970.
(233) Sukhishvili, S. A.; Granick, S. *Macromolecules* **2002**, *35*, 301–310.
(234) Shutava, T. G.; Prouty, M.; Kommireddy, D.; Lvov, Y. *Macromolecules* **2005**, *38*, 2850–2858.
(235) Jiang, C.; Singamaneni, S.; Merrick E.; Tsukruk, V. V. *Nano Lett*. **2006**, *6*, 2254–2259.
(236) Nolte, A. J.; Rubner M. F.; Cohen, R. E. *Macromolecules* **2005**, *38*, 5367–5370.
(237) Zhu, X.; DeGraaf, J.; Winnik, F. M.; Leckband, D. *Langmuir* **2004**, *20*, 10648–10656.
(238) Minko, S.; Muller, M.; Motornov, M.; Nitschke, M.; Grundke, K.; Stamm, M. *J. Am. Chem. Soc*. **2003**, *125*, 3896–3900.
(239) Cellesi, F.; Tirelli, N.; Hubbell, J. A. *Biomaterials* **2004**, *25*, 5115-5124.
(240) Kamath, K. P.; Park, K. *Adv. Drug Deliv. Rev.* **1993**, *11*, 59-84.
(241) Sukhishvili, S. A. *Curr. Opinion Colloid. Interface Sci.* **2005**, *10*, 37-44.
(242) Franz, B.; Balkundi, S. S.; Dahl, C.; Lvov, Y. M.; Prange, A. *Macromol. Biosci*. **2010**, *10*, 164-172.
(243) Diaspro, A.; Silvano, D.; Krol, S.; Cavalleri, O.; Gliozzi, A. *Langmuir* **2002**, *18*, 5047-5050.
(244) Wilson, J. T.; Krishnamurthy, V. R.; Cui, W.; Qu, Z.; Chaikof, E. L. *J. Am. Chem. Soc*. **2009**, *131*, 18228–18229.
(245) Tiourina, O. P.; Radtchenko, I.; Sukhorukov, G. B.; Mohwald, H. *J. Membrane Biol*. **2002**, *190*, 9-16.
(246) Henry, A. C.; Tutt, T. J.; Galloway, M.; Davidson, Y. Y.; McWhorter, C. S.; Soper, S. A.; McCarley, R. L. *Anal. Chem.* **2000**, *72*, 5331–5337.
(247) Venyaminov, S. Y.; Kalnin, N. N. *Biopolymers* **1990**, *30*, 1243–1257.
(248) Chang, M. C.; Tanaka, J. *Biomaterials* **2002**, *23*, 4811–4818.
(249) Izumrudov, V. A.; Kharlampieva, E.; Sukhishvili, S. A *Biomacromolecules* **2005**, *6*, 1782–1788.
(250) Moshnikova, A. B.; Afanasyev, V. N.; Proussakova, O. V.; Chernyshov, S.; Gogvadze, V.; Beletsky, I. P. *Cell. Mol. Life Sci.* **2006**, *63*, 229–234.
(251) Szarpak, A.; Cui, D.; Dubreuil, F.; De Geest, B. G.; De Cock, L. J.; Picart, C.; Auzely-Velty, R. *Biomacromolecules* **2010**, *11*, 713–720.
(252) Sukhishvili, S. A.; Kharlampieva, E.; Izumrudov, V. *Macromolecules* **2006**, *39*, 8873–8881.
(253) Fery, A.; Weinkamer, R. *Polymer* **2007**, *48*, 7221-7235
(254) Lulevich, V. V.; Andrienko, D.; Vinogradova, O. I. *J. Chem. Physics* **2004**, *120*, 3822-3826.
(255) Skirtach, A. G.; Yashchenok, A. M.; Mohwald, H. *Chem. Commun*. **2011**, *47*, 12736 -12746.
(256) Chanana, M.; Gliozzi, A.; Diaspro, A.; Chodnevskaja, I.; Huewel, S.; Moskalenko, V.; Ulrichs, K.; Galla, H. J.; Krol, S. *Nano. Lett*. **2005**, *5*, 2605–2612.
(257) Koguma, I.; Sugita, K.; Saito, K.; Sugo, T. *Biotechnol. Prog*. **2000**, *16*, 456–461.
(258) Dash, Ph. R.; Read, M. L.; Fisher, K. D.; Howard, K. A.; Wolfert, M.; Oupicky, D.; Subr, V.; Strohalm J.; Ulbrich, K.; Seymour, L. W. *J. Bio. Chemistry* **2000**, *275*, 3793-3802.
(259) Steffens, G. C. M.; Nothdurft, L.; Buse, G.; Thissen, H.; Hocker, H.; Klee, D. *Biomaterials* **2002**, *23*, 3523–3531.
(260) Omenetto, F. G.; Kaplan, D. L. *Nat. Photonics* **2008**, *2*, 641-643.
(261) Lewis, R. *Chem. Rev.* **2006**, *106*, 3762-3774.
(262) Omenetto, F. G.; Kaplan, D. L. *Science* **2010**, *329*, 528-531.
(263) Nogueira, G. M.; Swiston, A. J.; Beppu, M. M.; Rubner, M. F. *Langmuir* **2010**, *26*, 8953-8958.
(264) Jin, H.-J.; Kaplan, D. L. *Nature* **2003**, *424*, 1057-1061.
(265) Hermanson, K.; Huemmerich, D.; Sheibel, T. S.; Bausch A. R. *Adv. Mater*. **2007**, *19*, 1810-1815.
(266) Hermanson, K.; Harasim, M. B.; Sheibel, T. S.; Bausch A. R. *Phys. Chem. Chem. Phys.* **2007**, *9*, 6442-6446.
(267) Lammel, A.; Schwab, M.; Slotta, U.; Winter, G.; Scheibel, T. *Chem. Sus. Chem.* **2008**, *1*, 413-416.
(268) Jiang, C.; Wang, X.; Gunawidjaja, R.; Lin, Y. H.; Gupta, M.; Kaplan, D. L.; Naik, R. R.; Tsukruk, V. V. *Adv. Funct. Mater.* **2007**, *17*, 2229-2237.
(269) Drummy, L. F.; Phillips, D. M.; Stone, M. O.; Farmer, B. L.; Naik, R. R. *Biomacromolecules* **2005**, *6*, 3328-3333.

(270) Gupta, M. K.; Khokhar, S. K.; Phillips, D. M.; Sowards, L. A.; Drummy, L. F.; Kadakia, M. P.; Naik, R. R. *Langmuir* **2007,** *23*, 1315-1319.
(271) Nazarov, R.; Jin, H.-J.; Kaplan, D. L. *Biomacromolecules* **2004**, *5*, 718-726.
(272) Rammensee, S.; Huemmerich, D.; Hermanson, K. D.; Scheibel, T.; Bausch, A. R. *Appl. Phys. A* **2006**, *82*, 261-264.
(273) Sukhorukov, G. B.; Rogach, A. L.; Garstka, M.; Springer, S.; Parak, W. J.; Munoz Javier, A.; Kreft, O.; Skirtach, A. G.; Susha, A. S.; Ramaye, Y.; Palankar, R.; Winterhalter, M. *Small* **2007**, *3*, 944-955.
(274) De Geest, B. G.; De Koker, S.; Sukhorukov, G. B.; Kreft, O.; Parak, W. J.; Skirtach, A. G.; Demeester, J.; De Smedt, S. C.; Hennink, W. E. *Soft Matter* **2009**, *5*, 282-291.
(275) Shulha, H.; Foo, C. W. P.; Kaplan, D. L.; Tsukruk, V. V. *Polymer* **2006**, *47*, 5821-5830.
(276) Chao, P.-H. G.; Yodmuang, S.; Wang, X.; Sun, L.; Kaplan, D. L.; Vunjak-Novakovic, G. *J. Biomed. Mater. Res., Part B* **2010**, *95*, 84-90.
(277) Murphy, A. R.; John, P. S.; Kaplan, D. L. *Biomaterials* **2008**, *29*, 2829-2838.
(278) Eisoldt, L.; Smith, A.; Scheibel, T. *Mater. Today* **2001**, *14*, 80-86.
(279) Vollrath, F. *Nature* **2010**, *466*, 319-319.
(280) Xu, M.; Lewis, R. V. *Proc. Natl. Acad. Sci. U.S.A.* **1990**, *87*, 7120-7124.
(281) Buehler, M.J.; Yung, Y.C. *Nature Mater*. **2009**, *8*, 175-188.
(282) Young, S. L.; Gupta, M.; Hanske, C.; Fery, A.; Scheibel, T.; Tsukruk, V. V. *Biomacromolecules* **2012,** *13*, 3189-3199.
(283) Vepari, C.; Kaplan, D. L. *Prog. Polym. Sci.* **2007**, 32, 991-1007.
(284) Jin, H. J.; Kaplan, D. L. *Nature* **2003**, *424*, 1057-1061.
(285) Leal-Egaña, A.; Scheibel, T. *Biotechnol. Appl. Biochem.* **2010**, *55*, 155-167.
(286) Wang, X.; Kluge, J. A.; Leisk, G. G.; Kaplan, D. L. *Biomaterials* **2008**, *29*, 1054-1064.
(287) Haider, M.; Cappello, J.; Ghandehari, N.; Leong, K. W. *Pharm. Res.* **2008**, *25*, 692-699.
(288) Kharlampieva, E.; Zimnitsky, D.; Gupta, M.; Bergman, K. N.; Kaplan, D. L.; Naik, R. R.; Tsukruk, V. V. *Chem. Mater.* **2009**, *21*, 2696-2704.
(289) Kharlampieva, E.; Kozlovskaya, V.; Gunawidjaja, R.; Shevchenko, V. V.; Vaia, R.; Naik, R. R.; Kaplan, D. L.; Tsukruk, V. V. *Adv. Funct. Mater.* **2010**, *20*, 840-846.
(290) Ariga, K.; Ito, H.; Hill, J. P.; Tsukube, H. *Chem Soc Rev*. **2012**, *41*, 5800-5835.
(291) Caruso, F.; Trau, D.; Mohwald, H.; Renneberg, R. *Langmuir* **2000**, *16*, 1485-1488.
(292) Macdonald, M. L.; Samuel, R. E.; Shah, N. J.; Padera, R. F.; Beben, Y. M.; Hammond, P. T. *Biomaterials* **2011**, *32*, 1446-1453.
(293) Pantos, A.; Tsiourvas, D.; Paleos, C. M.; Nounesis, G. *Langmuir* **2005** *21*, 6696-6702.
(294) Zelikin, A. N. *ACS Nano* **2010** *4*, 2494-2509.
(295) Mertz, D.; Wu, H.; Wong, J. S.; Cui, J.; P. Tan, R. Alles, F. Caruso, *J. Mater. Chem.* **2012**, *22*, 21434-21442.
(296) Eisoldt, L.; Hardy, J. G.; Heim, M.; Scheibel, T. R. *J. Struct. Biol.* **2010**, *170*, 413-419.
(297) Foo, C. W. P.; Bini, E.; Hensman, J.; Knight, D. P.; Lewis, R. V.; Kaplan, D. L. *Appl. Phys. A* **2006**, *82*, 223-233.
(298) Ye, C.; Shchepelina, O.; Calabrese, R.; Drachuk, I.; Kaplan, D. L.; Tsukruk, V. V. *Biomacromolecules* **2011,** *12*, 4319-4325.
(299) Wallet, B.; Kharlampieva, E.; Campbell-Proszowska, K.; Kozlovskaya, V.; Malak, S.; Ankner, J. F.; Kaplan, D. L.; Tsukruk, V. V. *Langmuir* **2012**, *28*, 11481-11489.
(300) Gupta, M. K.; Singamaneni, S.; McConney, M.; Drummy, L. F.; Naik, R. R.; Tsukruk, V. V. *Adv. Mater*. **2010**, *22*, 115-119.
(301) Wang, X.; Kim, H. J.; Hu, P. X.; Matsumoto, P.; Kaplan, D. L. *Langmuir* **2005**, *21*, 11335-11341.
(302) Kharlampieva, E.; Slocik, J. M.; Singamaneni, S.; Poulsen, N.; Kroger, N.; Naik, R. R.; Tsukruk, V. V. *Adv. Funct. Mater.* **2009**, *19*, 2303-2311.
(303) Payet, L.; Ponton, A.; Leger, L.; Hervet, H.; Grossiord, J. L.; Agnely, F. *Macromolecules* **2008**, *41*, 9376-9381.

(304) Antipov, A. A.; Sukhorukov, G. B.; Donath, E.; Mohwald, H. *J. Phys. Chem. B* **2001**, *105*, 2281-2284.
(305) Milner-White, E. J.; Poet, R. *Trends Biochem. Sci.* **1987**, *12*, 189-192.
(306) Stevenson, C. L. *Curr. Pharm. Biotechnol.* **2000**, 1, 165-182.
(307) Kim, U.-J.; Park, J.; Li, C.; Jin, H.-J.; Valluzzi, R.; Kaplan, D. L. *Biomacromolecules* **2004**, *5*, 786-792.
(308) Vrbka, L.; Vondrasek, J.; Jagoda-Cwiklik, B.; Vacha, R.; Jungwirth, P. *Proc. Natl. Acad. Sci. U. S. A.* **2006**, *103*, 15440-15444.
(309) Serdakowski, A. L.; Dordick, J. S. *Trends Biotechnol.* **2008**, *26*, 48-54.
(310) Zhou, C. Z.; Confalonieri, F.; Jacquet, M.; Perasso, R.; Li, Z. G.; Janin, J. *Proteins* **2001**, *44*, 119–122.
(311) Asakura, T.; Suita, K.; Kameda, T.; Afonin, S.; Ulrich, A. S. *Magn. Reson. Chem*. **2004**, *42*, 258–66.
(312) Drachuk, I, Gupta, M. Tsukruk, V. V. *Adv. Funct. Meter.* **2013**, *23*, 4437-4453.
(313) Fischer, D.; Li, Y. X.; Ahlemeyer, B.; Krieglstein, J.; Kissel, T. *Biomaterials* **2003**, *24*, 1121–1131.
(314) Lvov, Y. in *Protein architecture: Electrostatic layer-by-layer assembly of proteins and polyions*, (Eds. Y. Lvov, H. Mohwald), Marcel Dekker, Inc. New Yokr, NY, **2000**.
(315) Okamoto, T.; Suzuki, T.; Yamamoto, N. *Nat. Biotechnol*. **2000**, *18*, 438-441.
(316) Roda, A.; Guardigli, M.; Russo, C.; Pasini, P.; Baraldini, M. *Biotechniques* **2000**, *28*, 492-496.
(317) Roth, E. A.; Xu, T.; Das, M.; Gregory, C.; Hickman, J. J.; Boland, T. *Biomaterials* **2004**, *25*, 3707-3715.
(318) Xu, T.; Petridou, S.; Lee, E. H.; Roth, E. A.; Vyavahare, N.; Hickman, J. J.; Boland, T. *Biotechnol. Bioeng*. **2004**, *85*, 29-33.
(319) Ringeisen, B. R.; Pirlo, R. K.; Wu, P. K.; Boland, T.; Huang, Y.; Sun, W.; Hamid, Q.; Chrisey, D. B. *MRS Bull.* **2013**, *38*, 834-843.
(320) Xu, T.; Jin, J.; Gregory, C.; Hickman, J. J. Boland, T. *Biomaterials* **2005**, *26*, 93-99.
(321) Zheng, Q.; Lu, J.; Chen, H.; Huang, L.; Cai, J.; Xu, Z. *Anal. Biochem.* **2011**, *410*, 171-176.
(322) Nakamura, M.; Nishiyama, Y.; Henmi, C. In *Micro-Nano Mechatronics and Human Science, MHS 2008. International Symposium on IEEE*, **2008,** 451-456.
(323) Matsusaki, M.; Sakaue, K.; Kadowaki, K.; Akashi, M. *Adv. Healthcare Mater*. **2013**, *2*, 533-533.
(324) Hossain, S. M. Z.; Luckham, R. E.; Smith, A. M.; Lebert, J. M.; Davies, L. M.; Pelton, R. H.; Filipe, C. D. M.; Brennan, J. D. *Anal. Chem.* **2009**, *81*, 5474–5483.
(325) Cerf, A., Cau, J. C., Vieu, C., Dague, E. *Langmuir* **2009**, *25*, 5731-5736.
(326) Bolshakova, A. V., Kiselyova, O. I., Yaminsky, I. V. *Biotechnol. Prog.* **2004**, 20, 1615-1622.
(327) Ringeisen, B. R.; Othon, C. M.; Barron, J. A.; Young, D.; Spargo, B. J. *Biotechnol. J.* **2006**, *1*, 930–948.
(328) Cui, X.; Dean, D.; Ruggeri, Z. M.; Boland, T. *Biotechnol. Bioeng.* **2010**, *106*, 963-969.
(329) Mitchell, G. J.; Wiesenfeld, K.; Nelson, D. C.; Weitz, J. S. *J. R. Soc. Interface* **2013**, *10*, 1-7.
(330) Balkundi, S. S.; Veerabadran, N. G.; Eby, D. M.; Johnson, G. R. *Langmuir* **2009**, *25*, 14011-14016.
(331) Wang, S.; Guo, Z. *Colloids Surf., B* **2014**, *113*, 483-500.